Multiparameter Optical Diagnostics for High-Speed Flow Applications



Kharthik Chakravarthy

Somerville College

University of Oxford

A thesis submitted for the degree of

Doctor of Philosophy

Michaelmas 2021

Abstract

This thesis details the development of two multiparameter spatially-resolved optical diagnostic techniques for research in high-speed flow applications. This is motivated by the need to extract as much information as possible in physics-coupled, multidimensional flows, and flows generated in short duration test facilities.

Fluorescent Particle Image Velocimetry (FPIV) was developed with the aim of being widely accessible as a simultaneous velocimetry and thermometry tool for coupled fluid momentum and heat transport investigations. Alternative strategies to provide such simultaneous measurements exist, but these are typically more complex, expensive and invasive to implement, making them less conventional. To achieve this, droplet-based Planar Laser-Induced Fluorescence (PLIF) was added to PIV, enabling the use of a single tracer for measuring both velocity and temperature. This work focused on the novel discovery of temperature-dependent fluorescence properties of di-ethylhexyl sebacate (DEHS), an established PIV seeding substance. Liquid DEHS was found to be excitable by the fourth harmonic of an Nd:YAG laser, leading to a weak, but measurable ultraviolet (UV) fluorescence signal. Two Colour PLIF applied to liquid DEHS demonstrated a temperature-dependent red-shift, yielding a sensitivity of $0.019\,\mathrm{K}^{-1}$. A change in fluorescence properties was evident in droplet form, but this was still temperature-dependent albeit with a reduced sensitivity of $0.011\,\mathrm{K}^{-1}$. This discovery has the potential to make joint velocity and temperature measurements available to a wide audience of existing PIV users.

Polarised-depolarised Rayleigh Scattering was developed for simultaneous composition and temperature measurements in transpiration cooling, to enhance understanding of flow mixing interactions and cooling mechanisms. Previous experimental investigations of this cooling technology have focused mainly on surface temperature measurements, so this development would provide additional useful information about the effect of coolant coverage and effusion pathways. A bench-top demonstration of the technique achieved good quality results, with a mean signal-to-noise ratio of 7.5. The technique was then applied in a simultaneous experimental framework with infrared thermography to obtain combined gas composition, gas temperature, and surface temperature measurements in order to infer the internal cooling mechanisms of transpiring porous media. This framework was applied in a 1-D manner to extract the volumetric heat transfer coefficient for candidate transpiration cooling materials. Results demonstrated the enhanced ability of carbon-fiber-reinforced carbon composites over zirconium diboride Ultra High Temperature Ceramics for internal cooling, both of which are strong contenders for this technology. This discovery improves the accuracy of complete transpiration cooling systems-level designs, bringing the technology one step closer to implementation.

Acknowledgements

This thesis and the research that I have produced over the last 4 years would not have been possible without the support, advice, encouragement and guidance from a number of people.

My first and foremost thanks goes to my supervisor, Professor Ben Williams. I was privileged to be able to work with him as an undergraduate student on 2 projects - it was due to the interesting and challenging nature of these projects that I gained an interest in optical diagnostics, and decided to pursue a DPhil. His ability to explain the most complex theories, and patience to elaborate on the most simple concepts made my research experience a thoroughly enjoyable one. His supportive and understanding disposition kept me constantly motivated, and eager to deliver the best outcome. I owe most of my success in this thesis to his excellent supervision.

I am grateful to Professor Matthew McGilvray for welcoming me into the Hypersonics Research Group and for guiding the direction of my research, especially in applying diagnostics to high-speed flows. Many thanks also to Professor Richard Stone for giving me a place in the Thermal Propulsion Systems Research Group (TPSRG) and for providing advice and lending a hand whenever and wherever he could.

This research would not have materialised without the funding I received from the Oxford-Qatar Thatcher Scholarship from Somerville College. Alongside the financial support, I am grateful for the weekly development events, networking opportunities and personalised support I received from the Margaret Thatcher Scholarship Trust and Dr Claire Cockcroft. Thank you for providing me with a safety net during my time at Oxford and for making me feel like I could achieve anything I wanted.

I will forever be indebted to Dr Laurent Le Page, Dr-Ing Tobias Hermann and Dr Chris Willman who dedicated so much of their time and effort towards my research. Their invaluable knowledge, experience and expertise in optical diagnostic techniques as well as general numerical modelling turned out to be key factors for the success of my experiments. Their willingness to lend a hand whenever I needed it has not gone unnoticed. I am eternally grateful for all their support and encouragement.

I would like to thank the members of the TPSRG for creating a welcoming day-to-day atmosphere in the office, and for the frequent helping hand I received throughout my time here. Specifically to Sam Shen, thank you for your time and commitment dealing with fluorescence measurements and

visits to the spectrophotometer in the Physics Department! I am also grateful to Hassan, Marc, Imran and Michael from the Oxford Thermofluids Institute for their support in all things related to high-speed flows; from designing and assembling porous samples to general considerations of high-speed fluid dynamics. A special mention also goes to the support staff of the Engineering Science department, without whom, this DPhil would not have been possible.

To Maruthi, Hannah and Priyav, thank you for so many things - the late nights working together, the Marvel cinema viewings, the formal dinners, the punting trips and the birthday surprises. Your friendship made this entire experience immensely enjoyable, and dare I say it, worth repeating. To my housemates, squash and Somerville friends, notably Zach, Linus, Tai, Milad, Safa, Sebastian, Ignacia, Crescente, Carissa, Greg, Tomas and Gabriella - thank you for making the tough times easier and the good times better.

To Sajni - thank you for always being there, whether to hear me rant about a failed experiment, or to celebrate when things were finally working. You constantly believed in me and encouraged me to keep pushing, which fuelled me to try harder and not give up. To my mother, brother, sister-in-law and niece - thank you for your continued support, encouragement, love and care. You've all been a pillar of support for me throughout this experience, and I will always be grateful for that. I promise I will have more time for all of you from now on!

Finally to my dad. Thank you for everything. This thesis is dedicated to you - I hope I made you proud.

Contents

1 Introduction **1**
1.1 Motivation . . . 1
1.1.1 High-speed flow research . . . 1
1.1.2 Optical diagnostics . . . 2
1.1.3 Transpiration cooling . . . 4
1.2 Thesis objectives . . . 6
1.3 Thesis structure . . . 7

2 Background and Literature Review **9**
2.1 Particle Image Velocimetry (PIV) . . . 9
2.1.1 Basic theory . . . 9
2.1.2 Technique implementation . . . 11
2.1.3 Criteria for successful application . . . 15
2.1.4 Elastic scatter limitation . . . 22
2.2 Planar Laser Induced Fluorescence (PLIF) . . . 24
2.2.1 Basic theory . . . 24
2.2.2 Technique variations . . . 28
2.2.3 Droplet PLIF . . . 31
2.2.4 Tracer thermal equilibrium . . . 34
2.3 Rayleigh scattering . . . 38
2.3.1 Basic theory . . . 38
2.3.2 Simultaneous mixture fraction and temperature measurements . . . 39
2.3.3 Polarised-depolarised Rayleigh scattering (PDRS) . . . 40
2.3.4 Criteria for successful application . . . 44
2.4 Infrared (IR) thermography . . . 46
2.4.1 Basic theory . . . 46
2.4.2 Detection wavelengths . . . 50
2.4.3 IR measurement parameters . . . 51
2.5 Summary . . . 53

3 Particle Image Velocimetry **55**
3.1 Experimental setup . . . 55
3.2 PIV of flow past a cylinder . . . 60
3.2.1 Test section and procedure . . . 60
3.2.2 Results and analysis . . . 63
3.3 PIV of a fluidic switching device . . . 73
3.3.1 Test section and problem summary . . . 73
3.3.2 Results and analysis . . . 76
3.4 Summary . . . 78

4 Fluorescent Particle Image Velocimetry **79**
4.1 Elastic scatter reduction . . . 82
4.2 Candidate tracers for FPIV . . . 88
4.3 Properties of DEHS . . . 92
4.3.1 Liquid DEHS fluorescence spectra . . . 94
4.3.2 Fluorescence photobleaching of DEHS . . . 100

4.4 Droplet TC-PLIF . . . 105
4.4.1 Equipment and optics for DEHS TC-PLIF . . . 105
4.4.2 Proof of concept experiment . . . 108
4.4.3 Post-processing procedure . . . 116
4.4.4 Droplet DEHS fluorescence spectra . . . 120
4.4.5 Results and discussion . . . 124
4.5 Liquid vs droplet DEHS emission . . . 130
4.5.1 Phosphorescence . . . 131
4.5.2 Whispering Gallery Modes . . . 135
4.5.3 DEHS degradation . . . 139
4.6 Summary . . . 141

5 Polarised-Depolarised Rayleigh Scattering 143
5.1 Sensitivity analysis . . . 143
5.2 Demonstration of diagnostic . . . 150
5.3 Summary . . . 158

6 Internal Heat Transfer Modelling of Transpiring Porous Media 159
6.1 Motivation . . . 159
6.2 Theory of heat transport within porous media . . . 161
6.3 Impulse response convolution method . . . 164
6.4 Solid-fluid system behaviour . . . 168
6.5 Numerical scheme implementation . . . 173
6.5.1 Lateral heat loss estimation . . . 175
6.5.2 Code implementation . . . 178
6.5.3 Uncertainty analysis . . . 181
6.6 Summary . . . 182

7 Volumetric Heat Transfer Coefficient Measurements 183
7.1 Methodology . . . 183
7.2 Porous samples . . . 188
7.3 Method development . . . 190
7.3.1 Preliminary results . . . 191
7.3.2 Bottom surface temperature improvement . . . 196
7.4 Measurement calibrations . . . 197
7.4.1 Sample emissivity and initial ambient radiation . . . 197
7.4.2 Dynamic reflected temperature compensation . . . 201
7.4.3 Through flow area . . . 205
7.5 Data post-processing . . . 206
7.6 Results and discussion . . . 209
7.6.1 Siperm B: Packed bed of sintered bronze spheres . . . 213
7.6.2 UHTC: Zirconium diboride Ultra High Temperature Ceramic . . . 216
7.6.3 C/C: Carbon-fiber-reinforced carbon composite . . . 218
7.7 Summary . . . 220

8 Conclusions 222
8.1 Research summary . . . 222
8.1.1 Particle Image Velocimetry . . . 222
8.1.2 Fluorescent Particle Image Velocimetry . . . 223
8.1.3 Polarised-depolarised Rayleigh scattering . . . 224
8.1.4 Internal cooling of porous media . . . 225
8.2 Future prospects . . . 226

8.2.1 Fluorescent Particle Image Velocimetry 226
8.2.2 Polarised-depolarised Rayleigh scattering 228

Bibliography **230**

9 Appendix **239**
9.1 Application of PDRS to the Oxford HDT 239
9.1.1 Optical access 241
9.1.2 Other sources of elastic scattering 243
9.1.3 Achievable SNR 245
9.1.4 Summary of HDT feasibility 249
9.2 Improvements to diagnostics 250
9.2.1 Fluorescent Particle Image Velocimetry 250
9.2.2 Polarised-depolarised Rayleigh scattering 252

Chapter 1

Introduction

This thesis details the bench-top development of two multiparameter optical diagnostic techniques for use in research of high-speed flow applications. Chapter 1 begins by introducing the 'big picture' motivation behind this research. The specific objectives of this work which form a more narrow scope, are subsequently elaborated, followed by a description of the thesis structure.

1.1 Motivation

1.1.1 High-speed flow research

High-speed flows (encompassing high subsonic to hypersonic speeds) are encountered in various applications, for example in space flight, rocketry, defence weaponry and aviation. A rise in popularity and relevance of such applications is evident in recent years. One illustration of this is the renewed interest in designing reusable spacecrafts, spearheaded by institutions such as NASA, SpaceX and Boeing. The search for a suitable thermal protection system (TPS), that will protect vehicles from extreme heat loads experienced during atmospheric re-entry, is a principal challenge in fully realising this. Another example is the increasing recognition of the role played by the aviation industry in contributing towards climate change. Data collected for 2018 revealed that aviation accounted for 2.5 % of all CO_2 emissions, and 3.5 % of 'effective radiative forcing' (a measure of effective global warming) when non-CO_2 emissions are included [1, 2]. These figures are expected to increase in the years to come as demand for global aviation increases. In all such applications, experimental research of high-speed flows plays an integral part in informing novel technologies and establishing design criteria that will address challenges faced.

1.1.2 Optical diagnostics

In light of this, optical diagnostic techniques have been established as the preferred mode of experimental validation in thermo-fluids research. They show considerable advantages over their traditional counterparts (physical probes like thermocouples and pitot-static tubes). They can be multidimensional, non-intrusive, adaptable, accurate, and precise. Such qualities are desirable when measuring physical quantities in a fluid, such as velocity, temperature, concentration and pressure, as they produce an accurate representation of the processes taking place.

One significant disadvantage of optical diagnostic techniques is their substantial cost and higher complexity to implement. Several specialised pieces of optical equipment, such as cameras, lasers and optics, are required to perform these techniques. These items are expensive, and their costs increase significantly if refined functionalities are required (e.g. needing higher repetition rates or finer spatial resolution). Successful implementation of these techniques also requires specialist skill and substantial experience from the user. These disadvantages are severely inhibiting, especially when optical techniques are applied in high-speed flow research, for several reasons.

Many high-speed flows require specialised facilities to be generated, examples of which include shock tubes, supersonic wind tunnels and Ludwieg tubes. The test time (i.e. the duration for which relevant flow conditions are established) is generally short, ranging in the order of microseconds to several seconds depending on the facility [3]. Continuous operation is typically not possible, so a limited amount of experimental data is acquired per 'run' of the facility. In addition, there is usually a non-negligible turnover time to reset the facility - this constraints the amount of data that can be collected per unit time. These sorts of facilities are also few in number, due to the inherent complexity in their design and high costs to manufacture and maintain. Thus, it is typical for such facilities to operate on the basis of fixed duration experimental campaigns, to accommodate a large number of projects and investigations from internal and external collaborators.

Many such flow facilities have also not been built with the intention of applying optical diagnostics. This leads to problems such as reduced optical access for lasers or detectors, and reduced signal-to-noise ratio, which can increase complexity of their application. The compounded effect of significant complexities and specialist skill requirement in implementing optical diagnostic techniques to high-speed flows, reduces the probability of successful data collection from each 'run'. Coupling this to the limited amount of data that can be acquired from a finite investigation time, makes the cost of optical systems per unit data extremely high. Research of high-speed flows would benefit significantly from the use of optical diagnostic techniques, if more data or information could be acquired from the same system, i.e. for the same cost, in a single 'run'.

It should be noted that not all research of high-speed flow applications requires use of these facilities, or *actually* generating high-speed flow conditions, as is the case in this thesis. Nonetheless, a number of limitations to optical diagnostic techniques exist, even when applied to low-speed characterisations that are relevant to the application. Many useful techniques produce single parameter results. While this is generally useful, a large proportion of high-speed flow applications involve coupling of physics, the most common of which is that of momentum and heat transfer. An example of such an application is transpiration cooling, introduced as the application of interest for this work in the following section. Fluid parameters such as velocity, pressure, concentration, and temperature become inter-dependent in such flows, and so furthering understanding can only be achieved by making simultaneous multiparameter measurements that can highlight these inter-dependencies. This is typically achievable by compounding several optical techniques simultaneously, which has widely been employed in the literature. As before, this leads to a significant increase in cost and complexity. Specific examples include using more than one laser beam, camera, and flow tracer.

For these reasons, this work aims to develop and advance cost-effective multiparameter optical diagnostic techniques, with a particular focus of using them in high-speed flow research. Two

specific diagnostics were chosen for their significant potential to add value to transpiration cooling research. These techniques are introduced in the subsequent section. This study begins by identifying inherent requirements and limitations to the chosen techniques, which could be detrimental when used for transpiration cooling. Variants of these techniques are subsequently proposed to combat the identified limitations. Finally, each technique is characterised for its feasibility, tested in proof-of-concept experiments, and applied in bench-top transpiration cooling experiments to add value. It should be noted, that while this work details the development and specifically addresses the potential use of some optical diagnostics *in high-speed flows*, no actual implementation in such flows was attempted.

1.1.3 Transpiration cooling

Transpiration cooling is the high-speed flow application of interest in this work. It is a cooling technology proposed for use as a TPS on hypersonic vehicles, as well as in jet engine turbine stage components. Figure 1.1 shows a schematic of how transpiration cooling is implemented, specifically in the case of a hypersonic vehicle.

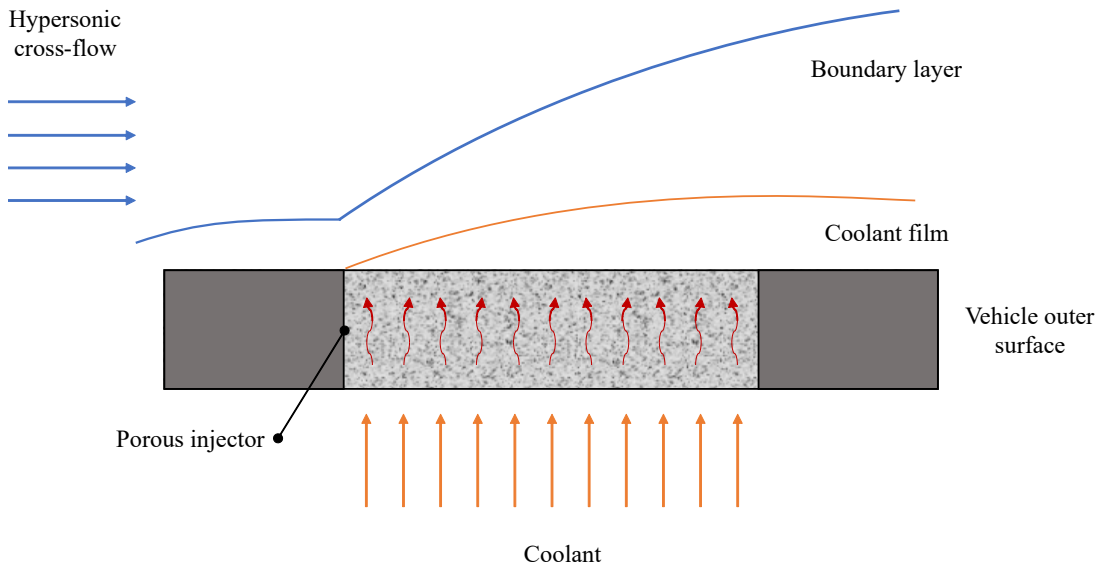


Figure 1.1: Schematic of transpiration cooling as a TPS applied to a hypersonic vehicle

Transpiration cooling is an active cooling technology that involves injecting coolant gas into an external boundary layer. In hypersonic vehicles, this is through a porous material that forms part of the vehicle's external surface. In jet engines, this is through holes or slots on turbine blades. There are several mechanisms through which this technology achieves cooling. Firstly, heat is exchanged between the hot solid structure and the coolant during internal effusion. Next, convection of coolant by the external boundary layer covers the downstream solid surface with a lower temperature fluid film that reduces incident heat flux. Specifically in hypersonic vehicles, this protective film prevents recombination reactions and catalytic heating typically encountered in high-enthalpy flows from taking place near the vehicle surface, which can otherwise increase the heat load. Additionally, an inert protective film allows surface materials to operate at higher temperatures without risk of oxidation, maintaining material strength and enabling enhanced radiative cooling. Transpiration cooling promotes re-usability and improved shape stability of hypersonic vehicles, which are significant advantages compared to ablation-based TPS.

To investigate the applicability of transpiration cooling for gas turbines, fundamental flow mixing mechanisms between coolant and external boundary layer need to be examined in detail. Here, coupling between flow speed and temperature is relevant, so such investigations require a suitable diagnostic technique that provides simultaneous near wall velocity and temperature measurements. The long-term goal (not attempted in this thesis) would be to make such measurements in a large-scale low speed wind tunnel in order to highlight the velocity-temperature inter-dependencies in transpiration cooling with enhanced resolution.

To investigate the efficiency of transpiration cooling for hypersonic vehicles, analysis of internal coolant effusion, external film formation, and heat transfer effectiveness is required. Here, simultaneous gas composition and temperature measurements would adequately highlight the effect of mixing and heat transfer between two gas streams. Such characterisations of the various cooling mechanisms may be achieved using both bench-top experiments, as well as in a hypersonic flow

facility - this work focuses only on the former.

1.2 Thesis objectives

Fluorescent Particle Image Velocimetry (FPIV) is developed as a simultaneous velocimetry and thermometry tool for transpiration cooling investigations. The overall aim of developing FPIV in this thesis is to extend the use of Particle Image Velocimetry (PIV) to incorporate simultaneous temperature measurements through the addition of droplet-based Laser-Induced Fluorescence (LIF). To achieve this, the following objectives are set out:

- Identify the requirements for successful application of FPIV in high-speed flows
- Assemble a PIV system from scratch and test it on several flows over a range of speeds
- Demonstrate the ability of FPIV to make near-wall measurements
- Identify and characterise a suitable fluorescent tracer for transpiration cooling research
- Demonstrate the use of FPIV in a proof-of-concept experiment

Polarised-depolarised Rayleigh Scattering (PDRS) is developed as an optical diagnostic technique for simultaneous gas composition and temperature measurements. This diagnostic technique is relatively new, and has only seen use in combustion applications. The overall aim of developing PDRS is to apply it in a relevant transpiration cooling investigation. To achieve this, the following objectives are set out:

- Identify key criteria for successful application of PDRS in mixing flows
- Characterise the sensitivity of PDRS for gas mixtures relevant to transpiration cooling
- Demonstrate the use of PDRS in a proof-of-concept experiment
- Apply PDRS to a transpiration cooling characterisation

It should be noted again that this work focuses on developing and extending two novel diagnostic

techniques on bench-top configurations, with the long-term goal of applying them in high-speed flows. No wind tunnel experiments were conducted by the time of submission of this thesis.

1.3 Thesis structure

This section describes the structure of the thesis. In general, chapters can be grouped together based on their relevance as follows. Chapters 1 and 2 introduce the research and its motivations, Chapters 3 and 4 describe the development of FPIV, Chapters 5 to 7 present the development of PDRS, and Chapter 8 summarises the thesis' findings. The chapters are intended to lead on from one another. One exception is that the PIV chapters (3 and 4) are not related to the PDRS chapters (5 to 7), as they each detail parallel developments towards their individual goals.

The current chapter highlights the motivation and goals for this research. Chapter 2 introduces all the fundamental optical diagnostic techniques employed in this work, namely PIV, LIF, Rayleigh scattering and infrared (IR) thermography. Working principles of each technique are detailed, alongside a review of literature highlighting key considerations and limitations.

The assembly and test of a PIV system built in-house for high-speed velocity measurements is described in Chapter 3. Two experiments are discussed, the first of which tests the system for its veracity, and the second detailing its use in a novel device employing high-speed flow. Chapter 4 explores the FPIV technique, as a means to overcome one of the main limitations of PIV, while establishing itself as a simultaneous velocimetry and thermometry tool for gas flows. Particular focus is devoted towards the discovery and development of a novel fluorescent tracer, that will widen the reach of this diagnostic in the thermofluids research community.

In Chapter 5, the use of PDRS in non-combusting gaseous mixtures is explored. This involves a combination of numerical and experimental analyses, quantifying key criteria such as expected uncertainty and signal-to-noise ratio. Chapters 6 and 7 subsequently apply PDRS and IR thermography to a relevant investigation in transpiration cooling. A combined numerical and ex-

perimental framework is introduced, for investigating internal cooling mechanisms of porous materials during coolant effusion.

Research achievements are finally summarised in Chapter 8. Additionally, prospects for future investigations and further improvements to each diagnostic are explored.

Chapter 2

Background and Literature Review

This chapter presents established background and theory of the various optical diagnostics employed in this work. Emphasis is provided on the operating principle of each diagnostic, along with specific implementation details relevant to the experiments discussed in subsequent chapters. A review of the literature is also presented to highlight key developments and limitations of each diagnostic. Techniques elaborated in this chapter include Particle Image Velocimetry, Planar Laser-Induced Fluorescence, Rayleigh scattering and infrared thermography.

2.1 Particle Image Velocimetry (PIV)

2.1.1 Basic theory

Particle Image Velocimetry (PIV) is a laser-based interrogation technique, used to measure the velocity field in a moving fluid. Small-sized particles or droplets are introduced into a flow, with the aim of closely tracking the fluid motion. When a sheet of high-powered laser light illuminates the flow, these particles scatter light in all directions (a phenomenon known as Mie scatter). A suitable camera can then be used to capture this light, producing images of particle distribution in the flow. In PIV, the flow is illuminated twice, separated by a known time interval, producing a pair of images in which the particles have moved slightly. These images can then be processed using statistical interrogation techniques in order to determine the displacement of groups of particles, thus leading to a flow velocity field. Figure 2.1 shows an illustration of a typical PIV experimental configuration.

The velocity field mapping begins by dividing PIV images into square interrogation windows.

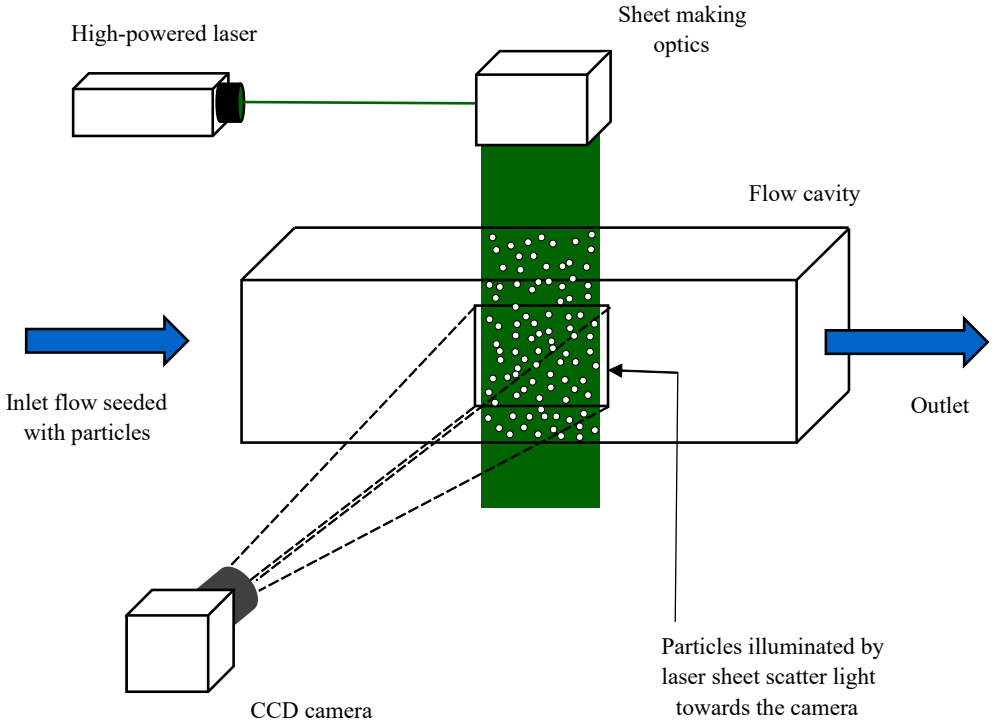


Figure 2.1: Illustration of a typical PIV setup

Each window in the first frame is cross-correlated with a search domain in the second frame. A peak in the cross-correlation function yields information about the displacement and direction of movement of the region in question, thus producing vector arrows across the images. This process is described in Figure 2.2. An image of a calibration grid, and the known time interval between frames, is then typically used to convert the units of these vectors from pixels per frame, into meters per second.

The accuracy of PIV velocity reconstruction can be brought down to sub-pixel levels. This is achieved by applying a Gaussian interpolation around a cross-correlation peak to find the exact displacement. Sub-pixel interpolation introduces a constraint to PIV implementations - particle image sizes should ideally be 2 to 3 pixels, in order to accurately resolve the shape of the Gaussian peak in the cross-correlation function. Single-pixel sized particles (or smaller) can lead to the phenomenon known as 'peak-locking', where reconstructed velocities have a bias towards integer values. An illustration of the impact this has on a velocity histogram is shown in Figure 2.3.

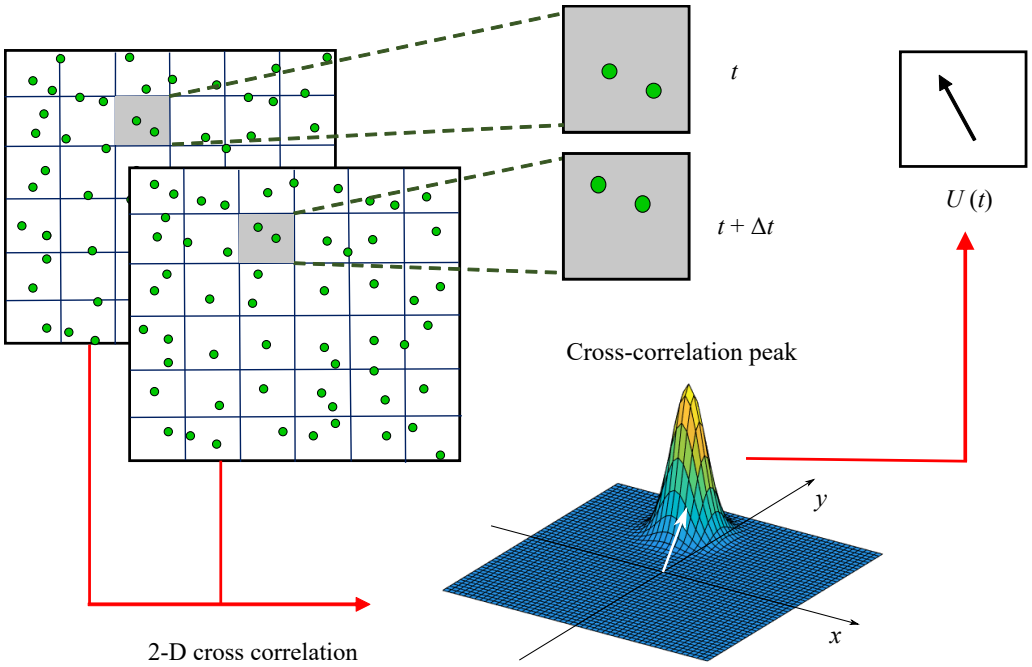


Figure 2.2: Cross-correlation algorithm which produces vectors throughout the image (adapted from [4])



Figure 2.3: Peak-locked reconstructions compared to data that has been resolved to sub-pixel accuracy

2.1.2 Technique implementation

Figure 2.2 provides an overview of the velocity reconstruction algorithm. This 'simplistic' view reveals a limitation - in order to successfully obtain a correlation peak, particles can only move

within interrogation windows between frames. Consequentially, the size of the interrogation region is dictated by the movement of the fastest particles. One vector is produced per window, so flows that exhibit a range of speeds will have a spatial resolution limited by the highest speed. In order to decouple window size from the maximum particle speed, most PIV algorithms employ a 'multi-pass' approach. Several iterations, or 'passes', of the method described in Figure 2.2 are performed, with the first pass having a large window size, and subsequent passes decreasing in window size. Each pass is provided a pre-shift displacement from previous passes, allowing the algorithm to search outside the current window, while maintaining a large number of vectors, as shown in Figure 2.4.

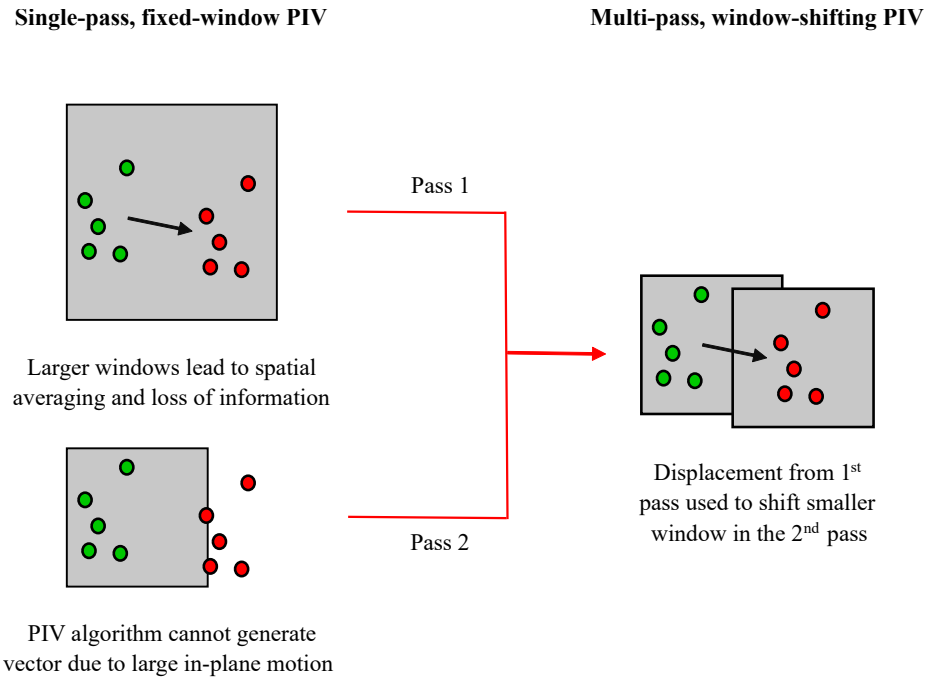


Figure 2.4: Comparison between single and multi-pass PIV approaches

Interrogation windows are typically overlapped by a percentage of the window size, as this increases spatial resolution. Particles at the edge of a particular window are more likely to have displaced out in the second frame, making them contribute less to a cross-correlation result. By overlapping windows, edge particles can be brought to the center of the next window, thus providing more spatial information. Most algorithms use an overlap of 50 % - too large an

overlap can lead to oversampling, while too small an overlap may not have any significant effect on spatial resolution.

The size of the interrogation regions is usually constrained by the spatial resolution required, and the signal-to-noise ratio (SNR) of the cross-correlation function. Large windows lead to spatial averaging, and sizeable gaps between vectors. However, this also guarantees more particles per window, leading to well-defined correlation peaks, and thus better SNR. Similarly, smaller windows provide greater spatial resolution, but only if there is no ambiguity in determining the right cross-correlation peak. Given this, the density of seeding particles needs to be optimised to a specific level throughout the PIV image. Too low a density leads to bad spatial resolution, while too high a density leads to particle overlap, and the potential to alter or influence the flow. Sometimes, tracer particles can selectively concentrate in, or avoid specific flow features (such as vortices and boundary layers), causing a non-uniform distribution. Thus, it is essential that a seeding system that deals with these issues efficiently is chosen (detailed in Section 2.1.3). Keane and Adrian [5, 6] used simulated data to show that a minimum of 10 particles are needed in the final pass interrogation window, for a distinguishable correlation peak.

When the SNR is too low, PIV software can wrongly select peaks, leading to incorrect vectors being produced (Figure 2.5). Apart from low particle density, other reasons for low SNR include in-plane and out-of-plane loss of particles, as well as spatial gradients in the flow. Keane and Adrian [5, 6] suggested limiting in-plane particle motion to less than a quarter of the smallest interrogation window size, and out-of-plane motion to less than a quarter of the laser sheet thickness. They also suggested limiting the difference in displacements (due to flow gradients) within each interrogation region to less than 3 % of the window size. Despite these measures, spurious vectors can not be avoided completely, thus PIV reconstructions require certain post-processing techniques to clean up the results.

The most commonly used vector-validation techniques include standard deviation and median

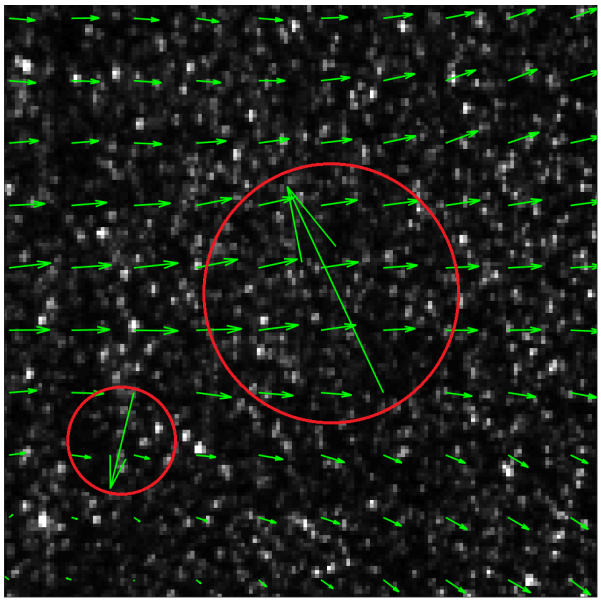


Figure 2.5: Spurious vectors generated from PIV reconstructions

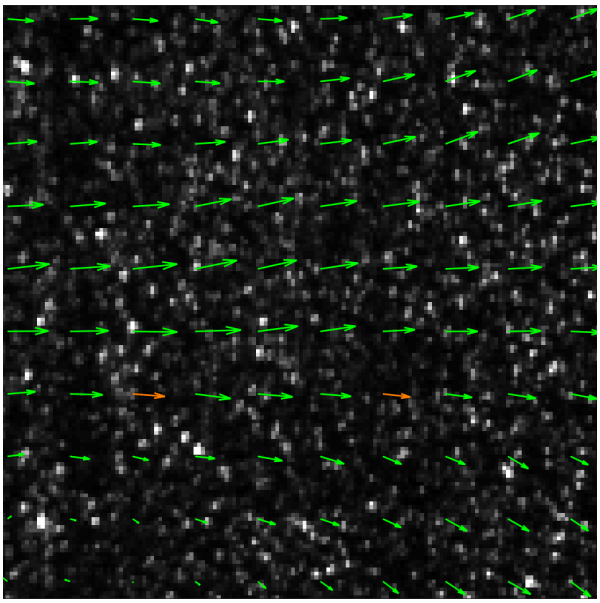


Figure 2.6: Spurious vectors replaced with new interpolated vectors (in orange)

filtering. In standard deviation filtering, vectors deviating from the mean by more than a specified multiple of the standard deviation are removed.

$$| U(x,y) - \bar{U} | \leq ns \tag{2.1}$$

where $U(x,y)$ is the velocity at coordinates (x,y), $\bar{U}$ is the mean velocity, n is a user-chosen multiplication factor, and s is the standard deviation of the velocities.

Median filtering orders neighbouring vectors in ascending order to determine a local median value. The central vector is then considered spurious if its difference with the local median exceeds a threshold value.

$$| U(x,y) - U_{\text{med}} | \leq \epsilon \tag{2.2}$$

where U_{med} is the local median velocity and ϵ is a user-chosen threshold. Most PIV algorithms also include the ability to define a velocity limit; any vectors exceeding this limit are removed. Spurious vectors that still exist after using filters can be rejected by manual selection.

Vectors that have been rejected leave gaps in the reconstructed velocity field. These gaps can be filled by interpolating velocities from neighbouring points, using linear, cubic, spline or sinc interpolation schemes (Figure 2.6). Vector-validation filters can be very useful to produce clean velocity plots, however, care must be taken as to ensure a minimal number of interpolated vectors. Excessive filtering can lead to flow averaging over large regions, which reduces accuracy and may cause a change in flow features. Another post-processing feature of PIV is the calculation of derived quantities from reconstructed velocity fields, using finite difference schemes. Examples of such quantities include velocity magnitude, vorticity, divergence, shear rate, path and area integrals.

Table 2.1 summarises the requirements for optimal PIV reconstructions.

Table 2.1: Design criteria for optimum PIV implementations, after Keane and Adrian [5, 6]. L_I is the interrogation window size, Δz_o is the laser sheet thickness and Δt_1 is the time between successive laser pulses

Parameter	Criteria
Image particle diameter, D_I	$2 \leq D_\mathrm{I} \leq 3$ pixels
Interrogation window particle density, N_IW	$10 \leq N_\mathrm{IW} \leq 15$
Particle in-plane displacement, Δx	$\Delta x \leq \frac{1}{4} L_\mathrm{I}$
Particle out-of-plane motion, Δz	$\Delta z \leq \frac{1}{4} \Delta z_\mathrm{o}$
Localised difference in velocity, ΔV	$\mid \Delta V \mid \Delta t_\mathrm{l} \leq 0.03\ D_I$

2.1.3 Criteria for successful application

Dual exposure camera

The inherent assumption in PIV is that particles displace by sufficiently small amounts between images, such that any acceleration effects can be neglected. As such, the motion of the particles between frames is assumed linear, implying minimal velocity averaging. Figure 2.7 illustrates the effect of flow acceleration on particle motion between frames.

Consequentially, particle image displacements tend to be limited to a few pixels. Control of this is gained by adjusting the time interval between laser pulses (hereafter referred to as the inter-pulse time) - the shorter the inter-pulse time, the smaller the particle displacement. For this

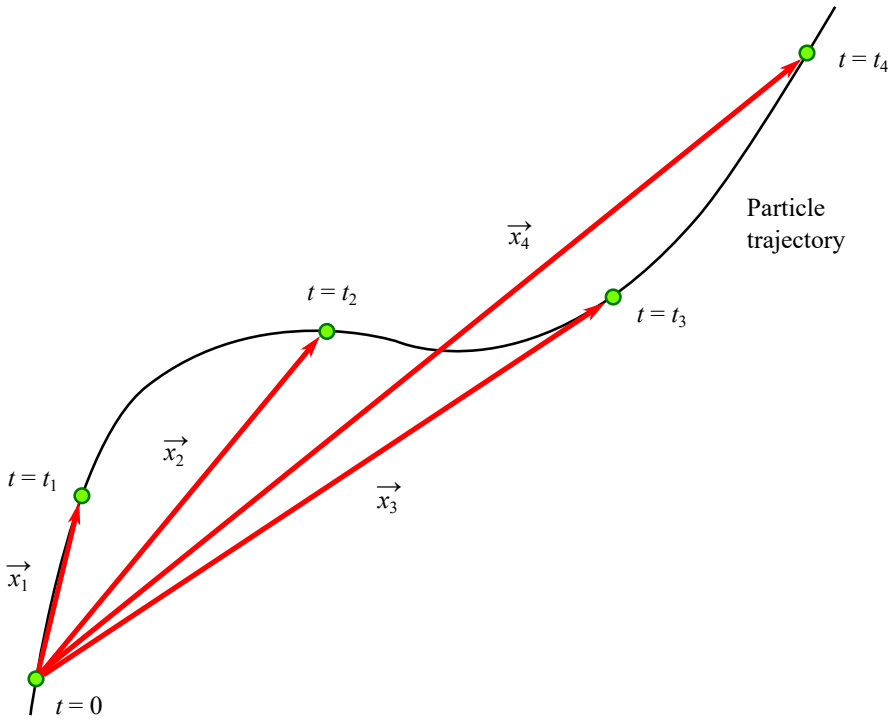


Figure 2.7: Velocity averaging effect as a result of flow acceleration. Red arrows indicate displacements extracted from the PIV algorithm. $\vec{x}$ refers to particle displacement, t refers to time, and subscripts 1 to 4 denote an increase in time. Note how the displacements calculated for t_2, t_3 and t_4 lead to a linear simplification over the particle trajectory

reason, high-speed flows and highly magnified images require very short inter-pulse times. While dual-cavity lasers are quite capable of achieving this, each pulse needs to appear in a separate frame taken by the camera. As such, the inter-pulse time is limited by the shortest amount of time a camera can take to start acquiring a new image, after finishing acquisition of the previous image (hereafter referred to as the inter-frame time). As a result, cameras with short inter-frame times become necessary when imaging high speed flows, or very small geometries.

Tracer-flow fidelity

PIV relies on the ability of the seeding particle to trace the motion of the fluid being interrogated. Assuming the particles follow the fluid motion accurately, then the velocity calculated from the particles can be taken as the velocity of the fluid. In reality, seeding particles have a finite inertia, which can introduce velocity lag in regions of large fluid acceleration. The following

analysis serves to demonstrate this, based on the work of Melling [7]. Each particle can be modeled as a sphere with an equivalent aerodynamic diameter, d_p. The equation governing unsteady particle motion in a fluid is given by the Basset-Boussinesq–Oseen equation [8, 9, 10]. For particle densities significantly larger than the fluid density (relevant to gaseous flows with solid or liquid particles, as experienced in this work), this equation can be simplified to two terms, as shown in Equation (2.3).

$$\frac{\mathrm{d}U_\mathrm{p}}{\mathrm{d}t} = C(U - U_\mathrm{p}) \tag{2.3}$$

where U_p is the particle velocity, U is the fluid velocity, and C is a characteristic frequency which depends on the particle drag coefficient, C_D, and the particle Reynolds number, $\mathrm{Re_p}$. The left-hand side of Equation (2.3) represents the acceleration of the particle, expressed in a Lagrangian frame of reference. The right-hand side describes the viscous drag term, which depends on the difference between fluid and particle velocities, or the slip velocity, $U - U_\mathrm{p}$. Equation (2.4) defines C, while $\mathrm{Re_p}$ is defined by Equation (2.5).

$$C = \frac{3}{4} C_D \mathrm{Re_p} \frac{\mu_\mathrm{f}}{\rho_\mathrm{p} d_\mathrm{p}^2} \tag{2.4}$$

where μ_f is the fluid dynamic viscosity, and ρ_p is the particle density.

$$\mathrm{Re_p} = \frac{\rho_\mathrm{f}(U - U_\mathrm{p}) d_\mathrm{p}}{\mu_\mathrm{f}} \tag{2.5}$$

where ρ_f is the fluid density. When $\mathrm{Re_p} \ll 1$, Stokes drag applies [11], and C_D can be modeled according to Equation (2.6).

$$C_D = \frac{24}{\mathrm{Re_p}} \tag{2.6}$$

By considering the case where a fluid undergoes a step change in velocity at time $t = 0$, Equation (2.3) can be solved to yield the particle step response function.

$$U_{\mathrm{p}}(t) = U_{\mathrm{p}}(0) + \Delta U\left(1 - \exp\left(-\frac{t}{\tau_{\mathrm{p}}}\right)\right) \tag{2.7}$$

where ΔU is the step change in fluid velocity, and τ_{p} is the particle response time constant, which is simply the reciprocal of C. In the case of Stokes drag, τ_{p} can be modeled using the expression for C_D given by Equation (2.6).

$$\tau_{\mathrm{p}} = \frac{\rho_{\mathrm{p}} d_{\mathrm{p}}^2}{18\mu_{\mathrm{f}}} \tag{2.8}$$

Equation (2.7) describes how a particle would theoretically behave through a shock wave. Instead of a step change, particles exponentially alter their velocity over a finite time to match that of the fluid. This illustrates that PIV of flows containing large accelerations or step changes will suffer severely from velocity lag and erroneous flow velocimetry, unless a sufficiently low τ_{p} value is used. Since τ_{p} varies quadratically with d_{p} (from Equation (2.8)), smaller sized particles are required in order to improve fluid tracking ability. Figure 2.8 shows how a particle takes much longer distances to recover velocity lag after an oblique shock as its diameter increases, from the work of Melling [7].

When evaluating tracer-flow fidelity, τ_{p} is non-dimensionalised by a relevant fluid time scale τ_{f}.

$$\mathrm{Sk} = \frac{\tau_{\mathrm{p}}}{\tau_{\mathrm{f}}} \tag{2.9}$$

where Sk is defined as the Stokes number. Sk is a measure of seeding particle fidelity; for $\mathrm{Sk} \ll 1$, particles are able to trace fluid motion accurately, while for $\mathrm{Sk} \gg 1$, particles deviate from fluid streamlines. According to Samimy and Lele [12], accurate flow tracing requires Sk to be at most

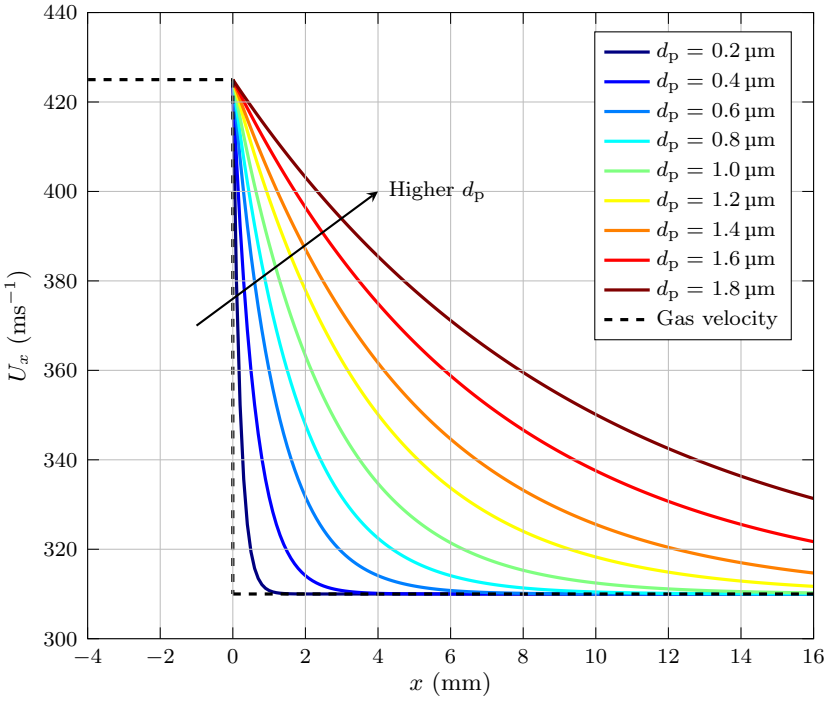


Figure 2.8: Response of differently-sized particles downstream from a shock (adapted from [7])

0.1. In most applications, τ_f is the Kolmogorov time scale of the flow, which expresses the turning-rate of the smallest turbulent eddies. Tracer-flow fidelity becomes a significant issue particularly in compressible flows with Mach number greater than 1. Notable PIV investigations where careful consideration of seeding particle size was given include an investigation of compressible flow in the wake of a two-dimensional blunt base by Scarano and van Oudheusden [13], application of PIV to a hypersonic flow by Schrijer et al. [14], and measurements on compressible mixing layers by Urban and Mungal [15]. All of these investigations utilised titanium dioxide powder TiO_2 as seeding particles, producing small d_p in the range 400 nm to 500 nm, in order to maximise tracer fidelity.

It should be noted that there is a limit to how small particles can be made while still ensuring flow fidelity. When particle sizes become comparable to the mean free path of molecules in the flow, Brownian motion can influence the particle trajectory, leading to loss of flow-tracking ability. For air at atmospheric conditions, this effect becomes significant for particle sizes < 100 nm.

Signal strength

While reducing the size of particles improves fluid-tracing ability, smaller particles generally scatter less light, due to their reduced cross-sectional area. The ability of particles to scatter light is described in Equation (2.10).

$$\sigma_{\mathrm{s}} = \frac{P_{\mathrm{s}}}{I_{\mathrm{o}}} \tag{2.10}$$

where σ_{s} is the Mie scatter cross-sectional area of the particles, P_{s} is the total scattered power integrated across all angles, and I_{o} is the incident laser intensity. Investigations have shown that σ_{s} is proportional to d_{p} raised to the power of two or higher [7]. Thus, in instances where incident laser power is scarce, larger sized particles must be used. Given this, the size of seeding particles is usually a compromise between the particle's ability to follow the flow, and its ability to scatter sufficient light. In the case of flows with large accelerations, smaller sized particles are necessary because of the high speeds and sudden changes that can be induced, making higher-powered lasers unavoidable.

Seeding method

The choice of seeding particle and seeding method plays a crucial role in successfully implementing PIV. When choosing an appropriate seeding substance, one should be aware that the physical properties of the seeding substance may influence the attainable particle size. For example, the density, viscosity and surface tension of seeding liquids affect the size of droplets produced in an aerosol generator. Tracer particles should also not alter physical properties of the flow being investigated. Other desirable qualities include being chemically inert, non-toxic and non-corrosive. Typical species used as tracer particles for gas flows include oils, smoke, aluminium oxide powder (Al_2O_3) and titanium dioxide powder (TiO_2).

The method of introducing seeding particles into the flow plays an important role in ensuring a uniform seeding density across the image plane. The most commonly used configuration for seeding gaseous flows with liquid droplets is through an atomizer, the simplest of which is shown in Figure 2.9. The seeding liquid is placed in a reservoir containing a tube leading to a constriction in the passage of air flow. This seeding liquid is drawn up the tube due to low static pressure and gets sheared due to the high speed of the incoming air. Individual droplets of a range of sizes are formed as a result of this, thus a baffle or impactor is typically used to 'catch' large-sized droplets and return them to the reservoir. Liquid-droplet atomizers have the advantage of being able to produce a large quantity of small-sized droplets at a steady rate. This improves tracer fidelity for high speed flows, and also increases the chances of producing a uniform seeding density. The disadvantage of seeding gaseous flows with liquid droplets is that the droplets have a high tendency to deposit on confined test section walls. This can reduce incident laser pulse energy and change the laser sheet intensity profile if the sheet enters the test section via a coated wall, or reduce the image quality if scattered light is captured through a coated wall.

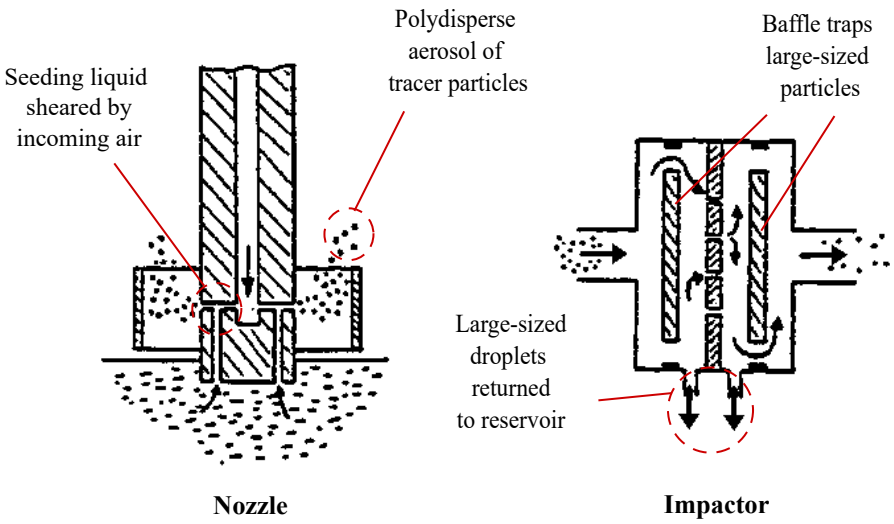


Figure 2.9: Generation of liquid droplets in an atomizer (adapted from [7])

Gaseous flows can be seeded with solid particles through the use of fluidised beds or cyclone gen-

erators. Solid particles are dispersed into the gas phase via a dry input stream effusing through, or tangentially entraining from a powder bed. Solid seeding particles are typically sought after for their nominal small sizes ($\sim 10\,\text{nm}$) which gives them high tracer fidelity. In addition, their ruggedness makes them well-suited for harsh environments, for example in applications involving high temperatures and pressures such as combustion. The main disadvantage of using solid seeding particles is agglomeration due to humidity in the test gas or surface affinity of powders, leading to a variable distribution in particle sizes. In addition, non-spherical shapes of particles can be produced, reducing the validity of the analysis of tracer fidelity presented previously. Solid seeding particles require larger powder quantities to attain appreciable seeding densities in a flow, so this method is typically more expensive. Thus, the work presented in this thesis is achieved using seeding of gaseous flows using liquid droplets only.

2.1.4 Elastic scatter limitation

One of the main limitations of PIV is strong elastic scatter, or laser flare from large surface area scattering bodies. PIV relies on collecting Mie scatter from particles, which is scatter at the same wavelength as the incident illumination (termed 'elastic', as there is no loss of photon energy). While particles can scatter light from the laser, other objects present in the flow cavity can also do the same, typically with greater efficiencies due to their comparatively larger size. Examples of bodies that scatter light effectively include surfaces such as test section walls or bluff bodies in the flow, as well as gas-liquid interfaces such as fuel sprays in engines. This typically leads to a mismatch in scatter signals captured by the PIV camera. Pixels imaging surfaces or sprays saturate before appreciable signals from particles are attained. Any subsequent increase in incident laser energy to 'see' particles better, can lead to overwhelming glare from surfaces or sprays that extends beyond the scatter interface into flow regions. This masks particles in the vicinity of the structure, leading to low SNR and thus erroneous velocity determination. In extreme cases, saturated pixels can permanently damage and become unusable. PIV cameras

are expensive, so care should be taken to ensure that this does not happen.

A number of investigations in the literature have attempted to address this limitation of PIV, proposing various solutions. Lawson et al. [16] simply avoided imaging close to the channel walls, limiting the visible interrogation area. Similarly, Mair et al. [17] used screens to optically isolate regions near the flow-wall boundary to prevent strong scatter being imaged by the PIV camera. This led to a slightly smaller measurement domain for comparison with LES results. Wernet et al. [18] investigated the flow field in compressors using black paint applied to the diffuser hub. Tape was also applied on optical access ports to mask areas of strong flare from blades, thereby limiting the interrogation region. Rostamy et al. [19] manufactured flow bluff bodies using black anodised aluminium to promote absorption of incident laser light and reduce unwanted surface reflections.

Paterna et al. [20] identified three main mechanisms for which surface scatter could be reduced, namely enhancing light absorption by the surface, enhancing light transmission through the surface, and reducing diffuse reflection from the surface. Their study compared different materials and surface treatments for their ability to suppress surface scatter. Fluorescent dye-doped paint applied to surfaces combined with the use of a narrow band-pass optical filter for only imaging Mie scatter from particles was found to be very effective at removing unwanted surface glare. Conceptually, a dye with high absorption cross-section at the laser wavelength absorbs a large fraction of the incident illumination, rather than reflecting it. Any light subsequently observed from surfaces coated with fluorescent dye is mostly at longer wavelengths to that of Mie scatter, allowing spectral isolation using a filter (see Section 2.2 for a description of fluorescence theory). In contrast, a similar application used by Watanabe et al. [21] found this method of glare removal unsuccessful, leading to spurious velocity determination up to 10 mm from the surface.

The works of Petrosky et al. [22] specifically addresses this limitation of PIV, demonstrating the deleterious effects of strong elastic scatter. A converse solution to that of Paterna et al. was

proposed, involving seeding particles doped with fluorescent laser dye. Two cameras simultaneously captured images of particles seeded into a boundary layer developing over a horizontal flat plate. One camera captured elastic scatter, while the other only captured fluorescence through the use of a long-pass optical filter. Velocity reconstructions were possible as close as 100 µm from the plate surface for the fluorescence images, while scatter images produced invalid velocity measurements up to 1 mm. The disadvantage of this method was highlighted as fluorescence signals from particles being more than 2 orders of magnitude weaker than that of Mie scatter.

2.2 Planar Laser Induced Fluorescence (PLIF)

2.2.1 Basic theory

Laser Induced Fluorescence (LIF) is a resonant spectroscopic laser-based diagnostic for measuring a range of different flow properties, including velocity, temperature, pressure and composition. In this work, focus will be devoted towards utilising the technique for making temperature measurements by probing molecules in a gaseous flow. The spatially-resolved version of this technique is commonly known as Planar Laser Induced Fluorescence (PLIF), which arises from the use of a laser sheet to interrogate a single 2-D plane of a flow.

All molecules have a unique distribution of energy levels, corresponding to discrete rotational, vibrational and electronic (commonly abbreviated to 'rovibronic') frequencies of motion, or so-called 'quantum states'. Molecules can absorb photons of light that carry a suitable amount of energy, causing a rovibronic transition (a change in frequencies of motion) of the molecule from a 'ground state' to an 'excited state'. After photon absorption, excited molecules typically undergo a number of competing energy transfer processes in order to relax toward the ground state again, some of which are radiative and others of which are non-radiative. The most relevant energy transfer processes for this work are highlighted in Figure 2.10.

One of the radiative processes is known as fluorescence, which involves spontaneous emission of a

new photon typically with equal or lower energy (which translates to equal or longer wavelengths) than that of the incident light [1]. Fluorescence can occur at longer wavelengths due to some internal redistribution of energy among the vibrational and rotational states of the molecule. This is indicated on Figure 2.10 as 'R-V R', or rotational-vibrational relaxation. Given that the emission process can initiate from various excited energy levels at different probabilities, fluorescence emission is typically broadband, that is, occurring at a range of wavelengths.

PLIF exploits this property of photon emission from excited molecules. By using a laser sheet of wavelength tuned to a specific rovibronic transition, molecules in a flow can be excited to produce incoherent fluorescence signals, which can be imaged with a camera. The intensity of fluorescence emission can then be related to a relevant property of the flow to be measured, for example temperature. In PLIF, fluorescent tracer molecules are typically seeded into a flow to be excited by the laser. Seeding is required because few liquids or gases of interest in fluid mechanics research have characteristic rovibronic transitions that are easily accessible with lasers.

Equation (2.11) provides an expression for the fluorescence emission intensity of excited molecules that have undergone a rovibronic transition, as captured by a detector.

$$I_{\mathrm{F}} = I_{\mathrm{o}}\, N\, V\, \sigma_{\mathrm{abs}}\, \Phi\, \Omega\, \eta \tag{2.11}$$

where I_{F} is the intensity of fluorescence emission, I_{o} is the incident laser intensity, N is the number density of molecules in the ground state, V is the probed volume, σ_{abs} is the absorption cross-section of the species, Ω is the fractional solid angle of detection, η is the light collection efficiency and Φ is the fluorescence quantum yield, given in Equation (2.12).

$$\Phi = \frac{n_{\mathrm{emit}}}{n_{\mathrm{abs}}} \tag{2.12}$$

[1] Emission of a photon with higher energy or shorter wavelength than that of the incident excitation, known as anti-Stokes fluorescence, is possible, but typically requires high gas temperatures. In this case, the additional photon energy is provided by the molecule as a result of loss of vibrational energy

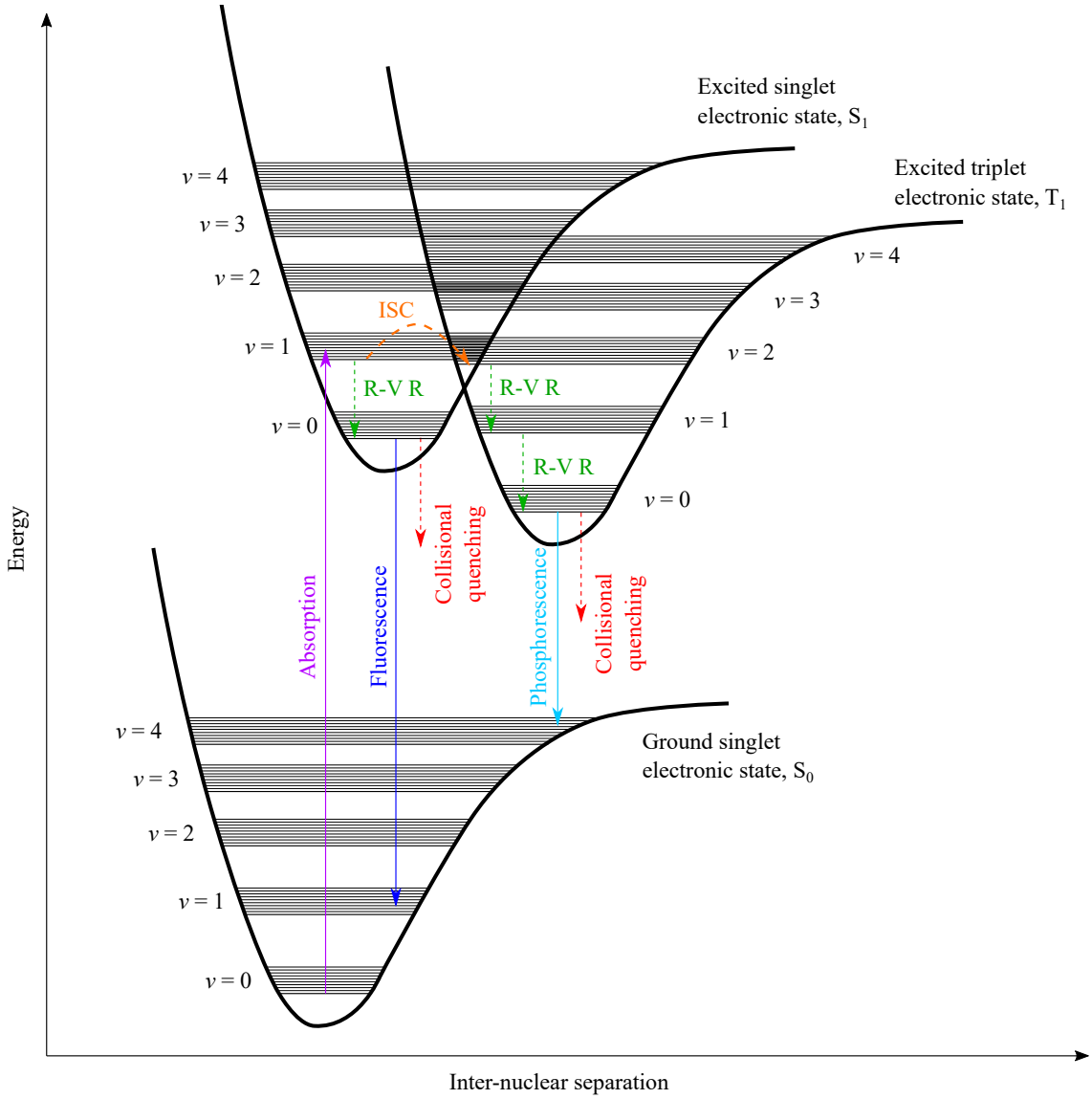


Figure 2.10: Example potential energy diagram illustrating discrete rovibronic energy states of a molecule, and the various processes of energy transfer. The ground and excited electronic states are indicated on the diagram, vibrational states are indicated by the ν symbol, and rotational states are represented by the fine structure within each vibrational state. Rovibronic transitions are indicated by arrows; radiative processes by solid arrows, and non-radiative processes by dashed arrows. 'R-V R' refers to rotational-vibrational relaxation, and 'ISC' refers to inter-system crossing

where n represents the number of photons, and subscripts 'emit' and 'abs' refer to emitted and absorbed respectively. The fluorescence quantum yield is a measure of the efficiency with which an excited molecule undergoes fluorescence - it is the ratio of emitted photons to absorbed photons. It arises in Equation (2.11) as a result of the competition between fluorescence and other non-radiative energy transfer processes. Examples of such processes are indicated in Figure 2.10;

they include collisional quenching and inter-system crossing (indicated as 'ISC'). Conceptually, the former is a de-excitation process caused by a transfer of energy via collision with another molecule, while the latter is an isoenergetic process resulting in the excited electron changing spin, modifying its so-called 'multiplicity' from a singlet to a triplet state. The fluorescence quantum yield ranges in value from 0 to 1 - large Φ values imply fluorescence being the dominant mechanism for relaxation of excited molecules, while small Φ values imply other processes dominating over fluorescence. Consequently, species that exhibit large Φ produce stronger fluorescence signals compared to species with low Φ.

In the context of making temperature measurements, a number of parameters in Equation (2.11) vary as a function of temperature, notably N, σ_{abs} and Φ. At any given temperature, a collection of molecules will be thermally-distributed across energy levels according to the established Boltzmann distribution, given in Equation (2.13).

$$\frac{P_2}{P_1} = \exp \frac{E_2 - E_1}{k_{\text{B}} T} \tag{2.13}$$

where P is the population density at energy level E, k_{B} is the Boltzmann constant, T is the temperature, and subscripts 1 and 2 refer to two different energy levels. As temperature increases, more molecules can populate higher rotational, vibrational and electronic quantum states. Consequently, the relative intensities of absorption (encapsulated in N and σ_{abs}) and emission (encapsulated in Φ) processes differ with temperature. Specifically in the case of N, flow conditions such as pressure and tracer concentration additionally have an effect. Thus, extracting temperature from fluorescence signals requires accurate knowledge of these functions. In practice, a number of variations of the PLIF technique are employed in order to simplify the temperature conversion process.

2.2.2 Technique variations

One-line excitation

In its simplest form, PLIF may be performed using a single excitation source and a single detection device collecting the entire fluorescence emission across all wavelengths. The fluorescence signal captured is given by Equation (2.11), from which temperature may be derived. This is experimentally and conceptually simple, but requires accurate knowledge of how N, σ_{abs} and Φ vary as a function of temperature, pressure, tracer concentration, position and time, for accurate thermometry. This can be very difficult using PLIF in isolation, without the help of an additional diagnostic to measure dependent variables such as pressure or tracer concentration. Fluorescence signals are also proportional to the incident excitation energy, so fluctuations in laser sheet intensity profiles must be accounted for. This is not always trivial, as it requires separate detection devices and potentially reduced incident excitation energy as a result of diverting a portion of available pulse energy for this purpose.

Example applications of this technique include measurements using toluene in an internal combustion (IC) engine by Dronniou et al. [23], Kaiser et al. [24] and Dec et al. [25]. Toluene concentration variations were neglected in all of these investigations, assuming uniformity throughout the cylinder and at all times. Conversion of signal to temperature required a separate calibration procedure, employing adiabatic compression equations to evaluate adiabatic mean core temperatures throughout the engine cycle. These were then matched to average signals obtained arbitrarily in the central image region, away from the cylinder walls where heat transfer was expected to be significant. Other examples of this technique include measurements using acetone in a heated laminar jet by Thurber et al. [26], and using both toluene and anisole in convection from a heated cylinder by Fanning et al. [27]. Both these investigations applied constant pressure and tracer concentration approximations, making the fluorescence signals solely dependent on temperature. Conversion of signal to temperature was then achieved by a separate calibration

using thermocouples.

Two-line excitation

In two-line excitation LIF, the temperature dependence of the tracer's absorption spectrum is exploited. This variant is performed by exciting tracer molecules using two laser pulses at different wavelengths (both of which lead to photon absorption), separated by a short time interval. The total fluorescence emitted from the excited molecules is then captured separately from each excitation pulse (integrated across all wavelengths). The ratio of these two signals is expressed in Equation (2.14)

$$\frac{I_{\mathrm{F},1}}{I_{\mathrm{F},2}} = C\,\frac{I_{\mathrm{o},1}\left(x\right)\sigma_{abs,1}\left(\lambda_1,T\right)\Phi_1\left(T\right)}{I_{\mathrm{o},2}\left(x\right)\sigma_{abs,2}\left(\lambda_2,T\right)\Phi_2\left(T\right)} \tag{2.14}$$

where C is a constant, x is a spatial coordinate, λ refers to the excitation wavelength, T refers to temperature and subscripts 1 and 2 refer to excitation pulse 1 and 2 respectively. For a molecule whose σ_{abs} and Φ change with temperature, the ratio of σ_{abs} multiplied by Φ at two different excitation wavelengths is a function of temperature, thus leading to a change in signal ratio with temperature. This function can be determined using a pre-experiment calibration, which will enable conversion of signal ratios obtained from experiments, into temperature. The benefit of this technique is the removal of signal dependence on N, effectively removing the need for a separate simultaneous diagnostic to measure pressure or tracer concentration. Two-line excitation generally results in high SNR, as a result of capturing all available fluorescence from each excitation pulse. However, one disadvantage of this method is a dependence on the incident laser energy I_{o} for two separate pulses which need to be accounted for. In addition, two laser sources operating at different wavelengths are required, which can increase experimental cost and complexity.

Example applications of this technique include measurements on indium atoms in an IC engine

by Kaminski et al. [28] and in flames by Borggren et al. [29], and on 3-pentanone in an IC engine by Einecke et al. [30]. Only average (not shot-by-shot) laser sheet intensity corrections could be applied in all of these investigations that already employed two lasers and cameras. Palma et al. [31] applied this technique on nitric oxide, NO, in a free-piston shock tunnel. The authors highlighted cost constraints that prevented them from using more than one laser and one camera. As a result, each run of the high-speed facility could only be used to probe a single molecular transition (and obtain one image), so signal ratios were obtained by averaging results across multiple runs. Thurber et al. [26] applied this technique on acetone in a heated laminar jet. The authors further highlighted the added complexities of this technique when compared to the one-line excitation variant, and could only acquire results from a steady low Reynolds number (laminar) jet, allowing the same camera to acquire both fluorescence signals one after another.

Two-colour detection

In two-colour detection LIF (commonly abbreviated to TC-PLIF), the temperature dependence of the tracer's emission spectrum is exploited. This variant is performed by exciting tracer molecules using a single laser pulse, leading to fluorescence emission. The total fluorescence is then split into two separate spectral bands, through the use of optical filters, to be imaged separately. The ratio of signals from these two spectral bands can be reduced to a form shown in Equation (2.15).

$$\frac{I_{\mathrm{F},1}}{I_{\mathrm{F},2}} = C\,\frac{\Phi_1\left(\Delta\lambda_1, T\right)}{\Phi_2\left(\Delta\lambda_2, T\right)} \tag{2.15}$$

where C is a constant, $\Delta\lambda$ refers to a chosen emission spectral band and subscripts 1 and 2 refer to the two separate emission spectral bands. A change in temperature leads to a change in the ratio of Φ across the two chosen spectral bands - thus the ratio of signals yields a function of

temperature. As before, this function can be determined with a pre-experiment calibration, which will enable conversion of signal ratios obtained from experiments, into temperature. Through careful selection of the emission spectral bands, a high sensitivity to temperature can be achieved in theory, for example by choosing $\frac{\mathrm{d}\Phi_1}{\mathrm{d}T} \gg 0$ and $\frac{\mathrm{d}\Phi_2}{\mathrm{d}T} \ll 0$. However, it should be noted that in practice, the temperature sensitivity is limited by the need to achieve sufficient SNR in each spectral band. Prenting et al. [32] presented a modelling strategy in which spectral bands were chosen so as to maximise both SNR and temperature sensitivity.

The benefit of this technique is the removal of signal dependence on a large number of parameters, such as N, σ_{abs} and I_{o}. It also only relies on excitation from a single laser source, making it simpler and cheaper to implement compared to the two-line LIF variant. The main disadvantage of this technique is that a low SNR can be expected, since each detection device only captures a portion of the total fluorescence emission. Example applications of this technique include measurements using toluene in an IC engine by Peterson et al. [33] and Luong et al. [34], using laser dyes in microfluidic systems by Natrajan et al. [35], and using toluene in a heated jet impinging on a cold surface by Cundy et al. [36].

In this work, the TC-PLIF technique was applied, due to the benefits described above and the lack of availability of a second laser operating at a suitable different wavelength.

2.2.3 Droplet PLIF

The use of PLIF in thermofluid research for flow thermometry has predominantly been achieved with tracers in the vapour phase. In this work, focus will be devoted towards applications of PLIF on liquid droplets in a flow, as it is more relevant to the experiments described in subsequent chapters.

The vast majority of relevant investigations in the literature on droplet PLIF have been to measure the temperature of the droplets itself, rather than to infer the temperature of the flow.

Such measurements have significance in applications such as combustion of fuel sprays, where the temperature of the droplets affects the rate of evaporation and thus energy delivery. The first attempt at such measurements was achieved by Lavielle et al. [37], who utilised the TC-PLIF method to measure the temperature of evaporating and combusting ethanol droplets seeded with Rhodamine B laser dye. Integrated temperatures of each droplet were evaluated, as fluorescence signals were collected using photomultiplier tubes without resolving individual droplets. The size of droplets investigated were fixed at either 100 µm or 200 µm, which is large in the context of this thesis. Castanet et al. [38] extended the work of Lavielle, by resolving internal temperature distributions of droplets using a smaller probe volume, where fixed droplet diameters of 200 µm were investigated.

Further studies conducting similar measurements on laser dye-doped droplets sought to highlight other factors relevant to the application of PLIF to droplets. For example, Labergue et al. [39] demonstrated the effect of fluorescence self-absorption when using large droplet sizes, or dye concentrations, leading to inaccuracy in temperature evaluation. It was suggested that this effect should be accounted for using a separate pre-calibrated function that incorporates both droplet size and dye concentration. Chaze et al. [40] investigated the consequences of using pulsed lasers with high peak irradiance on the temperature measurement sensitivity. It was shown that fluorescence saturation occurs when using intense pulses of light to excite dye molecules, leading to a change in temperature sensitivity. A specific two-dye combination was proposed as a solution, having demonstrated invariance in their temperature sensitivity at high laser irradiances.

In contrast, flow thermometry, that is inferring the *flow* temperature, via PLIF conducted on particles is rare. Vogt and Stephan [41] applied simultaneous flow velocimetry and thermometry using fluorescent dyes (two variants of Pyrromethene) microencapsulated in solid shells. A two-dye combination was used here along with the TC-PLIF method. Cellini et al. [42] similarly obtained flow velocity and temperature using custom-made particles encapsulated with

thermosensitive fluorescent polymers. Massing et al. [43] performed similar experiments using Rhodamine B laser dye incorporated into polystyrene particles. All of these works involved flow thermometry measurements made to liquid flows using solid particles. Similar use of PLIF on droplets or solid particles to extract gas temperatures could not be found in the literature.

Gas thermometry using solid particles is more common in the literature using laser-induced phosphorescence (LIP) measurements. Phosphorescence is a similar phenomenon to fluorescence, in that it involves light emission from excited molecules, but with emission lifetimes at least an order of magnitude longer. The process of molecular energy transfer for phosphorescence is indicated in Figure 2.10; it is initiated by ISC. Particles used for this purpose are known as thermographic phosphors, as they have temperature sensitive phosphorescence emission. Similar ratiometric techniques to those used in PLIF can be used with thermographic phosphors to deduce the temperature of a flow.

Several authors use thermographic phosphors in the literature for gas flow thermometry. This review will concentrate on those applied in tandem with PIV for simultaneous flow velocimetry. Omrane et al. [44] conducted a proof-of-concept experiment on a jet-flow demonstrating the combination of PIV and LIP using thermographic phosphors. Jain et al. [45] compared ratiometric LIP methods to lifetime decay methods for determination of high temperatures (as may be experienced during combustion) using thermographic phosphors. Fond et al. [46] applied similar simultaneous diagnostics to investigate turbulent flows produced by a heated jet. Abram et al. [47] employed high-speed (3 kHz) measurements on the wake of a heated cylinder. Witkowski et al. [48] measured the temperature and velocity in a free shear flow between a vitiated stream and a clean air stream. Neal et al. [49] applied simultaneous PIV and LIP to measure in-cylinder velocity and temperature distribution of a diesel engine. All investigations listed above used a single thermographic phosphor particle as the tracer for both velocity and temperature. PIV measurements were made by capturing Mie scatter from the phosphor particles, using one laser

beam and a PIV camera. LIP measurements were made by capturing temperature-sensitive phosphorescence signals, using a separate (resonant) laser beam and (at least) one more camera. Thus, more than one laser beam and at least two cameras were used in all the investigations listed. Fan et al. [50] demonstrated simultaneous PIV and LIP using a single tracer, a single laser beam and two non-intensified PIV cameras. Velocity reconstructions were obtained through cross-correlation of phosphorescence signals from droplets instead of Mie scatter.

2.2.4 Tracer thermal equilibrium

Consideration of particle thermal response is essential for flow thermometry studies. LIF applied to particles in a flow yields temperatures of the particles itself, and it is essential that these temperatures are representative of the flow of interest.

There are two main considerations when performing particle based thermometry experiments. First, particle temperature uniformity needs to be ensured. The Biot number, Bi, provides a measure of a particle's temperature uniformity - this is expressed in Equation (2.16). This non-dimensional parameter represents the ratio of conduction resistance within the particle to convection resistance on the particle surface. A large Bi indicates a high conduction to convection resistance, implying the presence of large temperature gradients within the particle. Conversely, a small Bi indicates low conduction to convection resistance, and thus high temperature uniformity across the particle.

$$\mathrm{Bi} = \frac{h d_\mathrm{p}}{6 k_\mathrm{p}} \tag{2.16}$$

where h is the convective heat transfer coefficient on the particle surface, and k_p is the particle thermal conductivity. The assumption of a constant temperature within a particle is typically valid for $\mathrm{Bi} < 0.1$ [51]. By modelling a particle as a sphere in a cross-flow, where the cross-flow velocity is the slip velocity (the difference between the particle and flow velocity), the

approximation in Equation (2.17) holds.

$$\mathrm{Nu} = \frac{h d_\mathrm{p}}{k_\mathrm{f}} \approx 2 \tag{2.17}$$

where Nu is the sphere Nusselt number and k_f is the gas thermal conductivity. This approximation is the asymptotic solution using the forced convection correlation for a sphere in a cross-flow, as the slip Reynolds number approaches 0. Substituting Equation (2.17) into Equation (2.16) reveals that the Biot number is independent of particle size and is simply a function of the thermal conductivities of both particle and fluid.

$$\mathrm{Bi} = \frac{k_\mathrm{f}}{3k_\mathrm{p}} \tag{2.18}$$

From Equation (2.18), it is evident that particle temperature uniformity can be ensured by having seeding particles with high thermal conductivities. The condition of $\mathrm{Bi} < 0.1$ is easily met when using solid seeding particles in gaseous flows, as there is a large disparity in their thermal conductivities. In the case of droplets in gaseous flows, this condition is typically met as well, but with a closer margin. Table 2.2 presents the Biot number for a number of different candidate particle LIF tracers seeded into air at room temperature and atmospheric pressure. These involve a combination of pure fluorescent tracer candidates, as well as solvents that may be used as carriers for fluorescent tracers.

Table 2.2: Biot numbers for various candidate tracers and solvents in air. Note that k_p of solid tracers have a range of values - Bi quoted is the most conservative estimate. Thermal conductivity of DEHS was obtained from an investigation by Cecil and Munch [52]. Thermal conductivity of air, $k_f = 25.9 \times 10^{-3}\,\mathrm{Wm^{-1}K^{-1}}$, was evaluated at STP

Substance	Bi
Water	0.014
Ethanol	0.052
Methanol	0.042
DEHS	0.058
Toluene	0.064
Acetone	0.048
Al_2O_3	< 0.001
TiO_2	< 0.001

The assumption in Equation (2.17) holds true for creeping flow i.e. when the slip Reynolds number is much smaller than 1. As Re_p increases, Nu increases as well, leading to an increase in Bi. Figure 2.11 shows the variation of Nu with Re_p using three different correlations from the literature [53, 54, 55]. From this figure, it is evident that a large change in Re_p is required before any significant change in Nu is encountered. To put this into perspective, doubling Bi for DEHS (thus no longer meeting the temperature uniformity condition) would require an almost double Nu - this in turn can only be achieved with a Re_p of about 20. At room temperature and atmospheric pressure for air, this equates to a slip velocity of about $0.8\,\mathrm{kms^{-1}}$ using a modal particle diameter of 380 nm based on a standard aerosol generator from LaVision (data for this device is presented in Section 4.5.2). If the maximum particle diameter is used instead (1 µm), a slip velocity of approximately $0.3\,\mathrm{kms^{-1}}$ is required. Such slip velocities are only encountered across strong shock waves in supersonic or hypersonic flows. Note that the required slip velocity for larger Nu decreases as d_p increases. Thus, both PIV and particle-based LIF require small-sized particles, as it ensures flow fidelity as well as particle temperature uniformity.

The second consideration for particle thermometry is ensuring adequate thermal equilibrium between flow and particle. In the same way that particles in a flow experience a momentum lag due to their inertia, a temperature lag is also present as a result of their thermal mass. It is essential that this lag is minimised, so that measured particle temperatures can be assumed

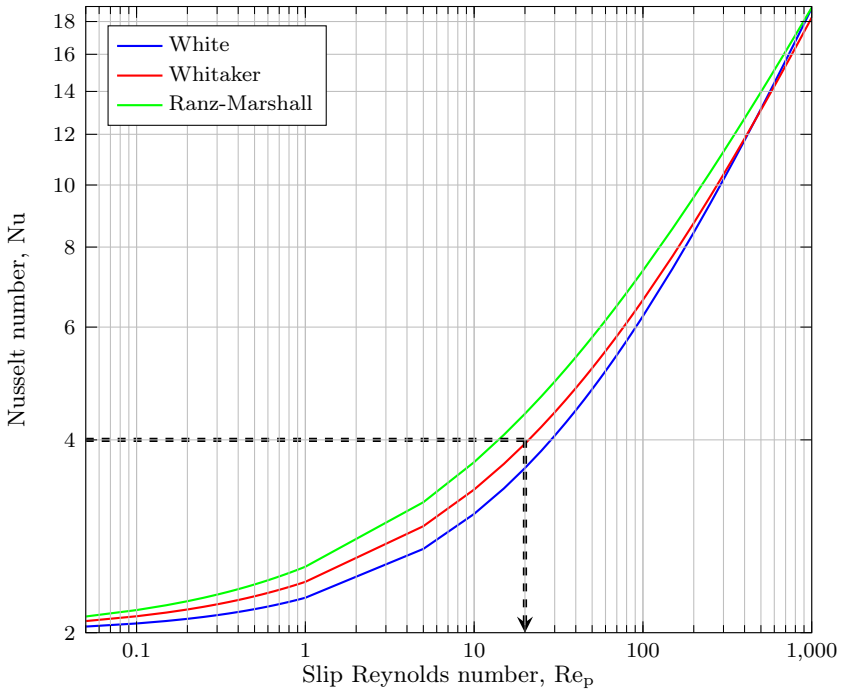


Figure 2.11: Nusselt number correlations for a sphere in a cross-flow. Note how doubling Nu from the asymptotic solution requires a high $\mathrm{Re_p}$ of ~ 20 (indicated by dashed line)

similar to flow temperatures. Since particles can be assumed to have uniform temperature, the lumped capacitance method is appropriate to solve for the particle's transient temperature response. This is expressed in Equation (2.19).

$$\frac{\mathrm{d}T_\mathrm{p}}{\mathrm{d}t} = \frac{1}{\tau_T}\left(T_\mathrm{f} - T_\mathrm{p}\right) \tag{2.19}$$

where T_p is the particle temperature, T_f is the flow temperature and τ_T is the particle thermal response time. This represents the time taken for the particle-flow temperature difference to drop by a factor of e when subjected to a unit lag, and is given by Equation (2.20)

$$\tau_T = \frac{\rho_\mathrm{p} c_\mathrm{p} d_\mathrm{p}^2}{12 k_\mathrm{f}} \tag{2.20}$$

where ρ_p is the particle density and c_p is the particle specific heat capacity. Analogous to the equations for velocity response, a small τ_T is desired, as this implies a fast thermal response of

the particle to a change in surrounding temperatures. This is achieved, again, by using small particle diameters - thus, having small d_p is beneficial for both tracer fidelity in velocimetry as well as thermal equilibrium in thermometry. The thermal Stokes number, Sk_T can be defined in a similar way to the usual Stokes number to provide a measure of particle-flow thermal equilibrium - this is expressed in Equation (2.21).

$$\mathrm{Sk}_T = \frac{\tau_T}{\tau_\mathrm{f}} \tag{2.21}$$

where τ_f represents a relevant flow thermal time-scale. $\mathrm{Sk}_T \ll 1$ implies a high degree of thermal equilibrium, while $\mathrm{Sk}_T \gg 1$ implies strong temperature lag between particle and flow.

2.3 Rayleigh scattering

2.3.1 Basic theory

Rayleigh scattering is a laser diagnostic technique that has found use in a range of applications, notably combustion and flames, for temperature measurements and species visualisation. It is the result of incoherent scattering of light from particles that are much smaller than the wavelength of the incident illumination. The oscillating electric field of incident laser light interacts with charges in a molecule, causing them to oscillate at the same frequency. The interaction thus generates a dipole; radiation from this dipole is seen as scattered light at the same wavelength as the incident illumination. Rayleigh signal intensities depend on a number of factors, as summarised in Equation (2.22).

$$I_\mathrm{R} = I_\mathrm{o}\, N\, V\, \Omega\, \eta\, \sigma_\mathrm{R} \tag{2.22}$$

where I_R is the intensity of the Rayleigh scattering signal, N is the number concentration of

species, V is the probe volume, Ω is the fractional solid angle of signal detection, η is the collection optics transmission efficiency and σ_{R} is the effective Rayleigh cross-sectional area. From Equation (2.22), it is evident that I_{R} is proportional to N. This property has been exploited to allow for flow visualisation and gas density or composition measurements, for example by Panda et al. [56], Pitts and Kashiwagi [57], Graham et al. [58] and Fiedler et al. [59]. All of these investigations were conducted on non-reacting jet flows, that is, for non-combusting applications.

For ideal gases, N at any point in a gas can be expressed in terms of the local pressure and temperature, according to Equation (2.23).

$$N = \frac{pA_o}{RT} \tag{2.23}$$

where p is the pressure of the gas, A_o is the Avogadro constant, R is the universal gas constant and T is the temperature of the gas. Substituting Equation (2.23) into Equation (2.22) reveals that the Rayleigh signal from a point in a gas is inversely proportional to the temperature there. Given this, Rayleigh scattering has extensively been used as a diagnostic technique to measure the temperature of a gas. The inherent assumption here is that the pressure of the gas is spatially uniform and constant with time, which is typically valid for many applications, notably flames. If this is not the case, pressure variations need to be accounted for when calculating temperature from Rayleigh signals.

2.3.2 Simultaneous mixture fraction and temperature measurements

A significant challenge when using Rayleigh signals for thermometry is evaluating σ_{R}

$$\sigma_{\mathrm{R}} = \sum_i z_i \, \sigma_{\mathrm{R},\,i} \tag{2.24}$$

where z_i and $\sigma_{\mathrm{R},\,i}$ are the mixture fraction and the Rayleigh cross-sectional area of gas i respec-

tively. The mixture fraction quantifies the extent of mixing between gases, and for the case of a binary mixture takes on a value between 0 (only gas 1 present) and 1 (only gas 2 present). In applications where a mixture of gases are involved, it becomes difficult to estimate z_i at every domain location, at all times. This becomes harder when species react with each other to form new species, such as in combustion. Experimentalists have tried to estimate σ_{R} through a number of methods. Smith et al. [60] obtained σ_{R} by simulating their combustion process, in order to obtain species composition as a function of space. Another approach taken by Bergmann [61] and Dibble et al. [62] involved choosing fuel-oxidizer combinations that would result in a relatively constant σ_{R} throughout the combustion process (premixed flames).

The most common method of evaluating σ_{R} involves combining Rayleigh scattering with a separate simultaneous diagnostic to determine z_i. Several works from Stårner et al. [63, 64, 65, 66] employed simultaneous Raman scattering to obtain mixture fraction measurements that would enable temperature evaluation from Rayleigh signals using Equation (2.22). Sevault et al. [67] performed an identical technique in his investigations of oxy-fuel flames. Frank et al. [68] demonstrated the use of acetone and acetaldehyde LIF in tandem with Rayleigh measurements for extraction of composition information. Each of these have associated disadvantages or limitations to their use. For example, LIF measurements are temperature-dependent, as previously described, making isolation of composition effects non-trivial. Raman scattering generally yields weak signals (about three orders of magnitude weaker than Rayleigh scattering), giving low SNR in measurements. In conclusion, the need to control or numerically estimate σ_{R} limits the applicability of Rayleigh scattering for gas thermometry.

2.3.3 Polarised-depolarised Rayleigh scattering (PDRS)

Polarised-depolarised Rayleigh scattering (PDRS) has been proposed as a solution to the problem of mixture fraction determination. There are few reported applications of this technique (mostly applied to flame investigations), however it shows great potential in a number of fluid

applications. PDRS extends traditional Rayleigh scattering, by exploiting the polarization state of the scattered light, to enable simultaneous measurement of temperature and mixture fraction of gaseous mixtures. Figure 2.12 shows how a PDRS experiment is typically performed.

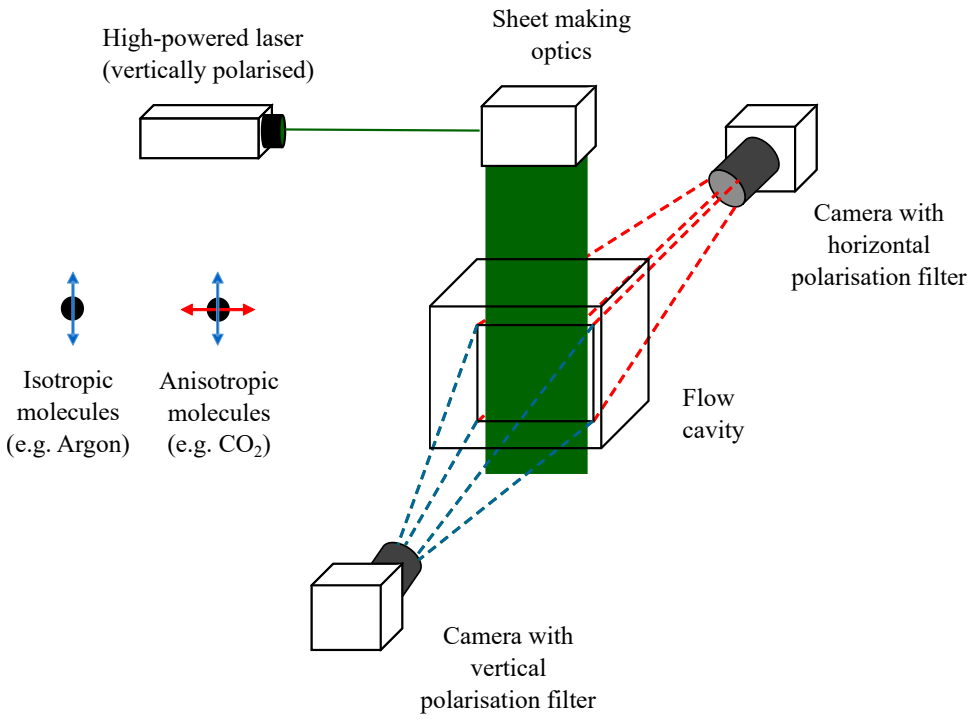


Figure 2.12: Illustration of a typical PDRS setup. Blue lines correspond to vertically polarised light, while red lines correspond to horizontally polarised light

PDRS may tackle the problem of accurately determining σ_{R} quite effectively, depending on the types of gases used. For a linearly polarised laser, light scattered from gas molecules is mostly polarised in the same orientation as the incident laser beam. However, some species scatter a small fraction of light (less than 7%) in the orthogonal polarisation state, due to the molecule's lack of spherical symmetry. This fraction of 'depolarised' light is called the depolarisation ratio, r_{p}, defined according to Equation (2.25).

$$r_{\mathrm{p}} = \frac{I_{\mathrm{dep}}}{I_{\mathrm{pol}}} \tag{2.25}$$

where I_{dep} is the intensity of orthogonally polarised scattered light ('depolarised') and I_{pol} is the

intensity of scattered light in the same polarisation state as the laser ('polarised'). Note that r_{p} varies depending on the wavelength of the laser used. Values of r_{p} used in this report have been taken from [69] and [70] - only those at 532 nm laser illumination have been quoted. In a gaseous mixture, regions containing pure gas 1 and pure gas 2 would have r_{p} values equal to that of gas 1 and gas 2 respectively. Regions where gases have mixed will have an intermediate r_{p} value, which is dictated by the mixture fraction, z_i of each gas. This distribution of r_{p} for different values of z_i can be easily modeled, knowing individual r_{p} values of the chosen gases.

In PDRS, two cameras are used to capture Rayleigh signals; each camera is fitted with polarisation filters oriented in orthogonal directions to one another, as shown in Figure 2.12. By taking the ratio of pixel intensities from both cameras at the same spatial locations, a value for r_{p} at that point can be obtained. The mixture fraction of each gas may then be evaluated by linear interpolation of the modelled relationship between r_{p} and z_i. Subsequently, σ_{R} can be calculated at every point in the domain, enabling temperature measurement using the normal Rayleigh method (Equation (2.22)).

The first demonstration of PDRS was by Fielding et al. [70] who applied it in a laminar methane flame. An argon-diluted flame was first investigated - argon and methane both have zero r_{p}, producing a large arithmetic difference in polarised and depolarised signals when imaging fuel rich regions. As such, the difference between polarised and depolarised Rayleigh signals was used to perform mixture fraction interpolations in their experiments (instead of a ratio). Subsequently the method was tested on an air-diluted methane flame. Due to the small depolarisation effect of air, the signal difference interpolation method was found to generate multiple values of mixture fraction for the same measurand, making it impossible to accurately determine species composition. To overcome this, a linear combination of polarised and depolarised signals was used instead, such that a one-to-one relationship between signal and mixture fraction could be established. Results using this technique in both flames were very similar to those obtained

by using coupled Raman and Rayleigh scattering. The authors stressed that PDRS generates roughly 10 times better SNR compared to simultaneous Raman/Rayleigh, making it a very useful diagnostic tool.

The extension of this technique to turbulent flames was then performed by Frank et al. [71, 72]. The authors reported using carbon monoxide (CO) Laser Induced Fluorescence (LIF) alongside PDRS - this is due to the decrease in PDRS sensitivity near stoichiometric mixture fractions, requiring a separate diagnostic to validate results. Almost 1.8 J of pulse energy was used in their experiments, leading to an SNR of 10 in the depolarised signals, and 70 in the polarised signals. Results from this investigation used mixture fraction measurements to derive the scalar dissipation rates and forward reaction rates of the combustion process. The authors demonstrated strikingly similar results when compared to single-point measurements made on the same rig using Raman scattering [73].

Zulkifli et al. [74, 75] demonstrated the use of PDRS in an oxy-fuel combustion application. Very high temperatures can form in oxy-fuel flames, leading to a large concentration of intermediate combustion species. This causes significant variation in σ_{R} - temperature uncertainties of up to 40 % can be incurred when using normal Rayleigh scattering. The use of PDRS on the other hand, was reported to produce mixture fraction and temperature uncertainties of less than 5 %. Results from their experiments were used to generate scatter plots of temperature against mixture fraction - these were compared to simulated results and found to have a high degree of agreement. The largest uncertainties (due to a spread in scatter data) came from high temperature regions, corresponding to stoichiometric mixture fractions. This range of mixture fractions lay in a shallow gradient area in the modelled r_{p} to z_i interpolation, meaning a lower sensitivity was to be expected. Chapter 5 provides a technique sensitivity analysis, which will highlight the effect of different r_{p} versus z_i gradients.

2.3.4 Criteria for successful application

Choice of gases

PDRS requires the chosen gases to have different r_{p} values to enable linear interpolation of z_i. The larger the disparity in r_{p}, the more sensitive the technique becomes. Table 2.3 lists r_{p} and relative σ_{R} values for a number of candidate gases for PDRS (note that values quoted here are for 532 nm illumination).

Table 2.3: List of r_{p} and relative σ_{R} values for some candidate gases in PDRS. Data presented here was collected from works by Sutton et al. [76], Fuest et al. [69] and Gardiner et al. [77]

Gas	r_{p} (%)	$\sigma_{\mathrm{R}}/\sigma_{\mathrm{R,\,N_2}}$
Argon	0	0.87
Helium	0	0.01
Hydrogen	0.90	0.21
Nitrogen	1.06	1
Oxygen	2.94	0.86
Carbon dioxide	4.08	2.39
Carbon monoxide	0.51	1.24
Methane	0.02	2.13

Noble gases like argon and helium are typically employed in PDRS experiments as they have zero depolarisation. These are then paired with highly anisotropic molecules like CO_2 to produce large disparities in r_{p}, thus maximising the technique's sensitivity. Some implementations of PDRS, as described in the previous section, have used linear and non-linear combinations of I_{pol} and I_{dep}, instead of a ratio, to create an interpolation model for z_i, which can improve sensitivity.

Laser pulse energy

High pulse energies are typically required for Rayleigh scattering, since gases have fairly small scattering cross-sections. The desire to measure the depolarised component requires even larger pulse energies, since depolarised signals are about two orders of magnitude weaker than their polarised counterparts. This is illustrated by the works of Frank et al. [71, 72] who used 1.8 J of pulse energy for appreciable SNR. Signal amplifying cameras, such as intensified or electron-

multiplying charge-coupled devices (CCDs), are typically required for this technique, especially for the depolarised signal component. Some previous investigations have succeeded in attaining sufficient polarised Rayleigh signal using non-intensified CCD cameras, as shown in works from Frank et al. [71, 72].

Particle-free environment

The main disadvantage of the Rayleigh scattering diagnostic is the need for a clean environment. Rayleigh scattering cross-sections of gases are small, thus expected signals are low. In contrast, Mie scattering cross-sections are considerably larger. Similar to the limitations of PIV previously described, this leads to a mismatch in energy requirements, as high pulse energies are required to able to 'see' Rayleigh signals, while low pulse energies are enough to saturate cameras from Mie scatter. However, this effect is significantly more deleterious here compared to PIV, due to the need for a signal-amplifying camera. The presence of particles in the imaging region, including dust or condensed water droplets, can lead to overwhelming signals that inevitably saturate and may damage the camera. To combat this problem, almost all investigations in the literature utilising Rayleigh scattering have employed some method of filtering and drying gases, in order to remove particles and water vapour from the probed region. In addition, investigations involving flames typically shield the mixing gases of interest through the use of a co-flowing clean gas (hereafter referred to as a 'co-flow').

Filtered Rayleigh Scattering (FRS), which was first proposed by Miles et al. [78], is a variant of Rayleigh scattering that would allow for measurements in a particle-laden environment. In FRS, the laser used is injection-seeded to ensure a narrow linewidth. Subsequently, a molecular filter is placed in front of the light collection device - this filter is chosen so as to have a narrow absorption feature at the wavelength of incident excitation. This way, Mie scattered light is absorbed before reaching the detector. While a significant proportion of the Rayleigh-Brillouin scatter will also be absorbed by this filter, Doppler-broadened and shifted light due to thermal

and bulk motion of molecules will be transmitted. This enables isolation of Rayleigh signals from background illumination. The drawback of FRS is the strong attenuation induced by the molecular filter; in eliminating Mie scattering much Rayleigh scattering is lost too. This leads to lower Rayleigh signals and poorer SNR.

2.4 Infrared (IR) thermography

2.4.1 Basic theory

Infrared (IR) thermography is an optical diagnostic technique which is typically used to make temperature measurements of solid surfaces. It involves capturing IR radiation emitted from an object, and converting this into a temperature measurement.

All objects emit electromagnetic radiation due to thermal motion of their molecules. The spectral intensity of this radiation is encapsulated by Planck's Law of black-body radiation, which is given in Equation (2.26).

$$I_{\mathrm{b}}(\lambda, T) = \frac{C_1}{\lambda^5 \left(\exp\left(\frac{C_2}{\lambda T}\right) - 1\right)} \tag{2.26}$$

where I_{b} is the spectral intensity of a so-called black-body, C_1 and C_2 are the first and second universal radiation constants (respectively equal to $3.7418 \times 10^{-16}\,\mathrm{Wm}^2$ and $1.4388 \times 10^{-2}\,\mathrm{m\,K}$), and λ is the emission wavelength. Equation (2.26) describes the spectral radiation intensity emitted by a black-body, which is both a function of λ and T. A black-body is an idealised object that absorbs all incident radiation, and emits the theoretical maximum electromagnetic radiation possible when in radiative equilibrium with its surroundings. Figure 2.13 shows the emission spectrum of a black-body for a range of equilibrium temperatures.

Real objects differ from black bodies, in that they emit a fraction of that described by Equation (2.26). This fraction is called the spectral emissivity of the object ϵ_λ, and is defined in Equation

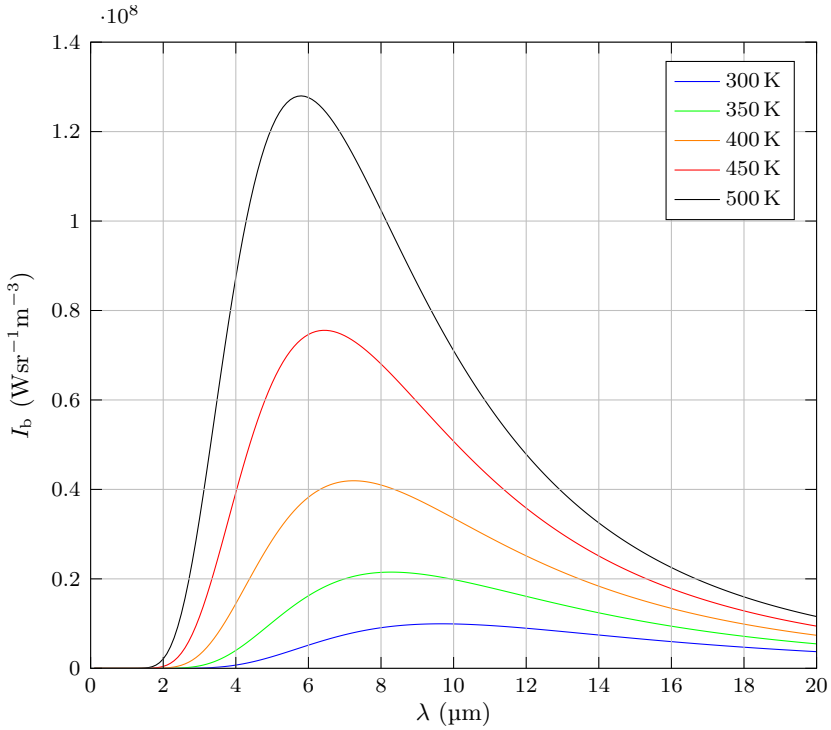


Figure 2.13: Spectral intensity of electromagnetic radiation from a black-body according to Planck's Law

(2.27).

$$\epsilon_\lambda = \frac{I_{\text{real}}(\lambda, T)}{I_{\text{b}}(\lambda, T)} \tag{2.27}$$

where I_{real} is the spectral radiative intensity emitted by a real object surface. Spectral emissivity is wavelength dependent, however in this work, all materials probed are assumed to be grey bodies, that is, they have spectrally uniform ϵ_λ values, and that they are opaque. Thus, wavelength dependence can be omitted from Equation (2.27), and ϵ_λ will simply be referred to as the emissivity, denoted as ϵ.

The spatially and spectrally integrated form of Planck's Law is given by the Stefan-Boltzmann law, which relates total emitted radiation from an object to its absolute temperature. This is given for a real body in Equation (2.28)

$$P = \sigma_{\mathrm{B}} A_{\mathrm{s}} \epsilon T_{\mathrm{s}}^4 \tag{2.28}$$

where P is the total radiative power emitted by a real body surface, σ_{B} is the Stefan-Boltzmann constant (equal to $5.67 \times 10^{-8}\,\mathrm{Wm^{-2}K^{-4}}$), A_{s} is the radiating surface area, and T_{s} is the surface temperature.

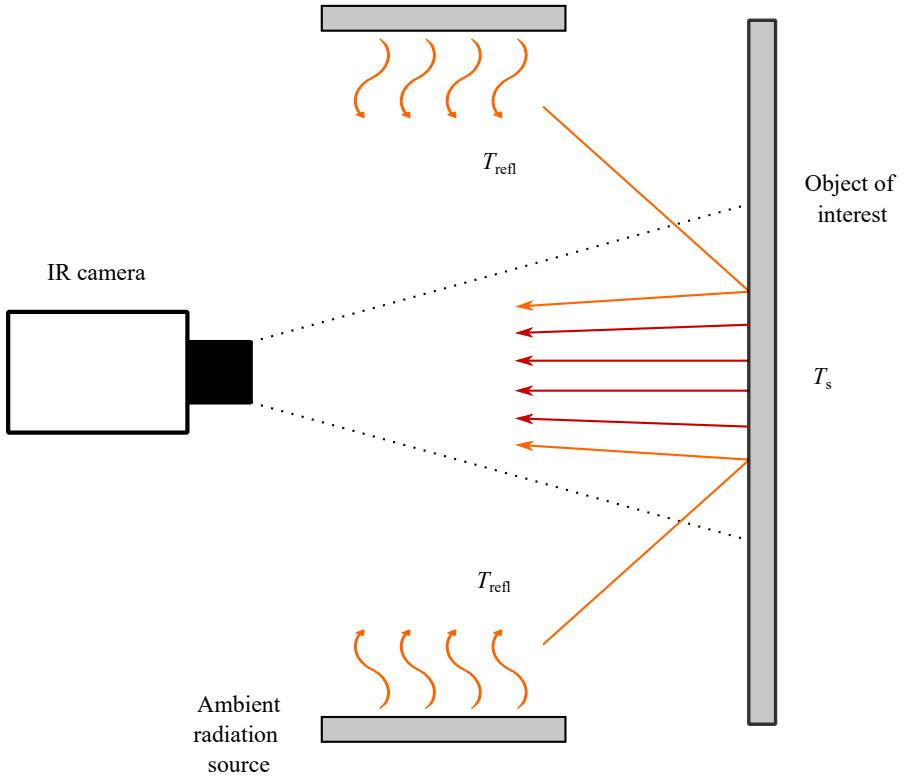


Figure 2.14: IR thermography in practice

In practice, IR thermography is performed by directing an IR collection device, such as a thermal imaging (IR) camera or a pyrometer, at the object of interest, in order to measure its temperature (as shown in Figure 2.14). Assuming no loss of radiation energy (due to reflection from windows and lenses, or scattering and absorption through an optical medium), the total radiation recorded by the IR device from a grey body will be the sum of the emitted radiation by the object and the reflected radiation from the surroundings. This is summarised in Equation (2.29)

$$P \;=\; \sigma_{\mathrm{B}}\, A_{\mathrm{s}} \left(\epsilon\, T_{\mathrm{s}}^4 + \rho\, T_{\mathrm{refl}}^4\right) \tag{2.29}$$

where ρ is the reflectivity of the object, defined as its ratio of reflected to total incident radiation, and T_{refl} is the reflected temperature of the surroundings, defined as the equivalent temperature of a theoretical black-body cavity surrounding the object.

Equation (2.29) can be reduced to a simpler form. Applying conservation of energy, the total radiation incident on an opaque surface is equal to the sum of the radiation absorbed and reflected by the object. This is expressed as

$$\alpha + \rho = 1 \tag{2.30}$$

where α is the absorptivity of the object, defined as its ratio of absorbed to total incident radiation. Applying Kirchoff's Law of Radiation to a grey body, α is equal to ϵ, thus simplifying Equation (2.29) through substitution of Equation (2.30).

$$P \;=\; \sigma_{\mathrm{B}}\, A_{\mathrm{s}} \left(\epsilon\, T_{\mathrm{s}}^4 + (1-\epsilon)\, T_{\mathrm{refl}}^4\right) \tag{2.31}$$

IR devices collect radiation from the surface of interest to produce a signal that is proportional to P. This is subsequently converted into values for T_{s}, when provided with the distance to object, and values of ϵ and T_{refl} by the user. Hence prior to conducting experiments, a few calibration steps should be taken to correctly enter ϵ and T_{refl} into the IR device, so as to ensure accurate evaluation of T_{s}. This is described in Section 2.4.3.

2.4.2 Detection wavelengths

An IR device is typically selected for an application based on the temperature range expected. From Planck's Law, it is evident that the spectral intensity of emission varies with temperature. The peak emission wavelength, λ_{peak}, at each temperature can be determined by differentiating Planck's Law with respect to λ, and setting this to 0. This results in Wien's displacement law, which is given by Equation (2.32)

$$\lambda_{\text{peak}} = \frac{b}{T} \tag{2.32}$$

where b is Wien's displacement constant (equal to 2898 µm K). For a given application temperature range, an emission wavelength span can be estimated from the expression for peak emission wavelength. This provides a reference as to the spectral range where most radiation signal can be collected by the device, thus maximising SNR. IR devices typically come in three spectral detection bands, denoted as 'short-wave', 'mid-wave' and 'long-wave' respectively. Table 2.4 lists the spectral detection range for each of these bands. As is evident from Equation (2.32), higher temperatures lead to shorter emission wavelengths, so 'short-wave' IR cameras are typically required here. Room temperature applications, as experienced in this work, typically require 'long-wave' IR detectors. For context, λ_{peak} at room temperature (293 K) is 9.9 µm. Poor choice of spectral range for the specific application can lead to low SNR and loss of temperature sensitivity when making measurements.

Table 2.4: Spectral bands commonly used in IR detectors

Spectral band	Wavelength range (µm)
Short-wave	1 - 3
Mid-wave	3 - 5
Long-wave	7 - 14

2.4.3 IR measurement parameters

Accurate knowledge of ϵ and T_{refl} is required prior to making IR measurements - incorrect use of these parameters can lead to inaccurate results. The reflected temperature, T_{refl}, is typically determined first, as it does not require knowledge of ϵ during evaluation. Note that the measured T_{refl} is specific to the particular experimental layout - changing the position and orientation of the IR device and object of interest can change the amount of reflected ambient radiation.

To measure T_{refl}, a so-called "perfect IR reflector" is placed directly in front of the object of interest. Its temperature is then probed with the IR device, having set an ϵ value of 1. A perfect reflector has $\rho = 1$, and thus an $\epsilon = 0$. This means that it does not emit any radiation of its own, but completely reflects all incident radiation. Thus, the temperature measured by the device on the highly reflective object will be purely due to diffuse ambient IR radiation. By setting the device's ϵ value to 1, the temperature measured will be equivalent to that of a black-body cavity surrounding the object of interest, that is, T_{refl}. Crumpled and re-flattened aluminium foil works well for this task; it has an ϵ value of less than 0.1, which is routinely neglected [79]. The measured temperature should be entered into the device as T_{refl} before any subsequent calibrations or measurements in the same experimental layout.

The ϵ value of an object can be estimated by calibration using another object of known ϵ. Tape or paint is typically used for this, as they usually have ϵ values larger than 0.9 that are documented in the literature and in IR device manuals [80]. To extract ϵ, a portion of the object of interest is painted, or affixed with a piece of tape. The object temperature is then probed with the IR device, setting the device's ϵ value to that of the tape or paint. The temperature of the region covered in tape or paint measured by the IR device is thus assumed to be the correct temperature of the object. The device's ϵ value is then adjusted until the temperature of the bare object (not covered in tape or paint) measured by the device reads the same value recorded for the tape or paint. In this report, ϵ values used were obtained by repeating this procedure at several object

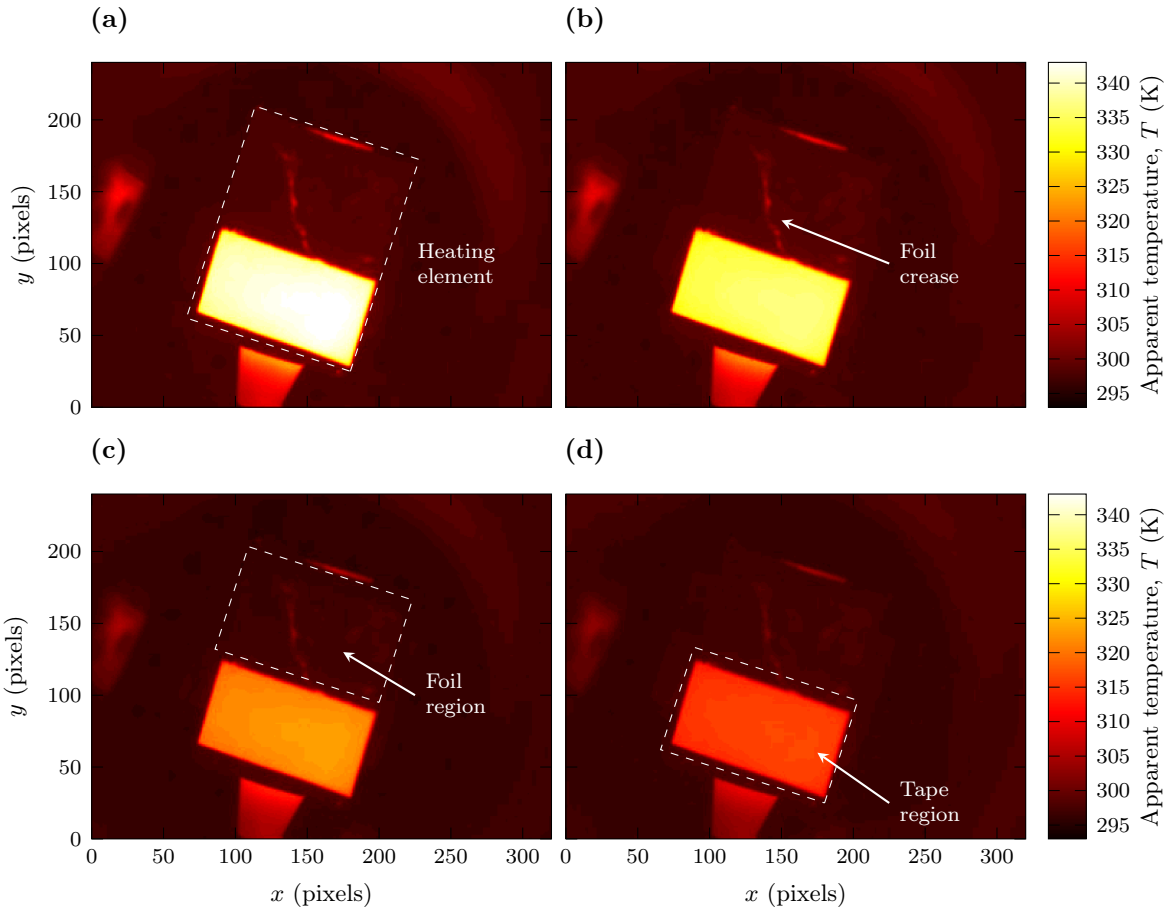


Figure 2.15: IR thermograph sequence of a heating element cooling down to room temperature, from (a) to (d). The colours indicated by the colour bar represent the apparent temperature, as the IR camera assumes a fixed ϵ across the image. Bright regions represent areas covered with tape, while dark regions are wrapped in aluminium foil. Note how the region covered in foil appears to be cold, despite being in contact with the heating element

temperatures and then evaluating an average ϵ.

Figures 2.15 and 2.16 demonstrate that foil can be assumed a perfect IR reflector, and electrical tape a strong IR emitter. In Figure 2.15, images of a 12 V aluminium heating element taken using an IR camera (FLIR E4) are presented. The element was wrapped in foil that was secured in place with black vinyl electrical tape - images were acquired after the element had been heated up to an arbitrary temperature and allowed to cool down back to room conditions. Tape and foil regions are indicated on Figure 2.15. As is evident, the IR camera recorded high temperatures in taped regions, and low temperatures in foil regions. A bright streak is apparent across the foil region - this is simply a crease that reflects radiation from the tape. Figure 2.16 plots mean temperatures of the tape and foil regions with time (an increase in time is indicated by an increase

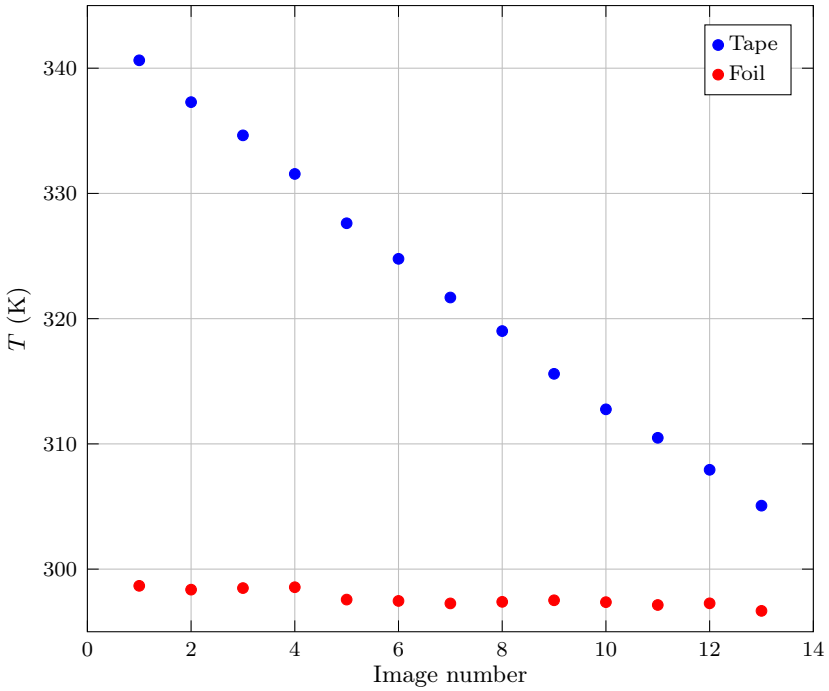


Figure 2.16: Mean temperature of tape and foil regions during cool-down of heating element

in image number). Temperatures in taped regions decreased by about 35 K over time, indicating a cool-down of the heating element, but hardly any change was seen in the foil regions, remaining constant at (297.7 ± 0.6) K for all times.

2.5 Summary

This chapter explored the background of several optical diagnostic techniques, namely PIV, PLIF, Rayleigh scattering and IR thermography. Key considerations and limitations for each diagnostic were discussed, along with relevant implementations in the literature.

The main criteria for successful application of PIV were identified as the need for small-sized tracer particles, a camera with short inter-frame time, and a uniform seeding method. These criteria would ensure adequate tracer-flow fidelity, velocity reconstruction accuracy and seeding density respectively. A significant problem of PIV was identified - strong laser flare from surfaces and gas-liquid interfaces can overwhelm PIV signals leading to low SNR. This generally inhibits the ability of PIV to resolve velocities near flow boundaries, which is typically crucial in high-

speed flow research. Chapter 4 aims to address this limitation through the development of Fluorescent PIV.

The extension of PIV towards measuring fluorescence signals from droplets motivated a survey of the literature on existing applications of droplet and particle PLIF. It was identified that flow thermometry, that is, measurement of flow temperature, from PLIF measurements on particles or droplets were scarce. Existing applications of LIF on droplets were intended for spray temperature evaluation, while the only investigations that applied flow thermometry using particles were for liquid flows. Gas thermometry using particles was found to be more widely employed using thermographic phosphors. These findings motivated the extension of Fluorescent PIV towards becoming a simultaneous velocimetry and thermometry tool - Chapter 4 details its implementation.

PDRS was identified as a technique capable of overcoming a significant limitation of traditional Rayleigh scattering. Its ability to measure both gas composition and temperature simultaneously has to date only seen use in combustion-related applications. Such multiscalar measurements can add significant value to investigations involving heat transfer in gaseous mixtures. This motivated the extension of PDRS to a high speed, non-combustion application, namely transpiration cooling. Chapter 5 details an investigation on the feasibility of applying this technique to non-combusting mixtures of gases. The criteria for successful application detailed in Section 2.3.4 are considered in this chapter, with the aim of applying PDRS to resolve mixture fraction and temperature profiles in a relevant transpiration cooling investigation. Subsequently, PDRS is applied along with IR thermography in a novel framework to investigate internal cooling mechanisms in transpiration cooling, as detailed in Chapter 7.

Chapter 3

Particle Image Velocimetry

In this chapter, the development and application of a PIV system is discussed. There were two main motivations. The first of these was to assemble a working system from scratch, capable of producing reliable single parameter (velocity) results before system enhancement for multiparameter measurements (elaborated in Chapter 4). The second motivation was to equip the system for accurate high-speed velocity measurements in a cost-effective manner, and to subsequently test it in a fast-moving fluid. To this end, two PIV experiments were conducted - the first experiment investigated a well-known fluid flow configuration at low speeds, while the second experiment involved visualising flow fields in a novel device at much higher speeds. The assembled setup for conducting PIV experiments is described in Section 3.1. Subsequently, Sections 3.2 and 3.3 elaborate on the two applications, explaining the flow being investigated in each experiment, before presenting the analysis performed and the results obtained.

3.1 Experimental setup

The establishment of PIV capability started with a blank slate. Figure 3.1 shows the layout of components ultimately used in PIV experiments. A dual-cavity Nd:YAG frequency-doubled laser (New Wave Gemini PIV 200-15) emitted 2 pulses of green light at its maximum frequency of 15 Hz. The light was directed through a telescope, formed by a $f = 60$ mm cylindrical lens and a $f = 350$ mm spherical lens, which expanded the beam from 5 mm to 35 mm in the horizontal dimension, while focusing the beam to a thin sheet at the imaging area. All light passing through the test section was then safely captured by a beam dump.

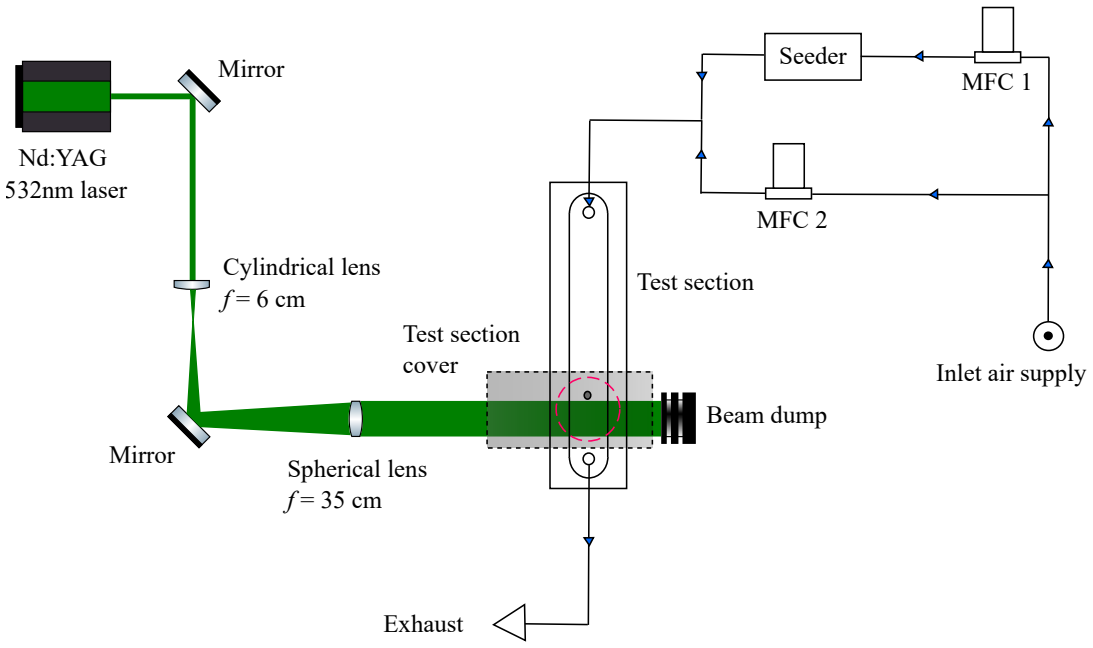


Figure 3.1: Plan view schematic of PIV experiment, with the imaging area circled in red. 'MFC' refers to mass flow controllers. The test section depicted here is that of the first experiment. This layout of optical and flow components was retained in the second experiment, but the test section was replaced

Having identified that a short inter-frame time camera is necessary for PIV of high-speed flows, a suitable charge-coupled device (CCD) camera was sourced for use in these experiments. The ImperX Bobcat B1621M was identified as the ideal candidate - its 'double exposure' mode enabled acquisition of two pictures within a very short time of one another. The exposure duration for the first frame was user-adjustable, while the second frame exposed for as long as it took to read out the first frame. The camera's fixed inter-frame time of 200 ns provided great flexibility in capturing flow phenomena at a range of speeds. A digital pulse delay generator (Berkeley Nucleonics Model 575) was used to trigger the camera and synchronise it to the laser pulses. Upon receiving a trigger signal, the camera exhibited a fixed intrinsic 11.4 µs delay before beginning the first frame exposure. This was taken into account, so as to ensure the first laser pulse arrived within the first image, as shown in Figure 3.2. For each test case, the laser inter-pulse time was set according to the anticipated flow velocity in the test section, ensuring the 'particle in-plane displacement' criteria described in Table 2.1 was met (refer to Section 2.1.2). The minimum inter-pulse time was the camera inter-frame time; this ensured each laser pulse

appeared in a separate frame.

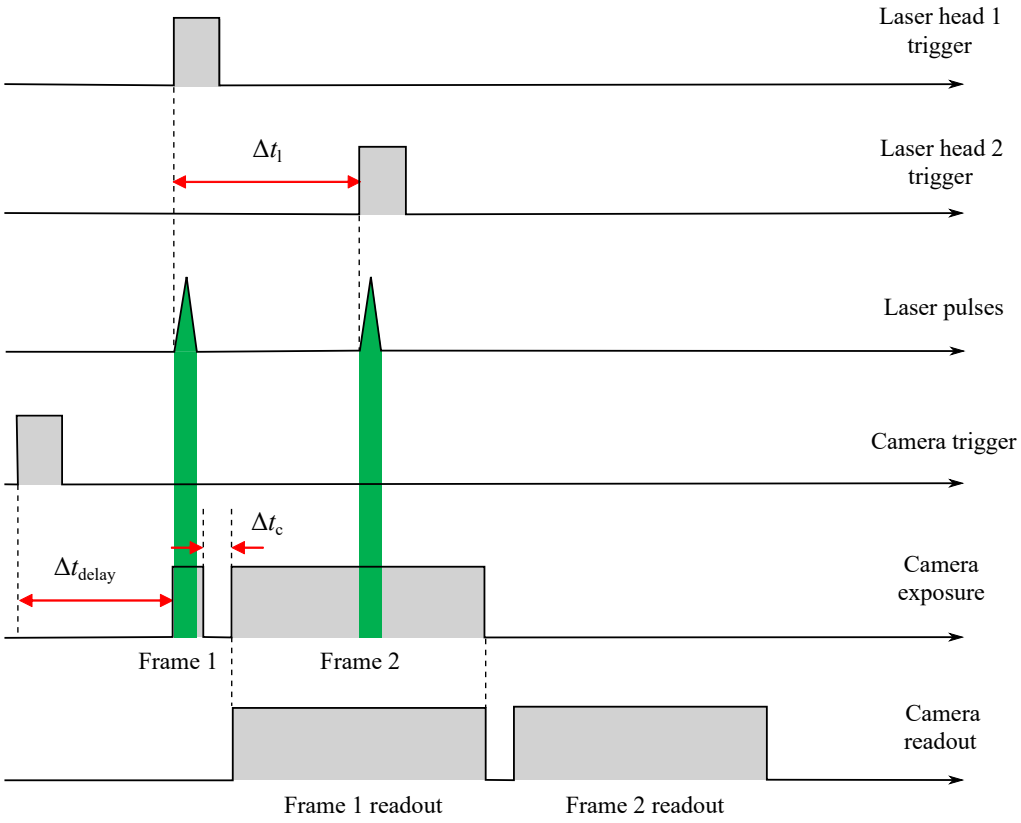


Figure 3.2: Timing diagram showing how the laser and camera were synchronised. Δt_l is the laser inter-pulse time, Δt_c is the camera inter-frame time (200 ns) and Δt_{delay} is the camera acquisition delay (11.4 µs). Laser pulse durations have been exaggerated for illustration purposes

Aluminium extrusion was used to mount the camera above the test section, and to allow translation in all directions (shown in Figure 3.3). The camera was focused onto the imaging plane, and aligned to the required field of view with the help of a calibration grid, shown in Figure 3.5.

As discussed in the assessment of tracer particles and seeding methods (Section 2.1.3), high spatial resolution and tracer fidelity in PIV requires a dense and uniform distribution of small-sized particles. Solid particles generally offer the smallest sizes (∼50 nm), however these require the use of cyclone generators or fluidised beds to prevent agglomeration. Liquid droplets on the other hand, have been produced in sizes small enough (∼1 µm) for supersonic PIV experiments [81], and can be generated in large quantities using readily-available atomizers. For these reasons, a droplet atomizer was sourced (LaVision Aerosol Generator) and used for these experiments.

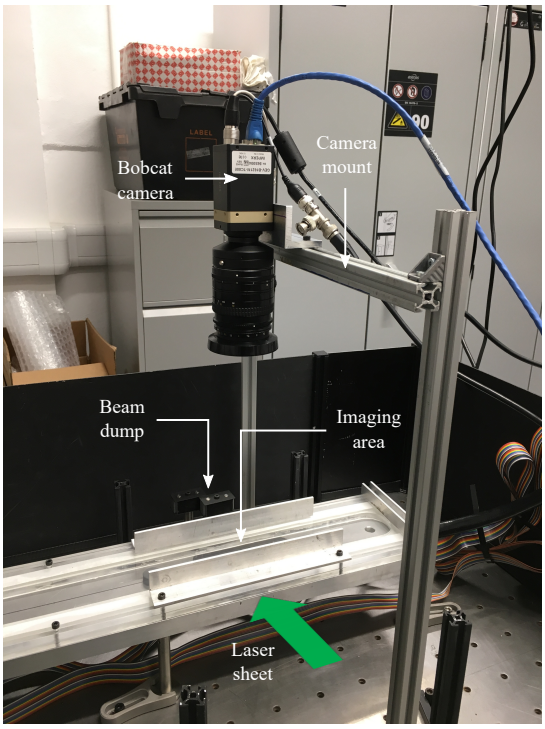


Figure 3.3: Camera mounted above the first experiment's test section using aluminium extrusion

The air entering the test section was seeded with diethyl-hexyl sebacate (DEHS) droplets generated from the droplet atomizer, shown in Figure 3.4. This seeding configuration reliably produced a fine uniform mist of DEHS droplets, ranging between 160 and 530 nm in diameter, based on the 10-90 percentile range of its distribution (presented in Section 4.5.2). Thus, a theoretical response time of $\tau_\mathrm{p} = 400\,\mathrm{ns}$ was established, using a modal diameter of $d_\mathrm{p} = 380\,\mathrm{nm}$, air at room temperature, and a Stokes drag estimate (calculated using Equation (2.8) in Section 2.1.3). This enabled large flow velocities to be investigated, while ensuring $\mathrm{Sk} \ll 1$ - estimates for Sk are provided for each experiment in the subsequent sections. The atomizer was capable of producing droplets at a rate of up to $4 \times 10^8\,\mathrm{s}^{-1}$, which can be too dense for many applications. In order to control the seeding density in the flow, a bypass air route was introduced, as illustrated in Figure 3.1. Mass flow controllers regulated the amount of air flowing through each flow path, so as to maintain a sufficiently high density of droplets in the imaging area.

Before an experiment, an image of a calibration grid of known size, placed exactly on the imaging plane, was obtained. This image served two purposes. Firstly, it enabled the PIV software

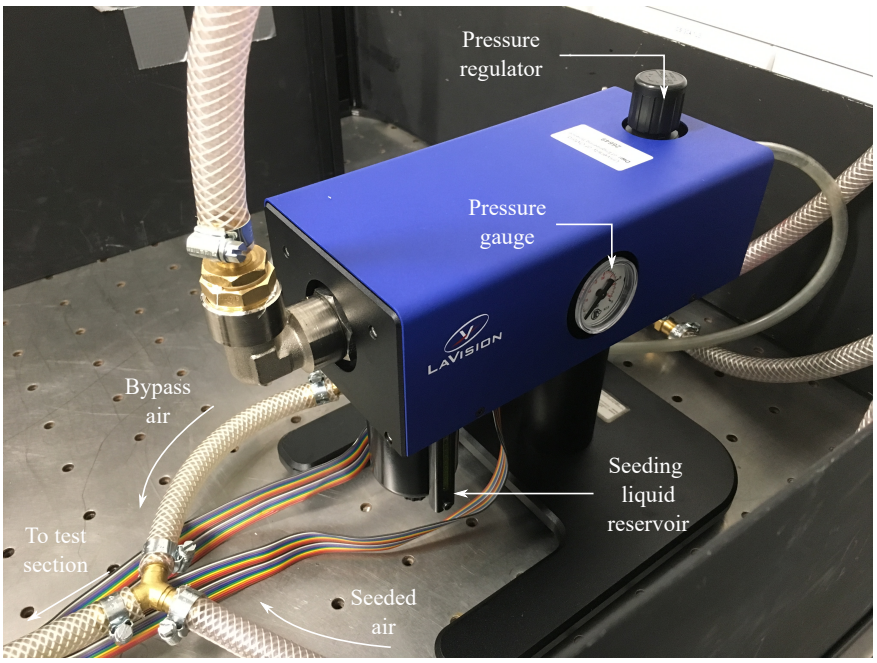


Figure 3.4: Liquid droplet atomizer with reservoir tank containing DEHS

to scale vector units from pixels per frame to meters per second. Secondly, it was used to correct experimental images obtained for optical distortion effects. The open source MATLAB Camera Calibration Toolbox produced by the California Institute of Technology [82] evaluated distortion correction coefficients from extracted grid corner positions. Subsequently, an image transformation operation was performed on all experimental images, correcting any distortion present. 'Dark' images of a laser-illuminated test section were also obtained - this image was subtracted from all acquired images to remove background light. A small number of pixels that attained negative values as a result of this operation was set to a value of zero.

PIV experiments typically involved assembling the test section as necessary, adjusting the flow rates of bypass and seeded air, firing the laser and obtaining the images. All experimental data was processed using the PIVlab MATLAB toolbox [83]. The toolbox contained all of the key functionalities described in Section 2.1, including evaluation of derived quantities such as the velocity magnitude, vorticity and shear rate. Processed images were filtered for spurious vectors, and subsequently analysed to extract relevant quantities as necessary.

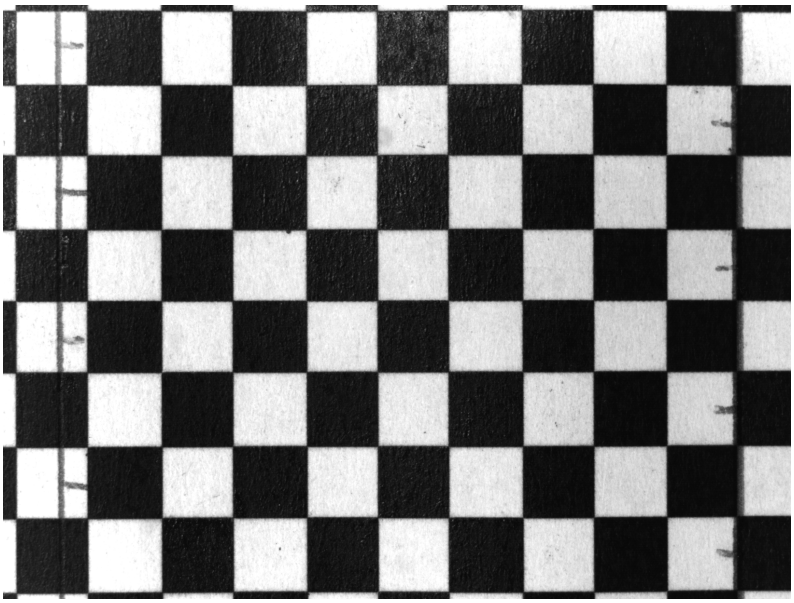


Figure 3.5: Example calibration grid used for aligning camera, scaling vector units and obtaining distortion coefficients. This particular grid was used in the first experiment, with an overall size of 43.0 mm wide by 32.0 mm tall. Each square had a length of 3.9 mm

3.2 PIV of flow past a cylinder

This section describes a proof-of-concept experiment conducted to ascertain the robustness of the established PIV framework. The velocity field in the wake of a circular cylinder placed in a confined channel was investigated. Flow passing around a cylinder encounters an adverse pressure gradient due to an increase in local area. When the Reynolds number exceeds a critical value, flow reversal takes place behind the cylinder, resulting in the formation of two standing counter-rotating vortices. At heightened Reynolds numbers, instabilities introduce an oscillatory behaviour to the wake. The most commonly known instability is the von Kármán vortex street, caused by an alternating shed of the vortices. The aim of this experiment was to test the assembled system's ability to image flow features from the wake, extract information such as instability frequencies, and validate these with existing results.

3.2.1 Test section and procedure

The test section (shown in Figure 3.6) consisted of a laminated structure, where three 720 mm long plates were fastened together and supported using optical posts. The bottom plate was

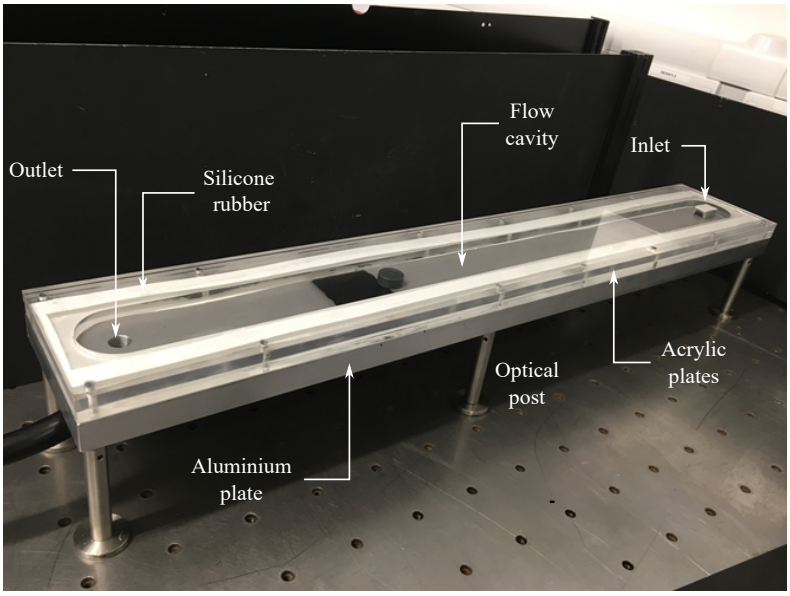


Figure 3.6: Laminated test section sealed air-tight with white silicone rubber sheets

made from aluminium - threaded holes on either end of the plate were used as an inlet and outlet for seeded air. The middle and top plates were made from clear acrylic, to allow optical access for both the laser and camera. An 8 mm × 40 mm profile was cut out of the middle plate, creating a cavity for air to flow in when all three plates were fastened together. Such a design was motivated by the need to easily place and remove a small cylinder in the way of the air flow, with minimal leakage. The chosen imaging area (Figure 3.7) was a 43 mm × 32 mm rectangle just behind this cylinder, capturing the wake generated in this region. In order to increase the contrast in PIV images, the imaging area was painted matt black, and shielded from surrounding light using a test section cover. Thin silicone rubber sheets were placed between each plate to minimise leakage from the test section.

The speed of the air flow in this experiment needed to be very low in order to establish suitable Reynolds numbers. This proved difficult because the atomizer had a minimum flow rate of $0.5\,\mathrm{m^3h^{-1}}$ below which no droplets would be produced. Due to the small cross-sectional area of the test section, this equated to a minimum Reynolds number of 220 when using a 10 mm cylinder. In order to investigate lower Reynolds numbers, an exhaust bypass and a valve were incorporated into the flow path just before the test section. By manually adjusting the valve

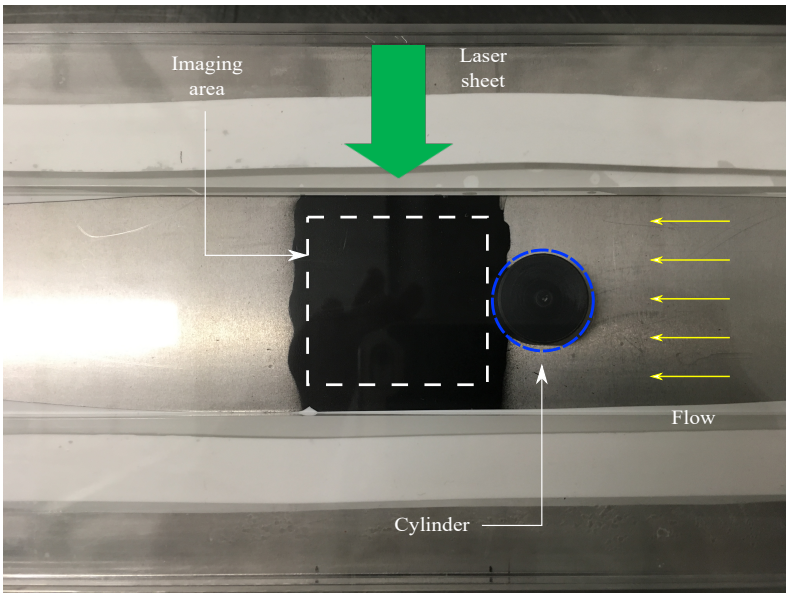


Figure 3.7: Imaging area (43 mm wide by 32 mm tall) in the cylinder wake experiment

position, a fraction of the seeded air could be diverted away from the test section, producing lower flow speeds. Continuous control of this was, nonetheless, hard to achieve, so Reynolds numbers below 140 could not be investigated reliably. Inter-pulse times ranged from 50 µs to 1 ms as a result of the low speeds used in this experiment. The Stokes numbers achieved in this experiment were very small - Sk ≥ 0.1 would require flow speeds in excess of 3.5 kms^{-1}.

Sets of 1000 images were obtained for each test case; properties such as the cylinder diameter and the total flow rate were varied between runs, in order to examine the effect of Reynolds number and flow constriction on derived quantities. Processed images were analysed over time in order to extract flow features at different stages of the unsteady flow, and to investigate periodic properties of the wake. A triple pass PIV approach was applied to analyse images, with standard decreasing square interrogation window sizes of 128, 64 and 32 pixels respectively. A default 50 % interrogation window overlap was also applied, producing a spatial resolution of 0.42 mm in the vector flow field.

3.2.2 Results and analysis

Analysis of the flow past a cylinder using PIV yielded positive results. Figure 3.8 shows typical velocity profile reconstructions obtained from the 10 mm, 20 mm, and 30 mm diameter cylinders. Velocity vectors have been drawn as black arrows across each image, while the colours represent velocity magnitude. The most evident flow feature observed in the cylinder wake was boundary layer separation, leading to the formation of a recirculation region. In Figure 3.8, this is highlighted with streamlines - two symmetric vortices formed downstream from the cylinder, dividing the channel perfectly into two halves. As expected, the width of the wake varied according to the size of the cylinder used - larger cylinders produced wider wakes, while smaller cylinders produced narrower wakes.

Given that a confined channel was used, blockage effects had to be considered. A blockage ratio, β, was defined according to Equation (3.1).

$$\beta = \frac{D}{H} \tag{3.1}$$

where D is the cylinder diameter and H is the channel width (fixed at 50 mm for all tests). According to theory, von Kármán vortex shedding begins after reaching a critical Reynolds number, $\mathrm{Re}_{\mathrm{c},\beta}$. Accounting for the effect of channel confinement, this $\mathrm{Re}_{\mathrm{c},\beta}$ was reported to range between 47 (for an unconfined flow) and 120 (for $\beta = 0.6$) [84]. Due to the flow rate limitation previously described, Reynolds numbers close to these values could not be established. Nonetheless, results from this investigation have demonstrated a symmetric shedding pattern observable across a range of tested Reynolds numbers (generally between 200 and 900). Figure 3.9 shows a sequence of PIV reconstructions obtained at 10 Hz, for a 30 mm cylinder at $\mathrm{Re} = 827$. In the first image (a), two symmetric vortices are seen, separated by a region of fast back-flow. These vortices are displaced downstream in the second (b) and third (c) images, still maintaining

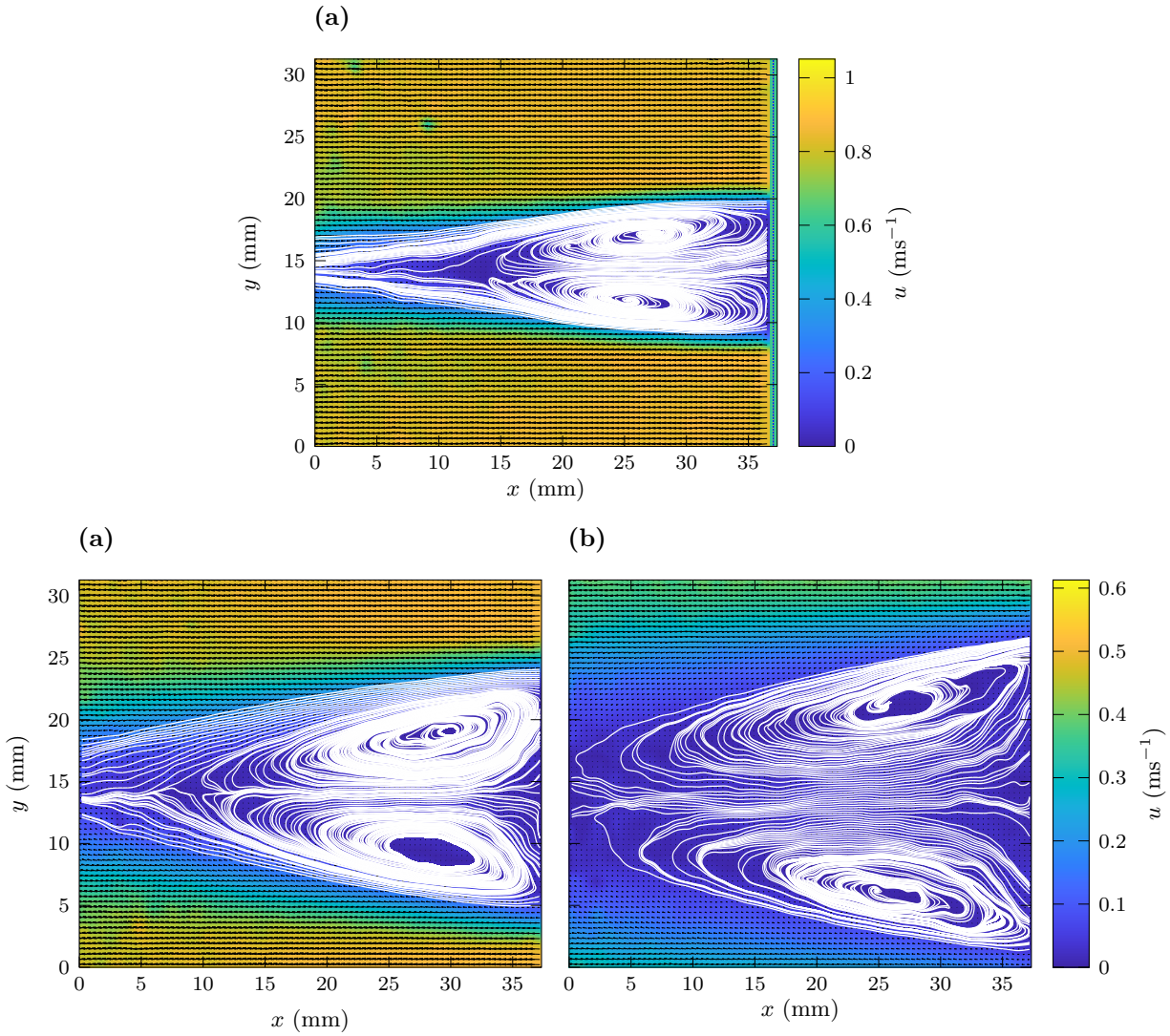


Figure 3.8: PIV reconstruction of the flow field behind a (a) 10 mm cylinder at Re = 599, (b) 20 mm cylinder at Re = 643, and (c) 30 mm cylinder at Re = 767 - streamlines have been drawn in white to aid visualisation of the recirculation region. The flow travels from right to left, and the cylinder is placed just outside the camera field of view (to the right), in line with the middle of each image

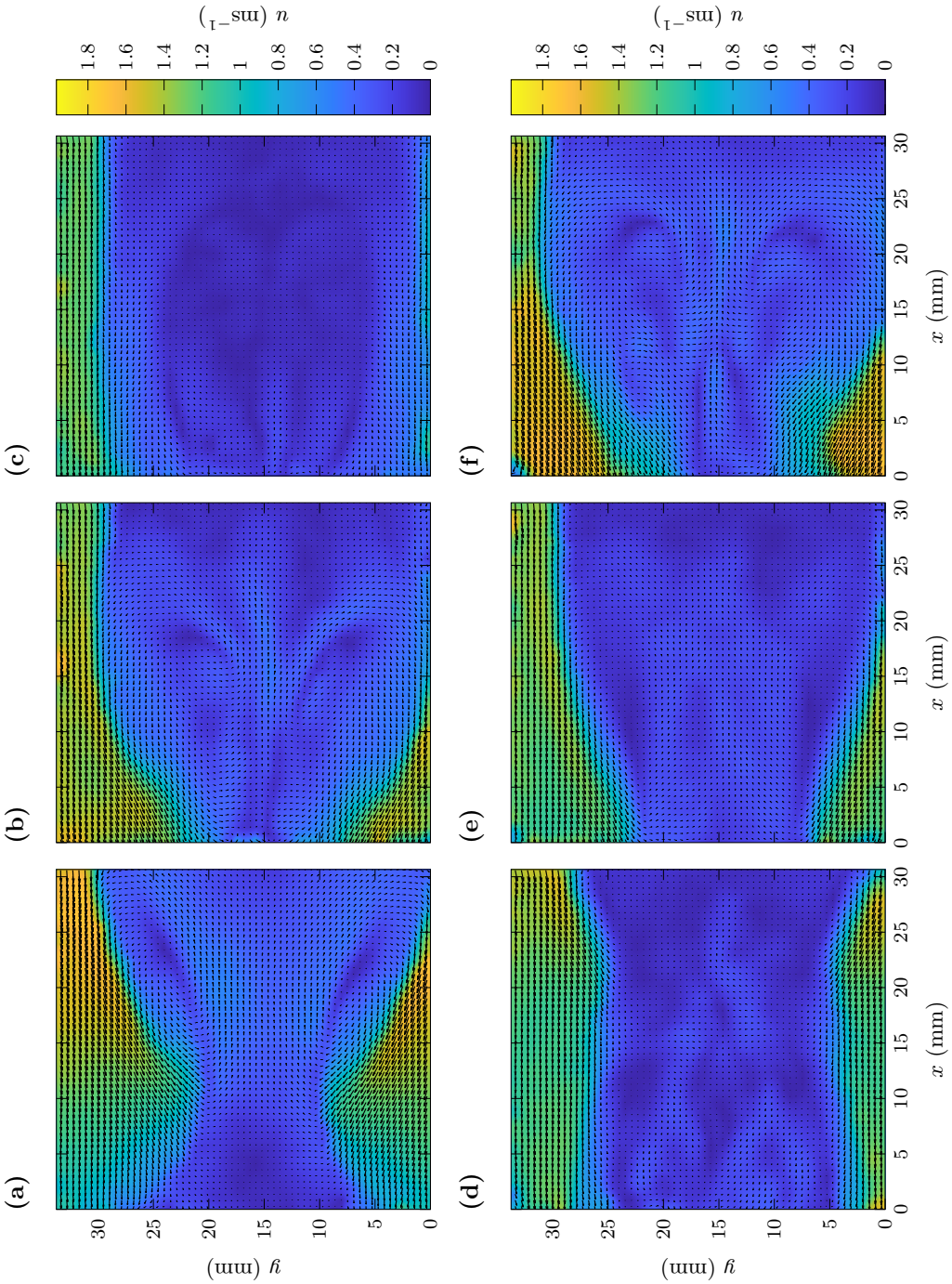


Figure 3.9: Sequence of 6 successive PIV reconstructions for a 30 mm cylinder at $Re = 827$, ordered from (a) to (f). The flow travels from right to left, and the cylinder is placed just outside the camera field of view (to the right), in line with the middle of each image

symmetry in the channel. Fully attached flow is seen to initiate immediately after the vortices move out of the near wake region - this causes a 'pinching' effect in the velocity profile, as seen in the fourth image (d), due to the flow being able to adhere closer to the cylinder wall. When the first pair of vortices have moved sufficiently far downstream, a new recirculation region forms behind the cylinder and the process repeats itself, as seen from the fourth (d) to the sixth (f) image. It is worth noting the visual similarity in Figures 3.9 (b) and (f); presence of such recurring patterns confirmed the existence of an absolute flow instability.

'Traditional' von Kármán vortex shedding occurs in an alternating manner. However, this only happens for configurations using fixed long cylinders. Symmetric shedding has been reported to occur for cylinder aspect ratios below 4 [85], matching conditions established in this experiment. The current test section produced a maximum aspect ratio of 0.8 with the 10 mm cylinder. Streamwise perturbations of the channel flow, or cylinder oscillation can also cause symmetric shedding, as shown in [86]. These factors did not contribute to the symmetric result obtained - the cylinder was kept stationary, and streamwise fluctuations (characterised using PIV in an empty channel) were random and indeterministic.

Apart from the periodic nature of the wake, another noticeable observation from PIV reconstructions was the increase in average recirculation region length (hereafter called the formation length) for different Reynolds numbers. The formation length was evaluated from PIV reconstructions, by plotting the horizontal velocity component along the cylinder's horizontal axis, and subsequently evaluating the distance along this line where the velocity changes direction. This is highlighted in Figure 3.10.

Figure 3.11 plots the variation of the mean formation length L, non-dimensionalised by cylinder diameter D, against the Reynolds number for different blockage ratios β. Extrapolating each line to the horizontal axis yields a theoretical critical Reynolds number, $\mathrm{Re}_{\mathrm{c},\beta}$ for the onset of vortex shedding. The values obtained for the 10 mm and 20 mm cylinders were in close agreement with

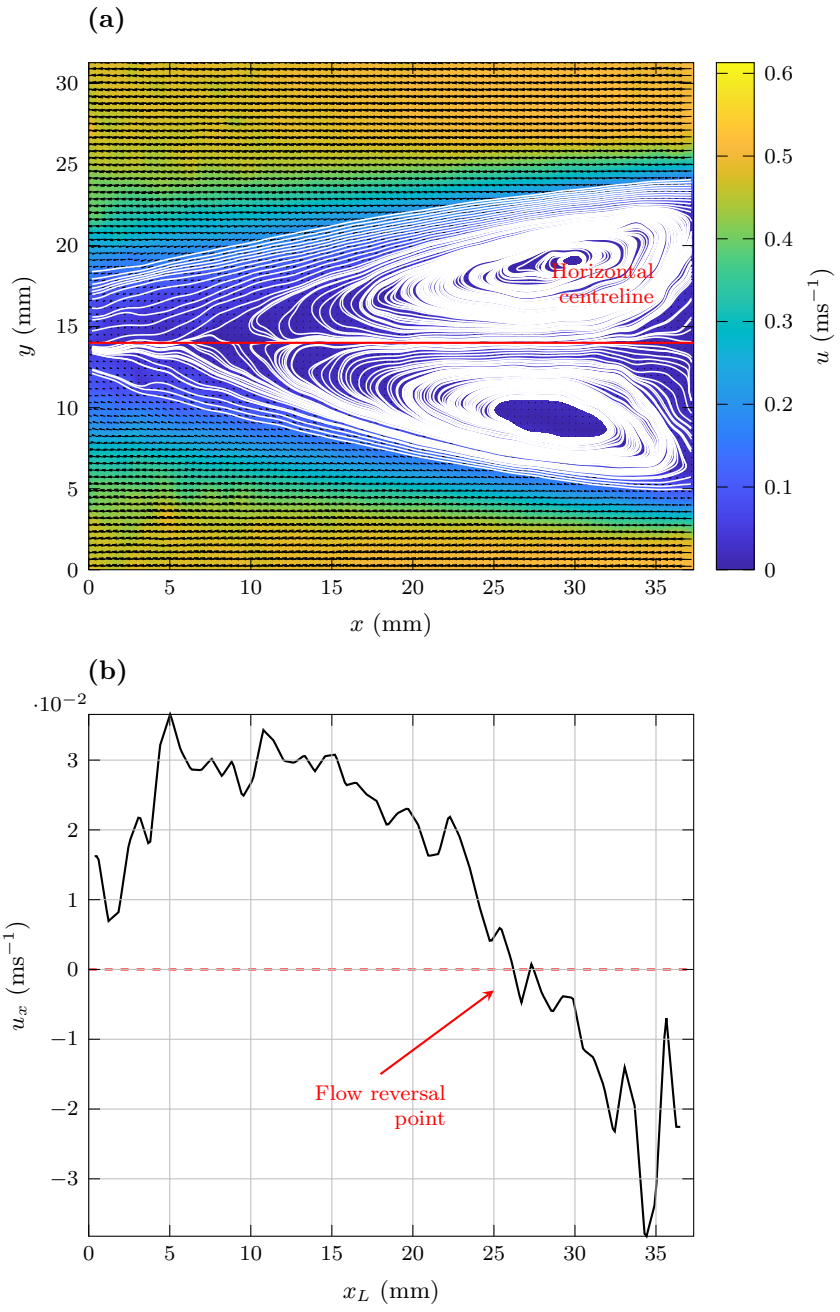


Figure 3.10: Procedure for extracting wake formation length. Note that x_L represents the distance from the cylinder. The flow horizontal velocity component (u_x) along the cylinder centreline is extracted from PIV reconstructions - this is indicated by a red line in (a). The formation length is then evaluated from the cross-over point between extracted velocities and the horizontal axis, where $u_x = 0$ (b)

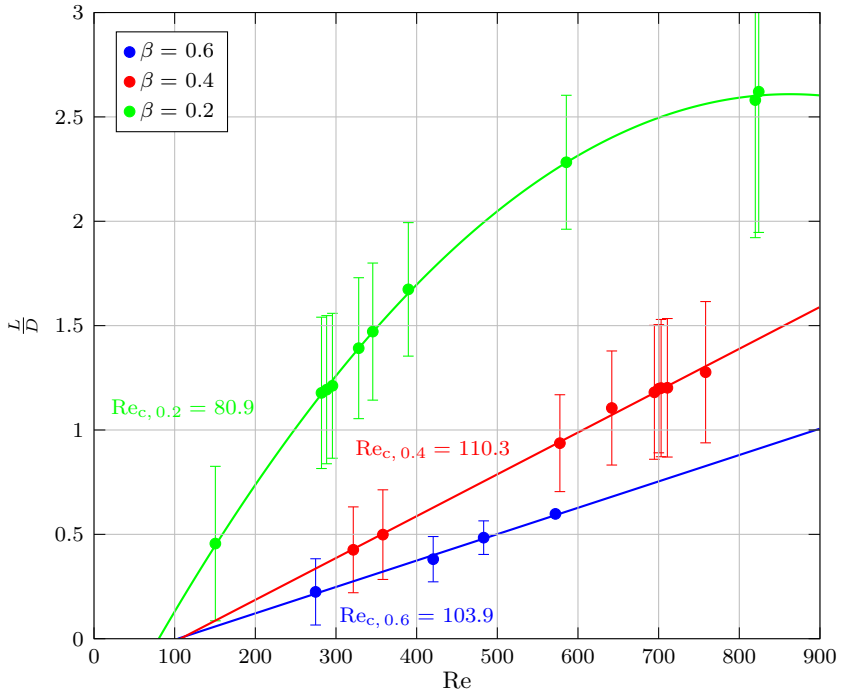


Figure 3.11: Wake formation length non-dimensionalised by the cylinder diameter, plotted against Reynolds number

those obtained by Sahin et al. [84] ($\mathrm{Re}_{c,\,0.2} = 80.9$ and $\mathrm{Re}_{c,\,0.4} = 110.3$, compared with 70 and 116 respectively). Similar agreement was not reached for the 30 mm cylinder (literature quoted $\mathrm{Re}_{c,\,0.6} = 120$), due to uncertainty in Reynolds number, as will now be explained.

The Reynolds number is defined in the context of vortex shedding from a cylinder in a confined flow according to Equation (3.2).

$$\mathrm{Re} = \frac{\rho \hat{U} D}{\mu} \tag{3.2}$$

where $\hat{U}$ is the maximum flow velocity rounding the cylinder. Given that the camera field of view had been set to 32 mm in the spanwise direction, almost all of the image was occupied by the wake in the case of the 30 mm cylinder, as seen in Figure 3.8 (c). This led to under-predicted values of $\hat{U}$, given that a region of higher speed flow just above the field of view was not imaged. Larger $\hat{U}$ values would lead to larger Reynolds numbers, which in turn shifts the blue line in Figure 3.11 to the right leading to a better estimate of $\mathrm{Re}_{c,\,0.6}$. A larger camera field of view

could not be used, as this introduced overwhelming surface scatter from the walls of the test section.

In most investigations involving flow around a bluff body, there is considerable interest in quantifying and understanding the variation of instability frequencies as a function of flow parameters. The frequency of vortex shedding from a cylinder is typically expressed in non-dimensional form as in Equation (3.3).

$$\mathrm{St} = \frac{fD}{\hat{U}} \tag{3.3}$$

where St is the Strouhal number and f is the frequency of vortex shedding. St typically remains constant for a large range of laminar and transitional Reynolds numbers, but has been shown to increase with increasing β. In this investigation, the fluctuation of the formation length was used to perform a spectral analysis, in order to extract the Strouhal number. Vortex shedding frequencies were extracted from the peak in power spectra, obtained using data from 500 consecutive PIV reconstructions.

Frequency calculations inevitably require adequate sampling rates. In order to accurately resolve cylinder shedding phenomena, the frequency of image-pair acquisition needed to be more than twice the shedding frequency, according to the Nyquist sampling theorem. Unfortunately, the laser used had a maximum frequency of 15 Hz, limiting frequency resolution to 7.5 Hz.

Figure 3.12 shows initial results from the spectral analysis. For each blockage ratio, there appears to be a decreasing trend in Strouhal number for increasing Reynolds number, contrary to what was expected. In order to validate these findings, documented Strouhal numbers were used to predict the expected shedding frequencies for each test case. Solid-coloured data points in Figure 3.12 were found to be the only test cases expected to produce shedding frequencies under 7.5 Hz. Further validation of this was seen from a trend in the extracted frequencies. For a constant

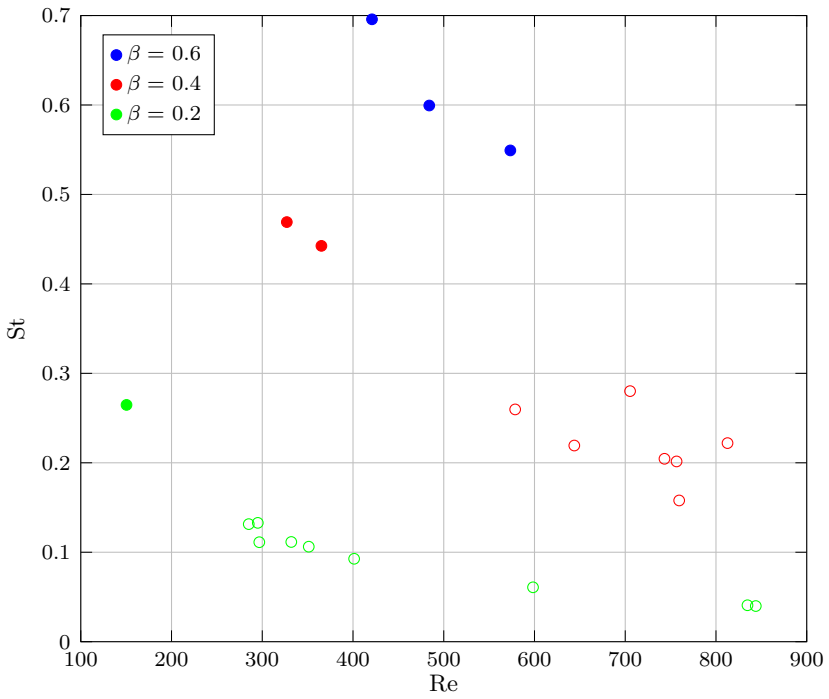


Figure 3.12: Strouhal number variation with Reynolds number. Solid-coloured data points represent test cases expected to produce shedding frequencies under 7.5 Hz

Strouhal number, an increase in Reynolds number (due to an increase in flow velocity) should lead to an increase in frequency. However, extracted frequencies for solid-coloured data points were found to be quite close to 7.5 Hz; frequencies for the subsequent data points were found to drop away to lower values. Assuming published data is correct, this implies that the shedding frequencies for non solid-coloured data points lie above the maximum resolvable frequency.

Figure 3.13 was then plotted using aliased frequency values. Mean Strouhal numbers for each blockage ratio have been displayed as straight lines on this figure. It is evident that the mean Strouhal number increases with increasing blockage ratio, consistent with trends observed in the past [87]. Published data indicates St = 0.20, 0.34 and 0.42 for $\beta = 0.2$, 0.4 and 0.6. In this study, we determined St = 0.203, 0.359 and 0.616. Agreement is good, apart from the 30 mm cylinder, which can again be explained by an underestimated $\hat{U}$.

At higher Reynolds numbers, the presence of a distinct shear layer with Kelvin-Helmholtz vortex structures was detected, as shown in Figure 3.14. The onset of this localised instability could not be determined accurately, given the large jump in Reynolds numbers between test cases. However,

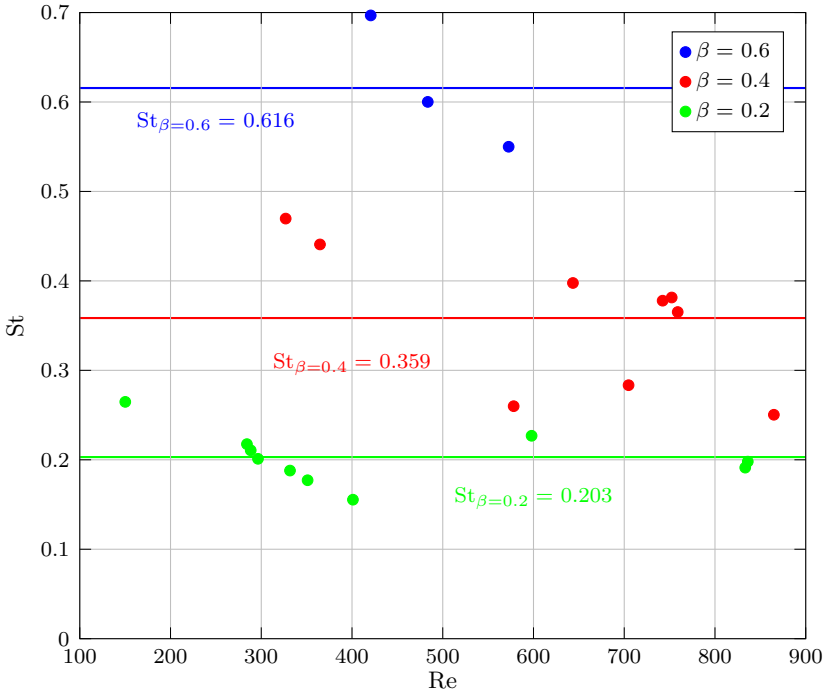


Figure 3.13: Corrected Strouhal number variation with Reynolds number

shear layer vortices could not be seen for $\mathrm{Re} < 1200$, and were observed to occur definitively for test cases above $\mathrm{Re} = 1600$, also in good agreement with published results [88, 89].

The Strouhal number for this shear layer instability, St_θ is defined according to Equation (3.4).

$$\mathrm{St}_\theta = \frac{f_{\mathrm{sl}}\theta_{\mathrm{m}}}{\bar{U}} \tag{3.4}$$

where f_{sl} is the frequency of the Kelvin-Helmholtz vortical structures, θ_{m} is the momentum thickness of the wake boundary layer and $\bar{U}$ is the free-stream velocity, taken to be the channel velocity in this case due to confinement. Experimental and analytical investigations in the past have evaluated St_θ to range between 0.01 and 0.017 [90, 91] - these values yield frequencies far above the resolvable 7.5 Hz, if a time-series analysis was performed. However, the distance between vortices was found to be small enough that more than one vortex could be seen in a single PIV image. Given that the shear layer instability propagates via a convective mechanism, the difference in velocities between the fluid above and below these vortices could be used to

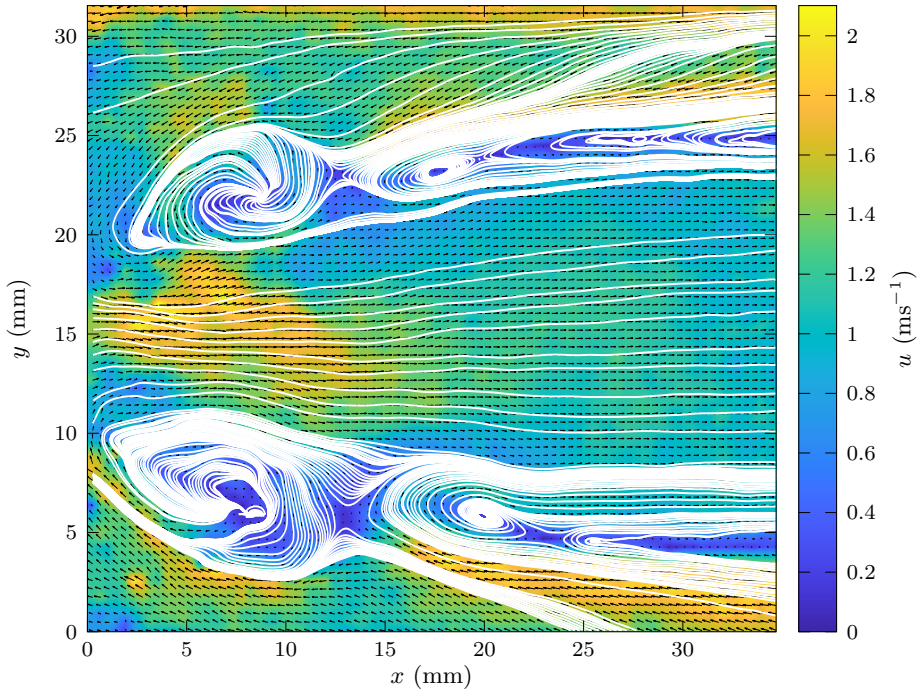


Figure 3.14: PIV reconstruction for a 20 mm cylinder at Re = 3000. The mean horizontal component of velocity was subtracted from all vectors, to aid visualisation of vortex structures

determine a convective velocity. This velocity was then used along with the vortex spacing to calculate a shedding period, without having to analyse the shedding variation in time. $\bar{U}$ was obtained by performing PIV on an empty channel at the same flow rate. θ_{m} was calculated according to Equation (3.5), by extracting the velocity profile along the wake behind the cylinder.

$$\theta_{\mathrm{m}} = \frac{1}{2}\left(a - \int_0^a \left(\frac{u(y)}{\bar{U}_{\mathrm{wake}}}\right)^2 \mathrm{d}y\right) \tag{3.5}$$

where a is the width of the wake, $u(y)$ is the velocity distribution across the wake, y is the vertical coordinate, and $\bar{U}_{\mathrm{wake}}$ is the mean velocity in the recirculating region.

Due to the large Reynolds number requirement, only three test cases could be investigated with existing mass flow controllers. These were all for the 20 mm cylinder at Re = 2371, 2993 and 3634. Extracted St_θ values for these cases were 0.018, 0.015 and 0.02 respectively, which all show strong agreement with published values. Further validation would be possible if a larger, and more continuous range of flow rates were used.

The results from this investigation have shown that a successful implementation of PIV is in place. Apart from being a useful flow visualisation tool, valuable quantitative information may be extracted from PIV reconstructions. As described previously, this task was necessary in order to set-up a working system capable of analysing flow fields and obtaining reproducible results.

3.3 PIV of a fluidic switching device

This section describes a collaborative experiment with the Active Flow Control research group of the University of Oxford. Results from this experiment have been published in the ASME Journal of Fluids Engineering [17]. Experimental set-up and data collection was performed by the author of this thesis using the established PIV system described in the previous section, while data analysis and computational modelling was performed by co-author Dr Michael Mair.

3.3.1 Test section and problem summary

This second PIV experiment analysed the flow field inside a novel active fluidic switching device [17]. Conceptually, this device provides flow control, by allowing users to spatially deflect or oscillate a fluid jet through the application of acoustic excitation, i.e. without mechanical actuation or secondary air supply systems. Such a device has potential for use in a range of flow control applications, such as boundary layer separation control, vehicle drag reduction, unsteady film cooling and combustion instability suppression. The novel device was built in-house to investigate the application of flow control in jet engines. This new technology demonstrated significant advantages over other passive and active flow control mechanisms, notably its ability to output any desired oscillatory switching pattern.

The test rig investigated contained a nozzle expanding into a dual-exit channel flanked by two acoustic transducers, as shown in Figure 3.15. A jet of air that exits the nozzle adheres to one side of the channel, as a lateral pressure gradient forms due to unsteady flow disturbances. The flow stays attached to the same side, as long as the established pressure gradient is not counteracted

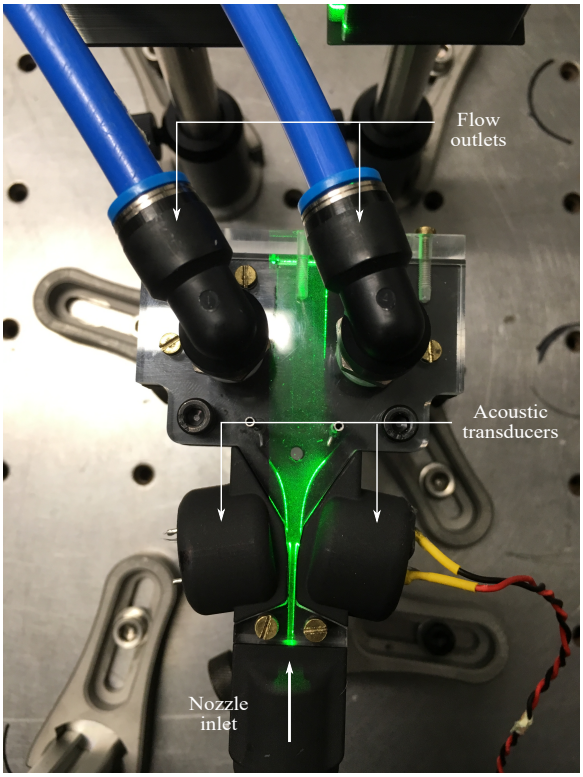


Figure 3.15: Fluidic switching device illuminated by laser sheet

by an opposite resultant force - this effect is called the Coandă effect. However by exciting the jet with acoustic waves at characteristic resonance frequencies, natural instabilities in the flow are amplified causing an increase in fluid entrainment into the shear layer of the jet. This causes a shift in pressure distribution, ultimately switching the attachment of the jet to the opposite wall. The specific mechanism of instability amplification differs, depending on the Reynolds number of the established jet. The main objective of this experiment was to validate the mechanism of flow switching for high Reynolds numbers, by visualising flow features inside the device during acoustic excitation. This would highlight the interaction between the acoustic control input and the main fluid jet, enhancing understanding for flow conditions that are relevant to jet engines.

Previous investigations had found two modes of acoustic excitation in this device - the so-called 'shear layer' mode and the 'jet preferred' mode. The former refers to the frequencies associated with small scale eddies in the jet shear layer ($\mathrm{St}_\theta = 0.012$) while the latter refers to

frequencies from a global instability, much like von Kármán vortices, within the jet. Large Eddy Simulations (LES) of high Reynolds number flow fields (Re = 5000) showed that by exciting the jet preferred mode of the nozzle exit flow, an increase in fluid entrainment occurs purely through the mechanism of vortex amplification. In addition, the location of shear layer roll-up was found to move upstream to a distance of about one to two nozzle diameters from the nozzle orifice. This is different to the switching mechanism and flow structures inherent of lower Reynolds number jets; flow switching is achieved in this case by exciting the shear layer mode, which increases fluid entrainment through merging of vortices. Besides this, the natural shear layer roll-up location for laminar jets was about five nozzle diameters from the nozzle orifice [92]. In this investigation, PIV was employed for the high speed case in order to validate findings.

The main challenge with implementing PIV for this device was its small size - the nozzle had a diameter of 1 mm, while the overall height of the flow cavity was 3 mm. A Reynolds number of 5000 needed to be established in the test section - this led to a flow speed of $\sim$100 ms^{-1} (due to its small flow area). Coupling this with the camera's small field of view (a square window measuring 7 mm $\times$ 7 mm) necessitated a short inter-pulse time, to avoid excessive flow averaging. Successful PIV reconstructions were achieved by setting laser pulses 400 ns apart - coming very close to the camera's specified inter-frame time of 200 ns. In addition, the use of small droplet sizes ensured a good level of tracer fidelity, with maximum Sk = 0.1 (using a maximum particle diameter of 1 µm). The procedure employed for this experiment was similar to the first, with the added task of timing acoustic excitation relative to the laser pulses. Since the laser operated at a maximum frequency of 15 Hz which was far too slow to resolve an entire switching process (4 ms), a phase-locked approach was employed. Different stages of the switching process were captured by acquiring PIV images at varying delays between laser pulse and acoustic excitation. A dual pass PIV approach was applied to analyse images, with standard decreasing square interrogation window sizes of 64 and 32 pixels respectively. A default 50 % interrogation window overlap was also applied as before, resulting in a flow field spatial resolution of 0.1 mm.

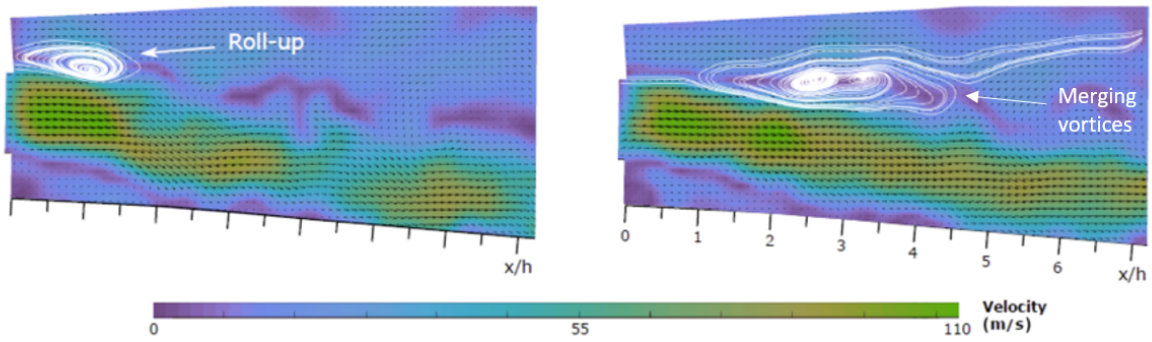


Figure 3.16: Natural shear layer roll-up location (left) and downstream merging vortices (right) indicated by PIV results

3.3.2 Results and analysis

Results from the fluidic switch experiment were very compelling. Firstly, PIV results confirmed an upstream shift of the shear layer natural roll-up location (pre-excitation) - this is seen in Figure 3.16. Merged vortices were seen further downstream, but this behaviour was less common.

Secondly, PIV reconstructions were shown to have a high degree of similarity with LES findings - Figure 3.17 shows these results. During excitation of the jet preferred mode, enhanced shear layer roll-up took place, resulting in the formation of large vortices. This is seen very clearly by comparing vortex sizing before, during and after acoustic excitation. Much like the excitation of the shear layer mode, vortex amplification promoted an increase in mixing, leading to enhanced entrainment in the jet shear layer and thus a switching process. However, throughout the datasets obtained, merging of eddies was not observed. In fact, vortex spacing was found to remain constant throughout the excitation phase. Further validation was obtained by estimating the shear layer roll-up frequency using PIV data. Here, the method used in Section 3.2 based on vortex convection speed and spacing was employed to estimate the instability frequency (since the laser operated at far too slow a frequency for a temporal analysis). A range of 27.5 kHz to 34 kHz was obtained corresponding to the slowest and fastest eddies in the shear layer respectively - these values were within 15 % of the LES predicted instability frequency. In summary, the expected switching mechanism for an active bistable fluidic device operating at

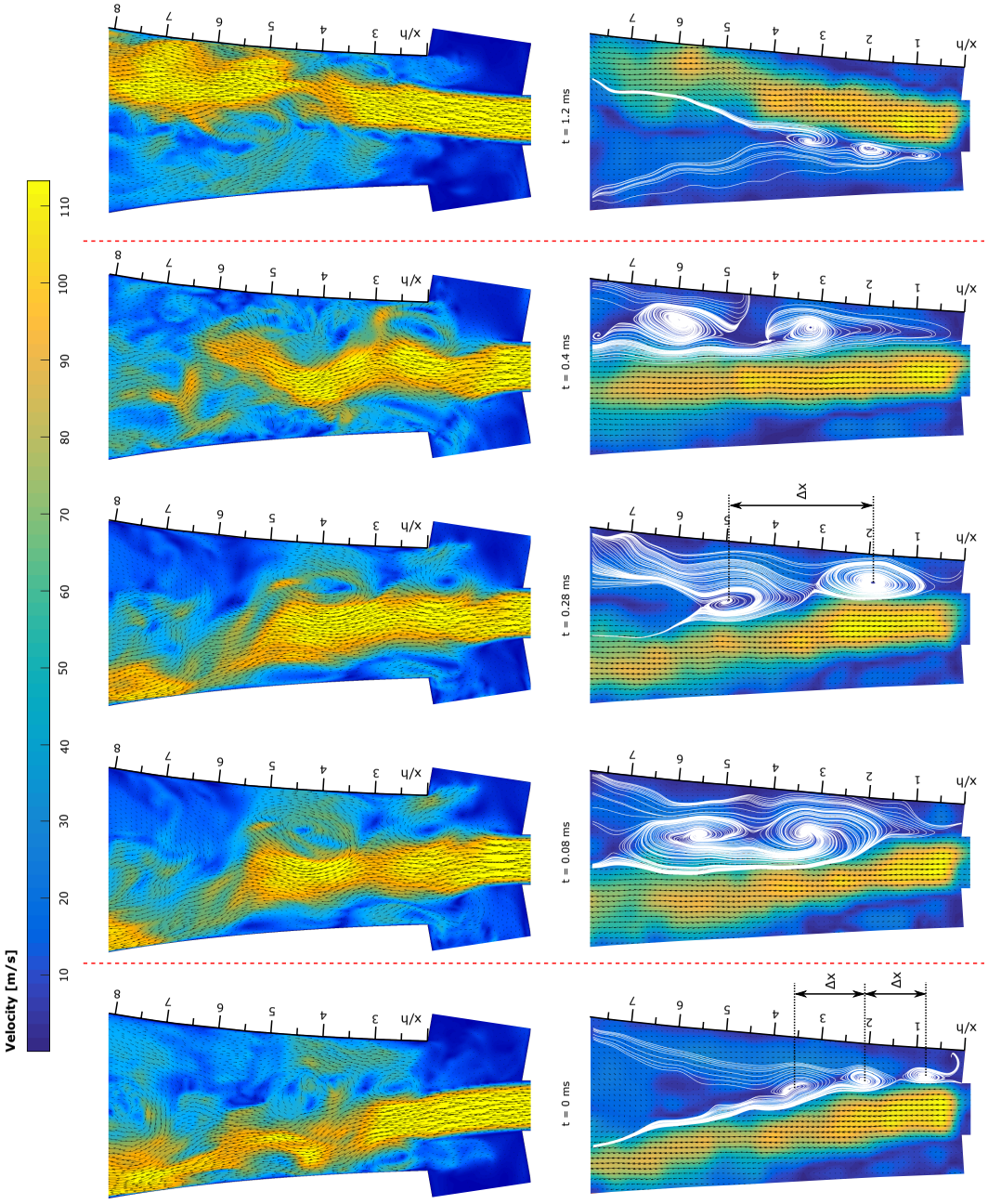


Figure 3.17: Comparison of PIV (bottom row) and LES (top row) results during switching process. Images at $t = 0.08$, 0.28 and 0.4 ms were all taken during excitation. Note how the vortex separation increases from $t = 0$ to 0.08 ms, stays constant throughout the excited jet phase, and then decreases again after switching

turbulent Reynolds numbers was validated using results from PIV.

3.4 Summary

This section detailed the development and testing of a new PIV system capable of imaging a range of speeds. The cylinder wake experiment described in Section 3.2 served its purpose as a trial investigation - flow features and parameters were successfully identified from PIV reconstructions. Having tested imaging at slow speeds, the PIV system was applied to a novel fluidic switching device that employed much faster flow speeds. An LES model of the device was successfully validated, highlighting the physical mechanisms of switching at high Reynolds numbers. These findings have extended the application of the novel flow control technology towards turbulent conditions that are relevant to jet engines, bringing it one step closer to physical implementation. The PIV system is operational, producing reliable single parameter (velocity) results.

Chapter 4

Fluorescent Particle Image Velocimetry

In Chapter 3, the key components required to successfully implement PIV in a high-speed flow were identified. These components were then integrated to perform velocimetry measurements on two separate flows; one at speeds less than $10\,\mathrm{ms}^{-1}$, the other at a challenging maximum speed of $120\,\mathrm{ms}^{-1}$. Results from these experiments demonstrated successful extraction of spatially resolved velocities at a range of speeds. In this chapter, a number of limitations to applying PIV for high-speed applications are addressed.

One of the main difficulties encountered when performing PIV experiments is strong elastic scatter from surfaces such as walls, windows, and sprays, that are present in the flow cavity. Scatter from such bodies is often stronger and more intense than that of seeding particles due to their large surface area. As a result, there is a mismatch in incident laser energy requirement for PIV - higher pulse energies are required in order to be able to see PIV particles, however too much laser energy will lead to saturation of pixels imaging surfaces or sprays. A consequence of this is so-called 'blooming', where saturated pixels leak charge into adjacent pixels, forming bright streaks or blobs that extend beyond the area in the image where the scattering body is present - an example of this is shown in Figure 4.1. In the specific case of CCD cameras, blooming can also lead to smearing, where charge from saturated pixels further leaks along the direction of the shift register as pixels are being read out, leading to bright streaks along a line across the image. Both blooming and smearing cause PIV droplet signals to be overwhelmed, particularly in the vicinity of the scattering body, leading to spurious velocity determination. These artefacts are detrimental for velocimetry studies investigating boundary layer physics, fuel

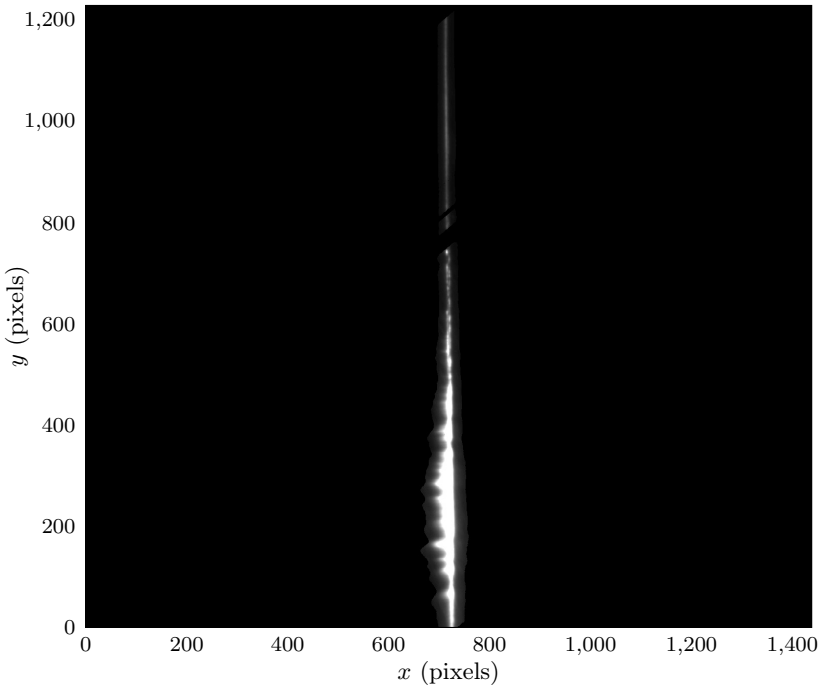


Figure 4.1: Example of minor CCD blooming, causing the formation of short bright streaks extending horizontally from the vertical line of illumination. This image was obtained unintentionally, following a vertical laser sheet striking a reflective aluminium panel

spray injection and fluid-structure interaction to name a few [22, 93, 19]. Intense pixel saturation can lead to camera sensor damage - this chapter explores how likely it is for this to happen.

Recent research in high-speed flow applications typically involve combinations of flow physics - of most interest is usually the coupled interaction between momentum and heat transfer. To this end, simultaneous multi-property experimental diagnostic techniques provide high value, as they precisely capture any physics inter-dependencies in a single run. Several simultaneous optical diagnostic techniques have been developed and reported in the literature, but these are usually very complex, typically utilising multiple laser sources, cameras and flow tracers [93, 94, 44, 47, 46]. Not only can this be costly, it also requires specialist skills to ensure proper set-up, calibration and operation of the techniques.

To address these limitations, a variant of the traditional PIV technique has been presented, called Fluorescent Particle Image Velocimetry (FPIV). Seeding particles introduced into a flow are either chosen as natural fluorophores, or doped with a laser dye. By tuning the wavelength

of laser light to an excitation wavelength of the fluorophore, particles will both elastically scatter the incident excitation, as well as spontaneously fluoresce at longer wavelengths. While this is the case for the particles, surfaces (that have not been coated by fluorescing particles) and sprays will mostly scatter light at the same wavelength as the incident excitation. Through appropriate spectral filtering, elastic scatter can be isolated from the longer wavelength fluorescence, improving signal-to-noise ratio (SNR) by only capturing light from the particles and not surfaces or sprays. In doing so, unwanted scatter artefacts are avoided, allowing velocity measurements to be made closer to surfaces and sprays while preventing sensor damage.

This change to measuring photoluminescence from seeding particles instead of scatter presents an additional advantage. Fluorescence emission inherently depends on a number of different factors, notably, the temperature of the substance. Choosing a fluorophore that varies its fluorescence emission with temperature allows extracting this for the seeding particles as well. This paves the way for FPIV being a multi-property diagnostic tool - it effectively acts as a simultaneous combination of PIV with Planar Laser-Induced Fluorescence (PLIF). A key advantage of FPIV is that only a single laser source and a single tracer is needed for simultaneous diagnostics. Results from this work will reveal that FPIV can also be performed using a single camera, although the use of two cameras is preferred.

The aim of this work is to develop FPIV as a simultaneous velocimetry and thermometry tool. Significant effort has been devoted in Chapter 3 towards making velocity measurements with tracer particles, so this chapter will focus more on thermometry measurements from particles. A number of FPIV proof-of-concept experiments are described in this chapter, mostly devoted towards exploring temperature-dependent fluorescence properties of a novel LIF tracer. Results from these experiments will highlight the various advantages of using this diagnostic technique. A number of further requirements and improvements that will enhance the performance of this tool are presented in Chapter 8.

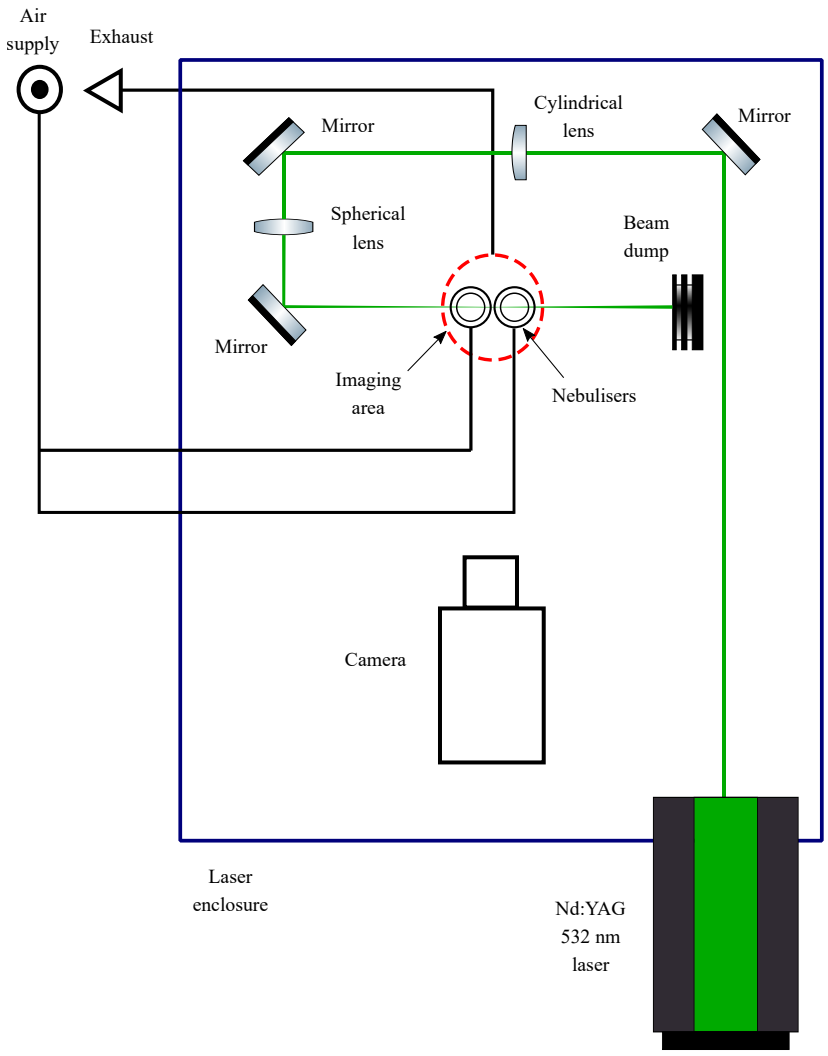


Figure 4.2: Experimental layout for elastic scatter tests

4.1 Elastic scatter reduction

This section describes a simple experiment to demonstrate FPIV's ability to suppress overwhelming scatter from large surface area bodies. Figure 4.2 shows the layout of optical components used to perform this test.

In these experiments, the laser, camera and sheet forming optics used are the same as those used in Chapter 3. Pulses from both laser cavities were fired simultaneously in order to double the amount of usable energy (allowing up to 200 mJ of pulse energy at 532 nm). A 35 mm tall, vertical laser sheet was formed and brought to a focus at the imaging area to interact with a scattering body. Scatter and fluorescence from this interaction was then imaged using the camera

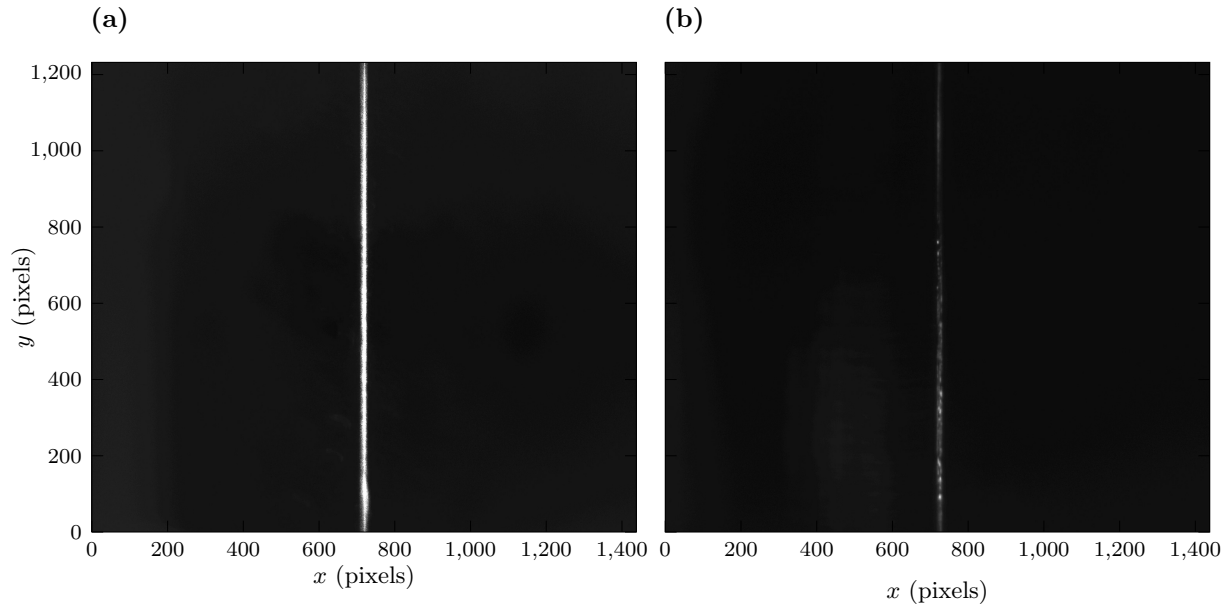


Figure 4.3: Scatter without spectral filtering using 1 mJ laser pulse energy (a) and with spectral filtering using 200 mJ laser pulse energy (b)

in two ways - with and without a filter placed in front of it. Images in the former configuration would demonstrate the deleterious effects of elastic scatter, while the latter would test the ability to suppress this when performing FPIV. The filter fitted to the camera was a long-pass edge filter (Thorlabs FELH0550) with a cut-on wavelength of 550 nm and an optical density of 6 at the laser wavelength of 532 nm.

In the first test, a black anodised aluminium panel was positioned vertically in the imaging area facing the incoming laser sheet. Scatter from such a layout simulates scatter from a wall in a flow test section, upon which a laser sheet is terminated, thus strong signals were anticipated. When the filter was absent, pixel saturation was expected, so the laser was set to output minimal pulse energy. This energy was ≤ 1 mJ, as limited by the sensitivity of the available energy meter (Sensor- und Lasertechnik PEM 45K USB). When the filter was placed in front of the camera, the laser was set to output its maximum energy of 200 mJ. These conditions sought to demonstrate the difference in scatter signals expected with and without spectral isolation, while also testing the limits of scatter suppression.

Figure 4.3 (a) shows the scatter signal from the aluminium panel without using the long-pass

filter. The line where the laser sheet impacts the panel is clearly visible in the centre of the figure. Pixels here are saturated despite the small pulse energy - under these conditions, scatter from the panel was barely visible when viewed with the naked eye. Building on experience from Chapter 3, for this field of view, at least 10 mJ of pulse energy is required for normal PIV - it is evident that at such illumination levels, pixels will definitely saturate, are likely to bloom and smear, and perhaps damage permanently.

Figure 4.3 (b) shows the scatter signal from the aluminium panel with the long-pass filter in place. The laser impact line is again visible, however despite at least 200 times more pulse energy, the pixels are far from saturated. The average signal across the impact line is approximately 30 counts (out of a possible 255) - such signals can be tolerated when performing standard PIV, or removed easily using background subtraction. Comparing signals and pulse energies from the two tests, the effective surface flare attenuation achieved is at least 3.2 orders of magnitude. Some brighter scatter artefacts can be seen in Figure 4.3 (b) due to localised scratches on the anodized coating. A simple calculation using the filter's rated attenuation of 6 orders of magnitude, indicates no signal should be visible at all. However the interaction between the laser and the aluminium panel is not purely elastic. Some inelastic scatter and fluorescence is present which can transmit through the long pass filter. Importantly, this demonstrates that surface scatter can be dealt with more easily when using FPIV.

It has been shown that surface scatter can be tolerated even at 20 times the usual pulse energy required for standard PIV. The next test sought to establish if it was possible to observe fluorescence from dye-doped droplets, while also attempting eliminating scatter from a jet. Here, two upright medicinal nebulisers supplied with compressed air were angled towards each other to produce two aerosol plumes that mix along a vertical centre-line. This central mixing jet was probed by the same laser sheet as before, and imaged with the same CCD camera and imaging optics (not intensified). One nebuliser was filled with water, while the other contained water

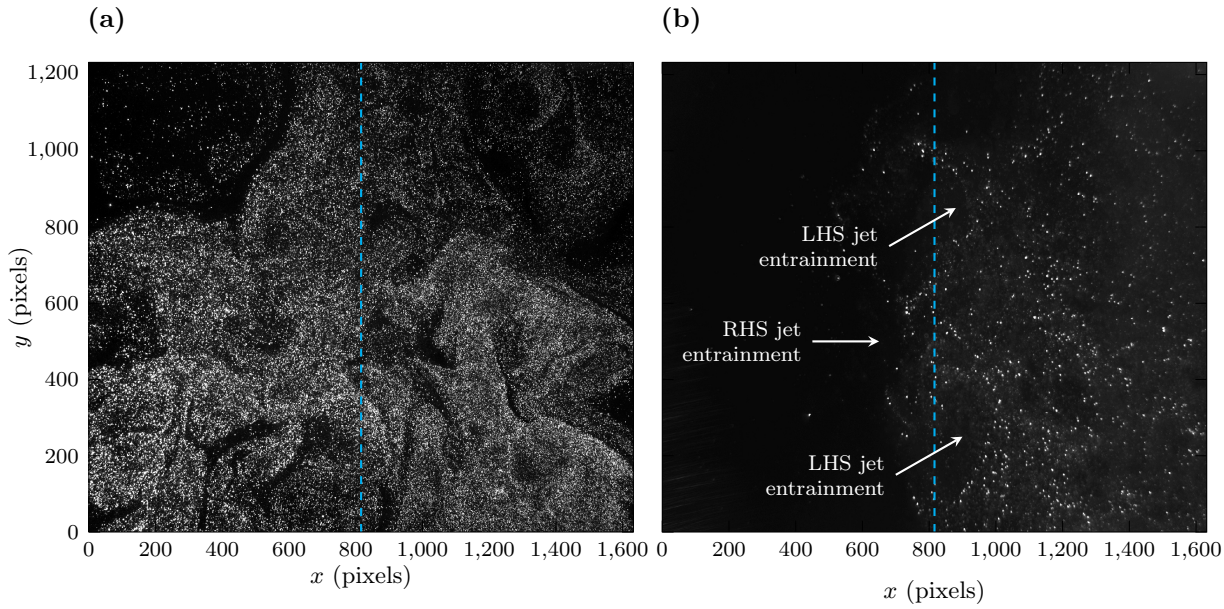


Figure 4.4: Aerosol droplets imaged without long-pass filter (a) and with long-pass filter (b). LHS refers to the 'left-hand side', while RHS refers to the 'right-hand side'

mixed with Rhodamine 6G laser dye. The concentration of the dye solution was not measured, rather, dye was added to the solution until appreciable signal was obtained. Both nebulisers operated at a nominal flow rate of 7 slpm.

Figure 4.4 (a) was obtained without the long pass filter, hence, it captures both elastic scatter and fluorescence from the droplets. 10 mJ of pulse energy was used, mimicking conditions in a standard PIV experiment, with the aperture on the camera lens stopped down to $f/4.0$. A wide plume of droplets is evident in this image - scatter, being stronger than fluorescence, dominates the signal and thus saturates pixels wherever droplets are present. Here, no distinction between the pure water jet and the dye-infused water jet can be made.

Figure 4.4 (b) was obtained with the long pass filter, thus eliminating elastic scatter. The camera lens aperture was fully opened to $f/1.4$ and the laser was set to output 200 mJ as before. Here, there is a clear distinction between the two separate jets - the left region appears to have no particles since pure water droplets are present here, while the right region displays particles since dye-infused droplets are present here. The influence of the shear layer between the two jets is also visible in this figure - two lobes void of droplets can be seen extending beyond the centre-line

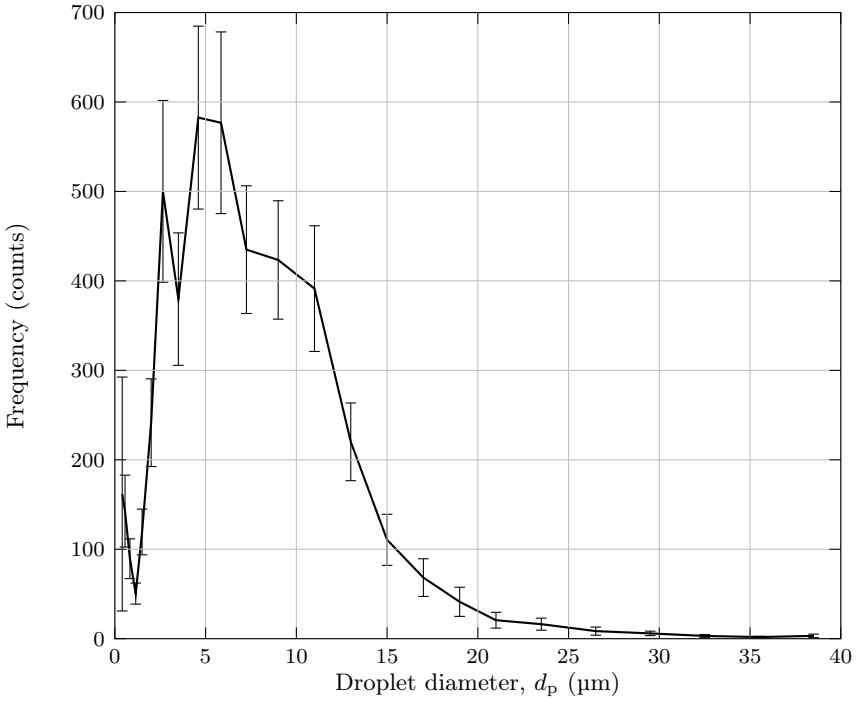


Figure 4.5: Droplet size distribution generated using a nebuliser. The error bars represent the standard deviation of 12 measurements

into the right hand region. Similarly a few dye-infused droplets can be seen having diffused into the left hand region.

There appears to be a difference in droplet density when comparing Figures 4.4 (a) and (b). Fluorescence signal from droplets appears to be more sparse, with an almost uniform haze cloaking the entire region. Meanwhile elastic scatter appears discrete, distinct and highly dense. This is caused by the disparity in signal dependence on droplet diameter between scatter and fluorescence, as will now be justified.

The nebuliser produces a particle size distribution as shown in Figure 4.5 - this was measured using a particulate matter sensor (Alphasense OPC-N3). The 10-90 percentile range of this distribution yields droplet sizes in the range of 1.5 µm to 15 µm. Figure 4.6 shows the Mie scattering cross-section dependence on particle diameter and incident laser wavelength. Over the range of d_p/λ produced by the nebuliser (> 3), there is a quadratic dependence of the scattering cross-section on the particle diameter [7]. Fluorescence on the other hand simply depends on the number of molecules present in the probed region. Providing the liquid is optically thin,

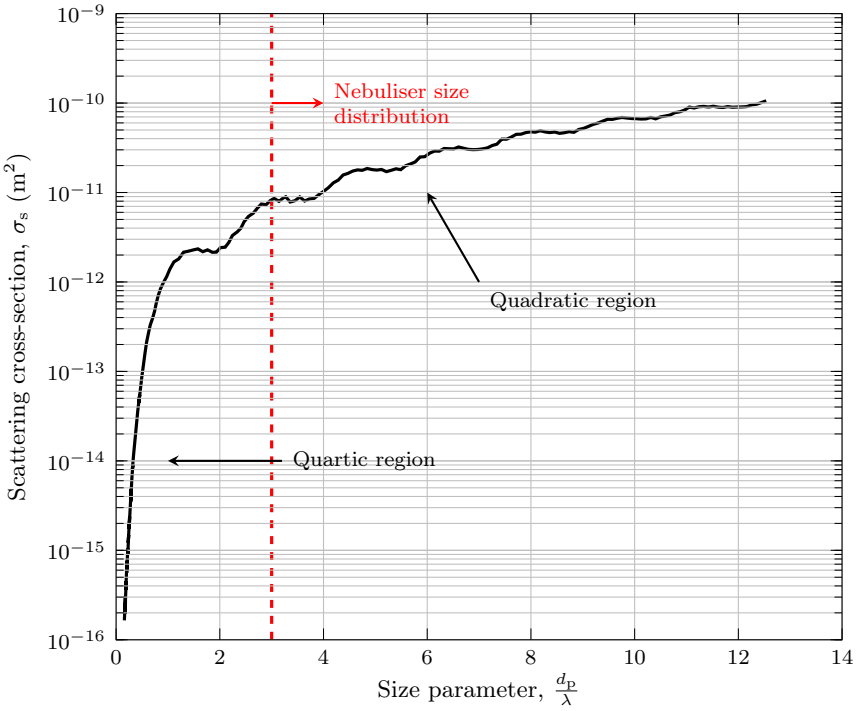


Figure 4.6: Scattering cross-section dependence on particle diameter - adapted from [7]

this means fluorescent signal depends on the volume of the droplet, or d_p^3 [95]. Using the range of droplet sizes listed above, the fluorescence signal disparity between the smallest and largest droplets is a factor of 1000, while scatter signal disparity is a factor of 100. When performing standard PIV, signal disparity between various droplet sizes is overcome by increasing the laser pulse energy until most droplets just saturate the camera pixels (while still not ideal, careful control of saturation should not lead to any damage of the sensor). However, if temperature information is to be extracted simultaneously from the fluorescing droplets, saturation should be avoided. A solution to this fluorescence signal disparity is to use a seeder that produces an almost mono-disperse distribution of droplets - an example of this is the LaVision aerosol generator that was used in Chapter 3 (results in subsequent sections of this chapter will show this). The LaVision aerosol generator was not used for these proof-of-concept tests, due to concerns about cleaning laser dye out of the device at the end.

This section has demonstrated the ability of using fluorescent droplets as a means to remove elastic scatter that can otherwise inhibit PIV measurements. These initial experiments used

Rhodamine 6G - a laser dye with a large fluorescence quantum yield (provided in the subsequent section) and known temperature-dependent fluorescence [96]. The goal was to demonstrate FPIV's abilities, as this dye produces strong fluorescence signals that are sensitive to changes in temperature. However, several drawbacks of using Rhodamine 6G for FPIV were observed. The main drawback is its propensity to permanently stain test sections and piping. In custom built test sections or small facilities, such as the ones described in Chapter 3, this may not be a problem - test sections at this scale can be manufactured via 3D printing and replaced as they become contaminated and unusable. In some cases, these could also be cleaned using appropriate solvents. This is not the case for large scale high-speed facilities such as wind tunnels. Cleaning facilities stained with laser dyes may prove impossible, with lasting effects on future studies in these facilities. In addition, Rhodamine 6G has known toxicity risks, as well as a number of other safety hazards (elaborated in the subsequent section). For applications beyond modest bench-top installations, it is evident that the use of FPIV would benefit from the use of a different fluorophore.

4.2 Candidate tracers for FPIV

When choosing a tracer for FPIV, a number of criteria should be considered:

- Health hazards

  The tracer should be non-toxic. Leakage from test sections could cause accidental inhalation of tracer particles, as well as eye and skin exposure. This is a much bigger hazard when dealing with large test sections and high flow rates.

- Solubility

  Dopant tracers should be soluble in existing PIV seeding liquids to ensure complete mixing and incorporation of tracer in each particle. A related problem is to identify solvents that can be used to clean tracer droplets deposited on surfaces.

- Boiling point

  Higher liquid boiling point is desirable to improve application to flows with raised temperatures. In addition, volatile tracers vaporise easily - this could cause changes in tracer concentration from droplet-to-droplet, leading to loss of signal and spatially-varying SNRs.

- Excitation wavelengths

  Tracers must be chosen with laser availability in mind. A high-energy, double-pulsing laser operating at an excitation wavelength of the tracer is required for FPIV.

- Emission wavelengths

  Visible fluorescence emission is typically advantageous, as cameras and optics for such applications are readily-available. Ultraviolet (UV) fluorescence emission would require the use of fused silica optics along with specialised cameras and objective lenses.

- Absorption cross-section

  Large cross-sections indicate stronger absorption of incident excitation photons. This leads to a higher chance of fluorescence emission, thus improving signal.

- Fluorescence quantum yield

  High quantum yields are desired, as they imply a high efficiency of converting absorbed energy into fluorescence, thus maximising signal. The use of tracers with large absorption cross-sections and high quantum yield is likely to deliver sufficient signal at reduced concentration and laser pulse energy, using standard camera technologies.

- Temperature sensitivity

  Higher sensitivity to temperature in the relevant range is preferred, but this is dependent on emission wavelength, and is typically a balancing act with signal strength. Pre-experiment calibration measurements are normally performed to gain better insight to the sensitivity-signal trade off.

- Fluorescence self-absorption

  Absorption and emission spectra of tracers typically overlap over a certain range of wavelengths. Fluorescence emission from tracer molecules in this overlap region can be reabsorbed by other tracer molecules on its way to the detector. The extent to which reabsorption occurs depends on factors such as particle density and tracer solution concentration, so without accurate knowledge or control, reabsorption can be detrimental to fluorescence based diagnostics. Choosing fluorophores with minimal self-absorption (i.e. a wider wavelength split, or Stokes shift, between absorption and emission) would be beneficial.

Laser dyes are the obvious first choice as tracers for FPIV, given their large absorption cross-sections (at their respective excitation wavelengths) and fluorescence quantum yield. Examples of these include the rhodamine, coumarin and fluorescein families of fluorescent molecules. Apart from these, some organic compounds such as toluene [23, 24, 25, 33, 36], acetone [26, 97, 98] and 3-pentanone [30, 98, 99] have been used extensively as PLIF tracers. Table 4.1 summarises the characteristics of a few candidates that are more commonly used in the literature for PLIF studies. Data presented in this table was obtained from [100] for Rhodamine 6G and B, [101] for Coumarin 151, [102] for toluene and acetone, and [103] for 3-pentanone.

Table 4.1: Characteristics of candidate tracers for FPIV. Absorption cross-section values presented are for the relevant Nd:YAG laser harmonic excitation wavelength, i.e. 532 nm for both Rhodamine 6G and B, 355 nm for Coumarin 151 and 266 nm for toluene, acetone and 3-pentanone

	Rhodamine 6G	Rhodamine B	Coumarin 151	Toluene	Acetone	3-pentanone
Absorption wavelengths (nm)	440 - 565	460 - 580	320 - 450	230 - 275	230 - 320	230 - 320
Emission wavelengths (nm)	510 - 700	520 - 700	420 - 650	265 - 330	340 - 660	320 - 600
Absorption cross-section (cm^2 $molec^{-1}$)	1.90×10^{-16}	1.36×10^{-16}	1.83×10^{-17}	2.00×10^{-19}	4.30×10^{-20}	5.00×10^{-20}
Fluorescence quantum yield	0.95	0.65	0.53	0.17	0.002	0.0008
Fluorescence self-absorption	High	High	Moderate	Moderate	Low	Low
Safety hazards	Respiratory tract, eye and skin irritation. Toxic	Respiratory tract, eye and skin irritation. Toxic	Eye and skin irritation. Mildly toxic	Respiratory tract and skin irritation. Flammable. Toxic	Eye irritation. Flammable	Respiratory tract, eye and skin irritation. Flammable
Solubility	Water, ethanol, methanol	Water, ethanol, methanol	Ethanol, methanol	Ethanol, acetone. alcohol	Water, ethanol, methanol	Ethanol
Boiling point (°C)	210 (Melting)	210 (Melting)	221 (Melting)	111	56	102

The use of laser dyes as tracers is beneficial as they have large absorption cross-sections and fluorescence quantum yields, which maximises signal strength. Most dyes also operate in visible wavelengths, further simplifying experimental requirements. These typically come in powder form, and need to be mixed with a solvent. Rhodamines are soluble in both water and organic solvents while coumarins are only soluble in organic solvents. Rhodamines are commonly excited with the second harmonic of an Nd:YAG laser while coumarins typically utilise the third harmonic. A drawback to using laser dyes is fluorescence self-absorption; rhodamine dyes notably have large overlaps in their absorption and emission spectra - this is less of an issue for coumarins but is still pronounced.

Certain organic compounds are candidates as FPIV tracers as well, given their widespread use in vapour-based PLIF studies in the literature. Extending their use to droplet-based measurements inevitably limits the operating range of temperature somewhat below their boiling points. Volatile tracers such as acetone should be used with care to avoid tracer concentration variations across droplets. These substances are UV-excitable and mostly fluoresce in the UV as well, thus requiring more specialised equipment. Fluorescence self-absorption is less evident for the organic substances listed in Table 4.1 when compared with the laser dyes - this makes liquid-based fluorescence characterisation simpler. Note that all substances listed so far present moderate to serious safety hazards (toxicity, flammability). Therefore, use of these substances require adequate safety protocols in order to mitigate any health risks.

4.3 Properties of DEHS

Diethyl-hexyl sebacate (DEHS) is an oily, colourless and odourless liquid typically sold with commercial PIV systems. It is an organic di-ester formed through a condensation reaction between 2-ethylhexanol and sebacic acid. It is mostly used as a plasticiser, however it is also widely used in PIV experiments because it exhibits a number of desirable properties:

- It is not known to be toxic
- It has a high boiling point of 212 °C
- It is cheap (£66.30 for 1 litre)
- Droplets smaller than 1 µm are produced using commercial aerosol generators. This generates low particle Stokes numbers and increases flow fidelity
- It has a non-zero vapor pressure at room temperature, meaning settled droplets eventually evaporate

As a result, suppliers of 'pre-built' optical diagnostics such as LaVision and Dantec Dynamics recommend the use of DEHS with their PIV systems. In the context of finding a suitable fluorophore for FPIV, it would be beneficial if said fluorophore were doped into DEHS - this would enable taking advantage of the physical properties of DEHS while also isolating elastic scatter and potentially extracting temperature information simultaneously. DEHS is an organic, water-insoluble compound, so organic fluorescent tracers such as toluene, acetone, biacetyl and 3-pentanone are suitable for mixing. However before attempting this, DEHS itself was tested for any photoluminescent properties in order to confirm it would not compete photophysically with the tracer candidates.

This section details novel experimental findings about the photoluminescent properties of DEHS. To the best of our knowledge, there exists only one other publication that describes photophysical properties of DEHS [104], in which constant temperature excitation-emission spectra of DEHS were presented. Figure 4.7 shows the absorption spectra of 3 different batches of DEHS, each only differing by purity, measured using a UV/Vis/NIR spectrophotometer (Shimadzu UV-1800). The spectra show strong absorption for wavelengths less than 300 nm - this means that DEHS molecules are electronically excited when illuminated with light at these wavelengths. Conveniently, this allows DEHS to be excited by some common UV lasers, such as

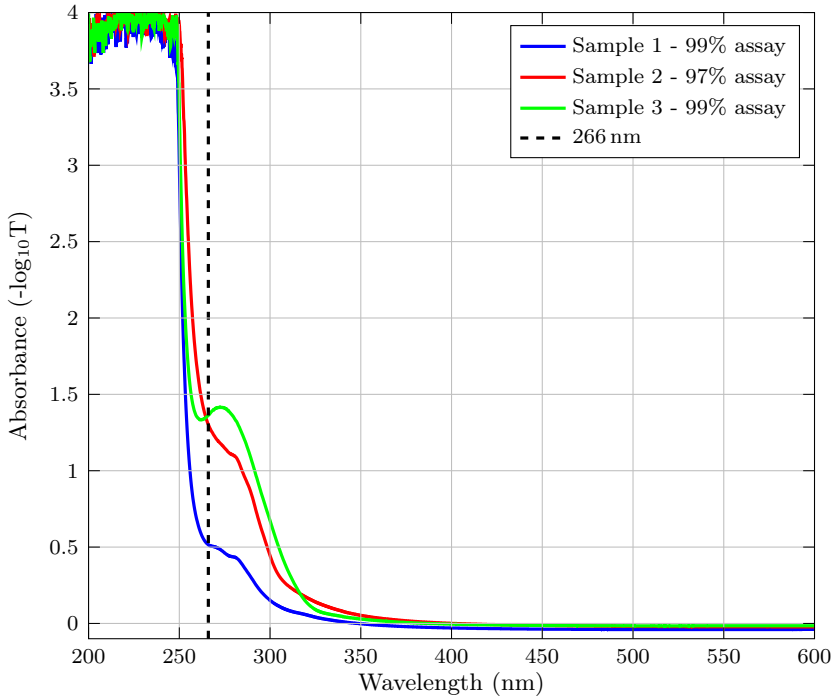


Figure 4.7: Absorption spectra of liquid DEHS measured with a UV/Vis/NIR spectrophotometer. The 4th harmonic of an Nd:YAG laser (266 nm) is indicated to demonstrate that DEHS absorbs at a convenient wavelength

Nd:YAG (frequency-quadrupled), KrF, argon-ion (frequency-doubled) and coumarin-based dye lasers (frequency-doubled). Figure 4.8 shows the result of illuminating a cell containing DEHS with a sheet of 266 nm light (at a pulse energy of 4 mJ) - an intense electric-blue fluorescence emission is visible from the cell.

These results show that DEHS is excitable by UV radiation, leading to fluorescence emission. Consequently, many existing PIV systems are already one step closer to performing FPIV, in that no modifications to flow seeding is necessary. This is beneficial as it means no added risks as a result of fluorescent tracer doping are introduced. A number of other upgrades and additions to these systems may be required in order to extract the maximum benefit - these will become apparent throughout the chapter and will be summarised at the end.

4.3.1 Liquid DEHS fluorescence spectra

Having demonstrated that DEHS fluoresces under 266 nm excitation, a spectrometer was used to measure its emission spectrum. Doing this would shed light on the best spectral isolation

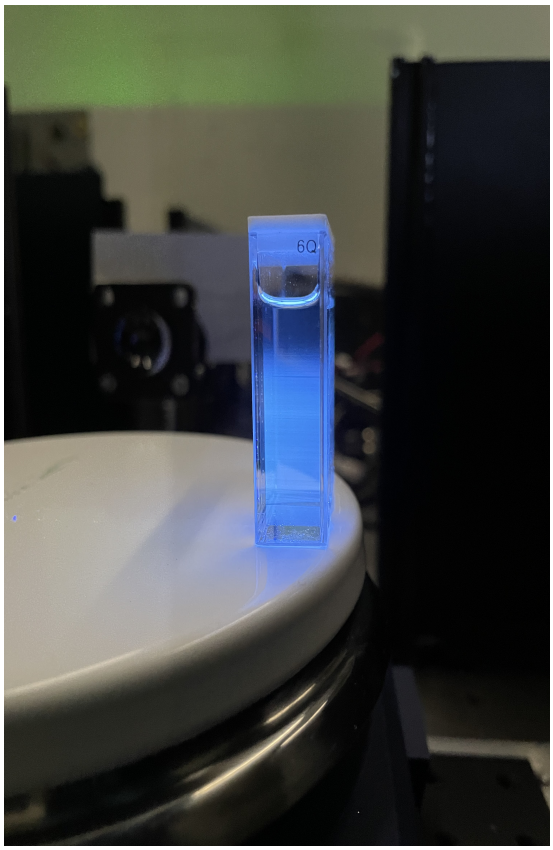


Figure 4.8: Visible fluorescence from a cell of DEHS excited by a 266 nm laser sheet

strategy when performing FPIV with DEHS, while also revealing any possible temperature-dependent fluorescence properties. Figure 4.9 shows a schematic of how this was achieved.

A Continuum Minilite laser was used to produce 4 mJ pulses of 266 nm radiation of ~ 5 ns duration. This beam of light was directed towards a quartz beaker containing DEHS and subsequently dumped on a beam trap. The quartz beaker was placed on a magnetic stirring hot plate (Sciquip GyroStir SP2230-280H), with a stirrer and thermocouple placed in the beaker. This device allows the contents in the beaker to be stirred at speeds ranging from 100 to 1500 rpm, while also being temperature controlled up to a maximum plate temperature of 280 °C. The purpose of using this plate was two-fold. Firstly, temperature control of the plate allowed measuring DEHS' fluorescence spectra at varying steady-state temperatures. Secondly, intense pulsed radiation can cause photobleaching of fluorophores - this is when high-energy photons cause chemical damage to molecules, altering and eventually diminishing their ability to fluoresce. Characterisation of this phenomenon is presented in the subsequent section. Through stirring DEHS, the molecules

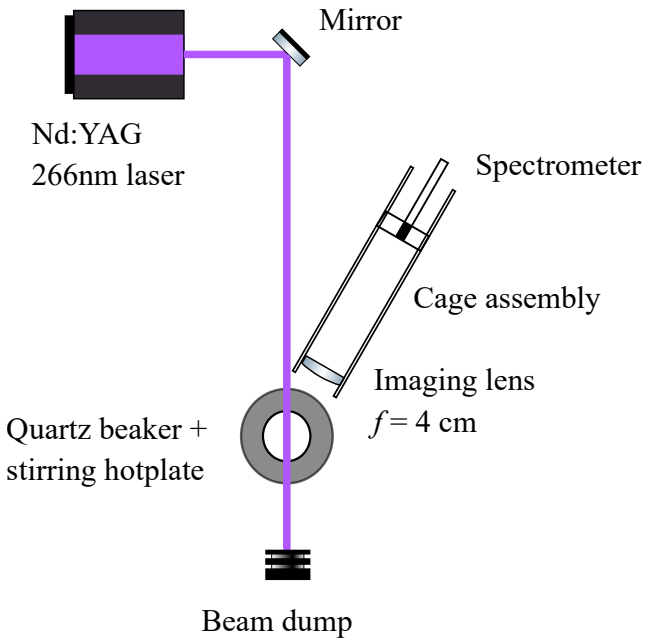


Figure 4.9: Experimental layout used to measure temperature-dependent emission spectra of liquid DEHS

being exposed to the UV beam were constantly being replenished, thus prolonging the ability to measure its unaltered fluorescence spectra. As an added precaution, the total number of pulses delivered to each sample of DEHS was also limited to 200 pulses (justified in the next section).

Emission from the excited DEHS was captured using a spectrometer (Ocean Optics USB4000). A 1" spherical lens ($f = 40\,\text{mm}$) was used to increase the light collection efficiency by coupling light directly into the fiber-tip of the spectrometer. Tests were performed by continuously stirring beaker contents (a nominal speed of 100 rpm was used), achieving steady-state DEHS temperatures, and subsequently sending 10 laser pulses into the quartz cell at a frequency of 2 Hz. The spectrometer was triggered to acquire the emission from each individual pulse - these 10 spectra were then averaged to form one spectrum for each steady-state temperature. Tests were performed from room temperature up to about 373 K in roughly equal steps of 5 K.

Figure 4.10 compiles the emission spectra of DEHS measured across a range of temperatures. Each curve represents the mean spectrum obtained per steady-state temperature (listed in the figure legend). The curves are coloured from blue to red, representing a change in temperature

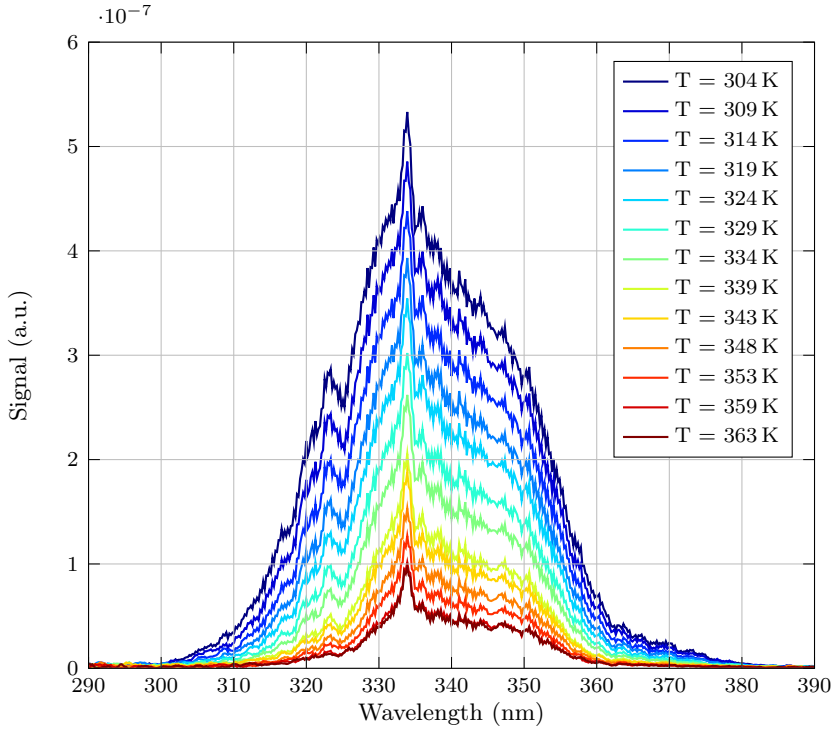


Figure 4.10: DEHS fluorescence spectra at varying temperatures

going from cold to hot, for ease of reference.

Qualitatively, the fluorescence emission of DEHS appears to be confined between 300.0 and 380.0 nm. The peak emission wavelength is 333.9 nm - fluorescence intensity builds up rapidly going from 300.0 nm to this value, and then displays a slower decay going from the peak to 380.0 nm. At this stage, it is not apparent whether DEHS exhibits fluorescence self-absorption, as the absorption and emission spectra do not overlap, but are also adjacent to one another. An appropriate check for this would be to dilute DEHS in a solvent and re-measure its emission. However this was not attempted as solvent addition could change the emission characteristics of DEHS, which would make comparison with droplet-based measurements incorrect. Subsequent sections address the issue of DEHS self-absorption appropriately.

It is apparent that DEHS fluorescence is affected by temperature - this can be seen by the general drop in signal intensity across the entire spectrum as temperature increases. This is not a consequence of a drop in laser pulse energy, or degradation of DEHS molecules from photobleaching, as the steady-state temperatures were tested in a random order. An increase

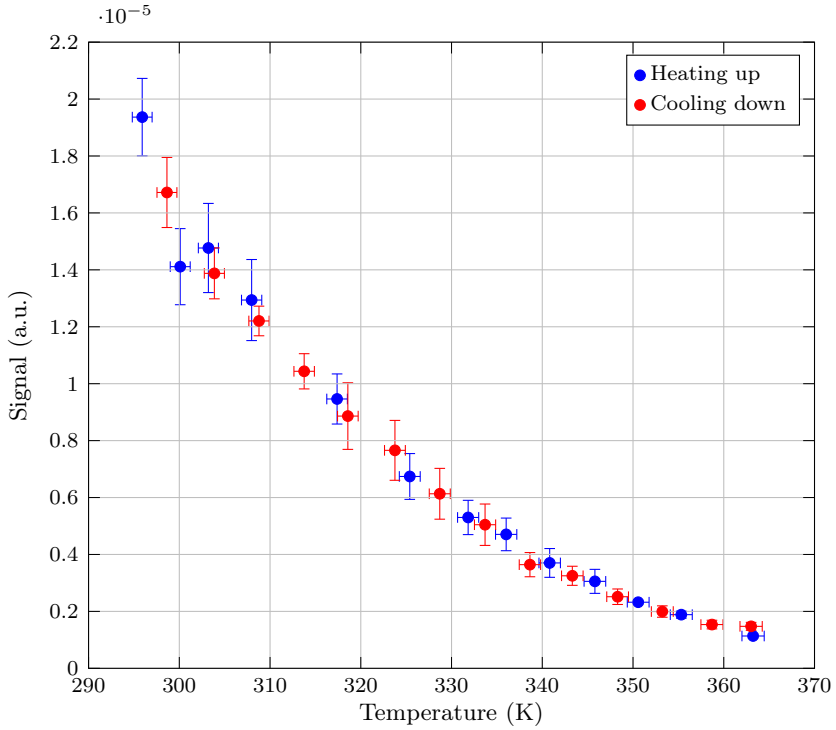


Figure 4.11: Total DEHS fluorescence signal variation with temperature. Horizontal error bars represent the measurement uncertainty of the thermocouple. Vertical error bars represent the standard deviation of total signal from 10 measured spectra

in temperature leads to an increase in kinetic energy of the molecules - this promotes collisions between molecules, leading to non-radiative decay back to the ground electronic state, thus leading to less fluorescence. Figure 4.11 shows the variation in total fluorescence signal (the area under each spectrum) with temperature - it is evident that PLIF thermometry studies using DEHS are possible.

A less apparent observation from Figure 4.10 is the general shifting of the spectra shape towards longer wavelengths - this is known as red-shifting, as it indicates a shift of a spectrum towards the 'red' side of the electromagnetic spectrum [1]. This effect becomes apparent when each spectrum is normalised by its area for wavelengths less than the peak emission - this is shown in Figure 4.12. As temperature increases, the left part of the spectra decreases, while the right part increases. This effect has been noted for other fluorescent tracers in the literature, notably toluene [105]. Red-shifting is normally accompanied by a translation of the peak emission wavelength as well,

[1] Conversely, a shift to shorter wavelengths is called blue-shifting

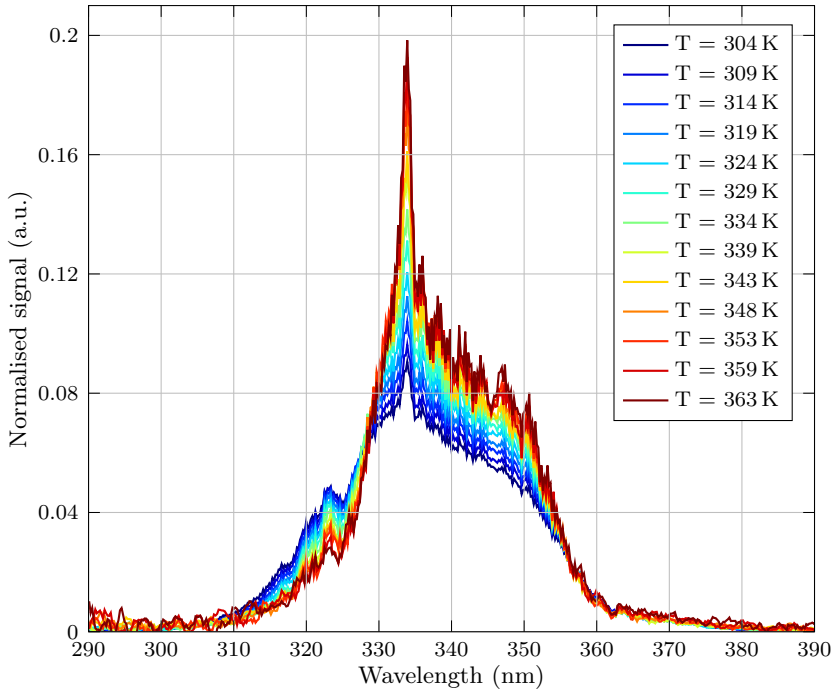


Figure 4.12: Normalised DEHS fluorescence spectra at varying temperatures. Each spectrum is normalised by the area underneath it for wavelengths $\leq 333.9\,\text{nm}$

however this is not seen here - this may become more apparent if a larger range of temperatures were tested [2]. Red-shifting enables the use of the two colour-PLIF (TC-PLIF) method for extracting temperature; since fluorescence intensity decreases much faster to the left of the peak compared to the right, the ratio of right-to-left intensities becomes a unique function of temperature.

Figure 4.13 was obtained by splitting DEHS' fluorescence spectra into two bands, integrating these bands separately and then taking their ratio. For ease of reference, spectral data from longer wavelengths are denoted R (for 'red') while those from shorter wavelengths are denoted B (for 'blue'). The DEHS R-band was obtained by integrating signal intensities to the right of the emission peak, i.e. from 333.9 nm up to the end of its emission at around 380.0 nm. The B-band was obtained by integrating the signal intensities to the left of the emission peak, i.e. from the start of its emission at around 300.0 nm up to 333.9 nm. Two datasets from separate experimental runs are presented in this figure - data from the 'heating' dataset was obtained in

[2] Toluene exhibits $\sim 2\,\text{nm}$ shift in peak emission wavelength over a temperature range of $\sim 100\,\text{K}$ [105]

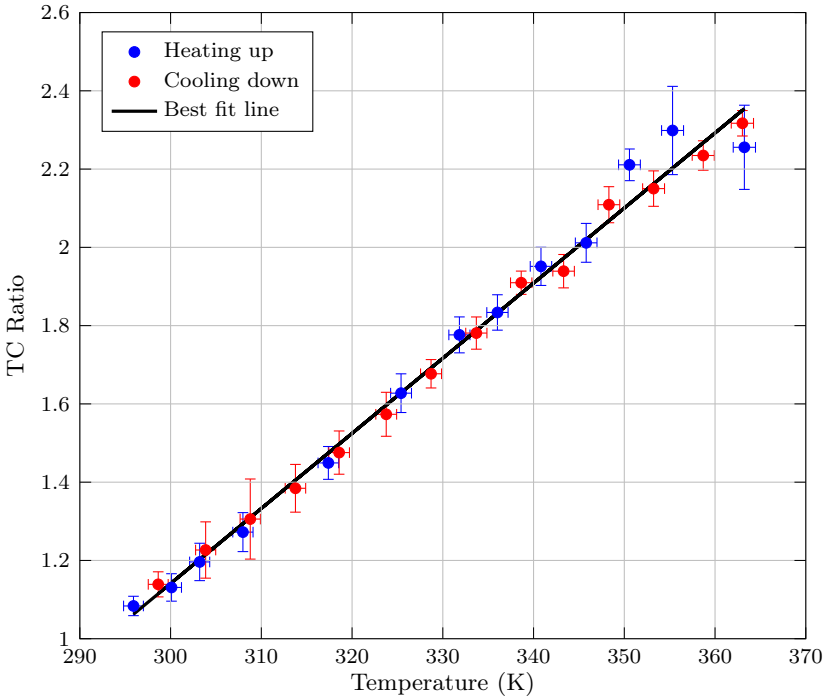


Figure 4.13: TC ratio variation with DEHS temperature. Horizontal error bars represent the measurement uncertainty of the thermocouple. Vertical error bars represent the standard deviation of TC ratio from 10 measured spectra

the general order of increasing temperature, while data from the 'cooling' dataset was obtained in the opposite manner. A strong and repeatable linear correlation can be seen relating the TC ratio to temperature. A slight falter from the line of best fit can be seen at higher temperatures, but this can be attributed to a lack of signal (as is evident from Figure 4.10) leading to extra noise and uncertainty. This fit between TC ratio and temperature would normally be used as a calibration curve for experimentally measured results - a measured TC ratio could be converted by using this fit to determine temperature. The gradient of this calibration line represents the sensitivity of the diagnostic - in this case, the sensitivity is $(0.0192 \pm 0.0008)\,\mathrm{K}^{-1}$.

4.3.2 Fluorescence photobleaching of DEHS

As previously mentioned, strong laser excitation can cause photobleaching of fluorescent molecules. Continuous photobleaching of DEHS causes its appearance to change from colourless, to yellowish-brown - this is shown in Figures 4.14 and 4.15. The criteria set out in Section 4.3.1 on limiting photobleaching was determined by subjecting a sample of liquid DEHS to constant UV excitation

for a total of 40,000 pulses at a frequency of 10 Hz. This was achieved in two separate runs of equal length, each lasting ~ 30 min, as the spectrometer was not able to save any more data than this on its internal memory. The same experimental layout described in Figure 4.9 was used, along with the magnetic stirring plate set to a constant (room) temperature and fixed mixing speed of 100 rpm. This was to ensure adequate replenishing of DEHS molecules, and that no temperature effects could influence analysis of the extent of photobleaching.



Figure 4.14: Fresh DEHS before exposure to any UV radiation

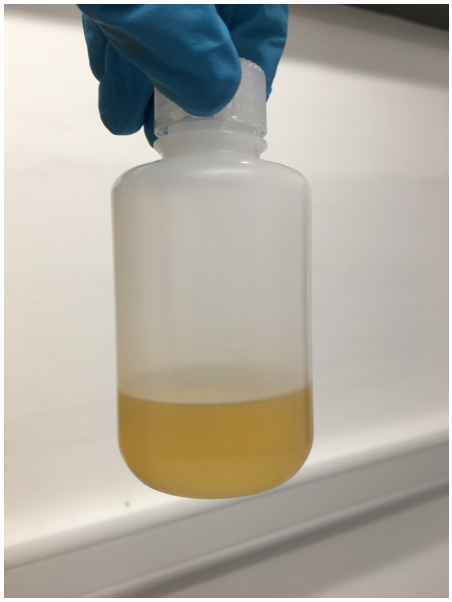


Figure 4.15: Degraded DEHS after exposure to a large number of UV laser pulses

Figure 4.16 shows the progression of constant temperature DEHS emission with time. Each curve represents a single scan, with colours changing from blue to red indicating an increase in time. Individual scans were picked out at 200 s intervals, as degradation progressed slowly given that the sample was constantly stirred. From this figure, it is apparent that the overall fluorescence signal intensity decreases with time, which is a similar observation that can be made with increasing sample temperature. The total fluorescence signal is plotted against pulse number in Figure 4.17. The plot is almost continuous going from the first to second run.

Peak-normalised emission curves are presented in Figure 4.18, where a similar red-shifting characteristic can be seen, although this is not identical to the behaviour seen with a rise in temperature.

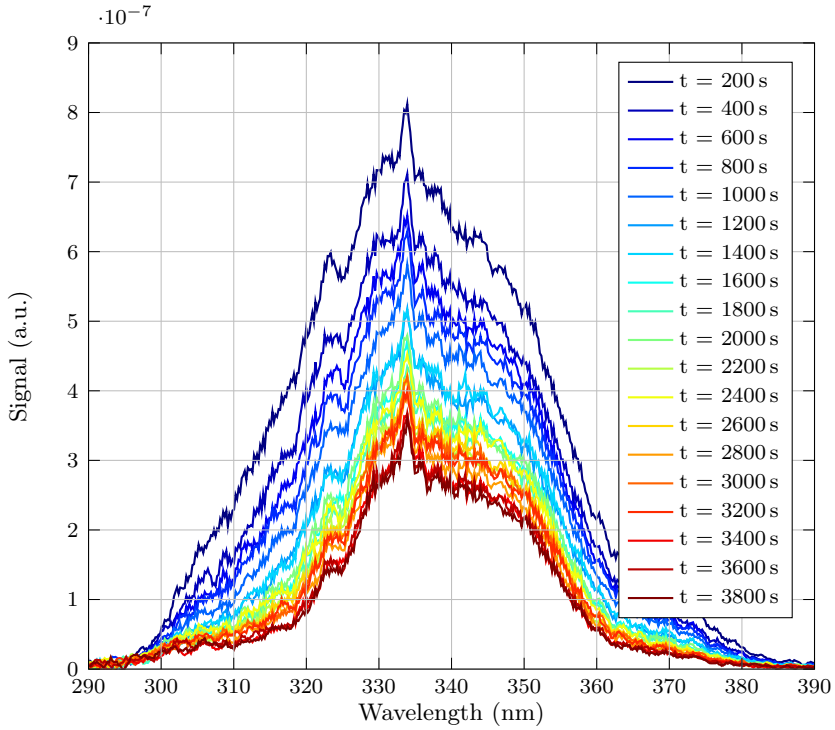


Figure 4.16: DEHS emission change with time due to photobleaching

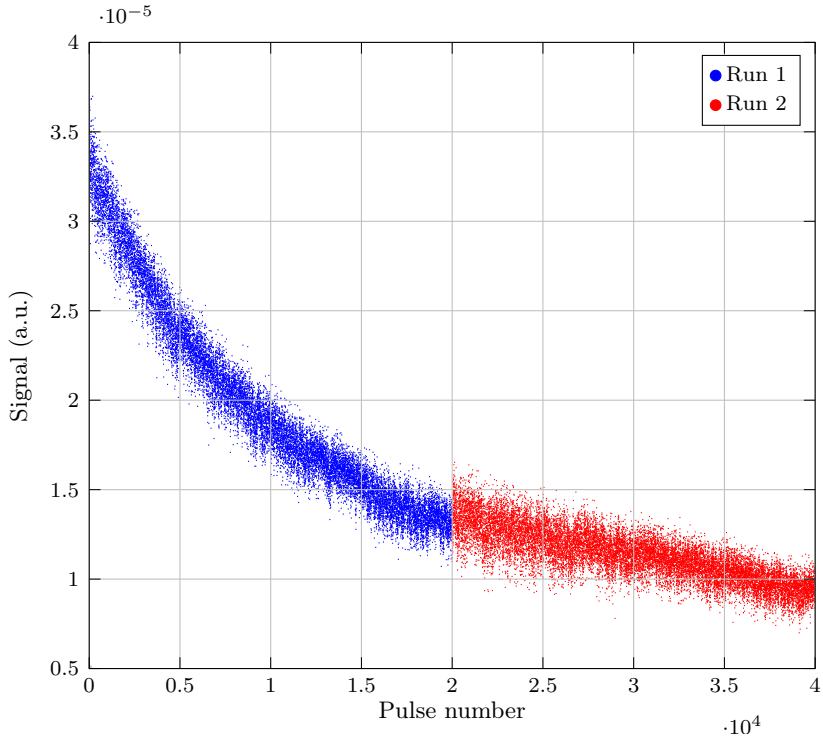


Figure 4.17: Total DEHS fluorescence signal change with time due to photobleaching

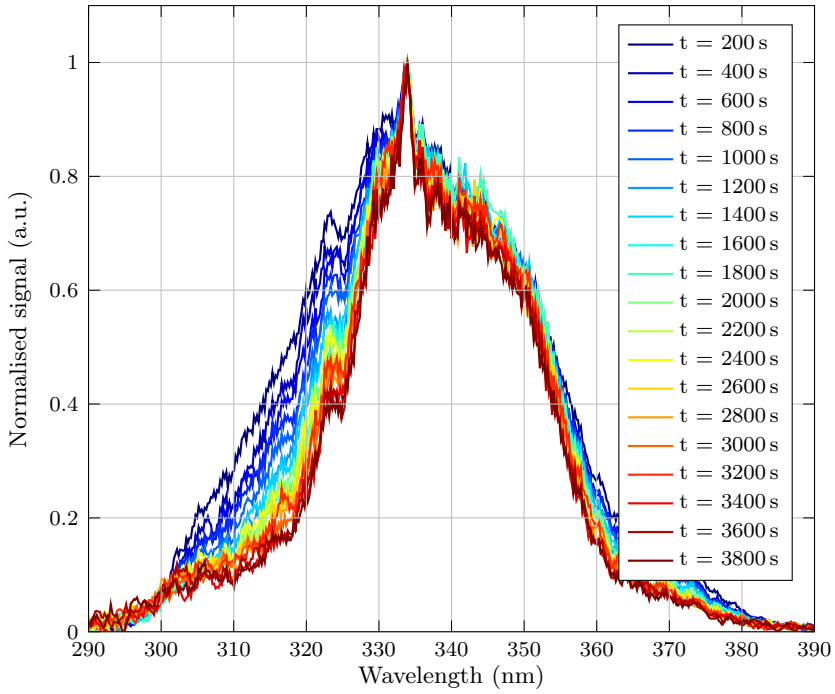


Figure 4.18: Normalised DEHS emission change with time due to photobleaching

Here, the 'red' part of the spectrum hardly changes as DEHS molecules are photobleached, while most of the change happens to the 'blue' part of the spectrum. Plotting TC ratio as a function of time, as shown in Figure 4.19, it is evident that this red-shifting causes a rise in the TC ratio as expected. Thus, care must be taken when performing TC-PLIF studies using DEHS to limit the total number of pulses a molecule is subjected to, otherwise erroneous temperature measurements could be made. Curiously, the moving average TC ratio lacks continuity going from the first run to the second. After a pause in excitation, while the overall signal intensity remains roughly constant, a recovery in the 'blue' emission profile of DEHS is seen.

It is clear from the analysis in this section that photobleaching can have a detrimental effect on TC-PLIF studies. From Figure 4.19, TC ratio increases monotonically with pulse number, with no initial 'safe' duration where the TC ratio stays constant. For this reason, the number of pulses delivered to a sample of DEHS was limited to not more than 200. From Figures 4.17 and 4.19, photobleaching contributes a modest 2.5 % drop in total DEHS fluorescence signal, and a negligible 0.1 % increase in TC ratio after this many pulses.

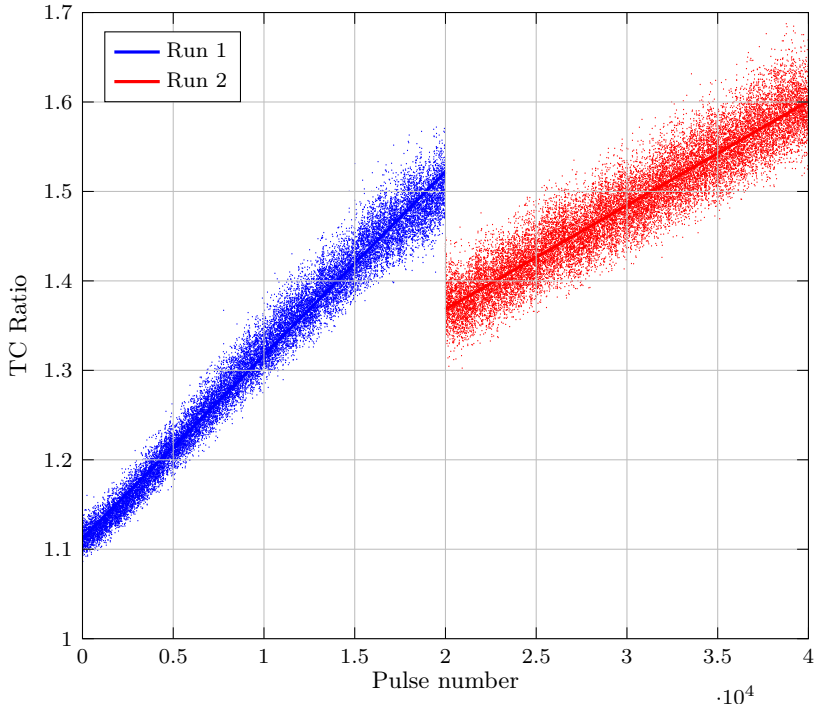


Figure 4.19: DEHS TC ratio change with time due to photobleaching

Future FPIV experiments involving DEHS will need to take this into account as part of the experimental design. Droplets used in PIV experiments will spend a finite amount of time in the flow cavity, as they will eventually be convected by the flow towards the exit. In high-speed flows, this residence time will be short given the high convective speeds. However, the nature of PIV experiments requires the droplets to be illuminated in quick succession, meaning that each droplet will be subjected to at least two laser pulses (potentially more if the flow speed is slower than that of the laser frequency). Figure 4.19 indicates that this may not be a problem, but these results could change in droplet form, as the photon density incident on each molecule is much larger for droplets compared to a bulk liquid. If this is the case, one solution may be to only perform thermometry using the first of the two PIV pulses, and to ensure that the laser frequency is smaller than the flow speed, so that each image used for temperature measurements includes fresh un-bleached droplets. Naturally, this limits the ability to time-resolve flow phenomenon. Further tests need to be performed in order to investigate this effect for droplets, and to determine how to compensate for it if necessary with pre-experiment calibrations.

4.4 Droplet TC-PLIF

In Section 4.1, the ability to isolate strong elastic scatter from PIV measurements using FPIV was demonstrated. Section 4.3 showed DEHS, a popular and widely-used seeding substance for PIV, exhibits temperature-dependent fluorescent properties when excited by UV radiation. This section focuses on temperature recovery from DEHS aerosols as a means to extend typical PIV experiments to also capture a temperature field. The section begins by discussing elements required to perform a DEHS TC-PLIF experiment. Subsequently, a proof of concept experiment will be described where spatially-resolved temperature measurements are made from fluorescence of DEHS droplets.

4.4.1 Equipment and optics for DEHS TC-PLIF

Results from the previous section provided several key pieces of information. Firstly, 266 nm light was required in order to excite DEHS molecules. Secondly, fluorescence emission of undiluted liquid DEHS was weak when measured on a spectrometer. Droplets are expected to produce even weaker signals, due to a smaller number of probed molecules per volume, so signal maximising steps would be necessary. Besides this, its emission was confined between 300 and 380 nm - this information aids in choosing a suitable filter that will strongly attenuate elastic scatter, while transmitting as much fluorescence as possible. Finally, a strategy was identified for separating the fluorescence of DEHS into two bands to perform TC-PLIF.

These findings informed equipment and optics requirements for successful implementation of TC-PLIF on DEHS droplets, and are summarised as follows:

- High energy pulsed UV laser

  A Continuum Powerlite pulsed Nd:YAG laser was used for subsequent experiments involving DEHS. This laser readily outputs 650 mJ per pulse at 532 nm, which is then frequency-doubled to 266 nm using an externally-housed potassium dihydrogen phosphate (KDP)

crystal with conversion efficiency of about 30%. Thus, UV pulse energies of at least 200 mJ were achievable with this system, however in practice, a lower limit of 100 mJ was maintained to prevent inducing laser damage on the crystal.

- Intensified camera capable of UV imaging

  The camera used was an Andor iStar sCMOS, an intensified camera with a quantum efficiency of roughly 20 % at the range of relevant wavelengths and a maximum relative-to-zero signal gain of 700.

- Spectral filters

  A 305 nm long-pass filter was inherited from legacy experiments to isolate elastic scatter. Subsequently, a 325 nm dichroic beamsplitter was purchased and used to split DEHS fluorescence into a B-band (305 nm to 325 nm) and a R-band (325 nm to 380 nm). This dichroic was chosen as its edge wavelength was as close to the peak emission wavelength of DEHS (333.9 nm) as possible. Table 4.2 summarises the filters used to split DEHS fluorescence.

Table 4.2: Filters used for spectral isolation of DEHS fluorescence

Filter	Filter type	Edge wavelength
SEMROCK Brightline FF01-300/LP-25	Long-pass	305 nm
SEMROCK Brightline Di01-R325-25x36	Dichroic beamsplitter	325 nm

Despite the large pulse energies available, an intensified camera capable of UV imaging was required, in order to amplify fluorescence signals from DEHS. Ideally, two cameras should be used for TC-PLIF, so that each camera can image an individual spectral band separately - this maximises resolution and also provides independent gain control of each band. Unfortunately only one functioning camera capable of UV imaging was available, thus a split-sensor imaging layout was implemented. Here, both bands of DEHS fluorescence were imaged on the same camera sensor, each on separate halves. Further information on how this was achieved is presented in Section 4.4.2.

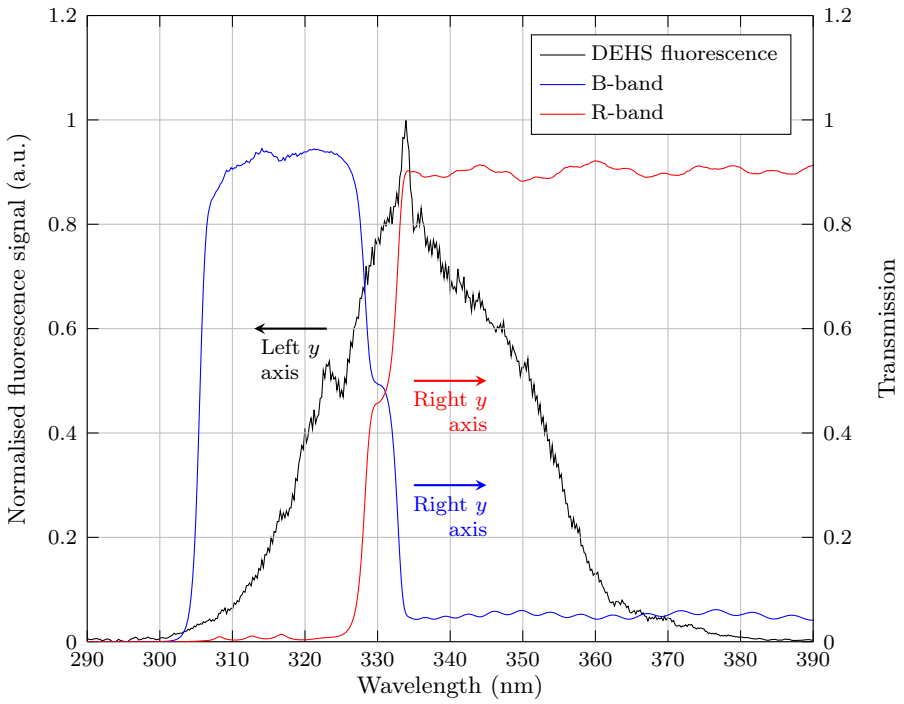


Figure 4.20: Transmission of spectral filter combination for R- and B-bands, compared to normalised emission spectrum of liquid DEHS

When determining a strategy for splitting fluorescence into two 'colours', some numerical modelling should be performed in order to optimise the sensitivity of the TC-PLIF method, as was demonstrated in [32]. Two bands should be chosen, such that both sensitivity and signal can be maximised. However, as DEHS fluorescence is weak, signal strength was prioritised in this work. In addition, the use of a single camera to image both spectral bands meant signal amplification could not be controlled independently. In other words, a mismatch in signal levels between the two bands could lead to the dynamic range of the camera being squandered, making analysis susceptible to noise. To this end, it is apparent from inspecting the fluorescence spectrum that splitting it at the peak emission wavelength would maximise signal in both bands while ensuring their ratios would be approximately 1 at room temperature. Further reducing each band to 10 or 20 nm wide channels (as is typical with many band-pass filters) would drastically reduce the amount of signal available, rendering the diagnostic impractical. Figure 4.20 shows the wavelengths captured by each band as a result of using these filters.

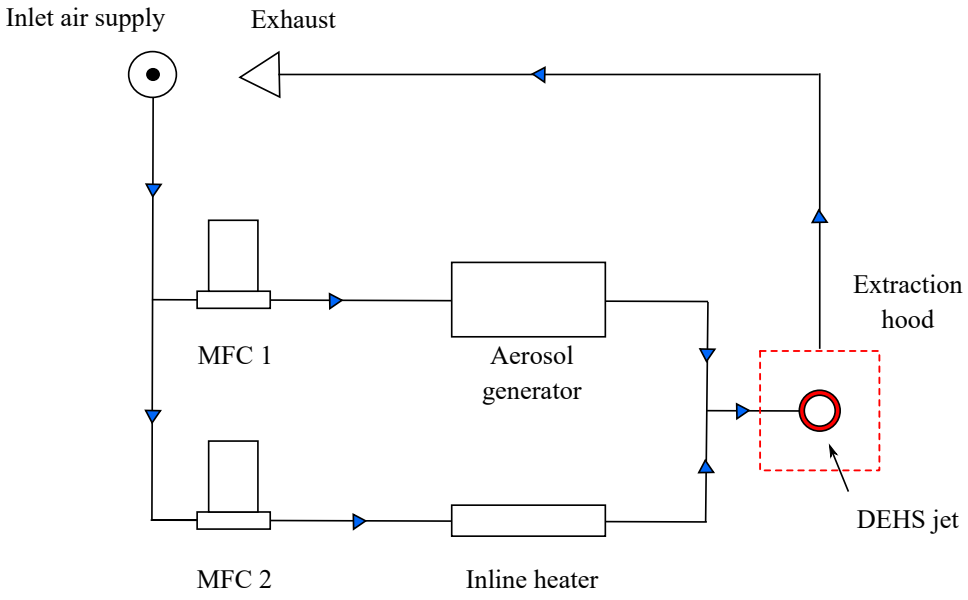


Figure 4.21: Schematic of single DEHS jet experiment

4.4.2 Proof of concept experiment

Having established the equipment and optics required, the TC-PLIF method was applied to DEHS droplets in a proof of concept experiment. Chapter 3 showcased the ability to perform high-speed PIV, thus this proof of concept experiment would serve as the final puzzle piece in demonstrating the ability to perform FPIV with DEHS.

Two layouts were tested. In the first layout, a single jet of DEHS droplets was produced with the aerosol generator from Chapter 3. Compressed air was split into two flow paths controlled by two separate mass flow controllers (Omega FMA-2609A and Omega FMA5520A). Air traveling through one path entered the aerosol generator to produce a cold flow of DEHS-seeded air. Air traveling through the other path encountered an inline resistive heater (Omega AHP-5052), controlled by an autotransformer, producing a hot flow of unseeded air. Both these flows were recombined to produce a single jet of seeded air, and by varying the voltage supplied to the inline heater, temperature control of the DEHS jet was achieved. A thermocouple was positioned

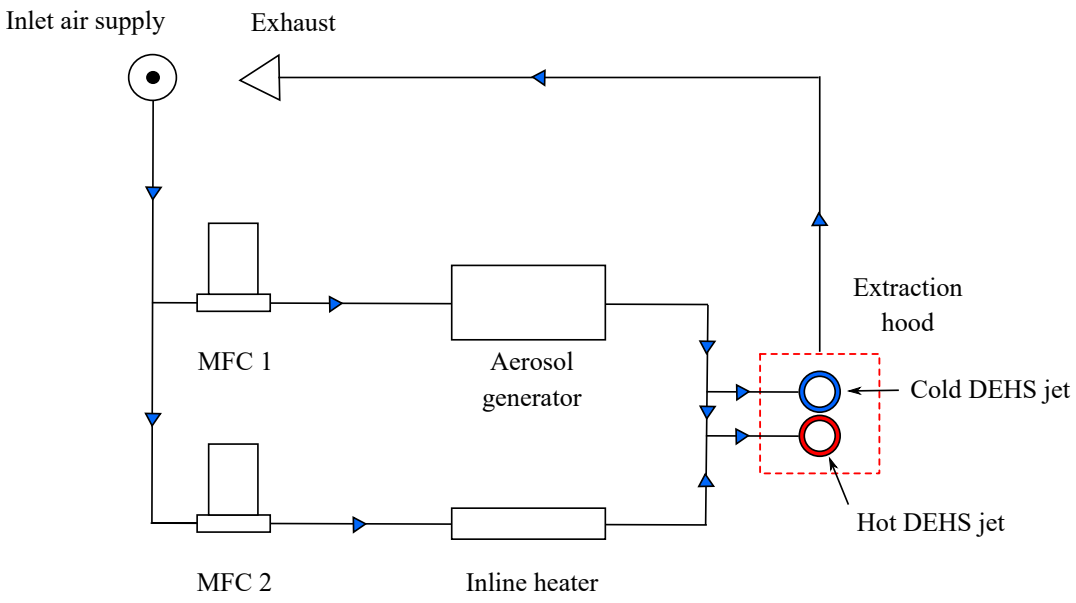


Figure 4.22: Schematic of dual DEHS jet experiment

at the exit of this jet to provide comparison with processed results. Temperatures from the thermocouple were logged using a PicoScope TC-08 Thermocouple Data Logger. A schematic of this layout is shown in Figure 4.21. In the second layout, the outlet to the aerosol generator was further split into two flow paths. One of these was sent directly to the imaging region while the other was mixed with the outlet of the unseeded hot flow path from before. This produced two separate jets of DEHS droplets, which were subsequently inclined towards each other. One jet was thus maintained at a cold temperature, while the other was heated - this was to produce a spatial temperature gradient that could be resolved using the TC-PLIF method. Here, the thermocouple was placed over the hot jet. A schematic of this layout is shown in Figure 4.22. For both layouts, a 3D printed funnel connected to an exhaust extraction system was mounted over the DEHS jets. The funnel provided a small distributed suction across the jet area, ensuring all droplets were safely collected and did not have a chance to leak out into the surrounding environment.

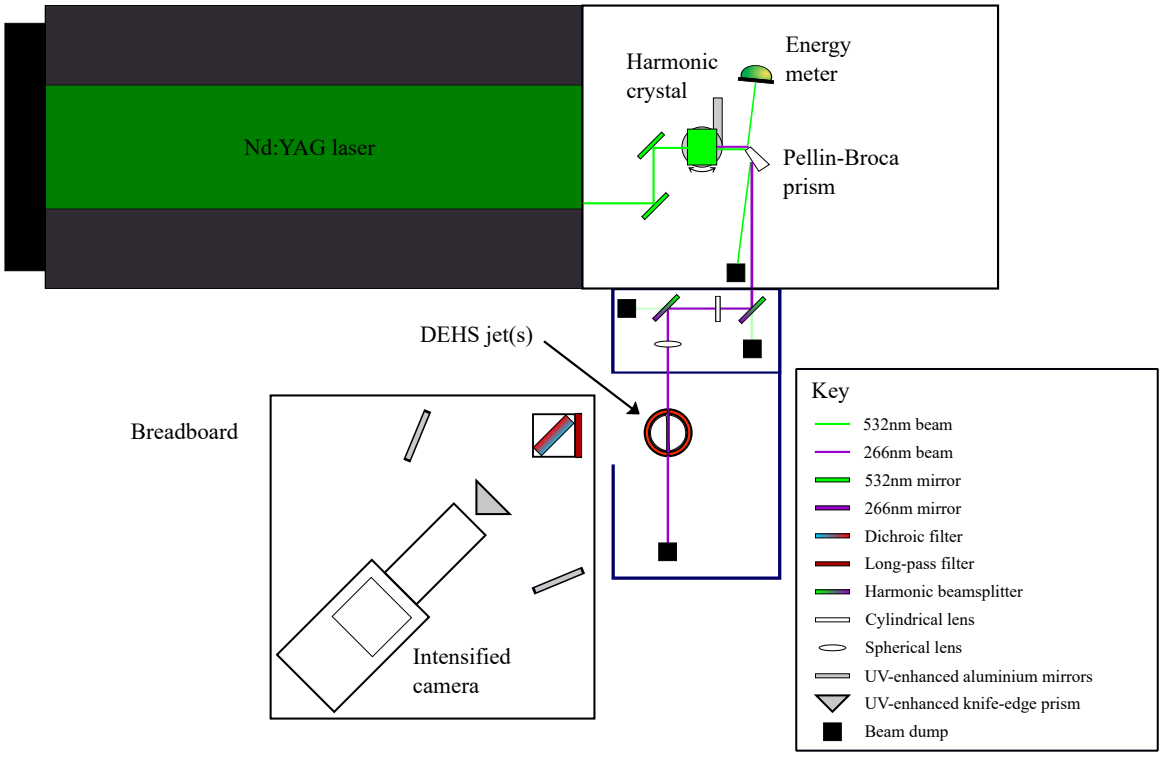


Figure 4.23: Layout of optical components for DEHS thermometry experiments

Droplets produced by these jets were probed by a UV laser sheet at 10 Hz. This sheet was produced by a series of optics as shown in Figures 4.23 and 4.24. The green output of the laser was directed using two 532 nm mirrors towards the KDP frequency-doubling crystal. The output of this crystal consisted of a combination of 266 nm and residual 532 nm light. Separation of both wavelengths was achieved using a Pellin-Broca prism, allowing the residual green beam to be caught in a beam dump. A reflection of the green beam coming off the input face of this prism was terminated on an energy meter (Sensor- und Lasertechnik PEM 45K USB), in order to monitor the conversion efficiency of the doubling crystal. The conversion efficiency varied as a function of the crystal's temperature and angular orientation with respect to the input beam. Due to laser heating from the beam, the optimal angle of the crystal for maximum conversion efficiency changed from time-to-time. For this reason, the crystal was held in a temperature-controlled housing capable of rotational adjustment. Before each test, the crystal's angular position was adjusted to maximise UV energy.

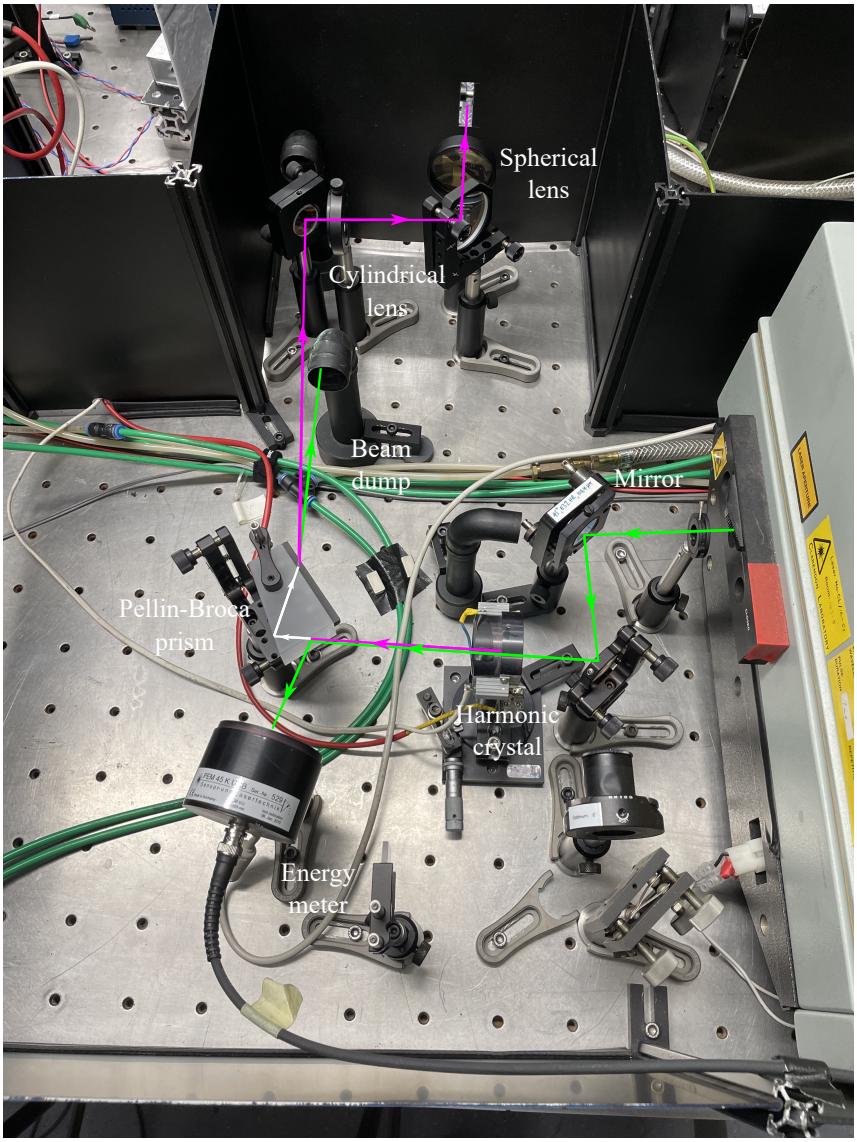


Figure 4.24: Image of optical components for DEHS thermometry experiments

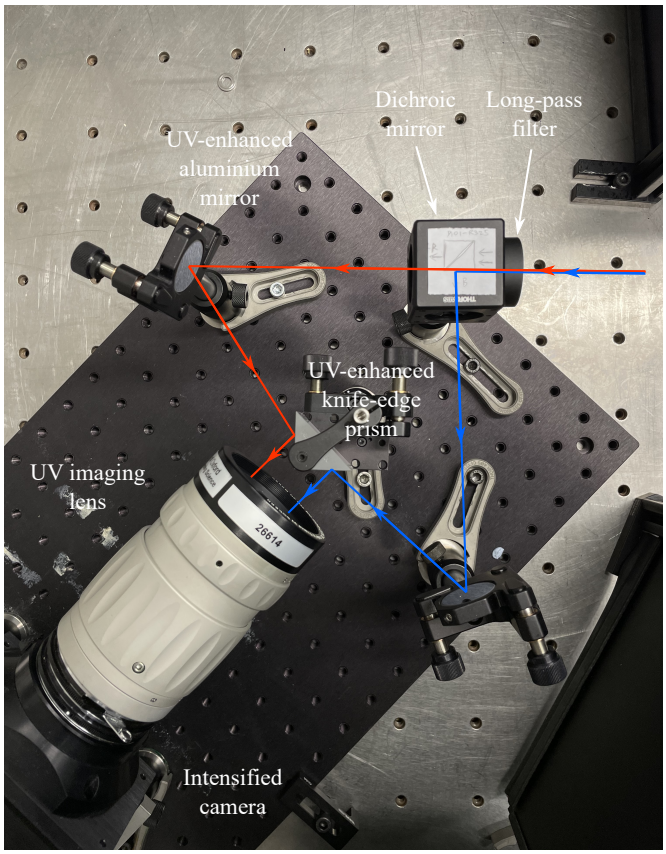


Figure 4.25: Layout of imaging optics to generate split-spectral imaging. R and B ray paths have been coloured respectively

The UV beam was directed towards the DEHS droplets using two harmonic beamsplitters to ensure that no residual green was present at the imaging region. Along this path, the beam encountered a 1" concave cylindrical lens ($f = -50\,\text{mm}$) and a 2" convex spherical lens ($f = 200\,\text{mm}$) that turned the beam into a 35 mm tall vertical laser sheet that focused precisely at the central axis of the DEHS jets. This sheet was finally terminated in a beam dump.

As described previously, fluorescence from DEHS droplets was split into a pair of spectral bands, namely the R- and B-bands, with each band being imaged on separate halves of a single camera sensor. This was achieved using a split-imaging layout as shown in Figure 4.25. Fluorescence from the region of interest first passed through the long-pass filter to remove elastic scatter. The remaining light was split by the 45° dichroic beamsplitter which transmitted the R-band, and reflected the B-band. Light from these bands travelled in orthogonal directions to one another, before being reflected by a pair of UV-enhanced aluminium mirrors onto a knife edge prism that

directed both bands towards the intensified camera. As a result, the B-band is imaged onto the right half of the sensor, while the R-band is imaged onto the left half of the sensor. It is worth noting that the use of the dichroic beamsplitter in this manner produced R and B images that are mirror reflections of one another - Figure 4.31 demonstrates this clearly.

Aligning this set-up required the use of a back-illuminated test pattern placed exactly in the line of the laser sheet, at the region of interest. Such a pattern would serve two purposes - first, to align all split-imaging optics, and second, to provide control points for image registration (transforming images from one band to allow pixel-to-pixel operations with the other). Under visible light imaging applications, a mounted image of a grid similar to the one used in Chapter 3 would work well. As this experiment involved capturing fluorescence from UV wavelengths, this exact approach would not work as well. Since the effective focal length of a lens varies as a function of wavelength, each half of the sensor needed to be aligned independently with a separate light source emitting the relevant wavelengths for that channel. The test pattern was a thin steel sheet that was laser cut to produce a grid of 2 mm $\times$ 2 mm square holes, separated by a centre-to-centre distance of 4 mm. A pair of LEDs, each emitting at the central wavelength of each band (310 nm and 340 nm), were used to back-illuminate this steel sheet. Figure 4.26 presents an image of the calibration grid post alignment of optics, to be used for image registration. As LEDs have angle-dependent intensity profiles leading to significantly stronger emission in the normal direction, a piece of lens paper was used to diffuse the incident illumination, in order to create more uniform back-illumination of the grid. This layout is shown in Figures 4.27 and 4.28.

The first step in the experimental procedure was to take pictures of the illuminated grid for image registration (elaborated in Section 4.4.3). Each LED providing back-illumination for the grid was turned on separately, providing individual grid images for the R- and B-bands. Acquired images were then added together to form a composite image, as shown in Figure 4.26. Care was taken to ensure only one LED was turned on at any one time, as turning both on could cause

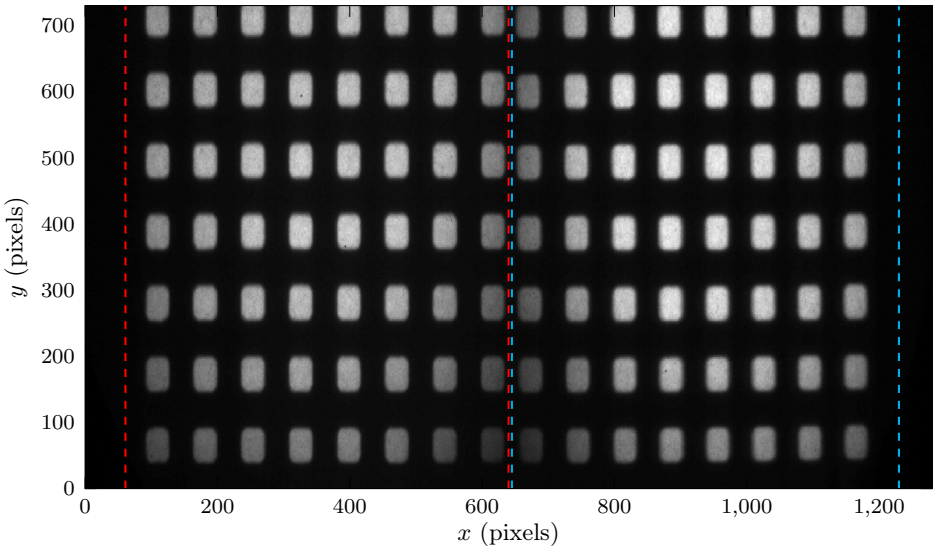


Figure 4.26: Image of calibration grid back-illuminated with LEDs. Dashed lines indicate sub-regions to be isolated (red for R channel, blue for B channel). Note that the B channel sub-image is inverted horizontally from that of the R channel

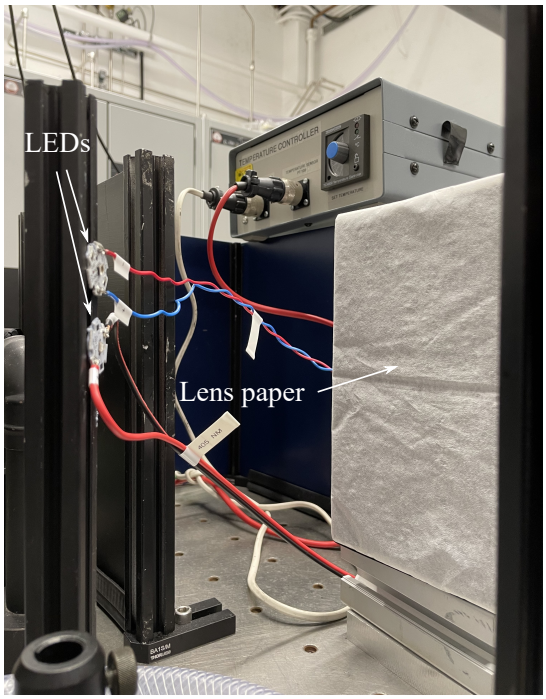


Figure 4.27: LED back-illumination

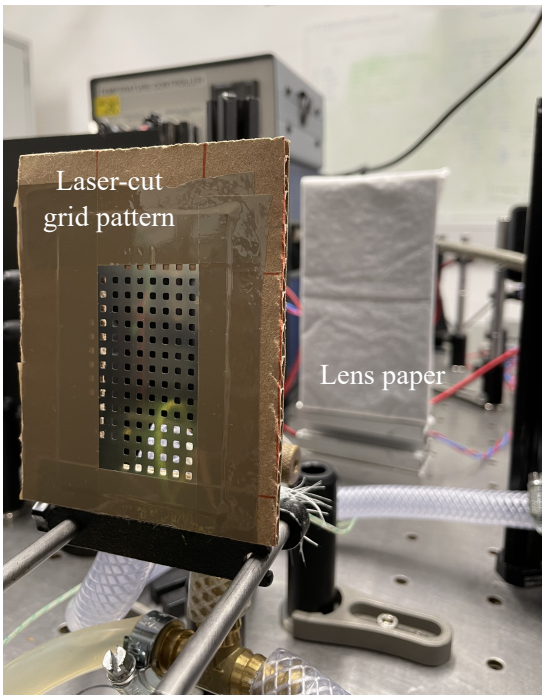


Figure 4.28: Grid image acquisition

spectral cross-talk from one channel to the other, leading to control point errors in the image registration step. Next, the intensifier on the camera was set to a gate width of 4 µs and a gain setting of 3500, which equates to a relative gain of 353. A 2×2 software pixel binning was applied to all acquired images in order to reduce the effect of shot noise. This effectively reduced the sensor to 1280×1080 pixels, with just under half this area in the final processed image due to spectral isolation. Subsequently, the laser shutter was opened, sending the beam towards the imaging area with no seeding droplets present. The doubling crystal was aligned to maximise UV energy by monitoring the amount of residual green energy incident on the energy meter[3]. At these conditions, several background images were acquired with the intensified camera. An average of these images would be subtracted from all data subsequently acquired. Note that any change to the gate width, gate delay and intensifier gain would require re-taking background images.

To start a test, flow through each path was initiated by setting the required flow rate on the mass flow controllers - 20 slpm of air was nominally used for the seeded flow path, while 5 slpm of air was sent through the heated path. A larger flow rate was used in the seeded flow path as this led to a higher droplet density, and thus a stronger signal. The autotransformer was set to the desired voltage, causing the temperature of the jet to increase. Once temperatures recorded by the thermocouple achieved steady-state, the laser shutter was opened once again, the crystal was optimised, and the camera was triggered to acquire 250 images. Pulse energies from the energy meter, as well as temperatures from the thermocouple were acquired simultaneously for use in subsequent data analysis. The ratio of cold-to-hot flow rates meant that a peak temperature of about 330 K could be achieved. Increasing the flow rate of the heated gas any further to achieve larger temperatures would result in a reduction of droplet density (and thus signal), while also turning the jet fully turbulent and causing droplet leakage from the extraction hood. This could lead to accidental inhalation of DEHS and also coating optics with droplets.

[3] A high conversion efficiency causes reduced green energy, so optimal UV produces the smallest reading on the energy meter

4.4.3 Post-processing procedure

Figure 4.29 shows the post-processing procedure applied to the experimental data obtained.

The first step in post-processing was image registration - this was the process of applying a transformation to a misaligned image (exhibiting any combination of translation, rotation, shear, enlargement, or reflection from a reference coordinate), in order to line it up with the spatial coordinates of another image. This enabled pixel-to-pixel operations to be performed. Image registration was a crucial step for pixel-to-pixel division - without spatially mapping pixels from the R and B channels onto one another, significant errors in results could be produced, especially in the vicinity of large signal gradients. By default, one channel remained fixed and acted as the reference, while the other was mapped onto the coordinate frame of the fixed image. In this work, the R channel was fixed and the B channel was warped to match it. Image registration was performed in MATLAB using the *imwarp* function - this took an image as well as a transformation matrix as inputs, and output the spatially transformed image. To use this function, a transformation matrix was required. This was obtained from the acquired grid images. First, R and B sub-regions were defined, splitting the dataset into two. Since the R channel was designated as fixed, the B sub-images were first reflected along the vertical axis using the *fliplr* function, in order to undo the mirror effect. Next, R and B grid sub-images were binarised using the MATLAB function *imbinarize*, applying a threshold to create a mask of the square holes. Noise and non-uniform illumination from the LED caused masked regions to be 'spotty', so the function *imfill* was used to ensure a continuous mask. Background light and noise also caused regions outside of the holes to be registered, so the function *bwareaopen* was used to only retain masked regions at least 200 pixels in size (this process is known as area opening).

Example masked and cleaned grid sub-images are shown in Figure 4.30. After binarising, the MATLAB function *regionprops* was applied to the masks - this output coordinate and size

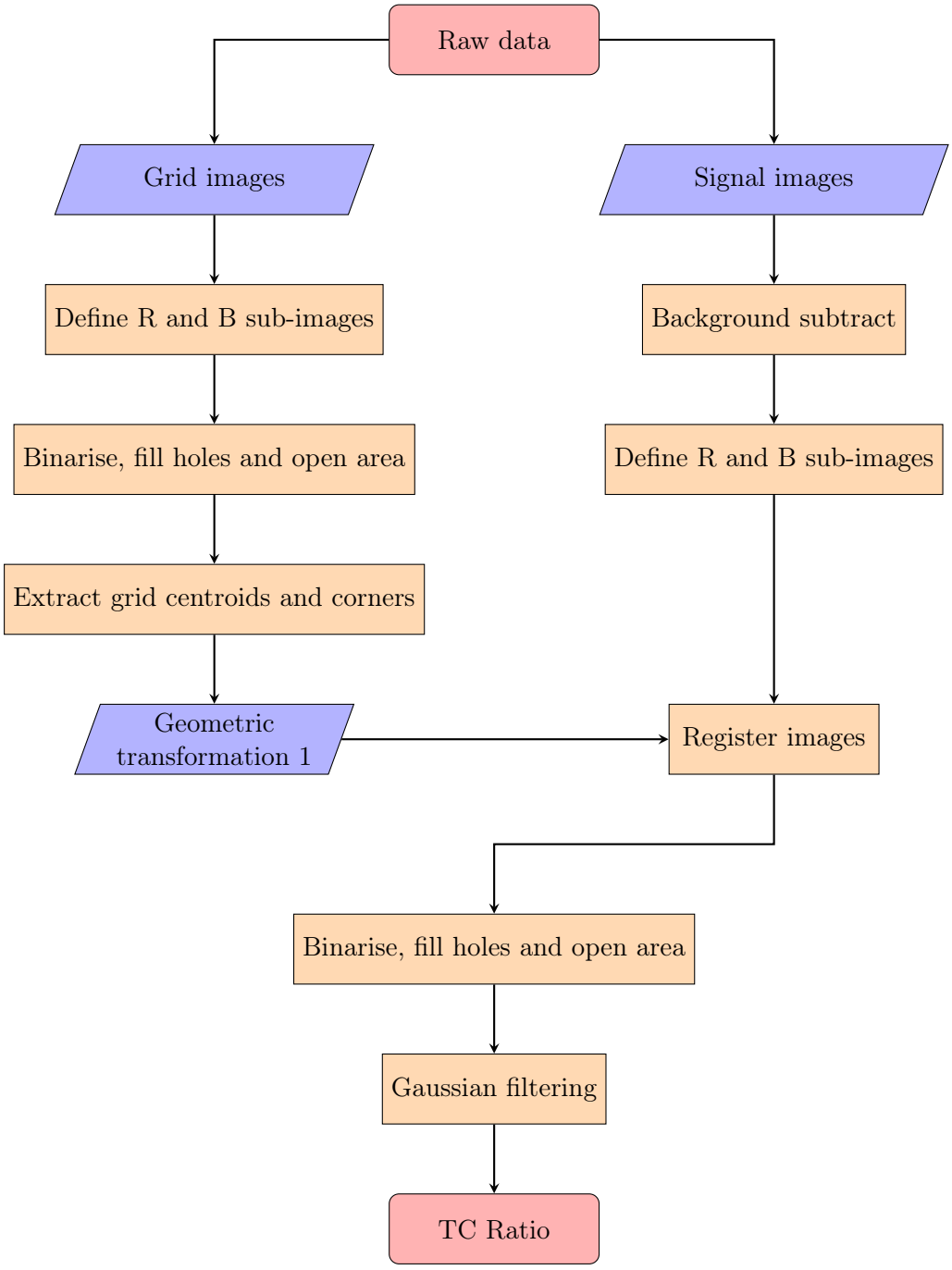


Figure 4.29: Flow chart describing image processing procedure for DEHS thermometry

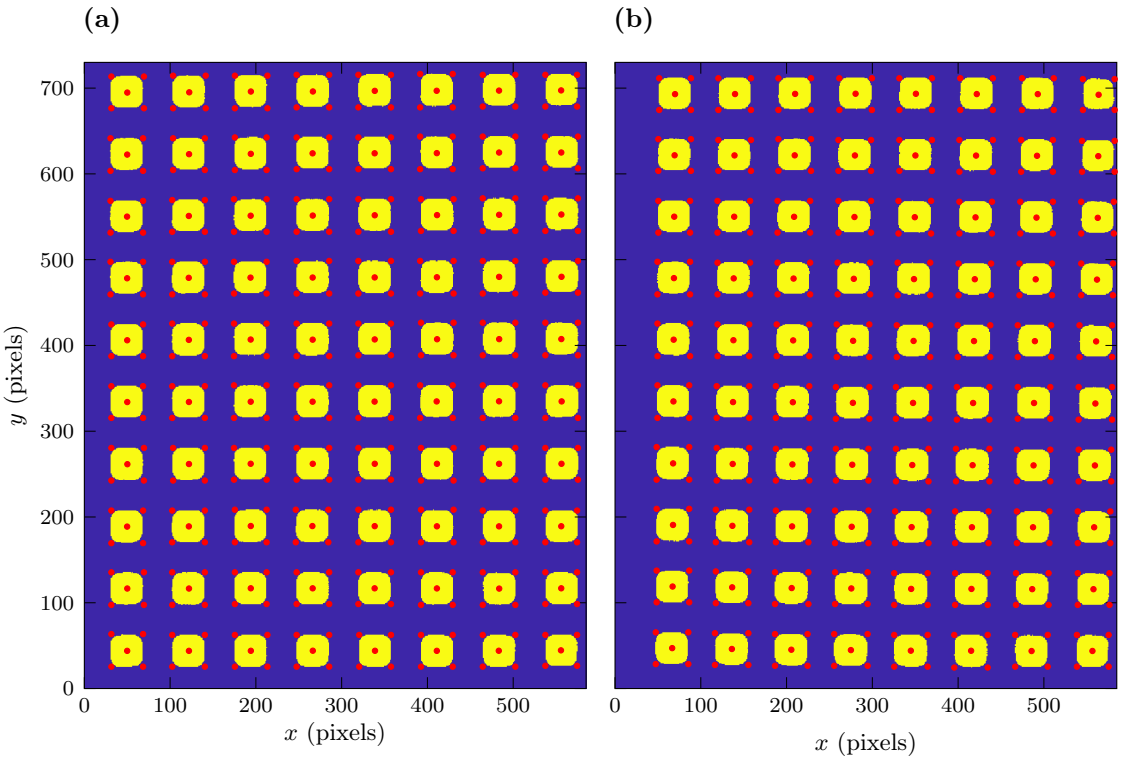


Figure 4.30: R (a) and B (b) grid images. Red dots represent transformation control points

information about filled areas. Through this, the pixel coordinates of the centroids and corners of each square hole were determined. These points were then used as control points in the *fitgeotrans* function in order to output a transformation matrix that maps coordinates from the B sub-image onto the R sub-image. Having obtained this transformation matrix, the *imwarp* function was finally applied to all signal images.

Figure 4.31 shows an example raw signal image. Before warping, signal images were background subtracted, isolated into sub-images and the B dataset reflected along the vertical axis as before. After warping, pairs of R and B signals that are spatially aligned were obtained. As can be seen in Figure 4.31, signals in both channels did not occupy the entire sensor region, and were typically confined to the centre of each sub-region. Performing pixel-to-pixel division directly on the entire sub region, including areas with no signal, led to highly unstable results, since background subtraction caused some pixels to attain values close to 0. For this reason, a mask was applied to signal images as well. The procedure was similar to that which was applied to

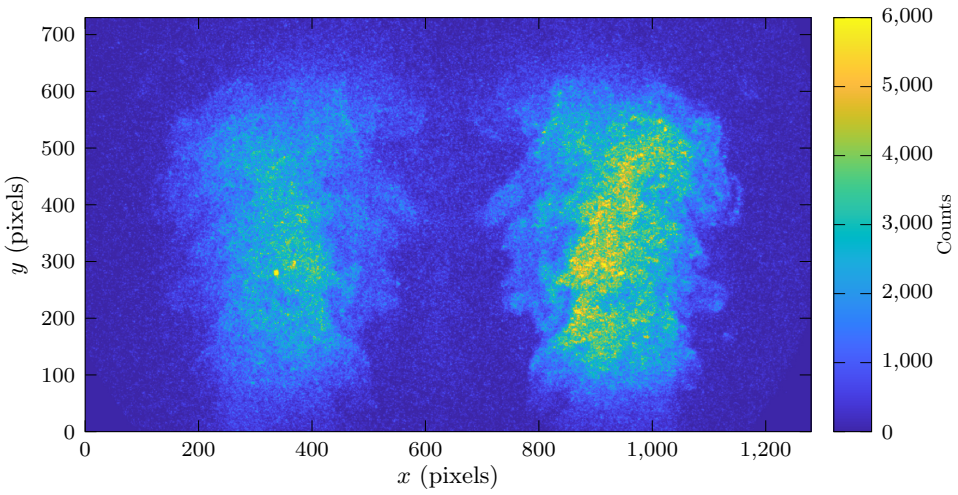


Figure 4.31: Full DEHS fluorescence signal image of both spectral windows; R channel captured on the left of the sensor, B channel captured on the right

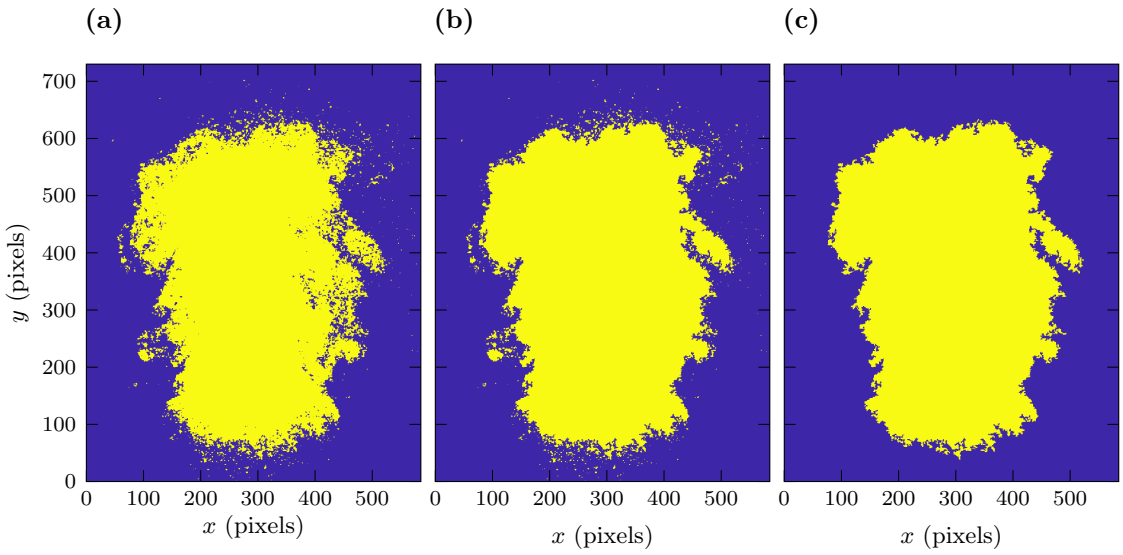


Figure 4.32: Masking procedure of signal images, starting with binarisation (a), then hole-filling (b) and finally area opening (c)

the grid images. A threshold was first applied to signal images, followed by filling any spots, and finally removing any unwanted dots outside the central mask (area opening). This procedure is demonstrated in Figure 4.32.

The final step before calculating pixel-wise TC ratios was to apply a Gaussian filter to the R and B signals. This reduced the spatial resolution of the signals, but was a necessary step to reduce the effect of noise or chromatic aberration creating large spatial gradients in TC ratio. Calculated TC ratios were then analysed as necessary. For steady-state analysis, the average TC

ratio of 250 images were evaluated, producing a ratio map for each steady-state temperature. For the mixing jet experiments, single shot TC ratios were analysed.

4.4.4 Droplet DEHS fluorescence spectra

Preliminary attempts at extracting temperature from DEHS droplets in a flow were unsuccessful. Changes in gas temperature produced no change in the TC ratio of droplets.

Based on the fluorescence emission spectra of DEHS presented in Section 4.3.1 and the spectral isolation strategy discussed, signals of similar magnitude were expected in both channels. However, it was observed that the B channel only collected ~ 10 % of the signal in the R channel. Factors arising from the split-imaging layout (e.g. losses from optics, variation in camera quantum efficiency with wavelength and even angular dependence of the dichroic beamsplitter edge wavelength) could not account for such a mismatch in signals. In addition, the dichroic beamsplitter exhibited R signal leakage (i.e. unintentional reflectance of R wavelengths into the B channel) of about 5 %, meaning that the real B signal was only about 5 % of the R signal. This meant that either the B signal was being significantly attenuated, or that unanticipated R signal was being captured. Further proof that the experimental set-up was not the cause for this problem is shown in Figure 4.33. Here, a cell of liquid DEHS was placed in the field of view of the camera, and was probed with the same laser sheet as before. Figure 4.33 shows the split-image fluorescence signal obtained from liquid DEHS - a ratio of approximately 2 was obtained between the R and B channels. This ratio matches the expected value at room temperature as a result of using the combination of chosen filters. This observation suggested that droplet fluorescence characteristics of DEHS differed to that of the bulk liquid.

A difference in emission characteristics between bulk liquid and droplets could be caused by fluorescence self-absorption - this would take place at wavelengths where an overlap in the absorption and emission spectra of a fluorescent molecule is present. Typically, this corresponds to the 'blue' part of the emission spectrum. If self-absorption was the cause of the problem, droplet

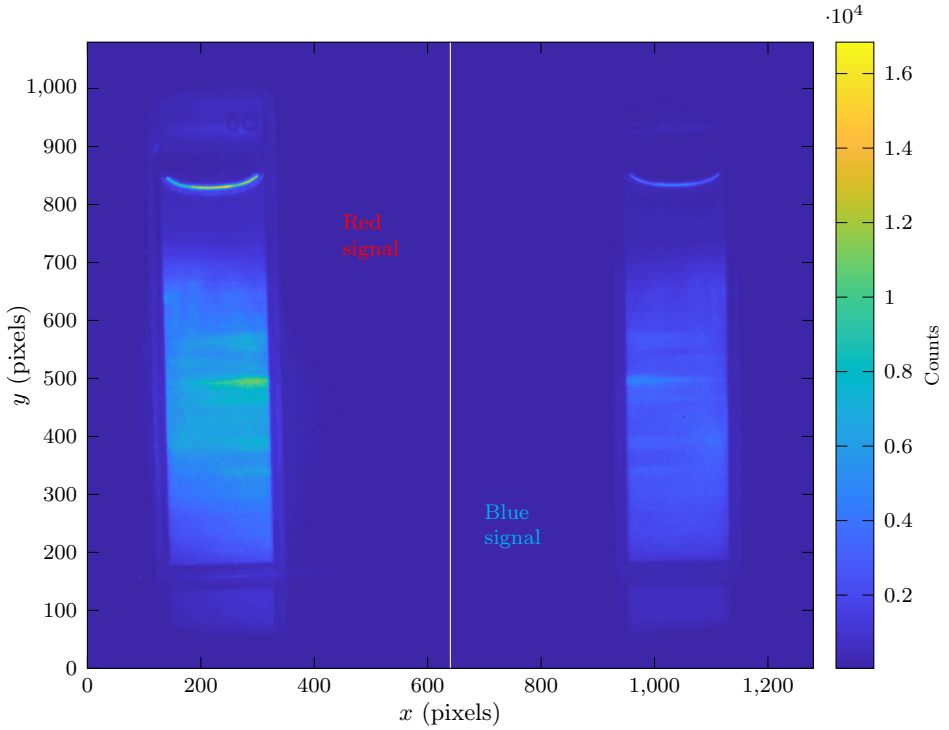


Figure 4.33: Liquid DEHS fluorescence signal obtained from a cell

TC (R/B) ratios would be *smaller* than that of a bulk liquid, since fluorescence from molecules in droplets will have less liquid length to travel through to reach the camera, leading to lower chances of self-absorption, and thus *stronger* B signals. However, this is the opposite observation to the initial results. Given this, it became apparent that the fluorescence emission of DEHS needed to be measured in droplet form for a better understanding of this discrepancy.

Since fluorescence emission of DEHS is weak even in a bulk liquid, it becomes even harder to measure the emission of DEHS in droplet form using a spectrometer. The layout used in Section 4.3.1 would produce insufficient signals for the available spectrometer. To this end, the experimental layout presented in Section 4.4.2 was utilised, with three modifications. Firstly, the concave cylindrical lens and convex spherical lens were removed, producing a beam of 9 mm diameter at the imaging region, instead of a tall sheet. This allowed more efficient conversion of laser light into photons sampled by the spectrometer. Secondly, the spectrometer was positioned orthogonally to the laser beam, to collect fluorescence from DEHS droplets with the help of two 1" convex spherical lenses in a telescope arrangement ($f = 30$ mm and 40 mm). This enabled getting

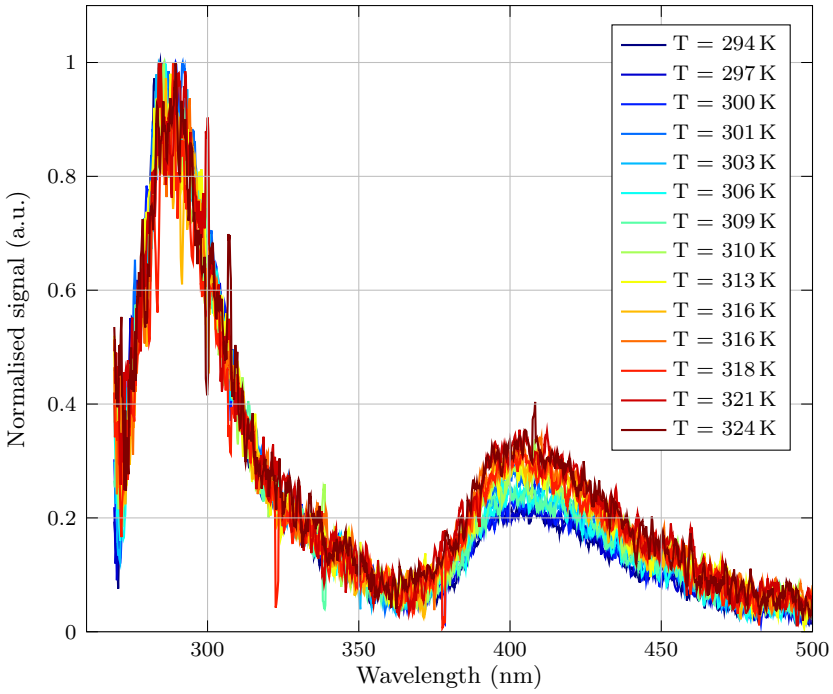


Figure 4.34: Normalised DEHS droplets fluorescence spectra at varying temperatures

as close as possible to the imaging region where the emission intensity was largest, while having a magnification less than 1 and not consuming excessive table space. Finally, the spectrometer was set to an exposure time of 25 s - this meant that signals from 250 laser pulses were accumulated to form 1 scan. As a result, the spectrometer was highly susceptible to stray light. To mitigate this, the spectrometer and imaging region were surrounded by a dark enclosure and background scans were subtracted from each spectrum. Scans were collected at several steady-state temperatures.

Figure 4.34 shows the peak-normalised emission spectra of DEHS droplets at several steady-state temperatures. As before, each curve is coloured from blue to red indicating a change from cold to hot temperatures. Qualitatively, it is evident that the emission characteristics of DEHS in droplet form differ from that of a bulk liquid (see Figure 4.10 for comparison). The main difference is a broadening of emission to both shorter and longer wavelengths. The broadening of the spectra towards shorter wavelengths is easily understandable as a consequence of reduced self-absorption, as previously discussed. Since DEHS begins to have appreciable absorption for wavelengths less than 300.0 nm (as shown in Figure 4.7), the effects of self-absorption are expected to be noticeable here. This also causes a shift in the peak emission wavelength from 333.9 nm to 285.0 nm.

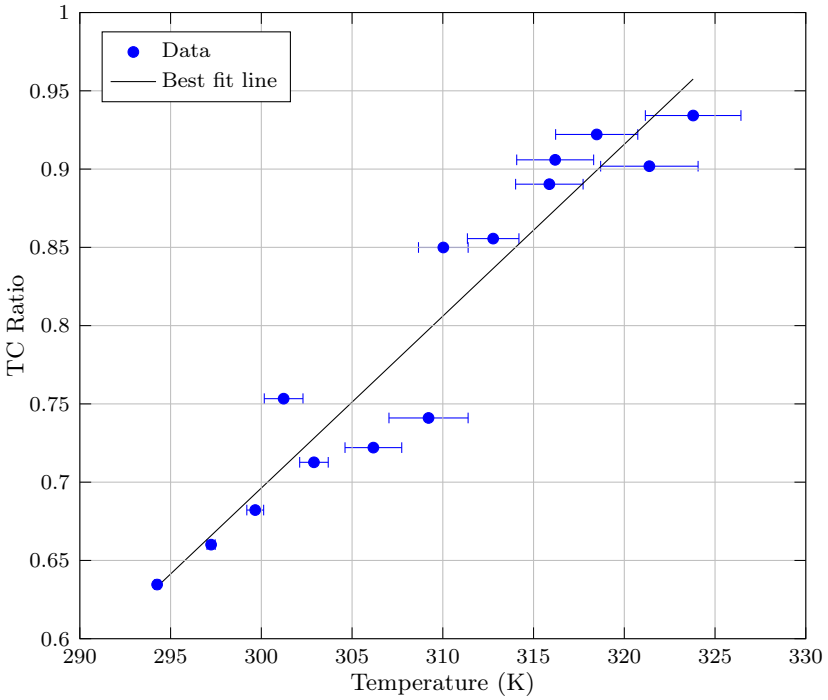


Figure 4.35: TC ratio variation with temperature for DEHS droplets. Horizontal error bars represent the standard deviation of temperatures measured using the thermocouple. Note that no vertical error bars could be provided as each scatter point was obtained from a single spectrum

Surprisingly, DEHS droplet emission is broadened to longer wavelengths as well, leading to the formation of a separate fluorescence peak at 405.0 nm. This new spectrum explains the previous observation of the signal on the R channel being much stronger than expected compared to the B channel - not only was this second peak not accounted for, but a significant source of signal for the B channel was also truncated with the use of the 305.0 nm long-pass filter. The presence of this peak cannot be explained by self-absorption, as DEHS has a negligible absorption cross-section at these wavelengths (refer to Figure 4.7). The cause for the formation of this peak is still unclear - Section 4.5 explores and tests several theories of the origin of this additional fluorescence. Fortunately, Figure 4.34 demonstrates that the TC-PLIF method still works, since DEHS emission is still temperature-dependent. Figure 4.35 shows the TC ratio variation for DEHS droplets with temperature, this time with the B-band defined as wavelengths from 270.0 nm to 325.0 nm and R-band from 325.0 nm to 500.0 nm. These bands are based on using the same dichroic beamsplitter as before, but replacing the long-pass filter for one with an edge wavelength of 270.0 nm.

A linear correlation between TC ratio and temperature was still achievable, albeit with a reduced sensitivity of $(0.0110 \pm 0.0021)\,\mathrm{K}^{-1}$. A larger scatter of data points is evident from Figure 4.35 when compared to results for the bulk liquid (Figure 4.13). A weak experimental signal creates noisy spectra, as is evident from Figure 4.34, which leads to uncertainty. Similarly, the temperatures recorded were averages over 25 s. During this time, shot-to-shot temperature drift and gradients across the area probed by the laser beam was present.

Based on these findings, the proof-of-concept experiment was repeated, this time swapping the 305 nm long-pass filter for a 266 nm version (SEMROCK Brightline LP02-266RU-25). The change in wavelengths captured within each fluorescence band also led to changing the calibration LEDs for alternatives centred at 295 nm and 405 nm.

4.4.5 Results and discussion

In this section, results from the two experimental layouts are presented. The aim of the first layout is to demonstrate a change in TC ratio with temperature in the steady-state approach. The second layout tests the ability to make spatially-resolved temperature measurements.

Figure 4.36 presents several steady-state TC ratio maps (averaged over 250 single shot images), ordered in increasing mean temperature. Black regions represent areas where no droplets were found, while brighter colours indicate higher ratios. It is evident that figures appear brighter as the temperature increases - this tallies with the expectation of having larger TC ratios for higher temperatures. Some spatial gradients in TC ratio are also discernible, particularly at higher temperatures in the horizontal and vertical directions. The TC ratio appears to reduce as you move away from the central core of the jet - this is also expected as the jet spreads and mixes with colder surrounding air.

Average TC ratios for each steady-state map are evaluated and plotted against temperature in Figure 4.37. Here, a similar increasing trend to Figure 4.35 is seen. As before, the nature of

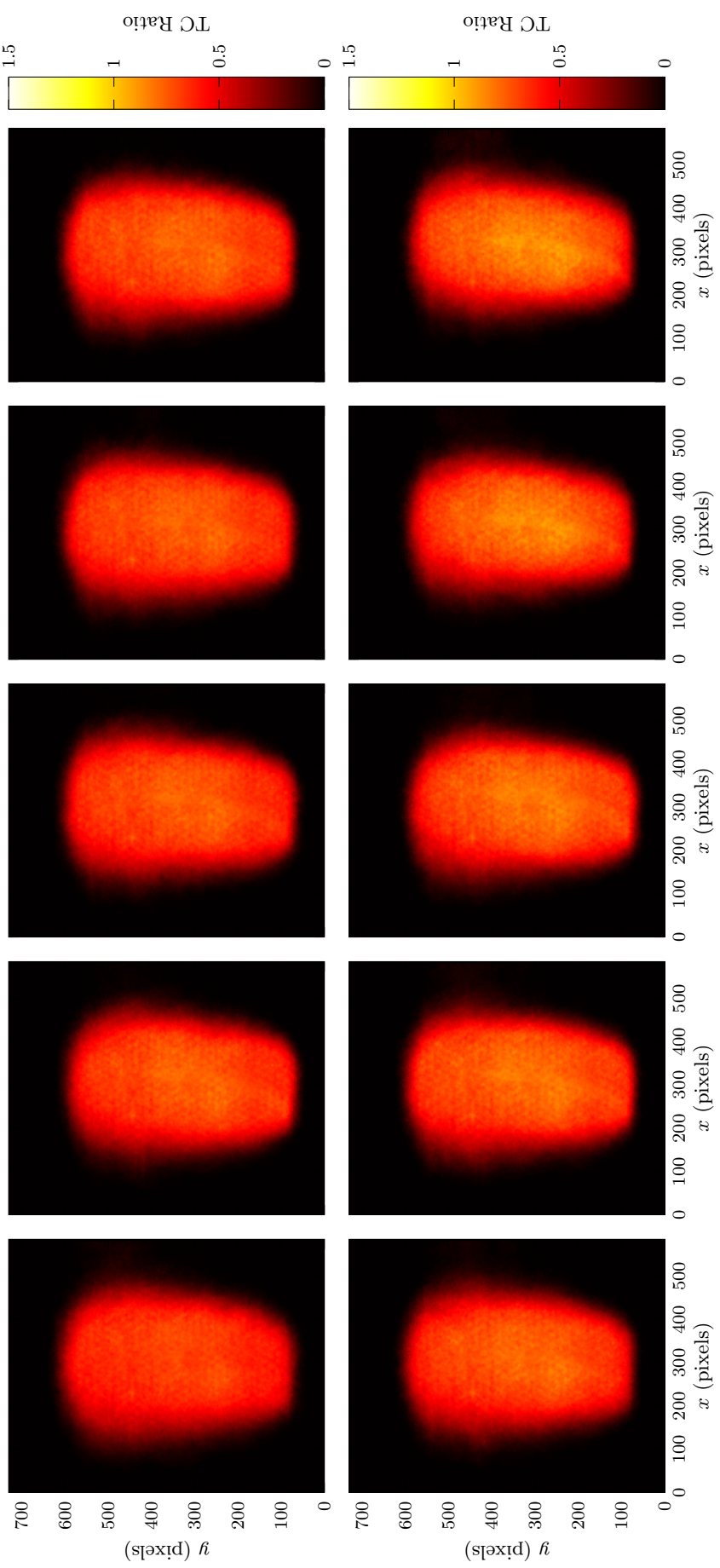


Figure 4.36: Variation of the steady-state run average TC ratios with temperature. Figures are ordered in increasing temperature from the top left to right, followed by bottom left to right

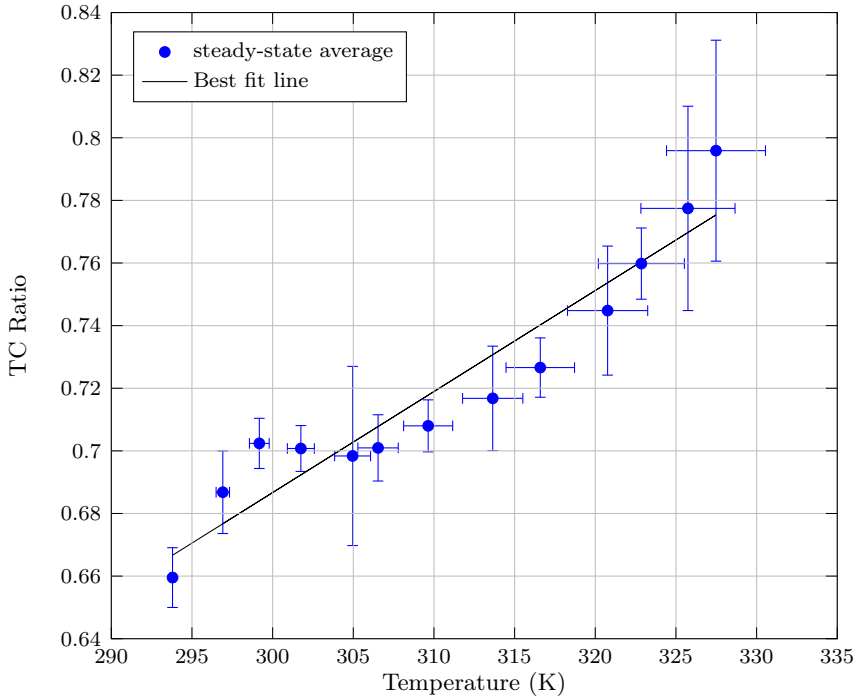


Figure 4.37: Variation of mean TC ratio with temperature for each steady-state run. Horizontal error bars represent the standard deviation of temperatures measured using the thermocouple over 250 samples. Vertical error bars represent the standard deviation of TC ratios evaluated for 250 images

this experiment meant that large temperature uncertainties are present. The reason for this is two-fold, firstly, results are collected for 25 s in which mean temperature fluctuations are present, and secondly, temperature gradients are present across the jet.

Further evidence that one-colour PLIF with DEHS is possible is shown in Figure 4.38 and 4.39. Here, the temperature of the jet was modulated within a single run by varying the autotransformer voltage to produce a transient temperature profile. The frame average B and R signals are plotted alongside the thermocouple measured temperatures. An inverse relationship between signal and temperature is evident. The variation in transient signal is able to reflect key features in the thermocouple transient, notably the point of maximum temperature at which the autotransformer was turned off in Figure 4.39. It is important to note that Figures 4.38 and 4.39 seek to demonstrate qualitative and not quantitative evidence of using one-colour PLIF with DEHS. Pulse energy fluctuations have a part to play in the data scatter, and this could not be accounted for, as only residual 532 nm was monitored. Sampling the UV beam for 266 nm pulse

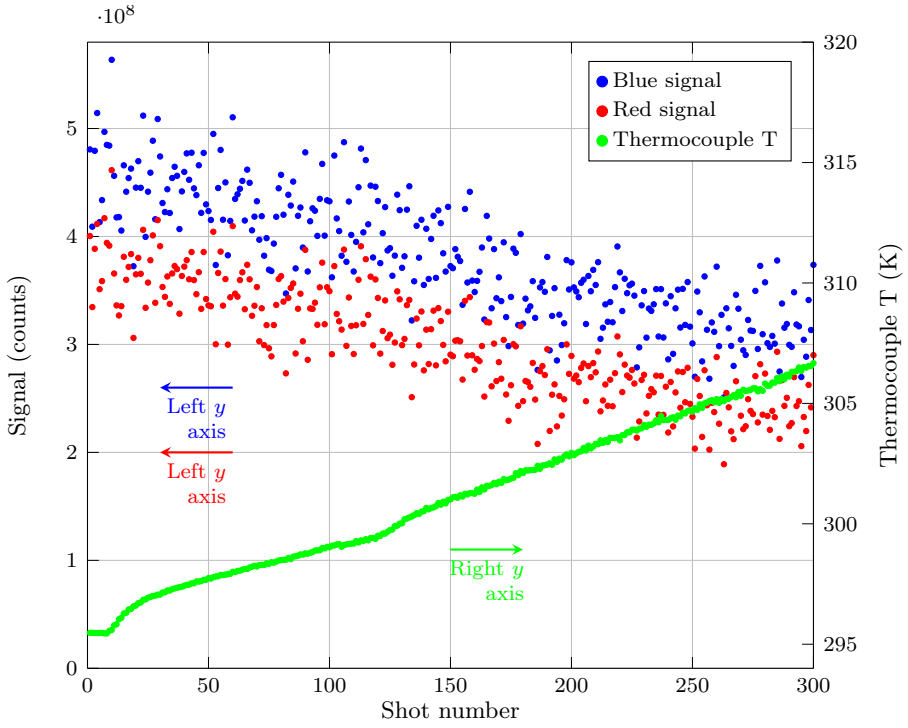


Figure 4.38: B and R signal variation with thermocouple measured temperature - linear heating profile

energy fluctuations would further reduce the incident excitation energy for DEHS droplets, thus this was not attempted. In addition, droplet size and density are assumed to be constant for a fixed seeding method and flow rate, but in truth, these fluctuate too and can affect the amount of signal obtained.

Results from the second layout involving a cold and a hot jet inclined towards each other are shown in Figure 4.40. Here, four single shot TC ratio maps are presented. Regions where droplets are absent have been masked leaving a white background. The cold jet was maintained at room temperature while the hot jet reached average temperatures of about 330 K. A clear distinction between the cold and hot jets is discernible, with the cold jet on the left having smaller TC ratios, and vice versa for the hot jet on the right. This shows promise for providing spatially-resolved temperature measurements using DEHS in FPIV.

It is evident from Figure 4.31 that a very high droplet density was used in these experiments, in order to maximise signal levels. An almost continuous signal is visible in both sub-regions. This is not ideal for normal PIV which typically requires discrete droplets. Average B signal

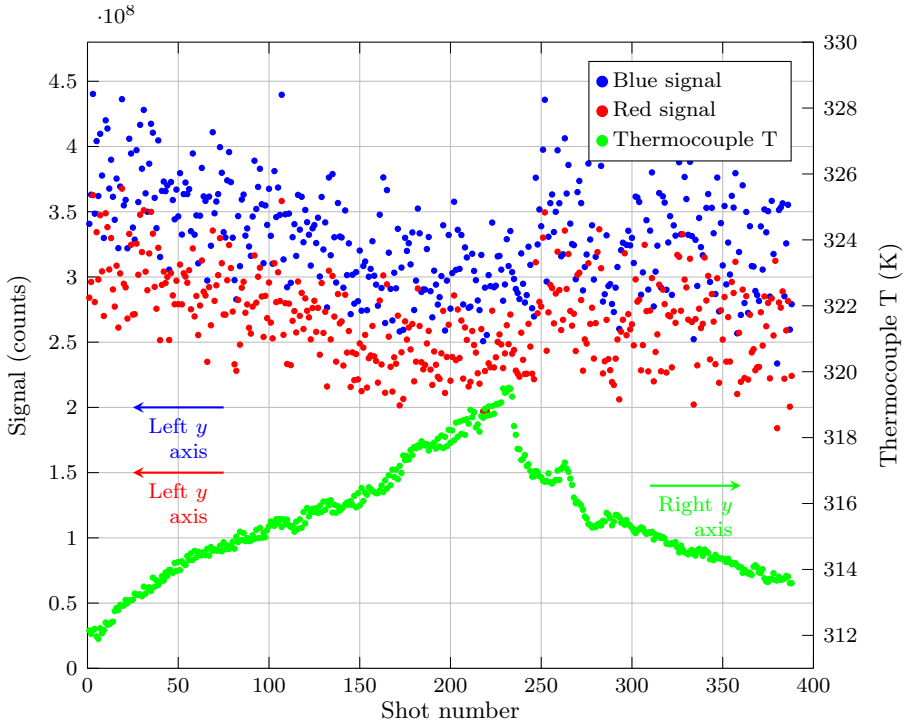


Figure 4.39: B and R signal variation with thermocouple measured temperature - arbitrary heating profile

at room temperature (larger than R signal) was about 6000 counts, utilising less than 10 % of the camera's dynamic range. This is despite using 100 mJ of UV pulse energy and applying intensifier gain of almost 350 times. As a result, single shot TC ratio maps are highly susceptible to noise. Gaussian blurring of signals improves this, but some level of 'patchiness' is still present. Future FPIV studies involving DEHS would clearly benefit from improved SNR.

Figures 4.41 (a) and (b) present TC ratio profiles extracted along a single row and column respectively from one of the images in Figure 4.40. Note that pixel positions are in increasing order from left to right, and from bottom to top. Here, an increasing trend in TC ratio is observed in both figures as expected. The temperature of the flow increases as you traverse from the cold to the hot jet. Similarly, jet spreading and mixing causes the temperature to drop from bottom to top i.e. in increasing pixel position along the vertical axis. As before, a large scatter in TC ratios is evident.

In this section, the ability to extract temperature information from DEHS droplets was demon-

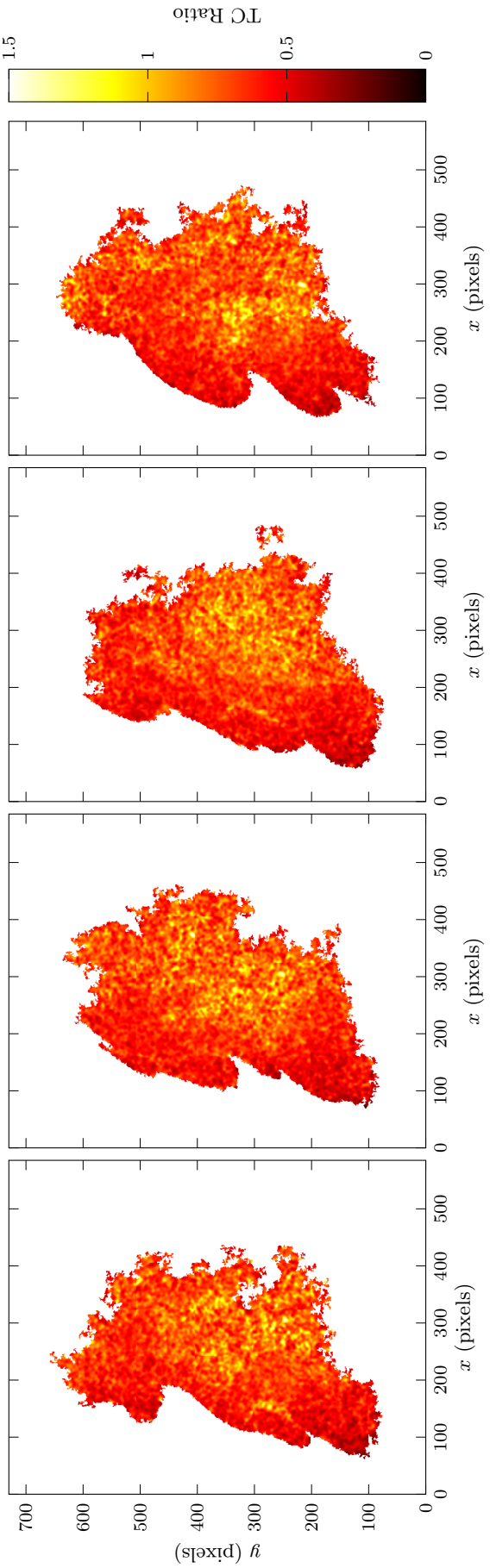


Figure 4.40: Single shot TC ratio fields of hot and cold DEHS jets mixing

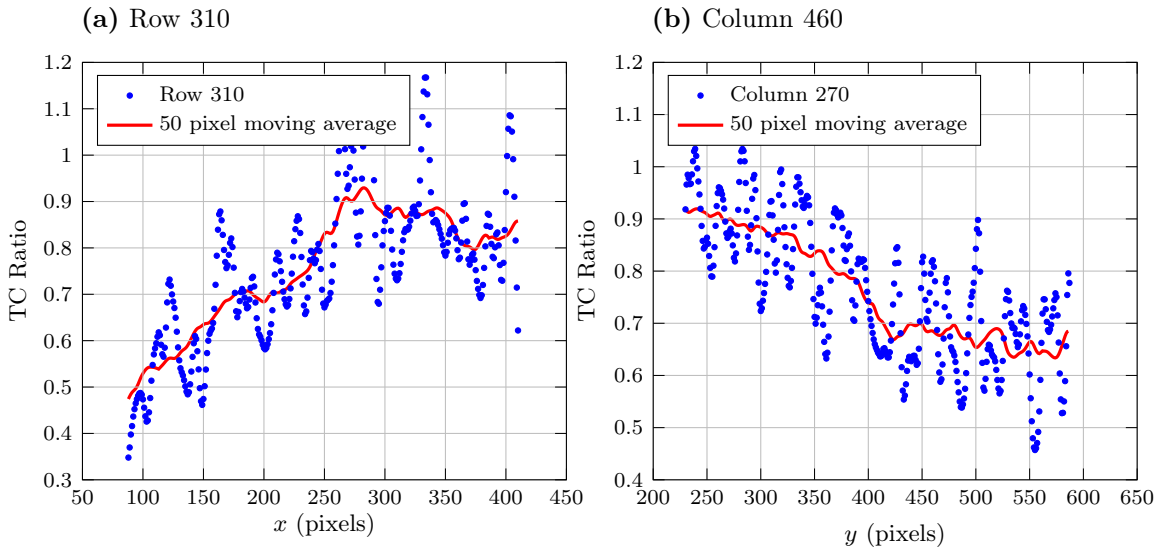


Figure 4.41: TC ratio along horizontal (a) and vertical (b) profiles of a single ratio image

strated in an example FPIV experimental set-up. Steady-state tests revealed an increasing trend in TC ratio with temperature, while single-shot images showed promise of extracting spatial temperature gradients. One-colour PLIF measurements were shown to also be possible. A number of improvements, specifically in enhancing SNR, are required for future applications of DEHS in FPIV, and will be discussed in more detail in Section 8.2.1.

4.5 Liquid vs droplet DEHS emission

Based on the results in Section 4.4.4, there are clear differences in the fluorescence emission characteristics of DEHS in bulk liquid and droplet form. As previously described, the main difference lies in the broadening of the fluorescence both towards shorter and longer wavelengths, the former caused by self-absorption leading to a shift of the peak emission wavelength, and the latter leading to the formation of a new peak altogether. Differences such as this are proof that TC-PLIF based studies require aerosol calibration methods, rather than that of bulk liquids, because this is more representative of actual experimental conditions where measurements are being made on droplets and not on a bulk liquid. Sadly, this is hardly the case in the literature - most characterisations of dyes for use in droplet-based TC-PLIF experiments were performed

in bulk liquid form [96, 32, 37].

Differences due to self-absorption are not unusual - many such characterisations have been reported in the literature in various TC-PLIF studies [32, 96, 37]. Self-absorption is typically addressed in bulk liquids by using small concentrations of the fluorophore, or by using small optical path lengths (achievable by reducing the cross-section of the bulk liquid cell), but neither of these were attempted for DEHS. Solvent addition could affect fluorescence characteristics, while significantly reducing output signal which could make it difficult to measure. In addition, designing a system that minimises photobleaching in a small cross-section cell is not trivial; a continuous flow through a spectroscopic cell pumped from a reservoir may be the only solution, but is messy, and could have contamination issues with the use of a pump. On the other hand, the formation of a new longer-wavelength peak not present in the bulk liquid is less easily explained. Similar observations could not be found in the literature for other PLIF tracers. This is not an effect of self-absorption, as the absorption spectra (Figure 4.7) clearly shows a negligible absorption cross-section at the wavelengths of this second peak. The TC-PLIF method has been shown to work in Section 4.4, but it would be beneficial to understand the physics behind DEHS photoluminescence. This would ensure that any change to experimental design does not hinder the ability to perform droplet thermometry. To this end, the following sections explore proposed theories that were investigated to try and explain the formation of this peak.

4.5.1 Phosphorescence

The first theory explored is that the 405 nm peak is phosphorescence rather than fluorescence. This theory investigates the possibility that the droplet form promotes activation of the forbidden triplet state. The motivation for this theory is the observation that the new peak occurs at longer wavelengths to the original fluorescence observed in liquid form.

Conceptually, when there is a large overlap in its energy levels, a fluorophore can be knocked from the singlet energy ladder into the forbidden triplet state energy ladder, leading to the fluorophore

returning to the ground state via longer wavelength phosphorescence decay. The triplet state exists as a result of the forbidden spin-spin coupling of electron pairs - according to Pauli's Exclusion Principle [106], electron pairs should have opposite spin. When an electron is excited to a higher electronic state it retains its spin, making it still opposite to its pair. If this electron is pushed into the triplet energy ladder, it changes its spin to be parallel to that of its pair. Given that the transition of this parallel spin excited electron back to the ground state is forbidden by quantum mechanics, the probability is low, which translates to phosphorescence emission being much longer in lifetime and weaker in intensity compared to fluorescence emission. Fluorescence decay lifetimes are typically in the order of nanoseconds, while that of phosphorescence is usually in excess of microseconds (some even lasting several full seconds) [4].

Given this, to test if the 405 nm peak is indeed phosphorescence and not fluorescence, the decay lifetimes of these peaks were measured and compared. If this theory were true, it is likely that the 405 nm peak should have a decay lifetime that is appreciably longer than that of the 285 nm peak. The same experimental layout and image acquisition strategy from Section 4.4.2 was used. A fixed gate width of 5 ns was set on the intensified camera. This fixed gate was then progressively delayed with respect to the arrival of the laser pulse. At each delay with respect to the laser, 250 images were acquired, from which mean R and B signals were evaluated. These were then used to plot emission decay curves for each peak, and fit exponential functions to obtain decay time constants. A simple exponential of the form shown in Equation (4.1) was used to fit the data.

$$I\left(t\right) = I_{\mathrm{o}} \exp\left(\frac{-\left(t - t_{\mathrm{o}}\right)}{\tau}\right) \tag{4.1}$$

where $I\left(t\right)$ is the signal at time t, I_o is the starting signal, t_{o} is the start time of emission and τ represents the decay time constant.

Figures 4.42 and 4.43 show the measured data and a fitted exponential curve. Note that the

[4] A small number of phosphors can have decay lifetimes in the order of ns, for example ZnO and ZnO:Ga [107]

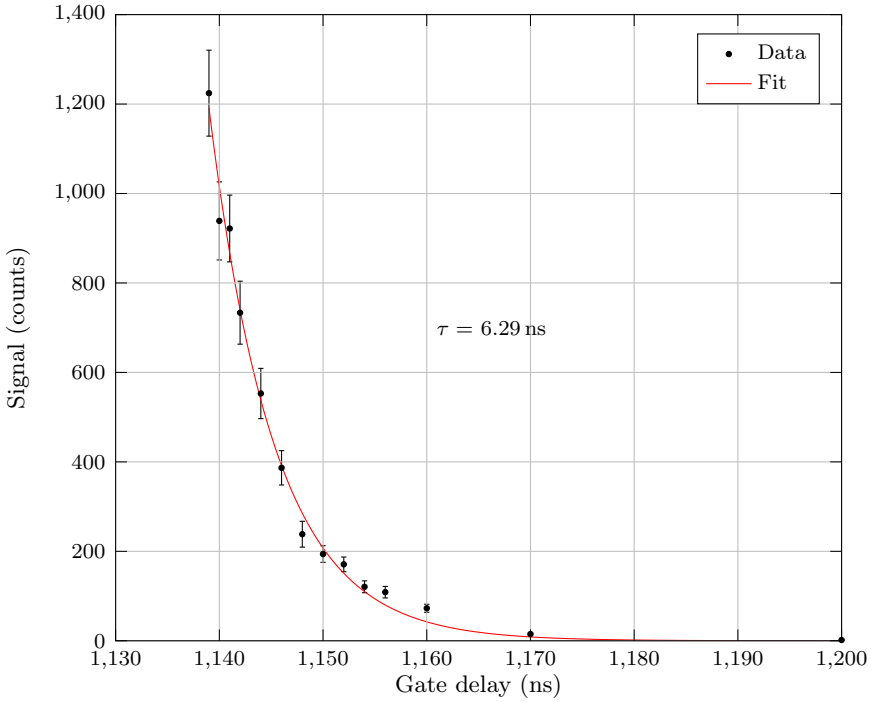


Figure 4.42: Blue fluorescence signal decay. Error bars represent the standard deviation of signal over 250 images

horizontal axis represents the gate delay with respect to a fixed starting time. This was nominally set to 1 µs before the laser Q-switch was triggered.

From the data collected it appears as though the fitted decay lifetimes are of a similar value - both have decay lifetimes of about 6 ns. Data from the B channel fits the exponential function adequately, however there is a slight deviation in fit for the R channel data. The use of a dual exponential function (of the form given in Equation (4.2)) for this data does not yield vastly different results, certainly not enough to validate the possibility of phosphorescence.

$$I(t) = I_{o,1} \exp\left(\frac{-(t - t_o)}{\tau_1}\right) + I_{o,2} \exp\left(\frac{-(t - t_o)}{\tau_2}\right) \tag{4.2}$$

A similar conclusion is obtained from the graph of TC ratio against gate delay, shown in Figure 4.45. From this, it is clear that the TC ratio stays equal in order of magnitude. At the early stages of the emission decay curve, i.e. from 1140 to about 1150 ns, it is evident that the TC ratio is uniform in value. The rise in TC ratio beyond this point is attributable to lack of signal

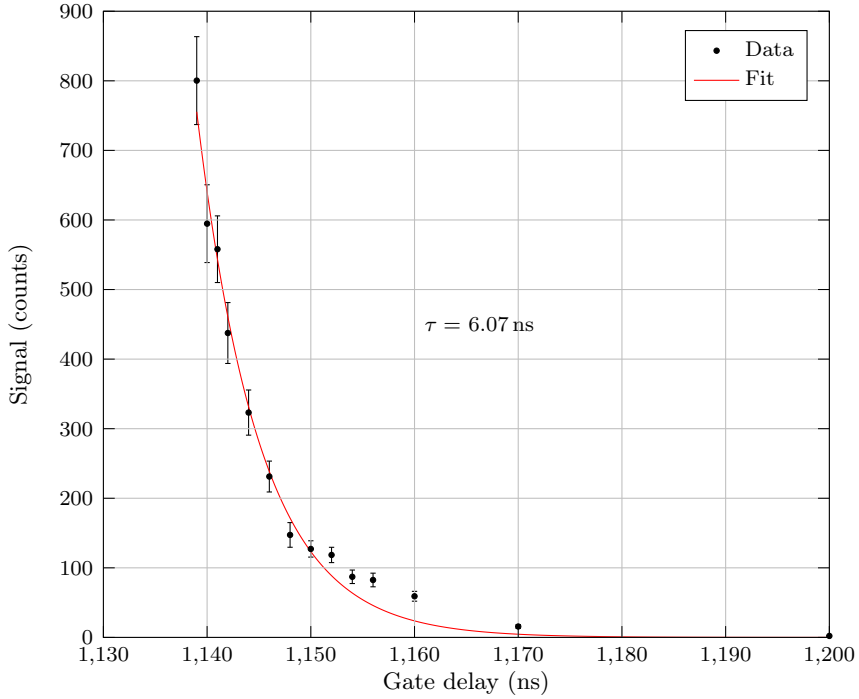


Figure 4.43: Red fluorescence signal decay. Error bars represent the standard deviation of signal over 250 images

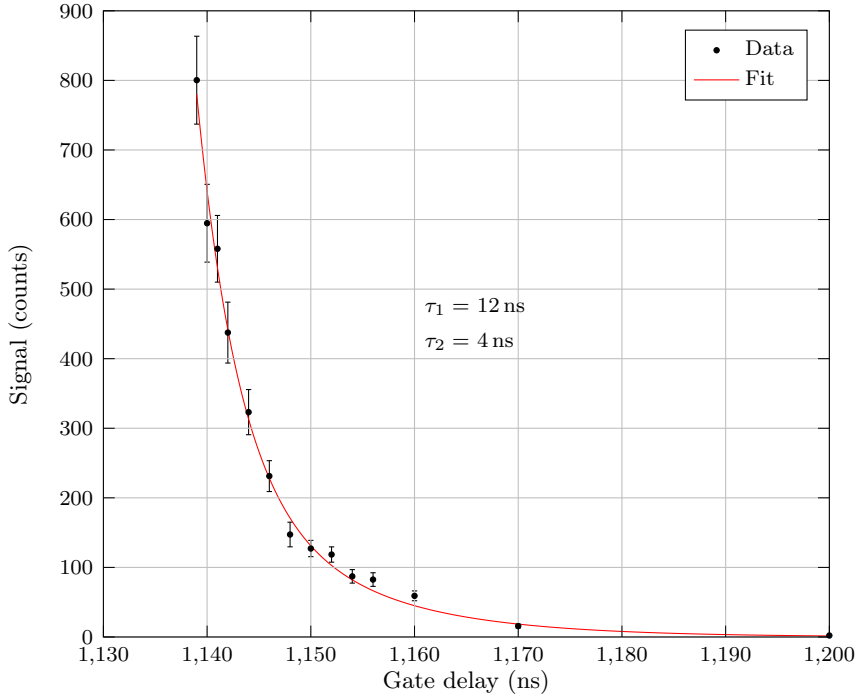


Figure 4.44: Red fluorescence signal decay with dual exponential fit. Error bars represent the standard deviation of signal over 250 images

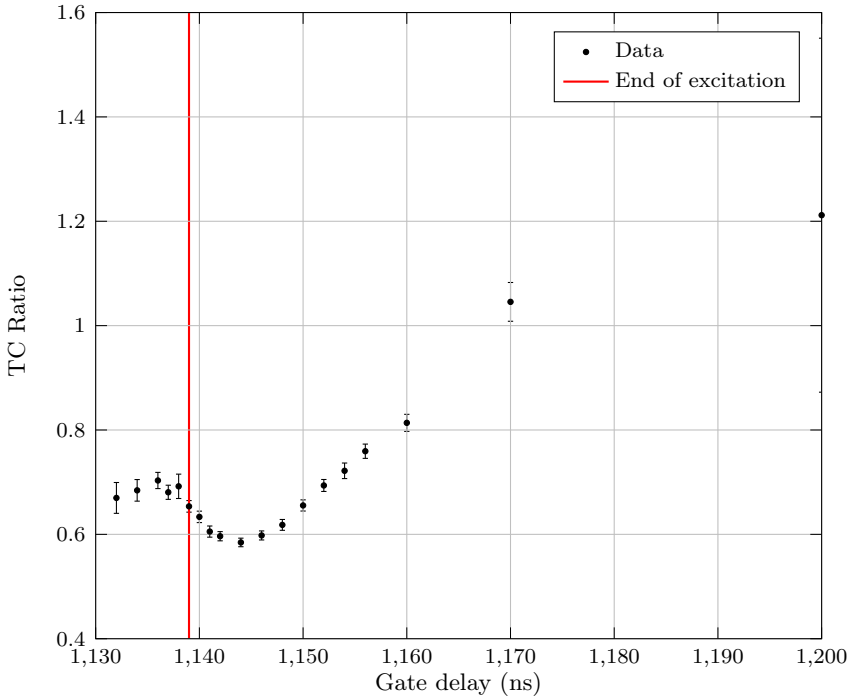


Figure 4.45: TC ratio variation with gate delay. Error bars represent the standard deviation of TC ratio over 250 images

strength, but might also indicate the presence of *some* phosphorescence. Nonetheless, the relative signals still remain of the same order of magnitude. If the phosphorescence theory were true, at the early stages of the emission decay, the TC ratio should be approximately 15 %, as the second peak would have yet to form, however this is not the case.

Given these observations, it is unlikely the 405 nm peak was caused by phosphorescence.

4.5.2 Whispering Gallery Modes

The next theory considers droplets that can act as small spherical resonant lasing cavities. In a laser oscillator cavity, light of specific wavelengths can form standing wave resonances if the geometry of the cavity in the direction of light propagation is favourable, i.e. it promotes constructive interference. Broadband spontaneous emission from the gain medium promotes initial stimulated emission, however, the presence of such resonances, or modes, within the cavity is what causes specific wavelengths to be most efficiently amplified. Effectively, light at the resonant wavelength gets amplified above all others. Spherical particles have the ability to form

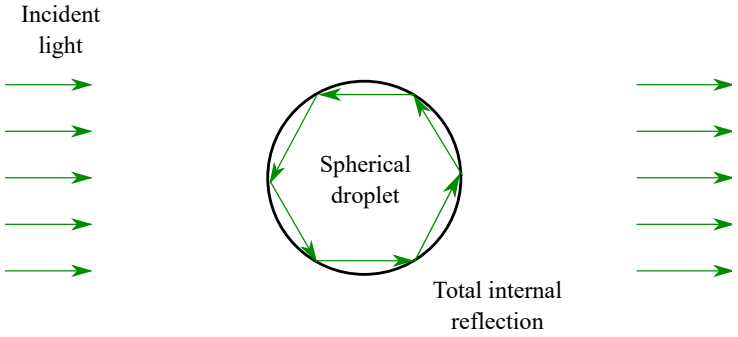


Figure 4.46: Schematic representation of a Whispering Gallery Mode. Resonant wavelengths are trapped within the walls of a spherical particle as a result of multiple total internal reflections

resonant cavities as well - this is achieved through multiple total internal reflections within the internal walls of the sphere as shown in Figure 4.46. Such modes are called Whispering Gallery Modes (WGM) [108].

Spherical aerosol droplets can act as micro-resonators, thus amplifying light of specific resonant wavelengths. This leads to the formation of a new emission peak that was absent in liquid form (as there are no cavity resonances present here). This theory was inspired by results observed in other publications [109, 110]. In [109], single spherical micro-droplets containing Rhodamine laser dye were suspended in air, and excited by a laser to produce spontaneous fluorescence emission from the droplets. By varying different parameters, such as laser pulse energy and dye concentration, changes in emission characteristics were observed. Notably, a new emission peak was formed, which was more prominent at higher concentrations and higher pulse energies. Given the similarity in observations, this theory was investigated.

The equation that describes WGM is given in Equation (4.3).

$$2\pi R n_{\text{eff}} = M\lambda_{\text{R}} \tag{4.3}$$

where R is the radius of the spherical particle, n_{eff} is the effective refractive index of the medium, M is the mode number and λ_{R} is the resonant wavelength of the mode. M represents the number

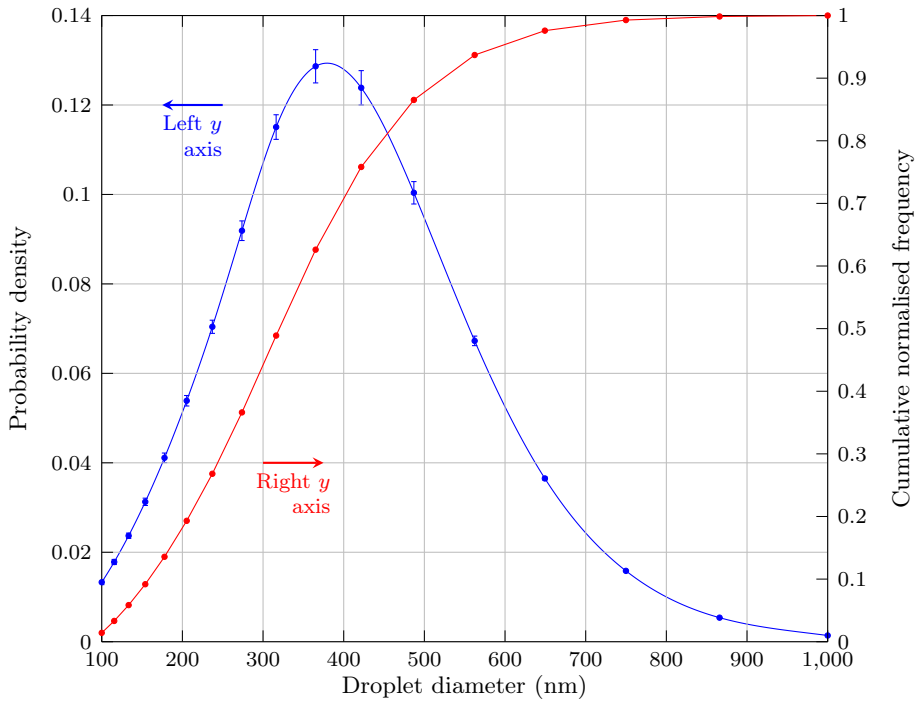


Figure 4.47: DEHS droplet size distribution generated using a LaVision aerosol generator

of wavelengths of light travelled in one trip around the spherical cavity. This theory was tested by attempting to model the shape of the 405 nm peak using the known droplet size distribution from the aerosol generator with various mode numbers. In essence, a droplet of a specific size will resonate one particular wavelength - the combined distribution of droplet sizes is thus assumed to be what produces a broadband secondary peak that is present in droplet form and not in liquid form. The particle size distribution of the LaVision aerosol generator is given in Figure 4.47 (measured using a Cambustion DMS500 Fast Particle Analyser).

By inserting this into Equation (4.3), rearranging for λ_R and trying various values of M, the curve that comes closest to the emission shape of the 405 nm peak was found. Figure 4.48 shows the result of this attempt.

In this figure, solid coloured lines represent the extents of each DEHS emission peak, i.e. the leftmost blue lines mark the start and end of the 285 nm peak, while the rightmost red lines mark the start and end of the 405 nm peak. This is provided for ease of reference to see whether the stipulated WGM emission lies within these bounds. As can be seen from this figure, the closest

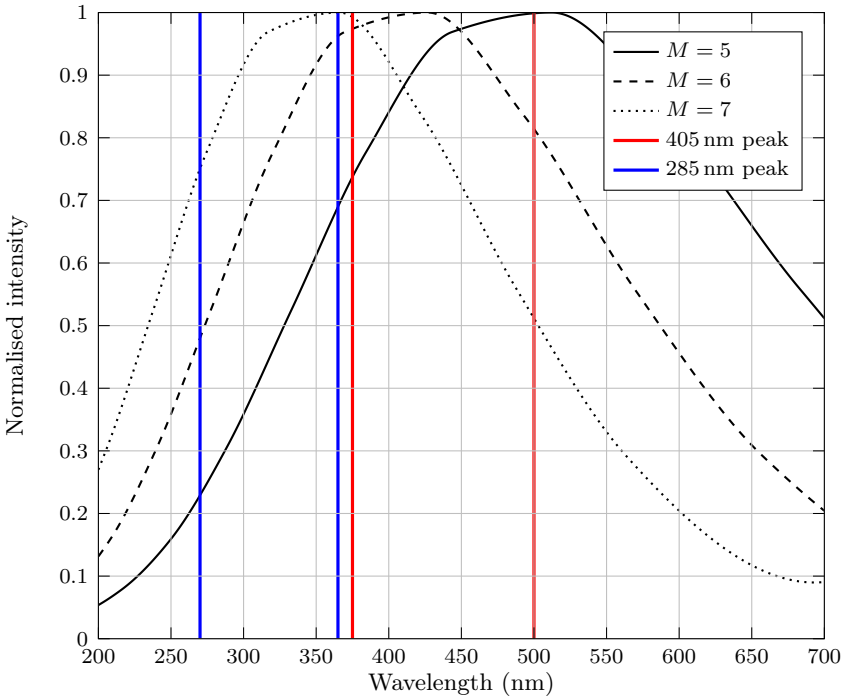


Figure 4.48: Modelled WGM emission for various mode numbers

mode number to the 405 nm peak is $M = 6$. This leads to the same peak emission wavelength. However, the emission range for the WGM model is significantly broader and extends well into the region of the 285 nm peak.

By comparing the predicted WGM model emission with the fluorescence emission from DEHS droplets, seen in Figure 4.49, it is evident that for this theory to hold true, light amplification should happen across a broader range of wavelengths. It may be reasonable to argue that at wavelengths less than 300 nm, WGM emission is hindered as a result of reabsorption by DEHS molecules. While *fluorescence* self-absorption is not a problem due to the spacing between droplets, here light trapped in a spherical cavity travels a supposed distance of 6 wavelengths, which could be argued is a significant enough path length for reabsorption. However, reabsorption is not an issue at wavelengths higher than this, so specifically, the trough in emission at around 360 nm should not be present if this theory is to hold true.

A secondary experiment to validate this model is based on the observations from literature [109, 111] where a single Rhodamine-doped droplet was excited, and its WGM and fluorescence

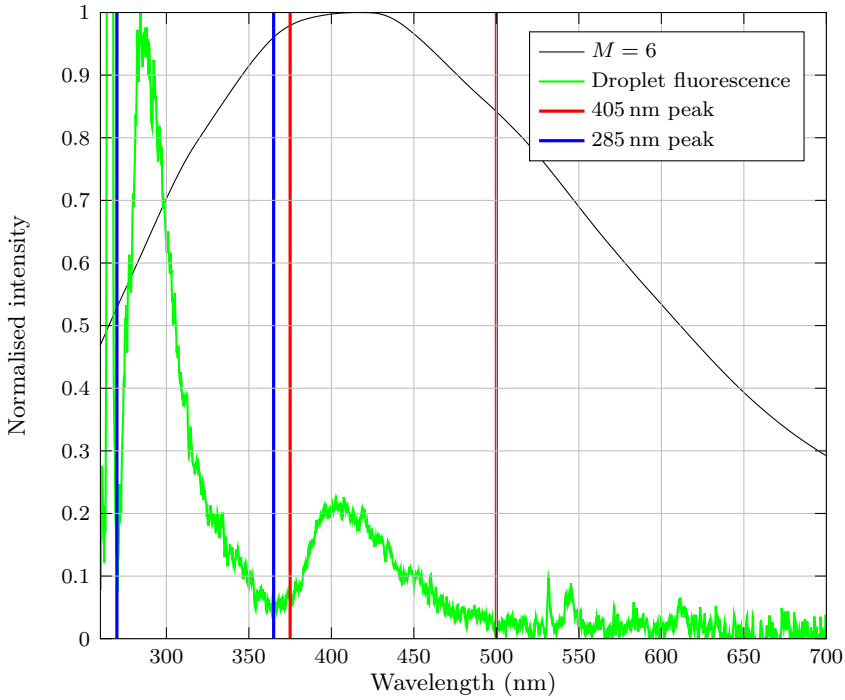


Figure 4.49: Measured fluorescence emission compared to predicted WGM emission

emission was recorded. The authors found that a characteristic threshold excitation laser energy was necessary before WGM emission was observed. Thus, this experiment set out to reduce the incident excitation laser energy to see if the 405 nm peak ceased to exist. The methodology used in Section 4.5.1 was repeated, this time gating the intensified camera for 4 µs to capture the entire emission phenomenon. Sets of data were collected at a range of laser pulse energies, and average TC ratios were evaluated at each pulse energy to determine if there was any change. Results from this test are shown in Figures 4.50 and 4.51. The change in both R and B signals with pulse energy remained uniform and linear, especially where appreciable SNR was achieved (532 nm pulse energies exceeding 50 mJ). This translated to uniform TC ratios for various pulse energies. No step change in signal was observed.

To conclude, the WGM explanation appears not to fit the data.

4.5.3 DEHS degradation

A possible cause for the formation of the 405 nm peak is DEHS degradation under strong laser excitation causing the alteration of its molecular structure, or ablation forming smaller con-

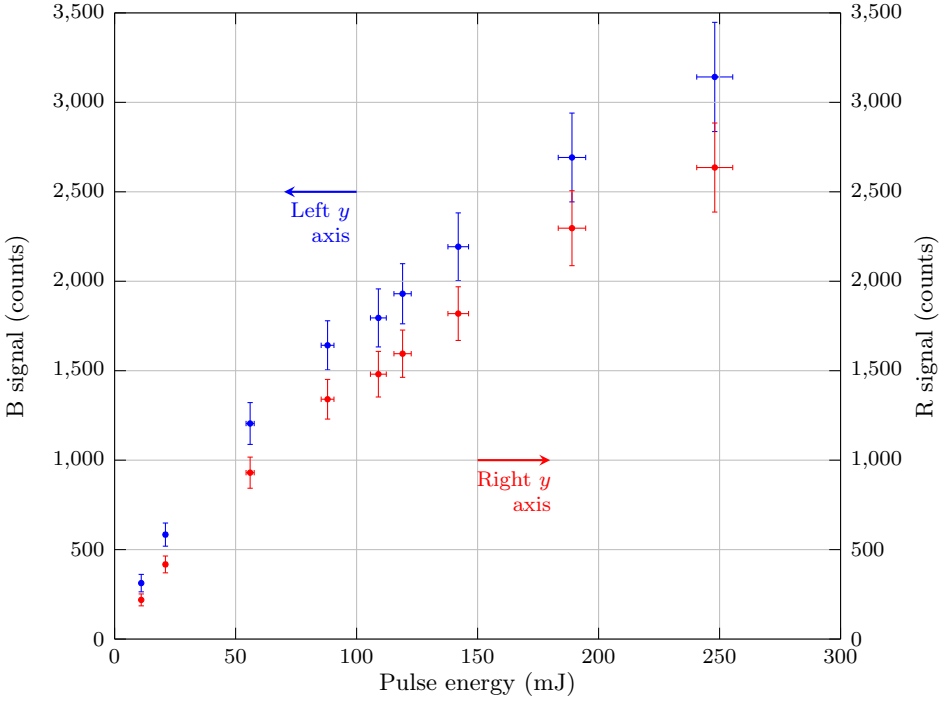


Figure 4.50: B and R signals as a function of pulse energy. Horizontal error bars represent the inherent measurement uncertainty of the energy meter, while vertical error bars represent the standard deviation of signal over 250 images. Note that the pulse energy indicated in this figure is at 532 nm, i.e. pre-frequency doubling

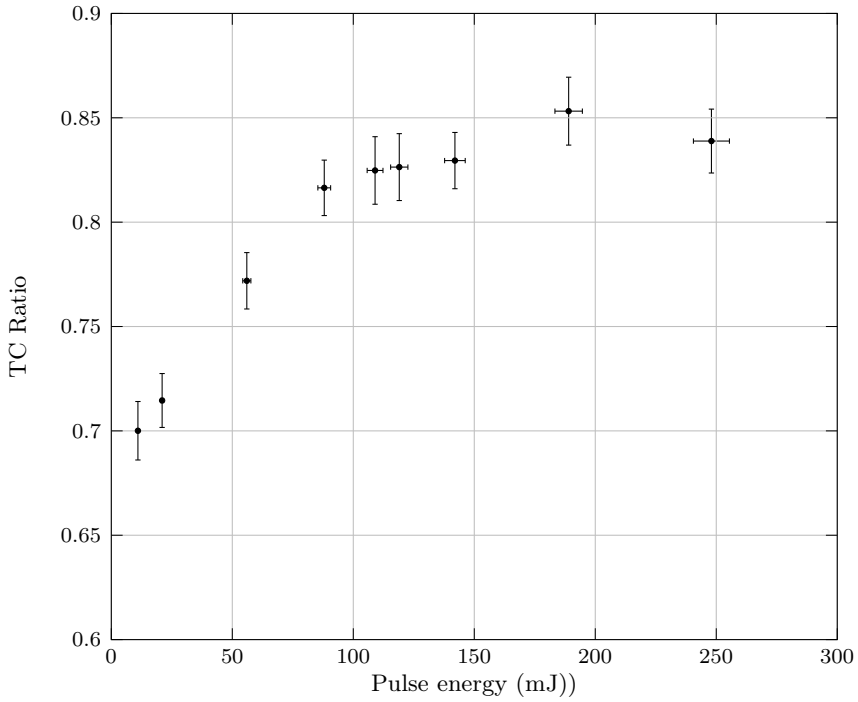


Figure 4.51: TC ratio as a function of pulse energy. Horizontal error bars represent the inherent measurement uncertainty of the energy meter, while vertical error bars represent the standard deviation of TC ratio over 250 images. Note that the pulse energy indicated in this figure is at 532 nm, i.e. pre-frequency doubling

stituent products that have unique fluorescent properties. Lizal et al. [104] have described and demonstrated how excitation and emission properties of DEHS change as it degrades under oxidation. In their work, 'degraded' DEHS emission is broadened towards the visible wavelengths when compared with non-degraded DEHS. These measurements were made in liquid form, and while this particular observation is true when compared with current results, they did not report the formation of a dip in emission (as seen in this work at around 360 nm). As described in Section 4.3.2, DEHS photobleaches easily, and even changes its appearance by eye when it is photobleached. This could be an indication of a change in substance properties. In all liquid based tests, the total number of laser pulses entering a sample of DEHS was controlled to limit the effect of photobleaching. Additional steps include using a relatively large volume of DEHS, a magnetic stirring machine to constantly replenish DEHS, and an unfocused relatively weak excitation beam. Observations have shown that a general red-shifting of the emission is visible, however no secondary peak forms even after 40 thousand pulses from the laser. Stronger excitation, a focused beam, no stirring and a smaller quantity of liquid DEHS may help to test whether a second peak forms with time. On the other hand, as described in the previous section, reducing the incident laser pulse energy subjected to an aerosol plume does not change the TC ratio from DEHS droplets. This may be an indication that pulse energy has no effect on the degradation of DEHS but perhaps the droplet form simply makes degradation much easier. It is also unclear whether the emission spectrum of DEHS has changed with laser excitation energy - the existing spectrometer is not sufficiently sensitive to measure this for lower pulse energies.

4.6 Summary

In this chapter, the benefits of FPIV were highlighted, both as a scatter reduction tool, as well as a multi-property diagnostic. Elastic scatter reduction was first demonstrated through the use of a fluorescent laser dye, Rhodamine 6G. Novel temperature-dependent fluorescence emission of DEHS was then investigated, which motivated its use as a PLIF tracer. Considerable effort was

subsequently devoted towards demonstrating the ability to extract temperature information from DEHS droplets using PLIF methods. Results presented show promise for expanding the use of existing commercial PIV systems to simultaneous velocimetry and thermometry with no impact on the non-intrusive nature of the underlying diagnostic. Future investigations performing FPIV using DEHS would benefit from signal enhancement measures, which are elaborated in Chapter 8. In addition, differences in fluorescence emission between droplet and bulk liquid forms of DEHS need to be analysed further to improve understanding of the underlying photophysics.

Chapter 5

Polarised-Depolarised Rayleigh Scattering

In this chapter, PDRS is proposed as a potential diagnostic tool for simultaneous composition and temperature measurements in high-speed flow research. As previously described, there are a number of inherent requirements for successful application of this technique. Firstly, Rayleigh signals are weak, requiring high energy pulsed lasers, along with intensified cameras. Secondly, gases having different depolarisation ratios, r_{p}, are required in order to distinguish between them. Finally, as will be discovered in this chapter, scatter from larger sized particles such as dust or condensed water droplets can overwhelm Rayleigh signals leading to camera saturation and erroneous results. Thus, 'clean' environments are typically required when performing this technique. The sections in this chapter seek to delve further into these requirements, probing whether any of these can realistically be met when applied to a high-speed flow investigation.

5.1 Sensitivity analysis

In order to inform future PDRS experiments, an investigation of the sensitivity of this technique was performed. PDRS is most effective when the gaseous species used differ substantially in r_{p}, as described in Section 2.3.4. As a reminder, r_{p} is the ratio of depolarised Rayleigh scatter to polarised Rayleigh scatter. When performing PDRS, depolarised signal captured by one camera is divided by the polarised signal captured by another camera, to produce a 2-D distribution of r_{p}. If two gases are used, this distribution will have r_{p} values between those of the two gases. By using two gases that differ substantially in r_{p}, the measured distribution will exhibit high contrast, making interpolation of the gas mixture fraction more accurate.

As the r_p values of each gas get closer to one another, PDRS becomes susceptible to noise; small fluctuations in measured r_p lead to large changes in predicted mixture fraction. Figure 5.1 shows a typical look-up curve generated from simulating polarised and depolarised Rayleigh signal intensities. It is evident that the measurement sensitivities differ for different gas combinations. Argon has a r_p value of 0, while CO_2 has a r_p value of 4.08 % [69]. The combination of CO_2 and argon produces a large disparity in r_p values. On the contrary, air has a r_p value of ∼1.40 %, meaning CO_2 and air mixtures span a smaller range of r_p values. Shallow gradients imply higher uncertainty, as small changes in r_p lead to large changes in mixture fraction. This becomes a problem when the SNR of a Rayleigh image is low. Many high-speed flow facilities utilise air as the test gas, due to its low cost and ease of availability. In the context of this work, the use of air is also representative of the application being investigated (transpiration cooling), as will be highlighted in Section 9.1. Changing the test gas of such facilities to a zero r_p gas would be beneficial for PDRS, but will quickly become a costly exercise. To this end, it is worth investigating the effect of using air as a facility test gas on the uncertainty induced in PDRS.

To assess the level of uncertainty for different gas combinations, the Poisson noise characteristic from a camera was used to model 'best-case' fluctuation in Rayleigh signals. Figure 5.2 (a) shows a histogram of pixel counts obtained from a CCD camera (ImperX 1M48-G) imaging a white background. The pixel intensities are distributed according to a Poisson distribution, due to fluctuations in the number of photons reaching the CCD sensor. At higher average intensities, this fluctuation can be approximated by a normal distribution, as shown in Figure 5.2 (a). Due to the random nature with which photons arrive at a sensor, Poisson noise becomes less apparent in brighter images as it contributes a smaller fraction of the total measured signal, and more apparent in darker images as it can contribute a larger fraction of the total measured signal [112]. This poses a problem for depolarised Rayleigh signals, as they are two orders of magnitude less bright than their polarised counterparts. In this investigation, Poisson noise estimates from this CCD camera were used to quantify PDRS measurement uncertainties for

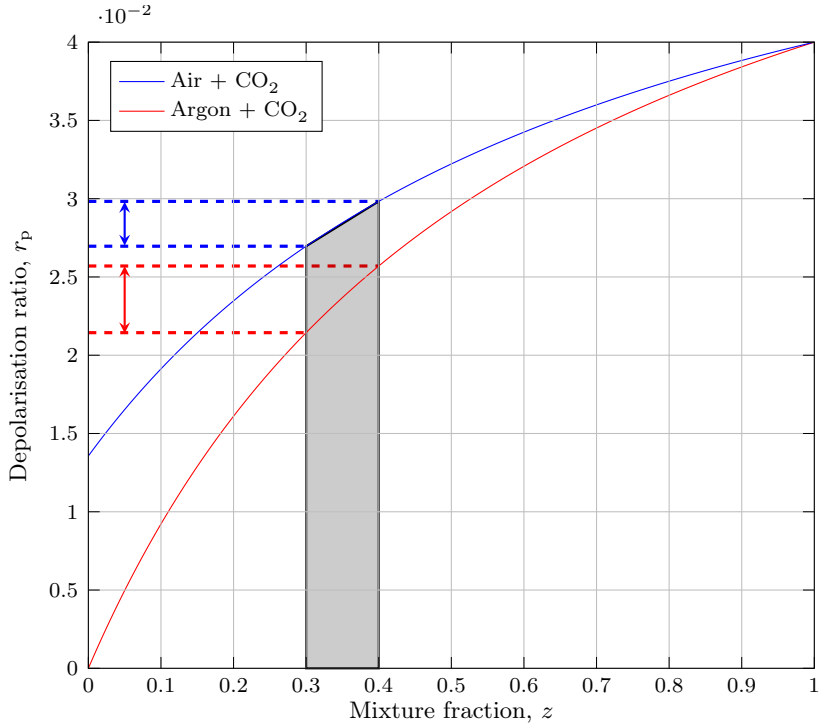


Figure 5.1: Graph showing sensitivity to changes in mixture fraction when using Air/CO_2 (blue line), and Argon/CO_2 (red line). Note how it takes a smaller range of r_p values to produce the same mixture fraction uncertainty (grey area) when using Air/CO_2 (blue double-sided arrow) as compared to Argon/CO_2 (red double-sided arrow)

different gas combinations. By imaging a white background with varying aperture size, Gaussian line-shapes were fitted to signals acquired at varying intensities. A graph of standard deviation against mean pixel intensity was then plotted, shown in Figure 5.2 (b); the gradient of this graph was used to scale the simulated measurement error, in the subsequent uncertainty analysis.

To investigate the uncertainty in PDRS measurements, a simulated mixture fraction and temperature map was fed into a MATLAB code. Figure 5.3 shows the arbitrary simulated maps used in this investigation. Polarised and depolarised Rayleigh signals were constructed by substituting these maps along with the Rayleigh scattering cross-sectional area, σ_R, and r_p for each gas into Equations (2.22) and (2.25) (refer to Table 2.3 for σ_R and r_p values used).

Subsequently, a Gaussian noise fluctuation was introduced to both the polarised and depolarised signals, at every pixel; the amplitude of this fluctuation was obtained by multiplying the pixel intensity by the gradient obtained in Figure 5.2 (b). Finally, these simulated Rayleigh signals were processed according to the method described in Section 2.3.3, to recreate the input mixture

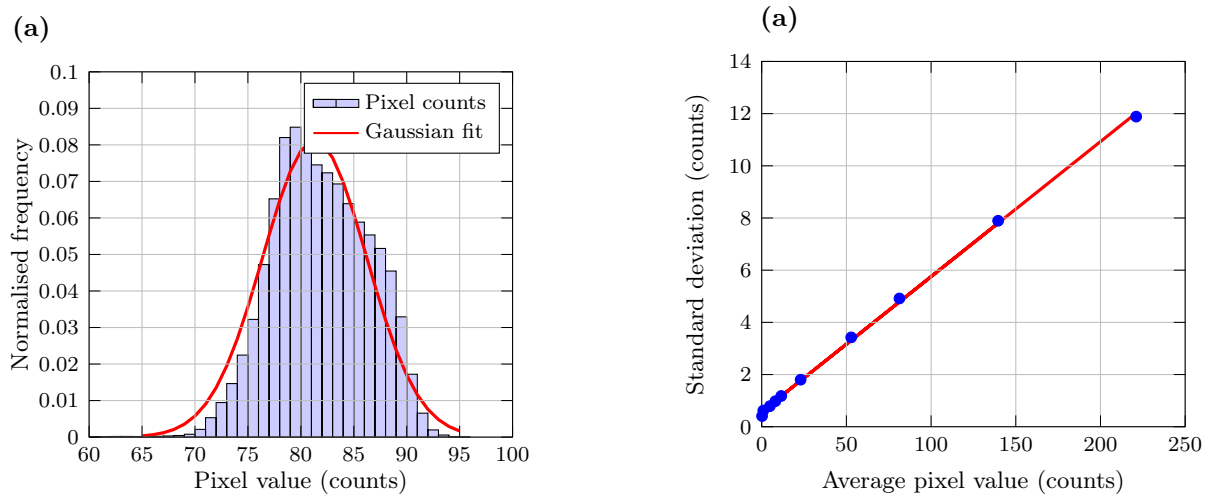


Figure 5.2: An example histogram of CCD pixel counts, fitted with a normal distribution (a) and a graph showing the relationship between average number of counts and standard deviation of the fitted distribution (b)

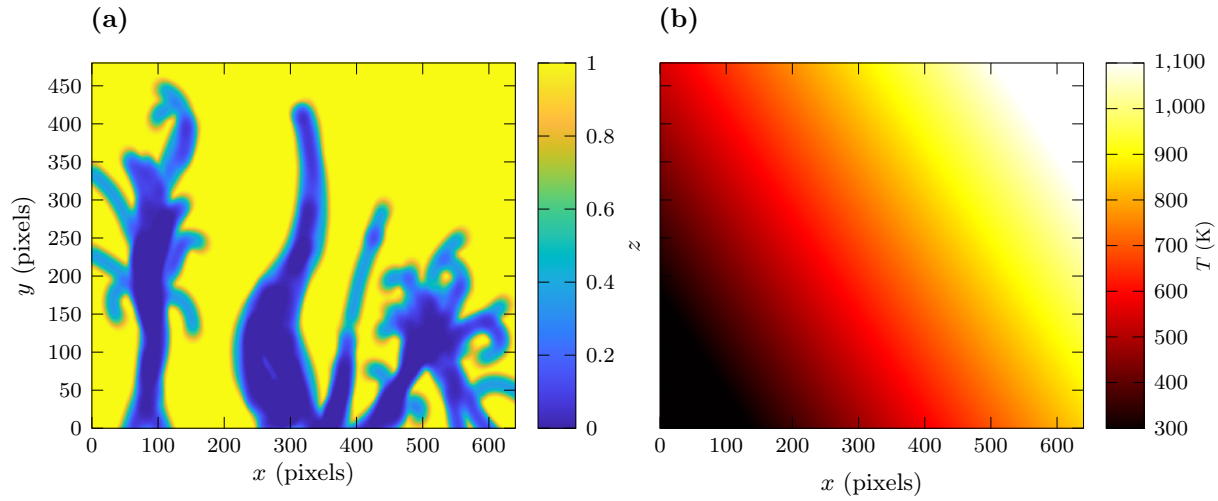


Figure 5.3: Simulated mixture fraction (a) and temperature (b) fields. A mixture fraction of 1 refers to CO_2, while a mixture fraction of 0 refers to air/argon

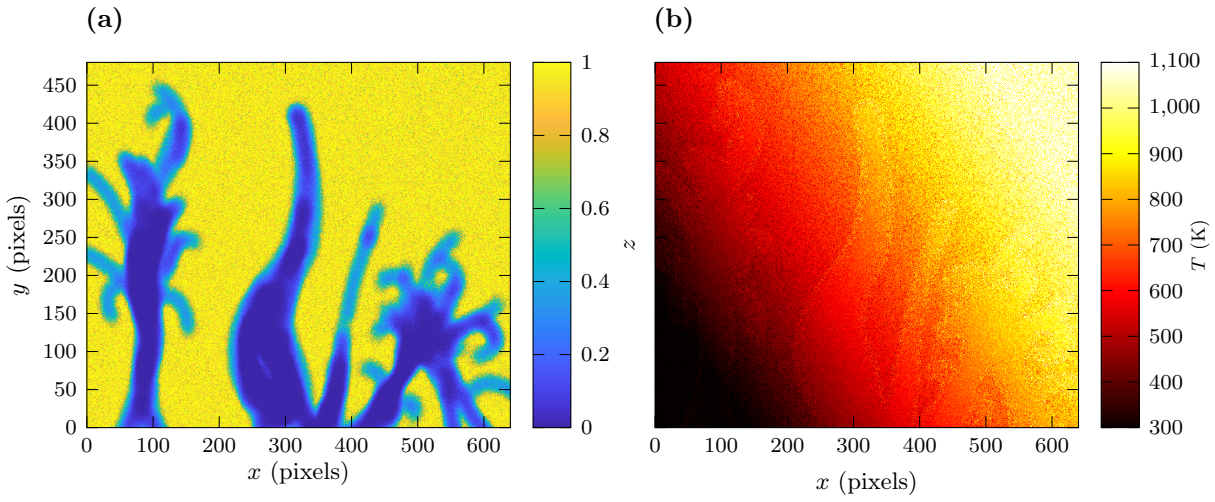


Figure 5.4: PDRS-reconstructed mixture fraction (a) and temperature (b) fields with added noise. A mixture fraction of 1 refers to CO_2, while a mixture fraction of 0 refers to air/argon

fraction and temperature map. Figure 5.4 shows the reconstructed fields; the effect of the noise is immediately apparent when comparing these images with the input maps.

By subtracting the input fields from the reconstructed fields, an uncertainty distribution was obtained, as shown in Figure 5.5 for mixture fraction. There are two distinct regions of uncertainty in this map, a result of the different r_p in each area. High error regions correspond to CO_2, which has a high r_p, while low error regions correspond to air or argon, which have lower r_p. While this may seem counter-intuitive, the reason for this behaviour is a dampening of noise fluctuations in the depolarised signal, when dividing by the much larger polarised signal to obtain r_p. In order to quantify an effective uncertainty for this reconstruction, two approaches were taken. In the first approach, the maximum uncertainty from the noise map was defined as the global uncertainty. The second approach involved segmenting regions of low and high error, and averaging them independently - this is shown in Figure 5.6. A global mean uncertainty was then defined as the average of both the low and high mean uncertainties.

The aforementioned analysis was repeated for varying number of images - this simulates taking multiple Rayleigh pictures and averaging the results. Figures 5.7 and 5.8 show the relative uncertainty distributions for both uncertainty approaches. The horizontal axis in both these

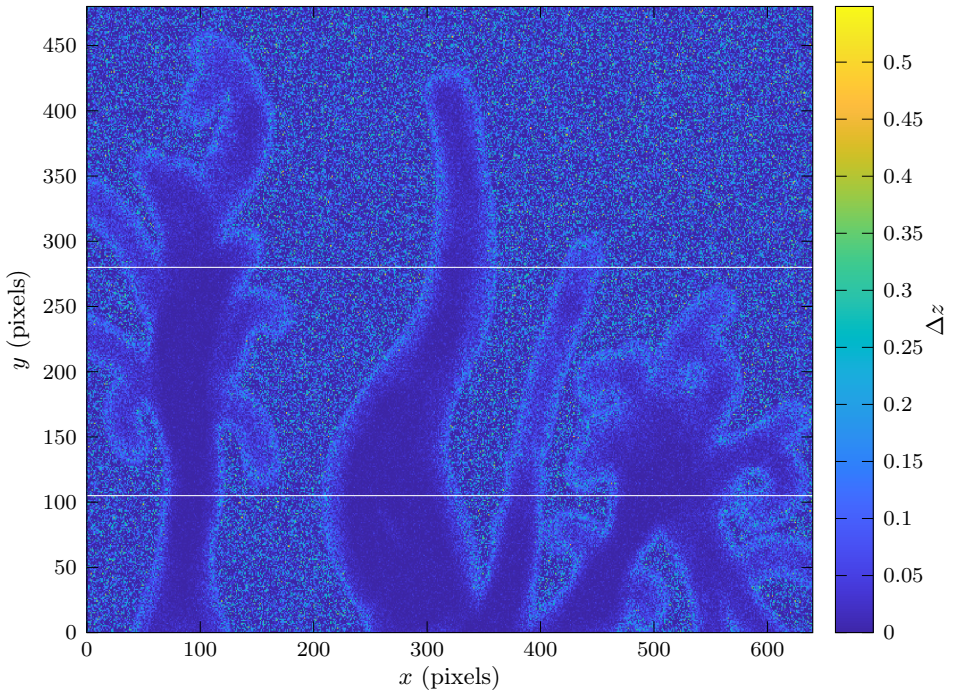


Figure 5.5: Uncertainty map in reconstructed mixture fraction image. Horizontal profiles extracted from rows 105 and 280, indicated as white lines, are shown in Figure 5.6

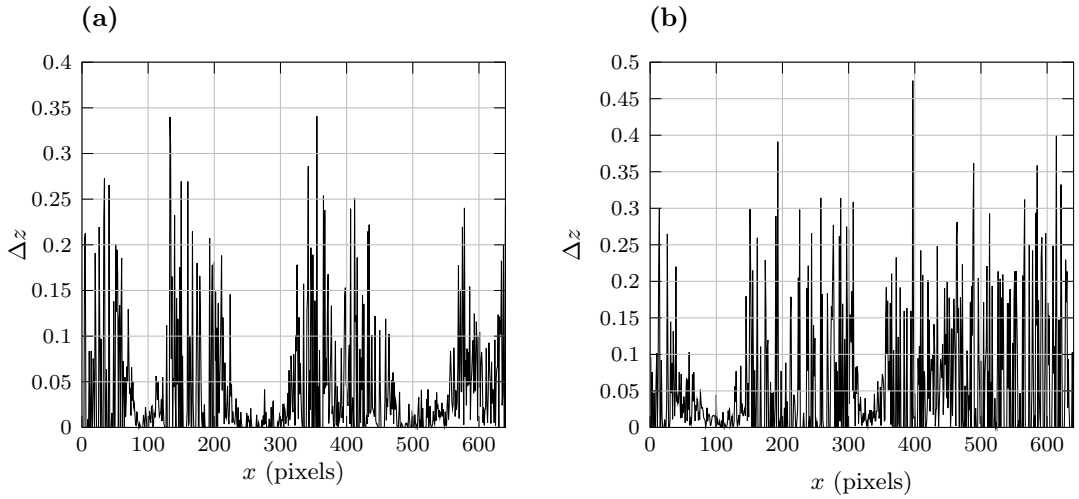


Figure 5.6: Error data extracted from rows 105 (a) and 280 (b). The data is clearly divided into regions of high and low amplitude fluctuations

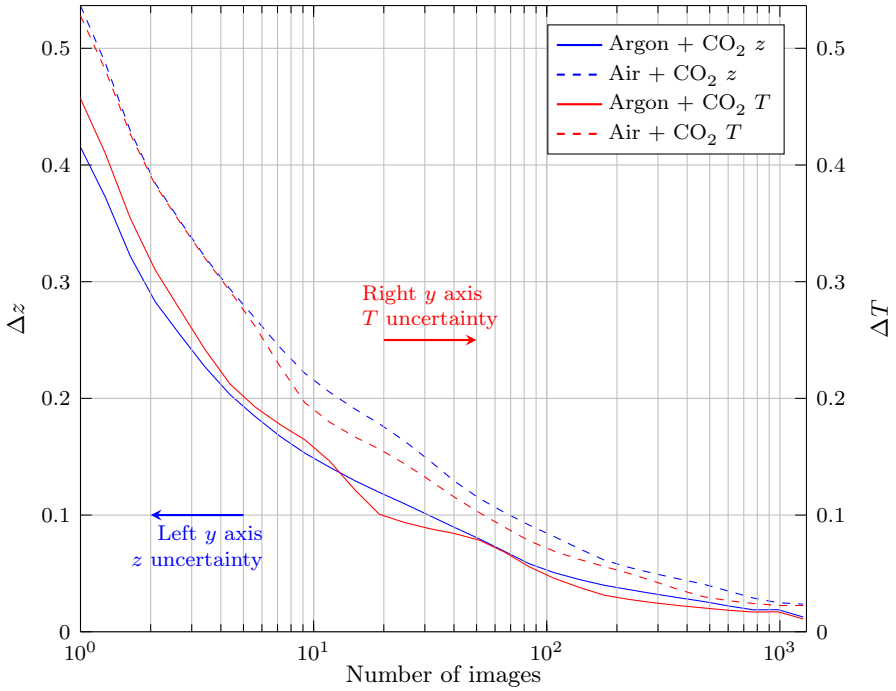


Figure 5.7: Variation of maximum relative error for mixture fraction and temperature with number of images. Blue lines represent mixture fraction, red lines represent temperature, solid lines represent an argon/CO_2 mixture, and dashed lines represent an air/CO_2 mixture

figures is drawn on a logarithmic scale.

The maximum uncertainty criterion (Figure 5.7) shows large values with almost 50 % uncertainty present for both mixture fraction and temperature when taking only one image, using both gas combinations. These large uncertainties were found to be isolated to a very small number of pixels, and as such do not adequately represent the entire interrogation region. However the trends shown in Figure 5.7 match trends obtained using the average uncertainty criterion, confirming the effect of averaging multiple images. The average uncertainty criterion (Figure 5.8) which is more representative of typical uncertainty across a whole image, shows significantly lower values. Nonetheless, it is worth noting that a 4 % uncertainty in mixture fraction from a single image is present when using air and CO_2 - more than twice the uncertainty compared to argon and CO_2. The temperature uncertainties scale similarly - this makes sense, as the temperature is calculated from the recovered mixture fraction. In both figures, it is evident that taking more images and averaging results reduces uncertainty. Averaging 10 pictures more than halves the uncertainty in all measurements, but only steady flow phenomena may be investigated

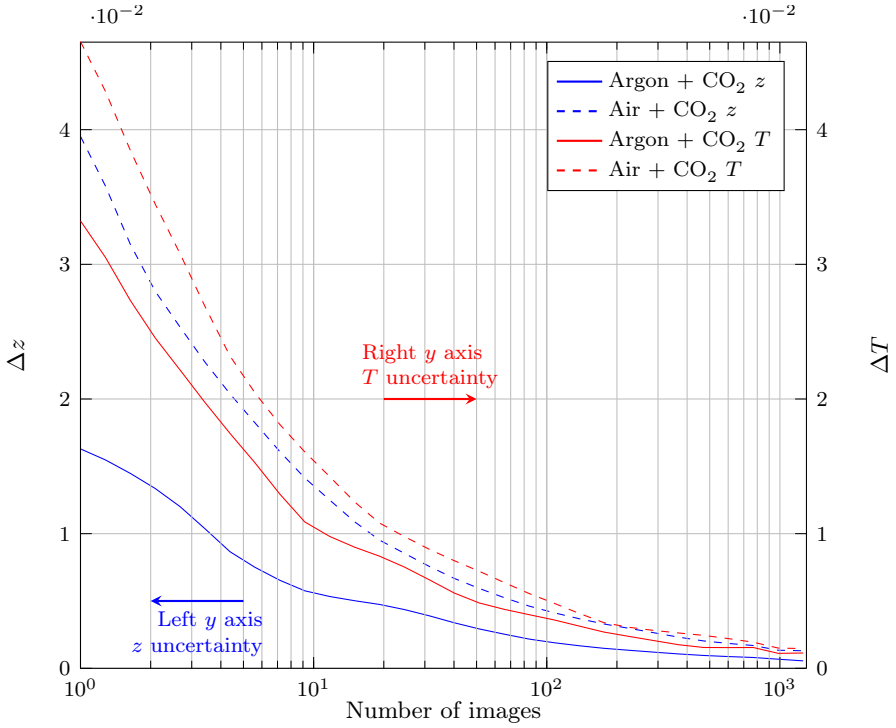


Figure 5.8: Variation of mean relative error for mixture fraction and temperature with number of images. Blue lines represent mixture fraction, red lines represent temperature, solid lines represent an argon/CO_2 mixture, and dashed lines represent an air/CO_2 mixture

if multiple pictures are to be averaged. High-speed flow measurements will inevitably rely on single shot results in order to accurately resolve unsteady flow phenomena.

This section investigated uncertainties that could be expected when using a more suitable gas for a high-speed flow facility, such as air. Simulations indicated a 4 % uncertainty in both mixture fraction and temperature - this seems reasonable, and is $\sim$ ten times better than the errors potentially incurred from using normal Rayleigh scattering [75]. As a result, significant cost savings can be realised, since test facilities do not need to be filled with an expensive gas like argon.

5.2 Demonstration of diagnostic

Having shown an air/CO_2 combination to be effective, PDRS was applied to a proof of concept experiment. The aim of this initial demonstration was as follows:

- To establish a working set-up that can be replicated in a more challenging environment

- To determine expected SNRs when applied to different configurations
- To reveal any potential limitations of the technique that need to be addressed

In this experiment, simultaneous composition and temperature measurements were extracted from a dual-jet mixed flow - a plan view schematic of the experimental layout is shown in Figure 5.9. A cold CO_2 jet was produced adjacent to a hot N_2 jet in static atmosphere. Both these jets were enclosed in a co-flow of cold N_2 - this was to prevent entrainment of dust particles into the experimental field of view. Mass flow controllers (Omega FMA-2609A and Omega FMA5520A) regulated the flow rate of each jet to 8 slpm. The hot flow was created by passing cold N_2 through an inline resistive heater (Omega AHP-5052). The voltage supplied to the heater was varied using an autotransformer in order to adjust the heat input to the gas. This layout consisting of two different gases of varying temperatures was intentionally chosen to create mixture fraction and temperature gradients that could be resolved using PDRS.

The flow was probed with a 650 mJ vertically-polarised laser pulse from a Continuum Powerlite Nd:YAG laser operating at its second harmonic wavelength of 532 nm. A Thorlabs Glan-Taylor Calcite polariser with an extinction ratio of 10^5:1 was used to 'clean' the laser beam by removing other polarisation components. This beam was formed into a 6 mm vertical sheet using a $f = 500$ mm cylindrical lens. Scattered 'polarised' and 'depolarised' light from the interaction region was acquired using two opposite-facing Princeton Instruments intensified charge-coupled device cameras (ICCD-512T and ICCD-576GRB), each fitted with 85 mm f/1.2 Mitakon Speedmaster lenses and orthogonally oriented polarisation filters (B+W XS-Pro Digital Käsemann). The laser sheet came to a focus at the centre of the jets and the cameras' field of view.

The polarisation filters were set to the correct angles to minimise leakage of polarised and depolarised light into the unintended camera. This was achieved by collecting signals from just the N_2 co-flow (with both jets turned off) for a range of filter angular positions. The average signal from 50 images was evaluated at each filter position and subsequently plotted - an example of

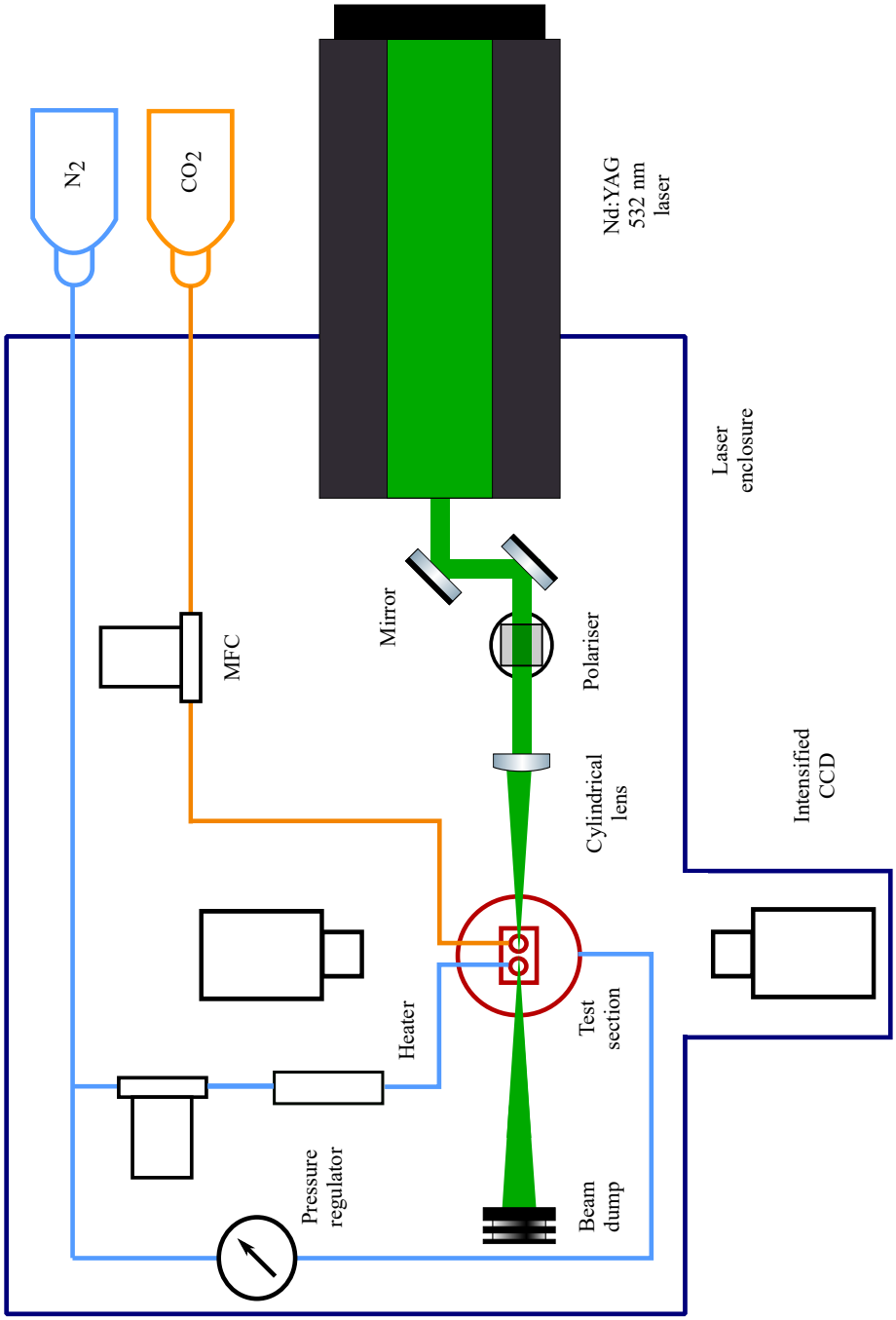


Figure 5.9: Plan view schematic of PDRS proof of concept experimental layout

this is shown in Figure 5.10.

Maxima indicated positions where the filter was aligned with the Rayleigh signal's main polarisation component (i.e. the 'polarised' component), while minima indicated the opposite. Thus, the camera used to image the 'polarised' Rayleigh component was set to the filter angular position that maximises signal, while that of the 'depolarised' Rayleigh component was set to the filter

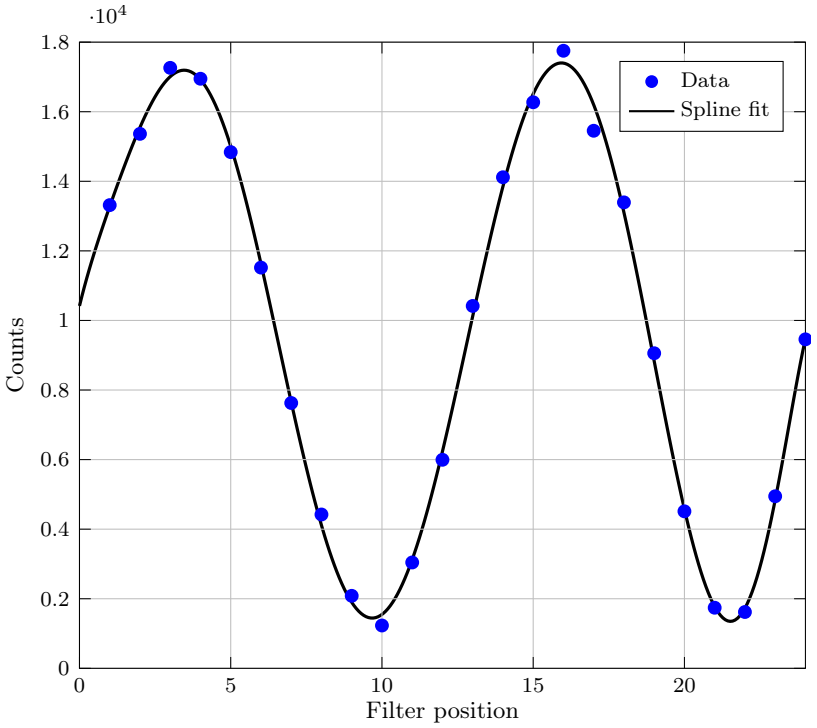


Figure 5.10: Variation in Rayleigh signal as a function of polarisation filter angular position. The separation between each position is 15°. Note that the signal does not go to zero, since N_2 has a non-zero r_p

angular position that minimises signal.

Mixture fraction evaluation during post-processing of results required pixel-by-pixel division of the polarised and depolarised images, each coming from separate cameras. In order to ensure accurate spatial mapping of pixels across both cameras, a double-sided grid pattern (similar to Figure 3.5) was placed in the field of view and imaged. Pixel coordinates of grid corners from both cameras were extracted using the open source MATLAB Camera Calibration Toolbox produced by California Institute of Technology [82]. These were used as control points in the *fitgeotrans* MATLAB function in order to determine a transformation that would accurately map depolarised signals onto polarised signals. Subsequently, this transformation was applied to all acquired depolarised signals in the *imwarp* MATLAB function to achieve spatial mapping.

After filter calibration and grid imaging, tests were initiated by turning on mass flow controllers to the desired flow rate. N_2 jet heating commenced by increasing the voltage set on the auto-transformer. A thermocouple was placed above the hot jet - temperatures were logged using a

PicoScope TC-08 thermocouple logger and monitored until steady-state conditions were achieved. Finally, the thermocouple was removed (to prevent overwhelming Mie scatter) and the laser aperture was opened, sending pulses towards the imaging area. Images were simultaneously acquired on both cameras using a gate of 500 ns at a frequency of 1 Hz.

A number of post-processing steps were applied to the images in order to extract mixture fraction and temperature. A summary of this procedure is presented in Figure 5.11. After image registration, shot-to-shot background signals were evaluated by averaging pixel values in image regions outside laser illumination. These background values were subtracted from all polarised and depolarised images, as shown in Figures 5.11 (a) and (b). Laser energy fluctuations and non-uniform sheet intensity profiles were corrected by dividing each polarised and depolarised image with a sheet correction map, shown in Figures 5.11 (c) and (d). This was obtained by separately averaging the left and right ten columns (where co-flow was present) from each *polarised* image to produce two vertical sheet profiles, and subsequently interpolating these profiles across the entire image. Note that using the depolarised signal to correct for sheet intensity fluctuations would lead to noisy results, since the depolarised signal in the co-flow was small in comparison. Next, strong scatter from stray particles was removed from images using the *regionfill* MATLAB function. This performed an inward interpolation of pixel values surrounding specified masked regions, demonstrated in Figures 5.11 (e) and (f). Finally, depolarised signals, shown in Figure 5.11 (g), were divided by polarised signals to produce r_p maps, shown in Figure 5.11 (h).

Since two separate cameras were used, each using different gain settings and image configurations, r_p maps obtained were proportional to actual r_p of the gases used. The average value in the pure N_2 region was used to normalise and convert these maps into values corresponding to the actual gas r_p. Next, a look-up curve was generated, from which r_p values were converted into a mixture fraction map, as shown in Figure 5.11 (i). Pixels exhibiting values larger than 1 or smaller than 0 due to noise were set to their respective limiting values. Final composition maps

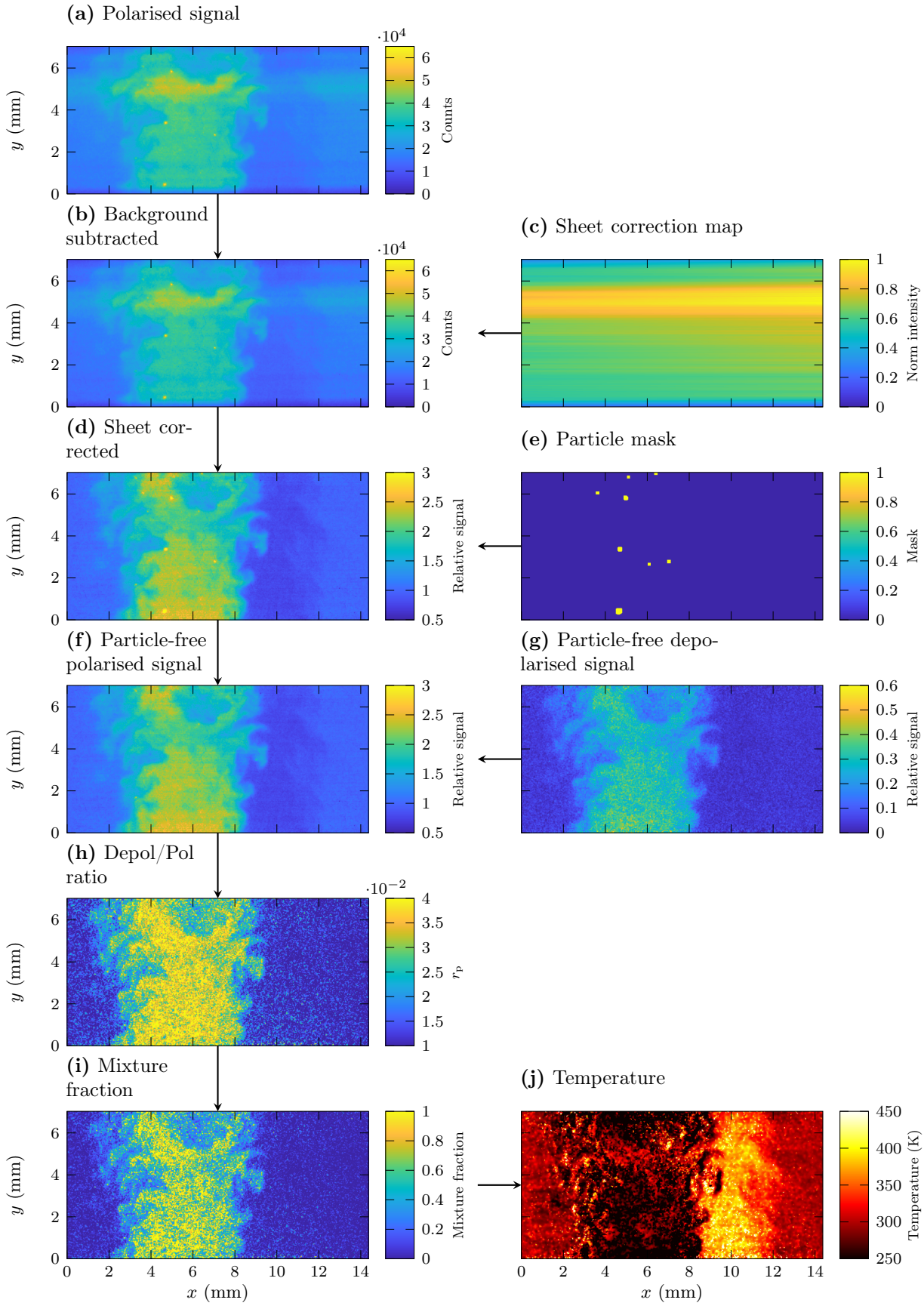


Figure 5.11: Post-processing procedure of extracting mixture fraction and temperature from PDRS

were then used to calculate the effective scattering cross-section at each pixel. This was then divided by the sheet-corrected polarised signals in order to produce a map that is proportional to temperature. Lastly, these maps were scaled to realistic temperatures using steady-state values measured on the thermocouple. This produced temperature maps as shown in Figure 5.11 (j).

Figure 5.12 shows the obtained results after post-processing. Here, each row represents a pair of single-shot composition and temperature maps. As before, mixture fraction values of 1 indicate pure CO_2 while values of 0 indicate pure N_2. A pixel size of 28 µm was achieved.

Mixture fraction maps show two distinct regions, i.e. regions occupied mostly by CO_2 as well as regions occupied by pure N_2. Radial composition gradients are evident in the CO_2 jet region, indicating entrainment of surrounding N_2 from the co-flow, as well as the hot jet. Temperature maps on the other hand indicate three distinct regions. The high temperatures of the hot N_2 are immediately noticeable - steady-state temperatures of 415 K were achieved at the base of the hot N_2 jet. Vertical temperature gradients are also evident, indicating a gradual loss of heat from the jet to the surroundings as it convects upwards. The temperature in the co-flow is moderate, and exhibits close agreement with room temperature - a mean temperature of 297 K was obtained across 128 images. CO_2 jet regions display the lowest temperatures, with a mean value of approximately 271 K across 128 images. The reason for such low temperatures here is the expansion of liquid CO_2 which undergoes a phase change to a gas at the nozzle.

Results from this preliminary investigation have shown that a working PDRS setup and processing procedure can be achieved. Single shot 2-D temperature and mixture fraction fields are obtainable as shown in Figure 5.12, in which the effect of gas mixing can be seen clearly. The minimum SNR in this configuration was 1.85 ± 0.08 - this was obtained in the depolarised signal at the region of the hot N_2 jet. The maximum SNR was 13.15 ± 3.64, attained in the polarised signal at the region of the CO_2 jet. These values are small when compared to SNRs achieved in other applications of PDRS [71, 72]. The effect of noise is evident from the lack of uniformity

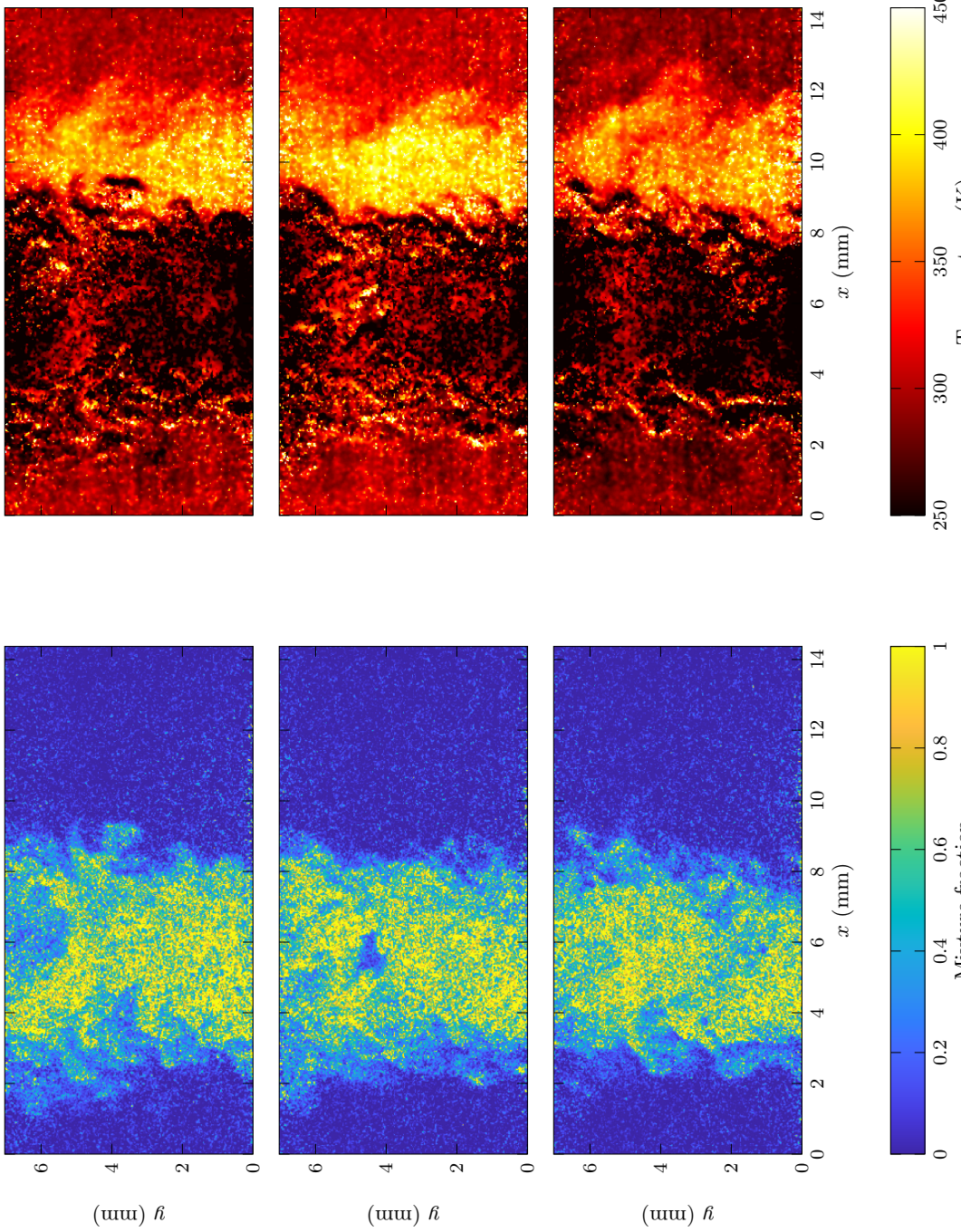


Figure 5.12: Single shot mixture fraction and temperature pairs from dual-flow experiment. A mixture fraction of 1 refers to CO_2, while a mixture fraction of 0 refers to N_2

in supposed uniform regions of reconstructed images, for example, bright spots in the mixture fraction maps in areas only containing N_2. Smoothing of images using Gaussian, or other, filters would remove these artefacts at the expense of a reduced spatial resolution. Future studies involving PDRS would benefit from steps taken towards improving SNR, so that reconstructed temperature and composition fields are more clean and exhibit minimal noise.

5.3 Summary

Results from this chapter have highlighted PDRS as a useful diagnostic tool; a proof of principle experiment highlighted its ability to measure composition and temperature simultaneously in a gaseous mixture. A mean SNR of 7.5 was achievable, leading to good quality results in a bench-top configuration.

Based on the proof of principle experiment, a feasibility study was conducted to determine the applicability of PDRS to a local hypersonic facility heavily used in transpiration cooling investigations, the Oxford HDT. This study, presented in Appendix 9.1, revealed that the application of this technique to the Oxford HDT (or most hypersonic facilities for that matter) would be unsuitable under current resources, primarily due to low predicted SNR. Given the success in implementing PDRS on a bench-top experiment, this configuration was replicated in an alternate transpiration cooling investigation using the technique, in order to guarantee success. The following chapter discusses a bench-top application of PDRS, where the technique is used to investigate the *internal* cooling mechanisms of porous materials during transpiration cooling.

Chapter 6

Internal Heat Transfer Modelling of Transpiring Porous Media

In the previous chapter, PDRS was demonstrated as a powerful multiscalar diagnostic for mixing flows. While it was established that applying this diagnostic to a high-speed facility using current resources was unfeasible, bench-top experiments were shown to produce reliable results. Given this, PDRS was instead applied to bench-top based characterisation experiments that would aid in furthering high-speed flow research. Specifically, this diagnostic was chosen to investigate the internal cooling of porous materials used in transpiration cooling for hypersonic vehicles. The motivation for this investigation follows.

6.1 Motivation

The internal heat transfer characteristics of a 1-D transpiring porous medium can be modelled by solving the coupled partial differential energy equations for both solid and fluid phases. An important parameter that governs the efficiency of heat transfer between solid and fluid phases within the porous medium is the volumetric heat transfer coefficient, h_{v} [113]. High h_{v} values lead to more efficient heat transfer between coolant and porous solid, which promotes an equalisation of their temperatures along the depth of the material. In a transpiration cooling system, the maximum performance is achieved when the coolant leaves the porous wall at the surface temperature. Thus, the impact of transpiration cooling on a vehicle can be optimised by maximising the value of h_{v} in targeted areas of high heat load.

Porous characteristics of a particular material influence h_v, since these properties define the characteristic solid-fluid contact length for heat exchange. Hence, the choice of porous material can have a profound effect on the performance of a transpiration cooling system. Besides this, the flow properties of the coolant used, such as its mass flux, also affect h_v - larger mass fluxes lead to higher h_v values. In this regard, the performance of a transpiration cooling system can be maximised by using high mass fluxes of coolant. However, there is an upper limit to mass flux which depends on the load-carrying capacity of the hypersonic vehicle - ideally, optimal cooling performance should be achieved with minimal coolant.

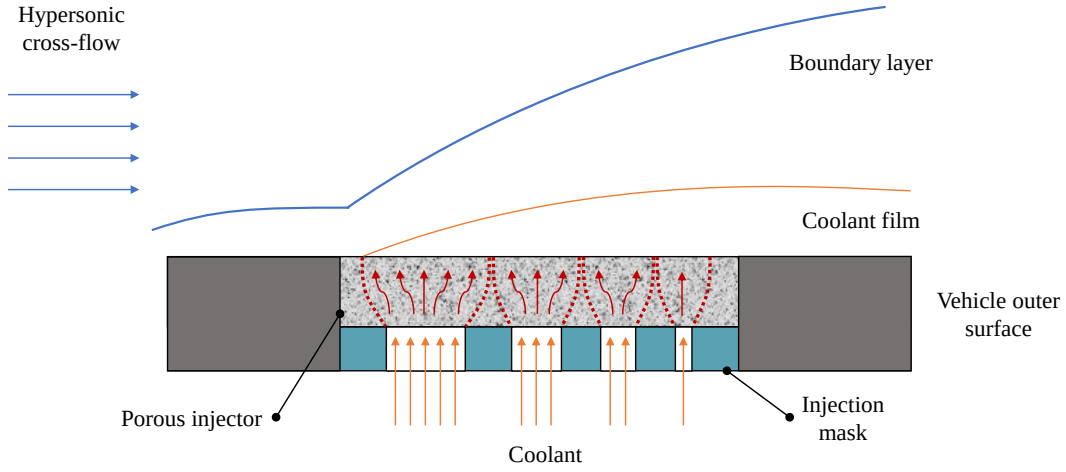


Figure 6.1: Schematic of non-uniform coolant injection applied to a hypersonic vehicle

In the past, complete systems-level analyses of the use of transpiration cooling have estimated h_v using correlations in the literature [114, 115, 116]. However, these correlations have been formulated based on an ablation-style thermal protection system (TPS) which is characteristically different to transpiration cooling [113]. It is apparent that a framework to measure this parameter for candidate porous materials and flow conditions would be beneficial in understanding the performance of a transpiration cooling system and designing the ideal solution. Prediction of this performance becomes challenging *ab initio* when the porous medium has spatially-varying properties. For example, internal cooling channels could be used to create preferential coolant

flow paths to direct more coolant to areas experiencing higher heat fluxes, as shown in Figure 6.1. However, this would introduce three-dimensional internal temperature and pressure fields, leading to varying degrees of thermal non-equilibrium between solid and fluid phase within the porous wall. To improve understanding of spatially inhomogenous transpiration cooling systems, spatially resolved measurements of gas and solid temperatures are necessary when characterising the internal cooling performance of a porous material.

To tackle this challenge, an experimental framework was developed using two simultaneous planar optical diagnostic techniques to probe the transpiring gas and the porous medium surface, in order to characterise its internal heat transfer mechanisms. The two diagnostics used were PDRS and IR thermography - details of how this was implemented are presented in Chapter 7. This framework provides 2-D measurements for investigating spatially inhomogenous porous materials, however, in the first instance, it was used to extract h_v for uniformly porous samples. Experimental results are compared to a 1-D numerical scheme in order to achieve this, and its working principles and implementation are described in this chapter.

6.2 Theory of heat transport within porous media

A semi-analytical treatment of internal heat transfer within porous media is presented here, based on the work of Hermann et al. [117]. Heat transport in porous media for both solid and fluid phases is governed by the porosity-dependent energy equations. This is given in 1-D form for a solid by Equation (6.1)

$$\underbrace{(1-\phi)\,\rho_\mathrm{s}\,c_{p,\mathrm{s}}\,\frac{\partial \hat{T}_\mathrm{s}}{\partial t}}_{\text{Heat storage (solid)}} = \underbrace{k_\mathrm{s}\,(1-\phi)\,\frac{\partial^2 \hat{T}_\mathrm{s}}{\partial x^2}}_{\text{Conduction (solid)}} + \underbrace{h_\mathrm{v}\left(\hat{T}_\mathrm{f}-\hat{T}_\mathrm{s}\right)}_{\text{Internal convection}} + \underbrace{a\left(\hat{T}_\mathrm{s}-\hat{T}_\mathrm{w}\right)}_{\text{Heat loss}} \tag{6.1}$$

and for a fluid by Equation (6.2).

$$\underbrace{\phi\,\rho_{\mathrm{f}}\,c_{p,\mathrm{f}}\,\frac{\partial \hat{T}_{\mathrm{f}}}{\partial t}}_{\text{Heat storage (fluid)}} \;+\; \underbrace{\rho_{\mathrm{f}}\,c_{p,\mathrm{f}}\,u_{\mathrm{m}}\,\frac{\partial \hat{T}_{\mathrm{f}}}{\partial x}}_{\text{Advection}} \;=\; \underbrace{h_{\mathrm{v}}\left(\hat{T}_{\mathrm{s}}-\hat{T}_{\mathrm{f}}\right)}_{\text{Internal convection}} \tag{6.2}$$

In Equations (6.1) and (6.2), ϕ is the material porosity, ρ is density, c_p is specific heat capacity, t is time, $\hat{T}$ is the difference between absolute and initial temperatures, T and T_0 respectively, k is thermal conductivity, x is spatial location through the depth of the material, a is a heat loss parameter, u_{m} is the bulk fluid velocity, and subscripts s, f and w refer to solid, fluid and wall, respectively. Note that the heat loss term in Equation (6.1) is included to account for the inevitable lateral heat conduction from the porous solid to its mount without extending the analysis to 2-D [117, 118]. The parameter a resembles an overall heat transfer coefficient that encapsulates thermal conduction and contact resistances between the porous sample, the bonding adhesive and its mount.

Through Laplace transforms, Equations (6.1) and (6.2) can be reduced to

$$s\,(1-\phi)\,\rho_{\mathrm{s}}\,c_{p,\mathrm{s}}\,\tilde{T}_{\mathrm{s}} \;=\; k_{\mathrm{s}}\,(1-\phi)\,\frac{\partial^2 \tilde{T}_{\mathrm{s}}}{\partial x^2} \;+\; h_{\mathrm{v}}\left(\tilde{T}_{\mathrm{f}}-\tilde{T}_{\mathrm{s}}\right) \;+\; a\left(\tilde{T}_{\mathrm{s}}-\tilde{T}_{\mathrm{w}}\right) \tag{6.3}$$

and

$$s\,\phi\,\rho_{\mathrm{f}}\,c_{p,\mathrm{f}}\,\tilde{T}_{\mathrm{f}} \;+\; \rho_{\mathrm{f}}\,c_{p,\mathrm{f}}\,u_{\mathrm{m}}\,\frac{\partial \tilde{T}_{\mathrm{f}}}{\partial x} \;=\; h_{\mathrm{v}}\left(\tilde{T}_{\mathrm{s}}-\tilde{T}_{\mathrm{f}}\right) \tag{6.4}$$

where s is the Laplace variable, and $\tilde{T}_{\mathrm{s}}$, $\tilde{T}_{\mathrm{f}}$ and $\tilde{T}_{\mathrm{w}}$ are the Laplace-transformed $\hat{T}_{\mathrm{s}}$, $\hat{T}_{\mathrm{f}}$ and $\hat{T}_{\mathrm{w}}$ respectively. By differentiating Equation (6.3) with respect to x and substituting this into Equation (6.4), a non-homogenous linear third order differential equation (DE) is obtained

$$C_3\frac{\partial^3 \tilde{T}_{\mathrm{s}}}{\partial x^3} \;+\; C_2\frac{\partial^2 \tilde{T}_{\mathrm{s}}}{\partial x^2} \;+\; C_1\frac{\partial \tilde{T}_{\mathrm{s}}}{\partial x} \;+\; C_0\tilde{T}_{\mathrm{s}} \;= P_1 \tag{6.5}$$

where coefficients C_{0-3} and P_1 are as follows.

$$C_3 = \frac{u_\mathrm{m}}{\phi}\frac{k_\mathrm{s}}{\rho_\mathrm{s}\, c_{p,\mathrm{s}}} \tag{6.6}$$

$$C_2 = \frac{k_\mathrm{s}}{\rho_\mathrm{s}\, c_{p,\mathrm{s}}}\left(s + \frac{h_\mathrm{v}}{\phi\, \rho_\mathrm{f}\, c_{p,\mathrm{f}}}\right) \tag{6.7}$$

$$C_1 = \frac{u_\mathrm{m}}{\phi}\left(\frac{a - h_\mathrm{v}}{(1-\phi)\, \rho_\mathrm{s}\, c_{p,\mathrm{s}}} - s\right) \tag{6.8}$$

$$C_0 = \frac{h_\mathrm{v}}{\phi\, \rho_\mathrm{f}\, c_{p,\mathrm{f}}}\frac{h_\mathrm{v}}{(1-\phi)\, \rho_\mathrm{s}\, c_{p,\mathrm{s}}} - \left(s + \frac{h_\mathrm{v}}{\phi\, \rho_\mathrm{f}\, c_{p,\mathrm{f}}}\right)\left(s - \frac{a - h_\mathrm{v}}{(1-\phi)\, \rho_\mathrm{s}\, c_{p,\mathrm{s}}}\right) \tag{6.9}$$

$$P_1 = \frac{a}{(1-\phi)\, \rho_\mathrm{s}\, c_{p,\mathrm{s}}}\left(s + \frac{h_\mathrm{v}}{\phi\, \rho_\mathrm{f}\, c_{p,\mathrm{f}}}\right)\tilde{T}_\mathrm{w} \tag{6.10}$$

The solution to Equation (6.5) is found by first solving the DE's auxiliary equation to obtain three eigenvalues, λ_{1-3}. The combined general and particular solution for $\tilde{T}_\mathrm{s}$ and $\tilde{T}_\mathrm{f}$ is then given by

$$\tilde{T}_\mathrm{s} = \sum_{i=1}^{3} A_i\, \exp\left(\lambda_i\, x\right) + \frac{P_1}{C_0} \tag{6.11}$$

$$\tilde{T}_\mathrm{f} = \sum_{i=1}^{3} A_i\, B_i\, \exp\left(\lambda_i\, x\right) + \frac{P_1}{C_0}\left(\frac{s(1-\phi)\rho_\mathrm{s}\, c_{p,\mathrm{s}}}{h_\mathrm{v}} + 1 - \frac{a}{h_\mathrm{v}}\right) + \frac{a}{h_\mathrm{v}}\,\tilde{T}_\mathrm{w} \tag{6.12}$$

where A_{1-3} are to be determined from boundary conditions, and B_i are given by

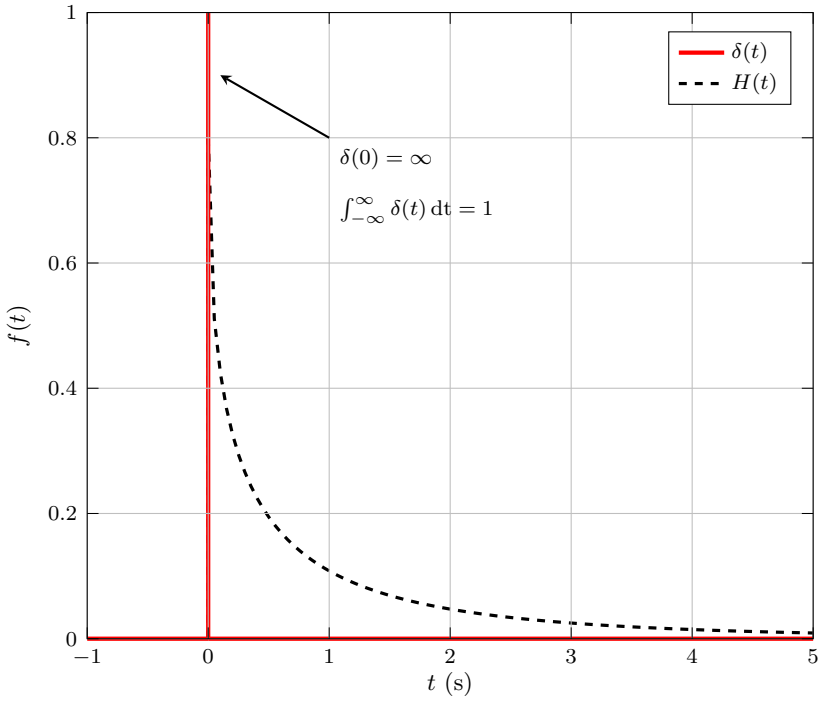


Figure 6.2: Unit impulse and example impulse response function of a dynamic LTI system

$$B_i = \left(\frac{s(1-\phi)\rho_\mathrm{s}\, c_{p,\mathrm{s}}}{h_\mathrm{v}} - \frac{k_\mathrm{s}(1-\phi)}{h_\mathrm{v}} \lambda_i^2 + 1 - \frac{a}{h_\mathrm{v}} \right) \tag{6.13}$$

Equations (6.11) and (6.12) can be inverted back into the time domain using a numerical scheme. In this work, a numerical inversion scheme proposed by Gaver and Stehfest is used [119, 120] - details of its implementation are provided in Section 6.5.2.

6.3 Impulse response convolution method

Equations (6.1) and (6.2) describe a linear time-invariant (LTI) dynamic system. Linearity implies that the response of the system to a combination of multiple different inputs, is simply the sum of the system's individual responses when subjected to each input separately. Time-invariance implies that a shift in time to the system input results in the exact system response, shifted in time identically. These properties allow the use of the impulse response convolution method to predict a system's response to any input - its working principles are summarised as follows.

The impulse response function, $H(t)$, is a transient reaction of a dynamic system when it is subjected to a unit impulse. Mathematically, the unit impulse is represented by the Dirac delta function, $\delta(t)$ - it takes on an amplitude of ∞ at $t = 0$ and an integral of 1 over all t. Figure 6.2 illustrates both the unit impulse and an example $H(t)$ of a system. The sifting characteristic of $\delta(t)$ allows considering an arbitrary system input, $x(t)$, as a sum of continuous time-delayed $\delta(t-\tau)$ applied to the system, each scaled by $x(\tau)$ - this is simply the convolution of $x(t)$ with $\delta(t)$. Since $H(t)$ is the response of the system to $\delta(t)$, linearity and time-invariance properties dictate that the system's response to $x(t)$ is similarly a sum of continuous time-delayed $H(t-\tau)$, each scaled by $x(\tau)$. Thus, the impulse response convolution method simply states that the response of a dynamic LTI system, $y(t)$, to any arbitrary input, $x(t)$, can be obtained by convolving the system's $H(t)$ with $x(t)$.

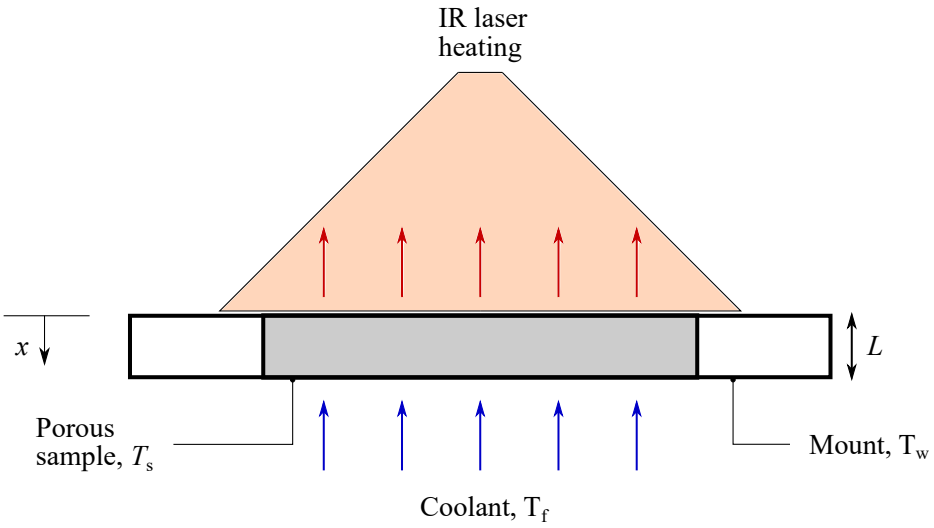


Figure 6.3: Surface heat flux via laser heating

Applying this method to Equations (6.1) and (6.2), the transient profiles of $\hat{T}_s(x, t)$ and $\hat{T}_f(x, t)$ can be modelled at any spatial location, as long as the transient heat input to the system and its associated $H(t)$ are known accurately [121]. Thus, the system's $H(t)$ for an experiment-specific transient heat input must first be modelled. The most common method of introducing heat to this system is via a heat flux to the top surface of the porous material (i.e. $x = 0$) as shown in Figure 6.3, simulating conditions experienced during re-entry. This is typically achieved via

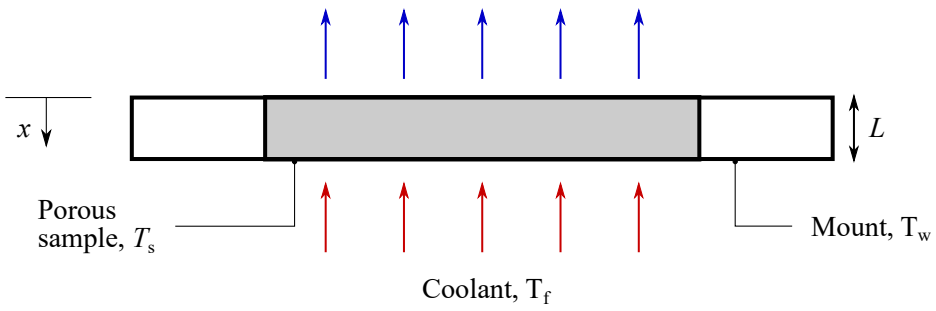


Figure 6.4: Coolant gas heating

IR laser heating, as was performed by Hermann et al. [117]. Since a suitable IR laser was not available, the experimental framework discussed in Chapter 7 mainly introduces heat to the system via gas heating as shown in Figure 6.4. Note that this is opposite to what is experienced during hypersonic flight - the 'coolant' in this case heats up the porous solid. For a mount with high thermal capacitance, $\tilde{T}_w = 0$ at all times, simplifying Equations (6.11) and (6.12). The following boundary conditions apply for a system that experiences an impulse fluid temperature rise at the back surface (i.e. $x = L$, where L is the thickness of the porous material) of the porous medium.

$$x = L, \qquad \underbrace{\hat{T}_f(t) = \delta(t)}_{\text{Temperature impulse}} \tag{6.14}$$

$$x = L, \qquad \underbrace{\frac{\partial \hat{T}_s(t)}{\partial x} = 0}_{\text{Adiabatic surface}} \tag{6.15}$$

$$x = 0, \qquad \underbrace{\frac{\partial \hat{T}_s(t)}{\partial x} = 0}_{\text{Adiabatic surface}} \tag{6.16}$$

The use of these boundary conditions leads to a linear system of equations that can be solved to yield coefficients A_{1-3}. These equations can be expressed in matrix form as follows

$$\begin{pmatrix} B_1 \exp(\lambda_1 L) & B_2 \exp(\lambda_2 L) & B_3 \exp(\lambda_3 L) \\ \lambda_1 \exp(\lambda_1 L) & \lambda_2 \exp(\lambda_2 L) & \lambda_3 \exp(\lambda_3 L) \\ \lambda_1 & \lambda_2 & \lambda_3 \end{pmatrix} \begin{pmatrix} A_1 \\ A_2 \\ A_3 \end{pmatrix} = \begin{pmatrix} 1 \\ 0 \\ 0 \end{pmatrix} \tag{6.17}$$

Substituting these coefficients into Equations (6.11) and (6.12) and inverting back into the time domain yields the zero input[1] impulse response functions, $H_\mathrm{f}(x\,,\,t)$ and $H_\mathrm{s}(x\,,\,t)$, for both solid and fluid phases, respectively. The transient responses $\hat{T}_\mathrm{f}(x\,,\,t)$ and $\hat{T}_\mathrm{s}(x\,,\,t)$ for an arbitrary gas temperature input, $\hat{T}_\mathrm{f}(x = L\,,\,t)$, can then be obtained via the convolution operations shown in Equations (6.18) and (6.19).

$$\hat{T}_\mathrm{f}(x\,,\,t) = \int_0^t H_\mathrm{f}(x\,,\,t-\tau) \cdot \hat{T}_\mathrm{f}(x = L\,,\,\tau)\,\mathrm{d}\tau \tag{6.18}$$

$$\hat{T}_\mathrm{s}(x\,,\,t) = \int_0^t H_\mathrm{s}(x\,,\,t-\tau) \cdot \hat{T}_\mathrm{f}(x = L\,,\,\tau)\,\mathrm{d}\tau \tag{6.19}$$

If $\tilde{T}_\mathrm{w} \neq 0$, as is the case in this work, due to the hot inlet gas heating the plenum walls, an additional heat input to the system is present. Exploiting the linearity property, the effect of this added heat input can be modelled separately using an additional impulse response convolution operation, and subsequently added to $\hat{T}_\mathrm{f}(x\,,\,t)$ and $\hat{T}_\mathrm{s}(x\,,\,t)$ obtained from Equations (6.18) and (6.19). The responses to this separate heat input are called the zero state[2] impulse response functions $G_\mathrm{f}(x\,,\,t)$ and $G_\mathrm{s}(x\,,\,t)$. They can be obtained using the same steps described in this section, but this time including the omitted particular solution terms in Equations (6.11) and (6.12), setting $\tilde{T}_\mathrm{w} = 1$ (impulse) and replacing boundary condition (6.14) as follows

[1] Zero input refers to a lack of a forcing term in the DE, i.e. the right hand side of the DE is zero. The response of the system is purely due to specified initial conditions, which is an impulse in this case

[2] Zero state refers to initial conditions being set to zero. The response of the system is purely due to the forcing term in the DE, which is an impulse in this case

$$x = L, \qquad \underbrace{\hat{T}_{\mathrm{f}}(t) = 0}_{\text{Temperature impulse}} \tag{6.20}$$

Additional transient responses from this heat input can be obtained, as before, using the convolution operations of Equations (6.18) and (6.19), replacing H for G, and changing the heat input from $\hat{T}_{\mathrm{f}}(x = L\,,\,\tau)$ to $\hat{T}_{\mathrm{w}}(\tau)$. Total $\hat{T}_{\mathrm{f}}(x\,,\,t)$ and $\hat{T}_{\mathrm{s}}(x\,,\,t)$ obtained from the sum of zero input and zero state solutions thus model how surface and gas temperatures change for arbitrary heat inputs, porous solid characteristics and fluid properties.

6.4 Solid-fluid system behaviour

This section aims to highlight the phenomenological behaviour of the coupled fluid-solid heat transport system using the impulse response convolution method described in Section 6.3. The analysis presented here is theoretical, and is intended to highlight the expected trends of temperature change inside a porous structure using gas heating as the heat input. Temperature constraints of the system are explored, which aids in ensuring validity of experimental results. In addition, this analysis demonstrates how the system's response changes to the use of different input parameters - of particular interest is how h_{v}, a, x and u_{m} cause a change in the transient temperature profiles of both solid and fluid. All trends presented in this section were obtained using the solid properties of a carbon-fibre-reinforced carbon matrix composite (details of which can be found in Section 7.6.3), and fluid properties of N_2. The gas heat input used to induce a system response was experimentally measured - temperatures are held constant for the first 100 s for calibration purposes, described in more detail in Chapter 7. Unless specified, default values of parameters used are as follows: $h_{\mathrm{v}} = 2.5 \times 10^4$ $\mathrm{Wm^{-3}K^{-1}}$, $a = -7 \times 10^3$ $\mathrm{Wm^{-3}K^{-1}}$ and $\dot{m}_A = 0.40$ $\mathrm{kgs^{-1}m^{-2}}$.

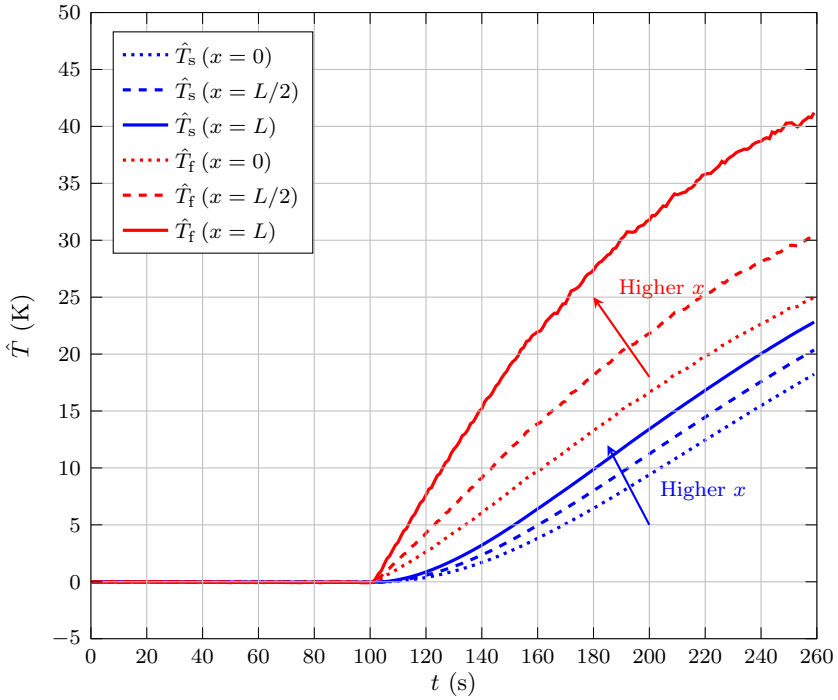


Figure 6.5: Transient solid and fluid temperature profiles across thickness of solid. Blue lines indicate $\hat{T}_s$ and red lines indicate $\hat{T}_f$. A change from dotted to solid lines indicate an increase in x. Note how temperatures differences are larger, and more thermal non-equilibrium between solid and fluid is seen at larger x, i.e. closer to the heat input

In general, a gas heat input system as shown in Figure 6.4 behaves as follows. Hot gas first enters the initially cold porous solid from the bottom surface. This initiates heat exchange, causing the temperature of the solid on the bottom surface to rise in response. As a transfer of energy between phases has taken place, the gas temperature starts to drop as it convects through the porous structure, gradually losing heat to the solid. This drop in gas temperature reduces the temperature difference between solid and fluid going from the bottom to top surfaces. As this fluid-solid temperature difference provides the driving force of heat transfer between phases, less heat exchange takes place at the top surface compared to the bottom surface. In other words, the temperature rise induced in the solid top surface is smaller than that of the bottom surface. A temperature gradient is thus established across the thickness of the solid structure - this creates an upward conduction heat flux. The net effect of both fluid-solid heat exchange and solid conduction is an increase in thermal equilibrium between phases going from the bottom to top surfaces. These trends are illustrated in Figure 6.5.

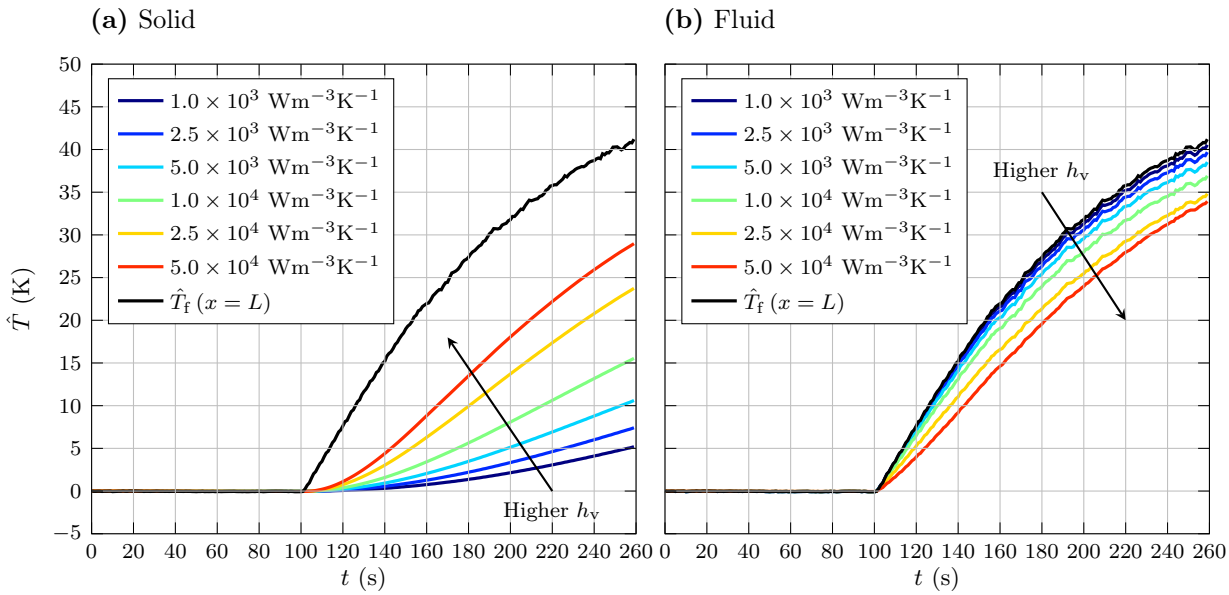


Figure 6.6: System responses at $(x = 0)$ to an experimentally measured gas heating input $\hat{T}_\mathrm{f}\,(x = L)$ for varying values of h_v. Note how an increase in h_v leads to an increase in solid heating rates and a decrease in fluid heating rates

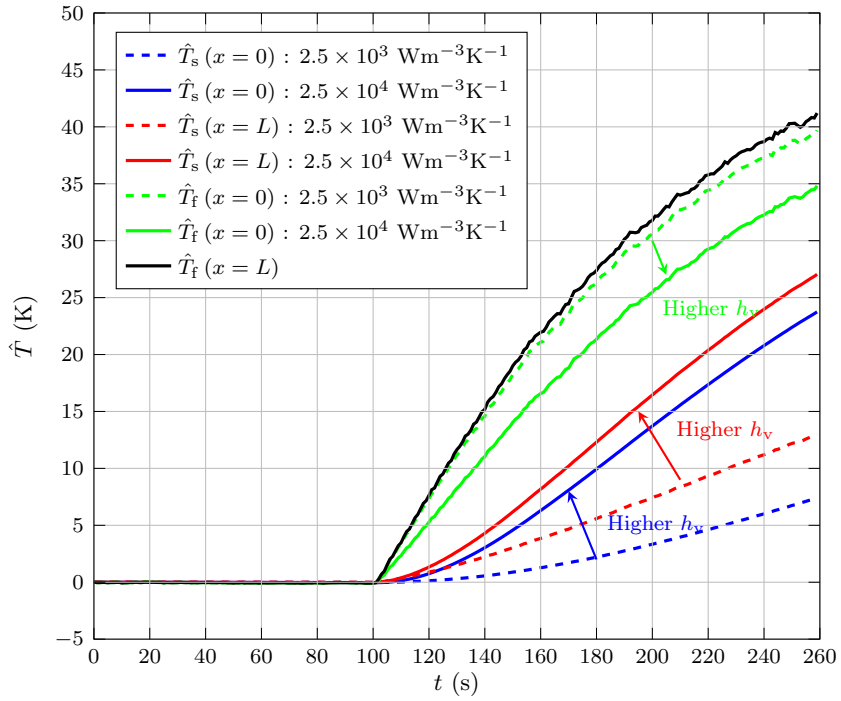


Figure 6.7: System responses across thickness of solid to an experimentally measured gas heating input $\hat{T}_\mathrm{f}\,(x = L)$ for two values of h_v. Blue lines indicate $\hat{T}_\mathrm{s}\,(x = 0)$, red lines indicate $\hat{T}_\mathrm{s}\,(x = L)$ and green lines indicate $\hat{T}_\mathrm{f}\,(x = 0)$. A change from dashed to solid lines indicates an increase in h_v. Note how an increase in h_v promotes equalisation of solid and fluid temperatures at any x

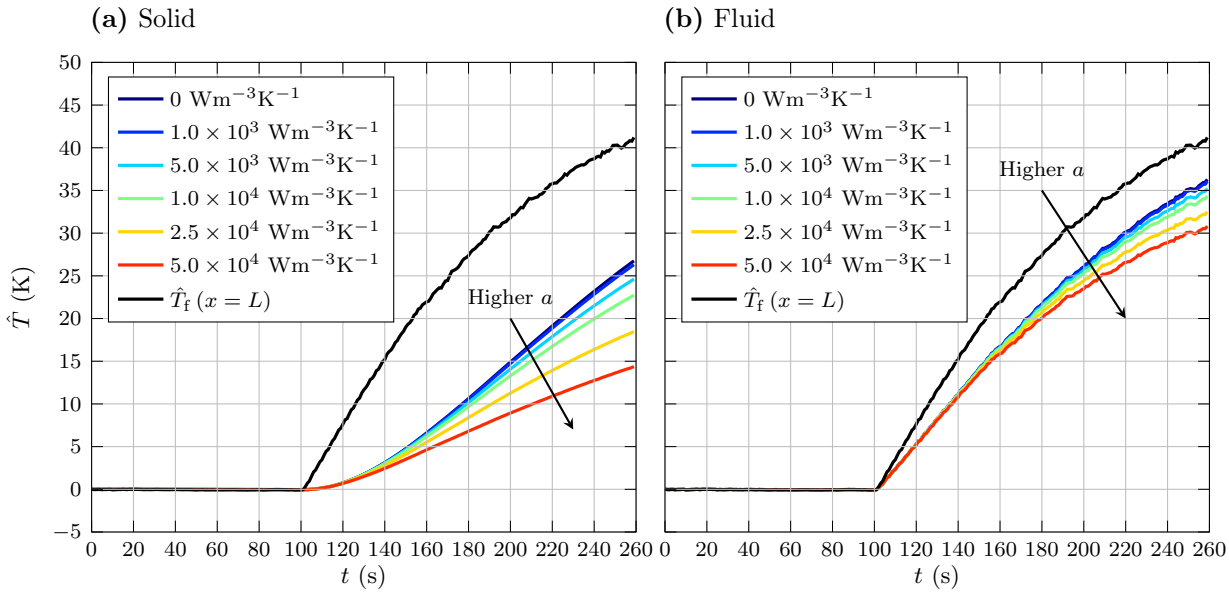


Figure 6.8: System responses at $(x = 0)$ to an experimentally measured gas heating input $\hat{T}_\mathrm{f}(x = L)$ for varying absolute values of a (negative sign omitted). Note how an increase in a leads to a decrease in both solid and fluid heating rates

Figures 6.6 and 6.7 show the effect of changing h_v on both the solid and fluid transient responses. As previously described, h_v dictates the efficiency of heat transfer between phases. Larger h_v values lead to higher rates of heat transfer from fluid to solid. As a result, solid heating rates become larger as h_v increases - this is evident from Figure 6.6 (a). Similarly, enhanced heat transfer leads to more loss of energy from the fluid, thus gas heating rates decrease with increasing h_v as seen in Figure 6.6 (b). The combined effect of both these trends is an increase in thermal equilibrium between solid and fluid at every spatial location. This is highlighted in Figure 6.7 - as h_v is increased, $\hat{T}_\mathrm{s}(x = L)$ moves closer towards $\hat{T}_\mathrm{f}(x = L)$, while $\hat{T}_\mathrm{s}(x = 0)$ moves closer towards $\hat{T}_\mathrm{f}(x = 0)$.

Figure 6.7 also highlights the spatial thermal constraints of the system. At any time t:

- $\hat{T}_\mathrm{f}(x = L)$ is the highest temperature of the system, as it is the source of heat input
- $\hat{T}_\mathrm{s}(x = 0)$ is the lowest temperature of the system, as it receives heat from the gas at the point of smallest temperature difference between solid and fluid

Both $\hat{T}_\mathrm{f}(x = 0)$ and $\hat{T}_\mathrm{s}(x = L)$ are thus constrained by $\hat{T}_\mathrm{f}(x = L)$ and $\hat{T}_\mathrm{s}(x = 0)$. The ratio of

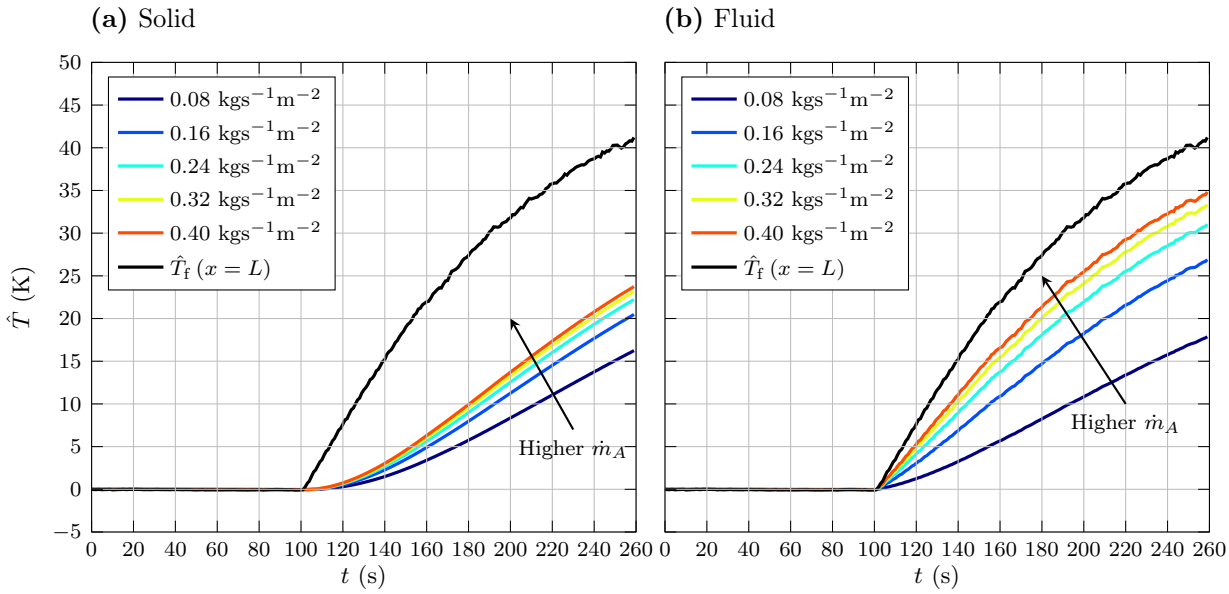


Figure 6.9: System responses at $(x = 0)$ to an experimentally measured gas heating input $\hat{T}_\mathrm{f}(x = L)$ for varying values of mass flux. Note how an increase in $\dot{m}_A$ leads to an increase in both solid surface temperature and fluid exit temperature

$h_\mathrm{v}L^2$ to $k_\mathrm{s}(1-\phi)$ dictates which of these end up larger than the other - a larger ratio leads to $\hat{T}_\mathrm{s}(x = L)$ being larger, while smaller ratios lead to $\hat{T}_\mathrm{f}(x = 0)$ being larger[3].

Figure 6.8 illustrates the effect of changing a on both the solid and fluid transient responses. Note that a takes negative values when implemented in the numerical scheme based on how it is incorporated into Equation (6.1) - the negative sign is omitted in Figure 6.8. Larger magnitudes of a imply more efficient loss of heat from the system to its mount. This is reflected as a drop in both the solid and fluid heating rates. The magnitude of a is linked to k_s of the porous solid, as it incorporates lateral heat conduction effects. As such, materials with high k_s tend to exhibit large magnitudes of a as well.

Figure 6.9 demonstrates the effect of changing $\dot{m}_A$ on both the solid and fluid transient responses. This can either be via an increase in magnitude of u_m or ρ_f. Note that u_m takes negative values when implemented in the numerical scheme based on how the coordinate axis of the system is defined, but the negative sign is omitted in Figure 6.9 for clarity. In practice, an increase in $\dot{m}_A$

[3]The ratio of $h_\mathrm{v}L^2$ to $k_\mathrm{s}(1-\phi)$ compares the rate of internal solid-fluid convection, h_v, to the rate of conduction through the solid, $k_\mathrm{s}(1-\phi)/L^2$. These terms were obtained from the respective coefficients of Equation (6.1)

should also enhance h_{v}, but since this analysis holds h_{v} at a fixed value, this effect will be ignored, in order to highlight trends in the behaviour of the system. Larger $\dot{m}_A$ causes a reduction in the fluid residence time within the porous structure, due to larger convective speeds. This translates to higher fluid exit temperatures as seen in Figure 6.9 (b), as there is now less time for heat exchange between phases. In general, this makes the fluid-solid temperature difference increase across the solid, thus leading to a rise in solid heating rates as well, as shown in Figure 6.9 (a).

6.5 Numerical scheme implementation

Previous sections have highlighted how the coupled solid-fluid porous system behaves and how its transient response to a measured input may be modelled. Prediction of the system response is conditional on successfully obtaining the system's impulse response function - to do this, accurate knowledge of all parameters used in Equations (6.1) and (6.2) is required. In the context of the experimental framework, most of these are set by the user and are known, or can be measured. The only unknown in this system is h_{v}. Thus, a value for this parameter can be extracted by varying it within the impulse response convolution method until a match between modelled and measured temperature transients is obtained. Figure 6.10 presents an overview of the numerical scheme that performs this iterative procedure.

In practice, this is achieved by first subjecting a porous system to a measured hot gas transient input $\hat{T}_{\mathrm{f}}(x = L, t)$ and recording any other transient temperature change of the system (e.g. $\hat{T}_{\mathrm{f}}(x = 0, t)$ or $\hat{T}_{\mathrm{s}}(x = 0, t)$ or $\hat{T}_{\mathrm{s}}(x = L, t)$). Using a least-squares curve fitting algorithm in MATLAB, experimentally measured temperature transients and code-calculated impulse response functions can then be passed to an optimisation routine that changes h_{v} until predicted temperatures match those obtained experimentally. The value of h_{v} that minimises the difference between modelled and measured transients is assumed to be the correct value. In this work, a nominal termination tolerance of 1×10^{-8} was used in the optimisation routine.

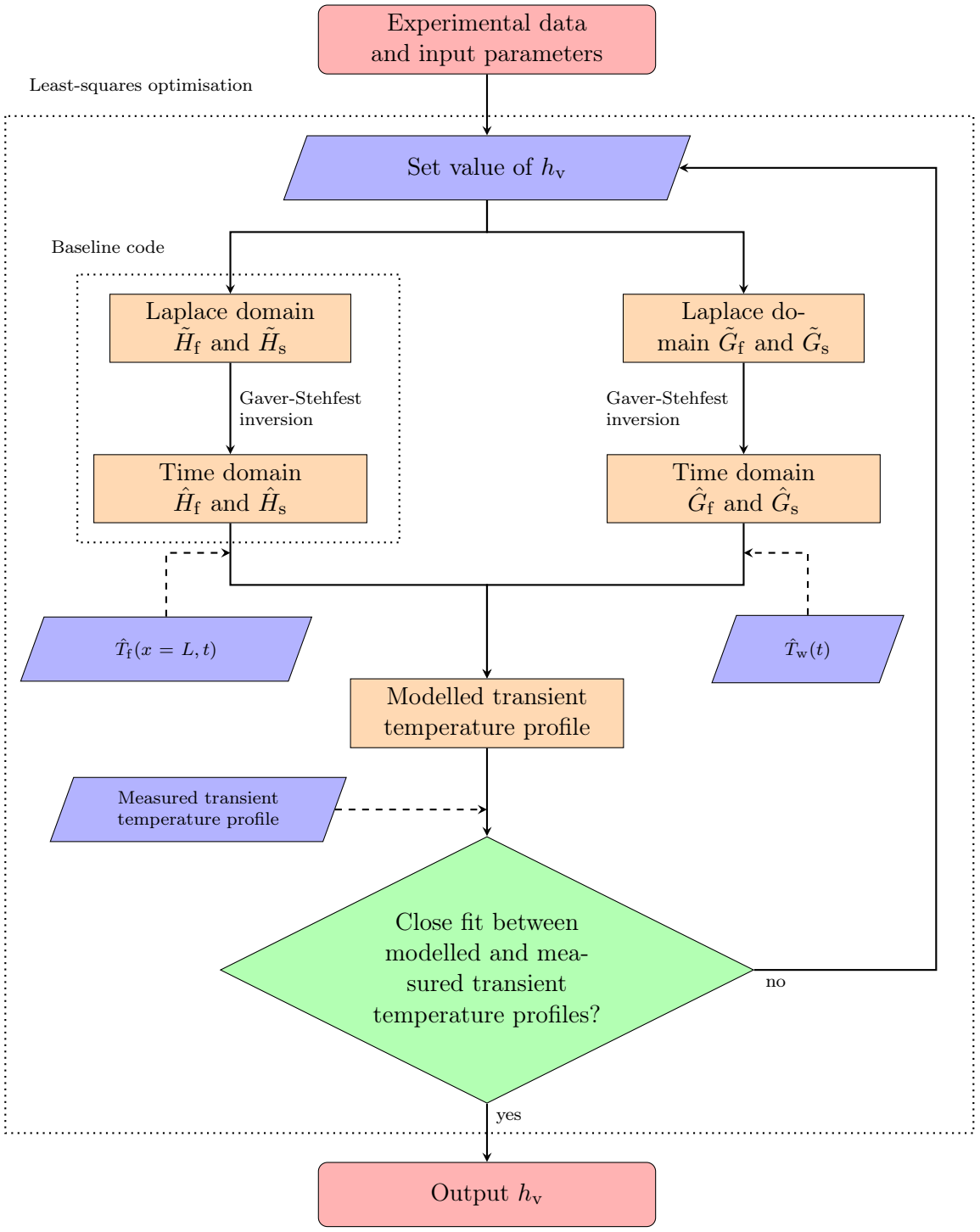


Figure 6.10: Flow chart describing 1-D numerical scheme for least-squares curve fitting of h_v. Steps performed by the baseline code are indicated by a dotted box

Chapter 7 specifically addresses the methods used to experimentally measure temperature transients. The following subsections describe the implementation of the numerical scheme in MATLAB for modelling temperature transients and calculating h_{v}. It should be noted that Hermann et al. provided the baseline numerical code to be used in this work, based off their previous investigation [117]. Figure 6.10 indicates the steps performed by the baseline code - all other steps were new, and accomplished in this work. In addition, a number of significant upgrades were applied to the baseline code. Firstly, the heat input to the system was modified, since this work applied gas heating instead of a surface heat flux. This involved changing the boundary conditions to those listed in Equations (6.14) to (6.16). Sections 6.5.1 and 6.5.2 list additional significant upgrades applied to the baseline code.

6.5.1 Lateral heat loss estimation

Prior to using the impulse response convolution method, knowledge of the magnitude of lateral heat loss from the porous sample to its mount is required. As such, an estimate of a is first obtained for each experimental case by analysing the transient temperature drop of the solid during cool-down (after gas heating) without effusion of gas. These estimates are then fed into the impulse response algorithm in order to extract h_{v}.

In the absence of gas flowing through the porous sample, Equation (6.1) can be rewritten as

$$\underbrace{(1-\phi)\,\rho_{\mathrm{s}}\,c_{p,\mathrm{s}}\,\frac{\partial \hat{T}_{\mathrm{s}}}{\partial t}}_{\text{Heat storage (solid)}} = \underbrace{k_{\mathrm{s}}\,(1-\phi)\,\frac{\partial^2 \hat{T}_{\mathrm{s}}}{\partial x^2}}_{\text{Conduction (solid)}} + \underbrace{a\,\left(\hat{T}_{\mathrm{s}}-\hat{T}_{\mathrm{w}}\right)}_{\text{Heat loss}} \tag{6.21}$$

During cool-down, $\hat{T}_{\mathrm{w}}$ remains steady, thus it is treated as a constant in Equation (6.21). Note that T_0 subtracted from all absolute temperatures in this analysis is the post-heating temperature (recorded as soon as coolant flow stops), and as such is not the same as the T_0 used in Section 6.2.

Through Laplace transforms, Equation (6.21) can be reduced to a non-homogeneous linear second order DE, given by

$$F_2 \frac{\partial^2 \tilde{T}_\mathrm{s}}{\partial x^2} \; + \; F_1 \frac{\partial \tilde{T}_\mathrm{s}}{\partial x} \; + \; F_0 \tilde{T}_\mathrm{s} \; = \; P_2 \tag{6.22}$$

where coefficients F_{0-2} and P_2 are given as follows.

$$F_2 \; = \; \frac{s\, k_\mathrm{s}}{\rho_\mathrm{s}\, c_{p,\mathrm{s}}} \tag{6.23}$$

$$F_1 \; = \; 0 \tag{6.24}$$

$$F_0 \; = \; \frac{a\, s}{(1-\phi)\, \rho_\mathrm{s}\, c_{p,\mathrm{s}}} - s^2 \tag{6.25}$$

$$P_2 \; = \; \frac{a\, \hat{T}_\mathrm{w}}{(1-\phi)\, \rho_\mathrm{s}\, c_{p,\mathrm{s}}} \tag{6.26}$$

The solution to Equation (6.22) is of a similar form to Equation (6.11), where the constant P_2 effectively behaves as a forcing term, driving the system from its initial conditions to a stable state of equilibrium.

$$\tilde{T}_\mathrm{s} \; = \; \sum_{i=1}^{2} D_i \, \exp\left(\lambda_i \, x\right) + \frac{P_2}{F_0} \tag{6.27}$$

where D_{0-2} are coefficients to be determined from boundary conditions.

$$x = L, \qquad \underbrace{\frac{\partial \hat{T}_{\mathrm{s}}(t)}{\partial x} = 0}_{\text{Adiabatic surface}} \tag{6.28}$$

$$x = 0, \qquad \underbrace{\frac{\partial \hat{T}_{\mathrm{s}}(t)}{\partial x} = 0}_{\text{Adiabatic surface}} \tag{6.29}$$

$\tilde{T}_{\mathrm{s}}$ can then be inverted into the time domain to model the transient cooling of the solid back to ambient conditions. By fitting experimentally measured cooling transients to those modelled using a least-squares curve fitting algorithm, a value for a can be extracted. In theory, two solid temperatures may be used for comparison - these are the bottom and top surface temperatures of the porous solid. In practice, only the top surface temperature is used and this is justified in Chapter 7.

In the baseline code, a was calculated by applying a heat flux to the material top surface, initially at ambient conditions, in the absence of gas effusion. Solid impulse responses were modelled by solving Equation (6.22) without the forcing term (since the solid was initially at ambient conditions), and using an impulse heat flux boundary condition on the top surface. This could then be convolved with the applied top surface heat flux, to produce a modelled temperature response of the top surface. A value for a could then be extracted by comparing this modelled response to a measured top surface temperature in a least-squares optimisation. This procedure was performed once in the work of Hermann et al. (independently to each experimental case) providing a single average value of a for all tested $\dot{m}_A$. As before, the absence of a laser for surface heating meant that this method could not be utilised in this work, and had to be modified in the baseline code as described in this section. Arguably, the method used in this work is more accurate, as it allows a case-by-case estimation of a.

6.5.2 Code implementation

The baseline code implements the equations described in Sections 6.2 and 6.5.1 through a numerical Laplace-inversion scheme proposed by Gaver and Stehfest [119, 120]. The following equation is applied repeatedly at discrete t values to obtain numerically-approximate transient time domain solutions.

$$f\left(t\right) \;=\; \frac{\ln 2}{t} \sum_{i=1}^{10} V_i \, F\left(\frac{\ln 2}{t} \cdot i\right) \tag{6.30}$$

where $f(t)$ is the time domain solution at time t, $F\left(\frac{\ln 2}{t} \cdot i\right)$ is the Laplace domain solution $F(s)$ evaluated at an s value of $\left(\frac{\ln 2}{t} \cdot i\right)$, and V_i is given by Equation (6.31).

$$V_i \;=\; (-1)^{i+5} \sum_{k=\left[\frac{i+1}{2}\right]}^{\min(i\,,\,5)} \left[\frac{k^6 \, (2k)!}{(5-k)!\, k!\, (k-1)!\, (i-k)!\, (2k-i)!}\right] \tag{6.31}$$

Due to the numerical inversion from Laplace to time domain, the impulse response convolution operation is performed by the code in a discrete method rather than continuous. This is given in Equations (6.32) and (6.33) (these are analogous to the continuous forms given in Equations (6.18) and (6.19))

$$\hat{T}_{\mathrm{f}}\left(x\,,\, t = k\,\Delta\right) \;=\; \Delta \sum_{j=0}^{k} H_{\mathrm{f}}\big(x\,,\, t = j\,\Delta\big) \cdot \hat{T}_{\mathrm{f}}\big(x = L\,,\, t = (k-j)\,\Delta\big) \tag{6.32}$$

$$\hat{T}_{\mathrm{s}}\left(x\,,\, t = k\,\Delta\right) \;=\; \Delta \sum_{j=0}^{k} H_{\mathrm{s}}\big(x\,,\, t = j\,\Delta\big) \cdot \hat{T}_{\mathrm{f}}\big(x = L\,,\, t = (k-j)\,\Delta\big) \tag{6.33}$$

where Δ is the size of the time step used in the numerical inversion scheme. The presence of Δ in the discrete convolution arises as a result of the definition of the discrete Dirac delta function, which is used when applying an impulse to a LTI system. This is shown in Equation (6.34) for

$t > 0$.

$$\delta(t) = \begin{cases} \frac{1}{\Delta} & 0 \leq t \leq \Delta \\ 0 & t > \Delta \end{cases} \tag{6.34}$$

The value of Δ used in the code is chosen with care - it needs to be small enough to resolve the shape of the impulse temperature rise for both solid and fluid phases at early t values. Large Δ values will cause the temperature rise due to impulse heat input to be inadequately sampled, leading to aliasing, and thus averaging of the impulse response, as shown in Figure 6.11. This is mainly a problem for the fluid phase, as the impulse temperature rise is convected through the porous solid at the bulk fluid velocity, u_{m}, leading to a rapid change in temperature. High thermal capacitance of the solid phase causes its response to the impulse to be slower. Thus, under-sampling of H_{s} is significantly less deleterious than that of H_{f}. Consequently, the choice of Δ was less important in the work of Hermann et al [117], as the heat input there was via a surface heat flux. Since the heat transfer direction was from solid to gas in their investigation, the impulse response of the gas was also limited by the speed at which the solid heated up, so large Δ values could be used. The following approach for selecting an appropriate Δ is a product of this work, and was not implemented in the initially obtained baseline code.

The maximum allowable Δ is dictated by the limiting rate of information transfer in the system, which in the case of this experiment, is the convective speed u_{m}. This investigation has found it beneficial to define a so-called convergence criterion, analogous to the Courant-Friedrichs–Lewy (CFL) condition [122], to limit the maximum allowable Δ. This condition is characterised by a non-dimensional length parameter Θ, and is given in Equation (6.35).

$$\Theta = \frac{u_{\mathrm{m}}\Delta}{L} \leq 0.1 \tag{6.35}$$

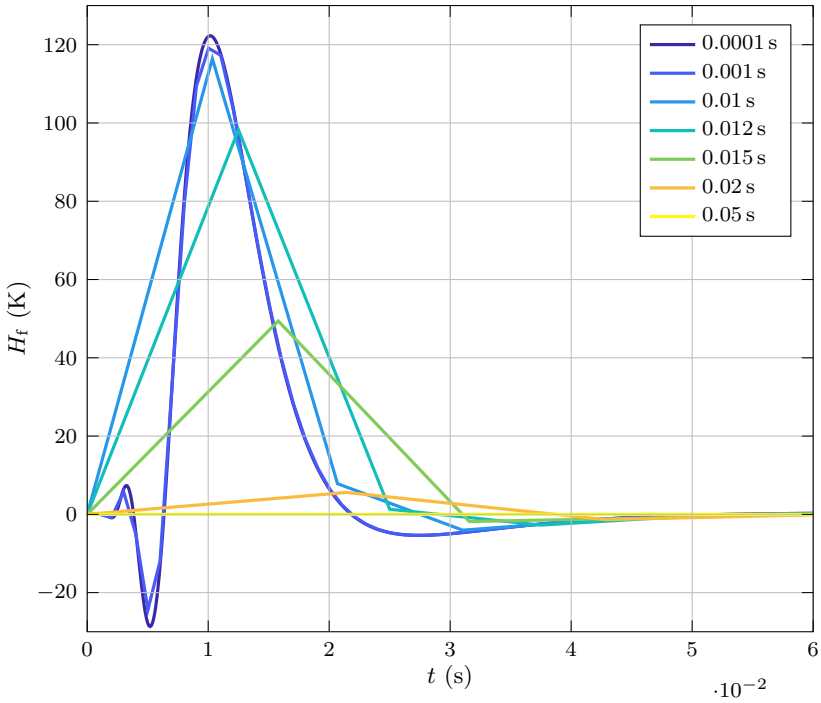


Figure 6.11: Top surface fluid impulse response for various time steps, Δ, given in legend

There is also a lower limit on how small Δ can be. From Equation (6.30), it is evident that the s variable depends on the inverse of t. Thus, for $t \sim 0$, the s variable takes on large values - this can lead to the computation of very large numbers, since the solutions for $\tilde{T}_s$ and $\tilde{T}_f$ as given in Equations (6.11) and (6.12) evaluate exponential functions with arguments that depend on s. The smallest possible Δ is limited by MATLAB's largest finite floating point number, which is $\sim 10^{308}$. Given these conditions, it is advised to inspect the shapes of H_f and H_s obtained from the code for arbitrary h_v values, so as to ensure

- a well-resolved shape of the impulse temperature rise
- a finite temperature response calculated for the first few time steps

Small Δ values have the disadvantage of causing long computation times, because the code needs to perform the Laplace-inversion for a large number of time steps. To tackle this, two different Δ values are used in the code. A smaller Δ dictated by the conditions listed above is used to resolve the shape of the impulse temperature rise in the initial fast decay region. A larger Δ is then used to evaluate the rest of the impulse response transient. Through linear interpolation,

a uniform fine temporal resolution is achieved - this saves a significant amount of computation effort and time. While this procedure is unnecessary for the solid phase due to its slower impulse decay, it is implemented anyway for code uniformity and simplicity. The added computation time as a result of this is negligible since the smaller Δ is only used during the fluid's rapid impulse decay ($\sim 10^3$ times less time steps than the rest of the response).

6.5.3 Uncertainty analysis

The uncertainties in extracted h_v values were calculated using the method of Moffat [123]. In this method, h_v was re-evaluated for each parameter used in the impulse response convolution analysis, perturbing the value of that parameter by its individual measurement uncertainty, while keeping all other parameters constant. The difference between original and each re-evaluated h_v is defined as a 'residual' - the overall uncertainty of h_v is thus given as the root of the sum of squared residuals.

Most of the parameters are perturbed in the code by simply adding their intrinsic measurement uncertainty to the value used. In the case of temperatures, the effect of measurement uncertainty is accounted for by evaluating the confidence interval for the fitted value of h_v. Half of the difference between upper and lower interval bounds is used as the 'residual' for temperature. In practice, this requires artificially introducing Gaussian noise, scaled by the temperature-sensing device's measurement uncertainty, to the measured temperature transient prior to the fitting algorithm. The most accurate method of evaluating the effect of temperature uncertainties is to perform the h_v fitting algorithm many times, each using a new random Gaussian-noise included transient, and subsequently evaluating the standard deviation of all obtained h_v values. However, this was not performed, as it would require an unrealistic amount of computational time to achieve statistical significance.

6.6 Summary

This chapter detailed the fundamentals of 1-D heat transport between solid and fluid phases in a transpiring porous medium. A semi-analytical solution of the coupled heat transfer equations was presented based on the impulse response convolution method. With this solution, the response of a transpiring porous medium to a heat input could be modelled. This would enable comparison with experimental results to extract h_{v} for a tested porous material. To this end, an experimental configuration was then designed to enable h_{v} measurement. The behaviour of this specific experimental system was elaborated in this chapter, along with implementation particulars of the numerical modelling. The following chapter details the assembled experimental framework, the samples tested, the h_{v} values obtained, and comparison of obtained results with those in the literature.

Chapter 7

Volumetric Heat Transfer Coefficient Measurements

Chapter 6 introduced a numerical scheme that simulates 1-D internal heat transfer between solid and fluid phases within a porous medium. This tool was used to model solid and fluid transient temperature changes for an arbitrary gas heating input. By comparing modelled results to measured experimental data, the volumetric heat transfer coefficient, h_{v}, can be measured for a particular porous material and flow condition. This chapter describes the complementary experimental framework that was used to measure transient temperature changes of the porous material. As discussed in Chapter 6, the goal was to create a framework that is able to make spatially resolved scalar measurements, such as composition and temperature, that would quantify the extent of internal mixing as a result of non-uniform coolant injection. To this end, 2-D PDRS and IR thermography were applied to the fluid and solid phases respectively. These processed temperature values were then used with the numerical scheme to evaluate h_{v}. Implementation details and internal cooling characterisation results are presented in this chapter.

7.1 Methodology

This section describes the simultaneous multiscalar diagnostic experimental layout and implementation. Figures 7.1 and 7.2 show the experimental layout used.

In order to experimentally infer the internal heat transfer characteristics of a candidate porous material, heated gas was effused through a sample of said material (initially at ambient condi-

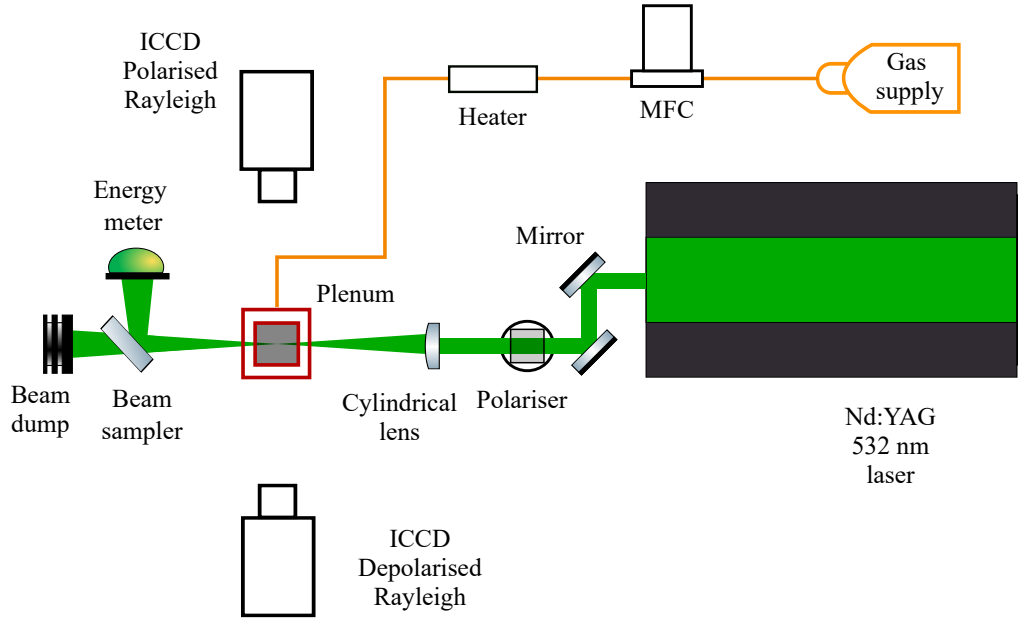


Figure 7.1: Plan view schematic of experimental set-up

tions) into static atmosphere via a pressurised plenum. Porous samples were glued using silicone adhesive onto plenum cover plates that could be bolted onto the plenum to seal it, allowing the use of a single plenum to test multiple samples. Gas composition and temperature immediately above the porous surface was obtained using PDRS (at $x = 0$, according to the defined coordinate system). A similar experimental configuration to the one described in Section 5.2 was used to probe the transpiring gas from the porous sample. In Section 7.3, cameras used were the Princeton Instruments ICCD-512T and ICCD-576GRB, the same as those in Section 5.2. However, subsequent experimental results presented in this chapter were obtained using a different camera (Andor Luca R 604 EMCCD) due to equipment availability. The pixel size was 20 µm per pixel for both configurations. The focus of the laser sheet was set to coincide with the centre of the porous sample and the cameras' field of view. An intentional gap of approximately 1 mm was left between the porous sample surface and the bottom of the laser sheet to minimise strong laser scatter from the surface being captured by either camera. A beam sampler was positioned just after the imaging area, reflecting a weak copy of the laser sheet onto a laser energy meter

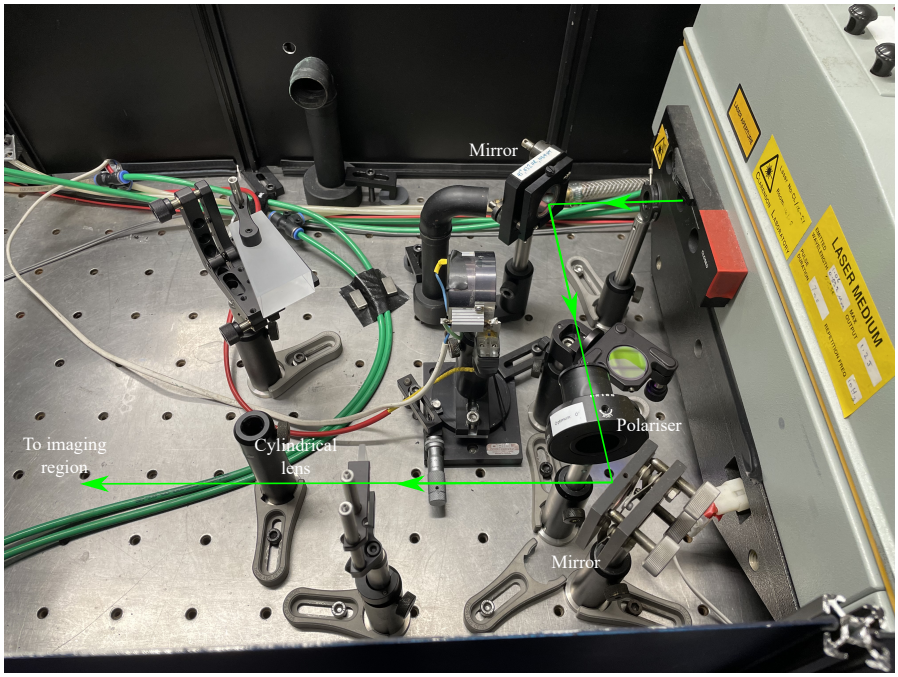


Figure 7.2: Layout of sheet-forming optical components

to enable fluctuations in incident pulse energy to be corrected.

The top solid surface temperature (at $x = 0$) of the porous sample was acquired using a FLIR E4 IR camera positioned 140 mm away, normal to the sample's surface. The IR camera viewed the sample through a 25.4 mm diameter hole on a thick aluminium plate, in place to protect users and instruments in case of brittle fracture of the sample caused by over-pressure. A pixel size of 25 µm per pixel was achieved. Figure 7.3 illustrates the arrangement of the IR camera and PDRS light sheet.

An Omega FMA-2609A mass flow controller (MFC) was used to regulate the gas flow rate before being passed through an inline resistive heater (Omega AHP-5052) to heat the incoming gas. A plenum chamber was used to ensure the gas remained at a constant positive pressure, feeding flow through the porous sample. The plenum pressure was monitored with a GEMS 3100 series pressure transducer - this ensured a maximum gauge plenum pressure (based on known sample fracture limit) was not exceeded. Two K-type thermocouples (0.5 mm diameter sheath) were placed in the plenum chamber to monitor the porous sample back surface temperature and the

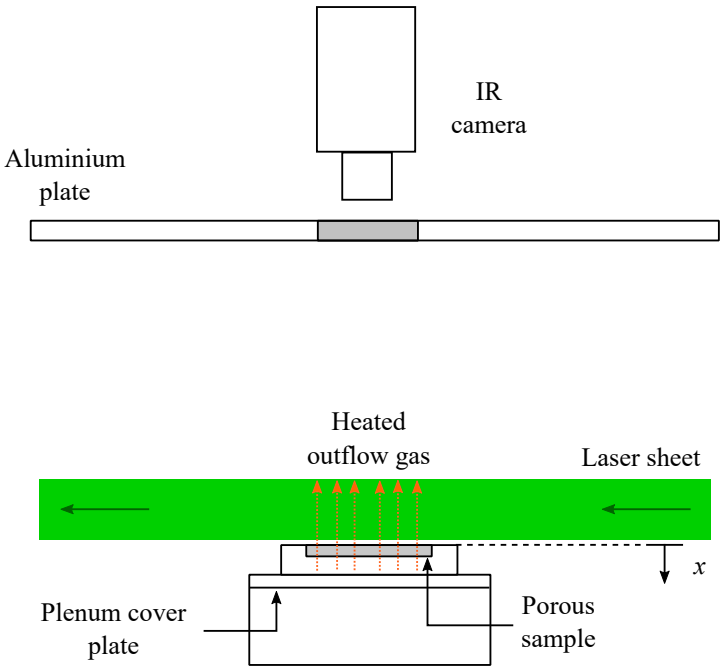


Figure 7.3: Side view schematic of experimental set-up

plenum gas temperature, respectively (at $x = L$). Data from these transducers was logged using a Pico Technology USB TC-08 Thermocouple Logger.

When making 2-D measurements of composition and temperature, CO_2 is preferred as discussed previously, since it distinguishes effused gas from stagnant ambient air. However the majority of the analysis in this chapter uses N_2 as the effused gas. There were several reasons for this choice. Firstly, N_2 is cheaper than CO_2. Secondly, its thermal properties such as ρ_f and $c_{p,\mathrm{f}}$ vary with temperature to a smaller extent than CO_2, thus reducing uncertainties in the fitting routine. In addition, CO_2 has absorption bands in the mid and long-wave IR wavelengths - this could have an effect on IR measurements, particularly if made in internal environments such as inside the plenum (this will become relevant in Section 7.4.2). Lastly, deriving material properties relies on model comparison. The only available model was 1-D, which meant gas composition variations had to be suppressed and temperature averaged across the field of view. To ensure a uniform gas output that is not affected by quenching from ambient air, a 3D-printed shroud was used, as shown in Figure 7.4. Four horizontal extrusions were built into the base of the shroud to allow optical access for both the laser sheet and the cameras. The top of the shroud

was partially covered, forcing effused gas to fill the column. As a result, stagnant ambient air on the sample surface was completely displaced a few seconds after the effusion flow was turned on and no 'new' ambient air could diffuse into the imaging region. Considering the need to ensure a uniform output gas composition, compressed air would be the other obvious gas choice for these experiments, as it is even cheaper and more easily available than N_2. However, small particles and droplets are observed in compressed air supplies, and this generates elastic scatter that interferes with Rayleigh measurements.

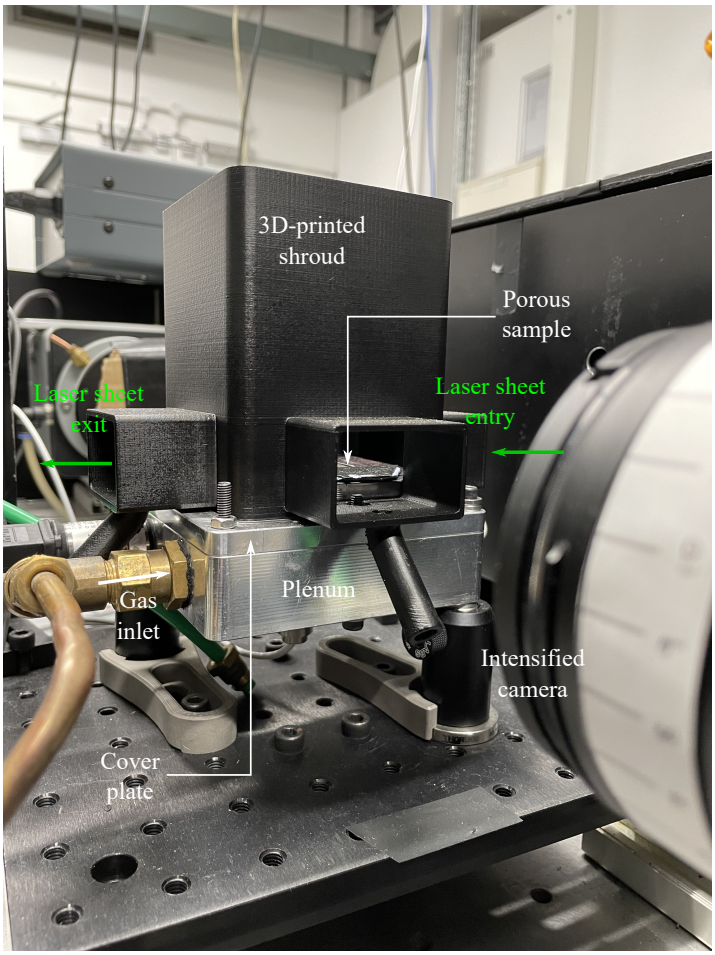


Figure 7.4: Vertical 3D-printed shroud used to prevent ambient air entrainment

The imaging and data acquisition apparatus were triggered to acquire data simultaneously, at a frequency of 1 Hz. Experiments were performed by first flowing gas through the porous sample at room temperature. This initial constant temperature period was used to calibrate Rayleigh

signals for temperature conversion. The assumption made is that both solid and fluid remain in thermal equilibrium, thus the temperature of the gas in the plenum (measured with a thermocouple) is equal to the temperature of the gas at the sample surface. Once flow through the sample was established, and monitored temperatures were stable, the plenum gas temperature was increased using the inline heater. Data was continuously logged for about 300 s, or until the temperature of the gas reached a value of approximately 338 K inside the plenum, whichever came first. This temperature limit was imposed as the silicone adhesive used to attach the porous sample onto its cover plate had a maximum working temperature of 343 K. Subsequently, the mass flow controller and inline heater were turned off, allowing the sample to cool back to room temperature. Data from the thermocouples and IR camera continued to be logged during this cool down period. As previously described, monitoring the sample surface temperatures enabled the heat loss parameter, a, to be estimated from case-to-case.

The experimentally measured plenum gas temperature, $\hat{T}_{\mathrm{f}}\,(x = L\,,\,t)$, was used as a driving input to the entire system. The other three measured temperatures, $\hat{T}_{\mathrm{f}}\,(x = 0\,,\,t)$ from PDRS, $\hat{T}_{\mathrm{s}}\,(x = 0\,,\,t)$ from the IR camera, and $\hat{T}_{\mathrm{s}}\,(x = L\,,\,t)$ from the surface thermocouple, were compared against modelled transients, obtained using the numerical scheme described in Chapter 6. Since three different temperatures were experimentally measured, three independent estimations of h_{v} were acquired. This enabled cross-validation of calculated h_{v} values. Section 7.5 describes the steps taken to convert acquired data into temperatures, before they were used in the least-squares h_{v} optimisation.

7.2 Porous samples

In this work, a total of three porous materials were tested. One was chosen as a validation sample to ensure reliability of the technique and of the numerical scheme, while the other two were candidate materials for transpiration cooling. Each sample was machined to have a square

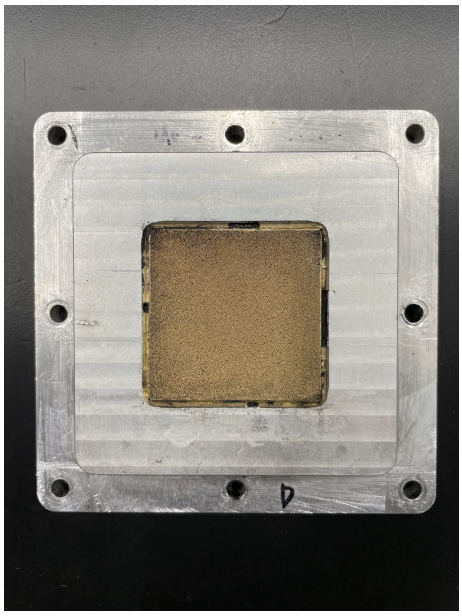


Figure 7.5: Siperm B sample

cross-section measuring 40 mm × 40 mm.

The validation sample tested was a porous bed of sintered bronze spheres, brand-named 'Siperm B' by manufacturers Tridelta Siperm GmbH. This specific sample was denoted a filter grade of B40, corresponding to an average sphere diameter of 286 µm. Figure 7.5 shows the sample tested. Internal convective heat transfer correlations exist in the literature for packed beds of spheres, thus results obtained from this sample could be validated to assess the accuracy of the technique.

The first transpiration cooling candidate is an Ultra High Temperature Ceramic (UHTC) made from zirconium diboride (ZrB_2). It has a melting point of 3519 K; such a high theoretical working temperature enables substantial passive re-radiative cooling [124]. It is made from partially sintering ZrB_2 powder, producing a refined pore structure. Figure 7.6 shows the sample tested, mounted onto a plenum cover plate. The second candidate is a ceramic matrix composite (CMC), made of carbon-fiber-reinforced carbon (C/C). This material has been tested extensively in a number of transpiration cooling investigations [116, 118, 125, 126, 127]. It is a lightweight, low thermal conductivity material with high specific strength and working temperature (1800 K) [128]. Figure 7.7 shows the sample tested, mounted on a similar plenum cover plate. Several



Figure 7.6: UHTC sample

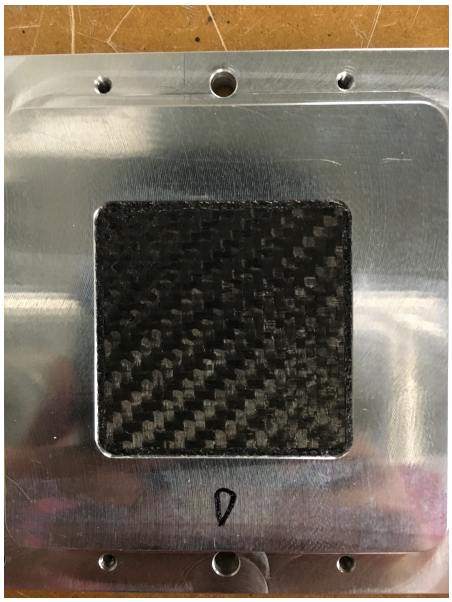


Figure 7.7: C/C sample

publications have investigated the use of such materials in transpiration cooling [115, 117, 116, 125, 129]. However, they have all relied on estimates or numerical fits for h_v, so it would be highly beneficial to accurately measure h_v to validate these studies.

7.3 Method development

In this section, the experimental framework discussed was first tested on a UHTC sample for a coarse range of mass fluxes. Results provided here were published in a conference proceedings [130]. CO_2 was used as the effused gas. A value of 0.75 for the emissivity, ϵ, was used for rapidness, based on a previous investigation [117]. Table 7.1 lists material properties of the ZrB_2 sample that was used in the experiments. Results from this investigation tested the validity of the uniform temperature assumption for 1-D analysis, and revealed a limitation of using thermocouples to make surface temperature measurements.

Table 7.1: Material properties of ZrB_2 sample, obtained from [117]

L (mm)	k_s ($Wm^{-1}K^{-1}$)	$c_{p,s}$ ($Jkg^{-1}K^{-1}$)	ρ_s (kgm^{-3})	ϕ
5	41.4 ± 2.1	437.6 ± 43.8	6080	0.41 ± 0.01

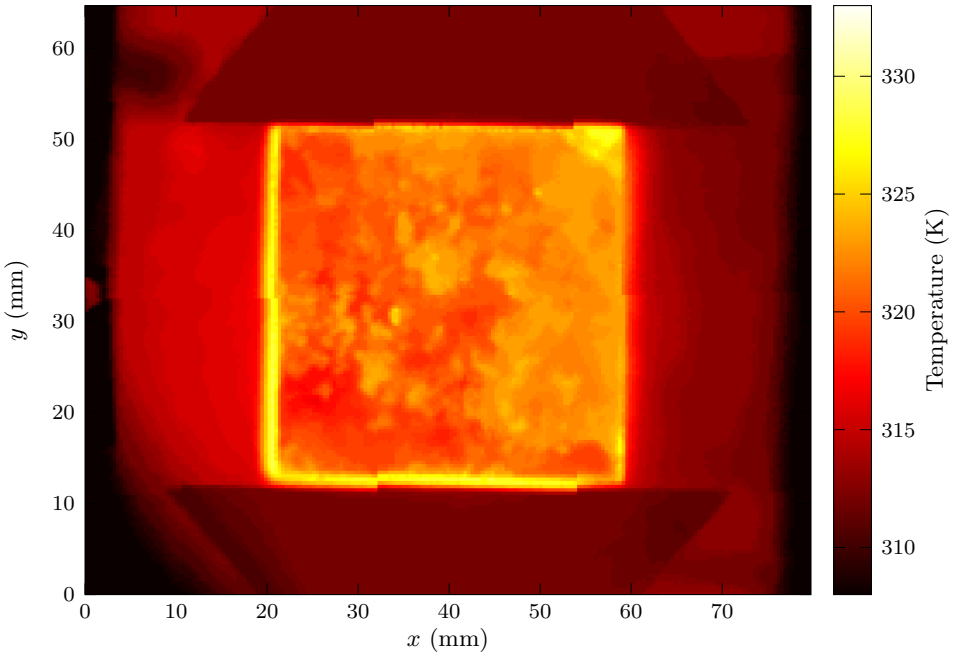


Figure 7.8: IR thermographic image of ZrB_2 sample surface

7.3.1 Preliminary results

Firstly, the assumption of uniform 1-D injection was tested to ensure that no internal preferential flow paths were present, leading to spatial non-equilibrium. Figure 7.8 shows an example porous sample surface temperature distribution recorded using the IR camera. This image was captured towards the end of the gas heating cycle during an experiment. A mean temperature was calculated by averaging across the entire sample surface.

The temperature distribution across the sample surface appeared mostly uniform, fluctuating by a standard deviation of approximately 2 K. Spatial temperature deviations were attributed to variations in emissivity on the sample surface - a qualitative comparison of the temperature field with a natural light image of the sample surface yields similarities in surface patterns. For example, the apparent 'high' temperature region on the upper right corner of Figure 7.8 spatially correlates with a light-grey discolouration in the same location in Figure 7.6. This was further supported by uniform composition fields extracted from PDRS, as shown in Figure 7.9. The ZrB_2 sample has a high porosity value and a very small pore size ($\leq 10\,\mu m$), leading to a homogenised

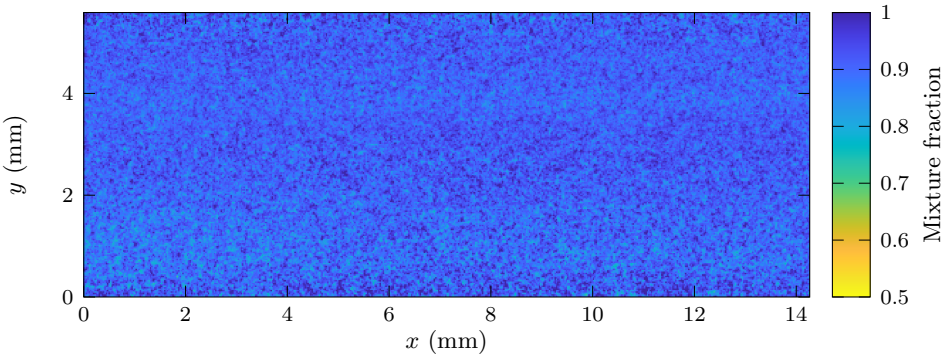


Figure 7.9: Uniform mixture fraction field above ZrB_2 sample surface

distribution of coolant effusing out of the sample surface [131, 124]. Any 'jetting' effects resulting from flow emanating from individual pores of the sample would take place immediately above the sample surface, so PDRS measurements would not be able to resolve these (since PDRS data was collected $\geq$1 mm above the sample surface as mentioned previously).

Figure 7.10 shows the h_v values obtained from fitting experimental data as a function of gas flow rate. Note that the error bars in this figure were not obtained using Moffat's method, as it required a long computation time. Instead, a worst case temperature deviation was added to each data point scaled by the measurement device's intrinsic uncertainty, producing a new biased transient. The error was evaluated as the difference between fitted h_v, and the value obtained when fitting this new transient - this saved a significant amount of time during development. The h_v values derived from all measurement methods exhibit a similar increasing trend with an increase in mass flux, as expected. However, h_v values obtained from fitting temperatures measured with the thermocouple, $T_s(x = L)$, were found to be almost an order of magnitude higher than those obtained from PDRS, $T_f(x = 0)$, and IR, $T_s(x = 0)$, temperatures. The reason for this discrepancy is attributed to additional heating effects, mainly forced convection from the incoming hot gas and radiation from the hot plenum, causing measured back surface temperatures to be larger than expected. This is consistent with the observations because increased solid temperatures imply a more efficient heat exchange between solid and gas phases (as described in Figure 6.6), thus leading to larger predicted h_v values.

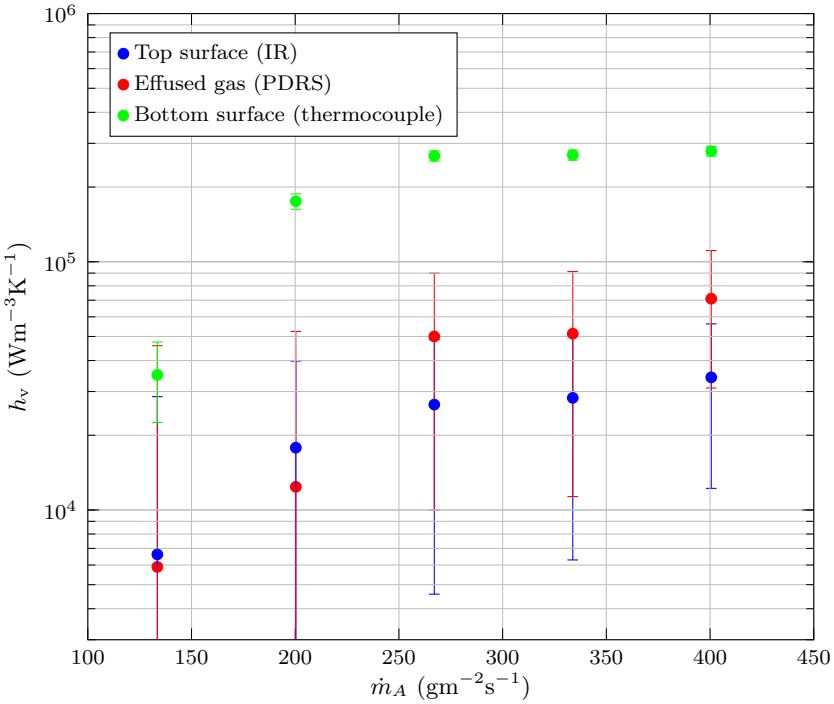


Figure 7.10: h_v calculated from fitting experimentally obtained transient temperature rise data for different mass fluxes. Error bars represent the (pessimistic) effect of applying the worst-case inaccuracy of each diagnostic.

Volumetric heat transfer coefficient values obtained from IR and PDRS temperatures were found to be similar in magnitude. For mass fluxes between 133 and 400 $\mathrm{gm^{-2}s^{-1}}$, h_v estimates from the IR camera ranged from 6.6×10^3 to $3.4 \times 10^4\,\mathrm{Wm^{-3}K^{-1}}$, while for PDRS, h_v ranged from 5.9×10^3 to $7.1 \times 10^4\,\mathrm{Wm^{-3}K^{-1}}$. Experimentally derived h_v values were compared to values obtained using correlations provided by Florio et al. [113]. These correlations were established for decomposing glass-filled polymer composites where cooling is achieved via removal of heat from gaseous products of pyrolysis. While such a configuration is different to the application at hand, these correlations have been used in several transpiration cooling system studies in the past [117, 116, 115]. First, a Nusselt number, $\mathrm{Nu}_{\sqrt{K_D}}$, was calculated based on the definition given in Equation (7.1).

$$\mathrm{Nu}_{\sqrt{K_D}} = \frac{h_v K_D}{k_f} \tag{7.1}$$

where k_f is the fluid thermal conductivity and K_D is the sample Darcy permeability coefficient.

K_D was measured for the ZrB_2 sample by fitting experimentally measured plenum pressure, p, and mass flux data (collected during the constant temperature part of each test, i.e. before the inline gas heater was turned on) to the spatially integrated Darcy-Forchheimer equation (given in Equation (7.2)).

$$\frac{p_\mathrm{in}^2 - p_\mathrm{out}^2}{2p_\mathrm{in}L} = \frac{\mu_\mathrm{f,in}}{K_\mathrm{D}} u_\mathrm{in} + \frac{\rho_\mathrm{f,in}}{K_\mathrm{F}} u_\mathrm{in}^2 \tag{7.2}$$

where subscripts 'in' and 'out' refer to conditions in the plenum and at the porous outlet respectively, μ_f is the gas dynamic viscosity and K_F is the Forchheimer permeability coefficient. The dynamic viscosity μ_f was calculated using Sutherland's law [132], given in Equation (7.3)

$$\mu_\mathrm{f} = \mu_\mathrm{ref} \frac{T_\mathrm{ref} + C_\mathrm{ref}}{T_\mathrm{f} + C_\mathrm{ref}} \left(\frac{T_\mathrm{f}}{T_\mathrm{ref}} \right)^{3/2} \tag{7.3}$$

with CO_2 reference viscosity $\mu_\mathrm{ref} = 14.8 \times 10^{-6}\,\mathrm{Pa\,s}$, reference temperature $T_\mathrm{ref} = 293.15\,\mathrm{K}$ and Sutherland's constant $C_\mathrm{ref} = 240\,\mathrm{K}$. The plenum was restricted to a maximum gauge pressure of 4 bar for the ZrB_2 sample, to prevent brittle fracture. As such, the achievable pressure drop, Δp, across the sample and u_m were well within the linear Darcy regime, allowing the Forchheimer term in Equation (7.2) to be neglected. This meant a linear fit could be used to obtain K_D, resulting in a value of $3.54 \times 10^{-14}\,\mathrm{m}^2$, which closely matched results reported by Ifti et al. [131] (sample UHTC-7). Calculated $\mathrm{Nu}_{\sqrt{K_\mathrm{D}}}$ were compared to the Florio et al. correlations, given in Equations (7.4) to (7.6).

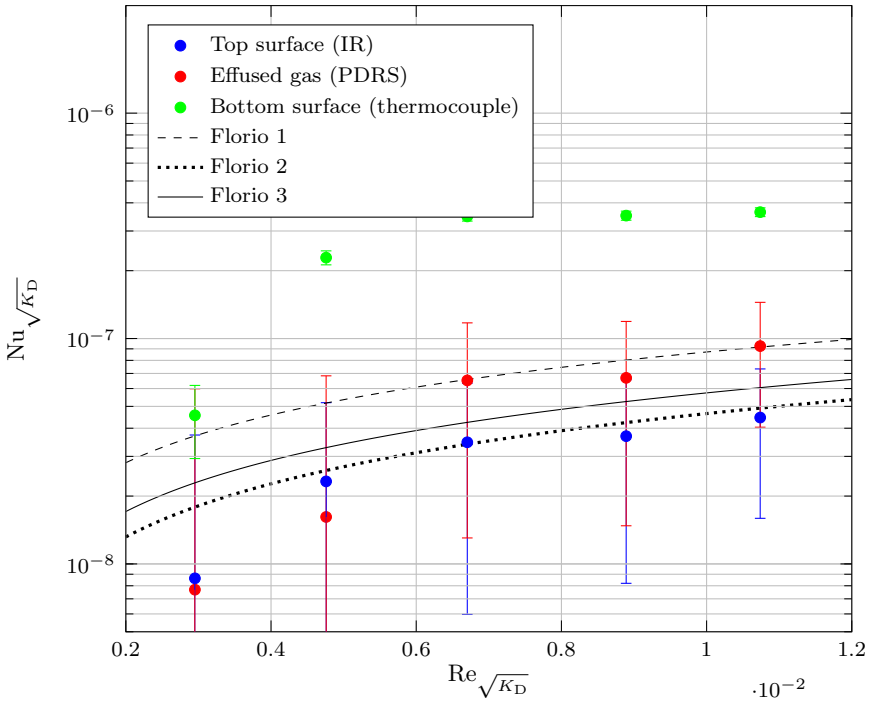


Figure 7.11: Calculated $\mathrm{Nu}_{\sqrt{K_\mathrm{D}}}$ numbers for different mass fluxes. 'Florio 1 - 3' refer to Equations (7.4) to (7.6), respectively

$$\mathrm{Nu}_{\sqrt{K_\mathrm{D}}} = 2.22 \times 10^{-6} (\mathrm{Re}_{\sqrt{K_\mathrm{D}}})^{0.703} \tag{7.4}$$

$$\mathrm{Nu}_{\sqrt{K_\mathrm{D}}} = 1.71 \times 10^{-6} (\mathrm{Re}_{\sqrt{K_\mathrm{D}}})^{0.783} \tag{7.5}$$

$$\mathrm{Nu}_{\sqrt{K_\mathrm{D}}} = 1.84 \times 10^{-6} (\mathrm{Re}_{\sqrt{K_\mathrm{D}}})^{0.753} \tag{7.6}$$

where $\mathrm{Re}_{\sqrt{K_\mathrm{D}}}$ is the Reynolds number defined by

$$\mathrm{Re}_{\sqrt{K_\mathrm{D}}} = \frac{\rho_\mathrm{f} K_\mathrm{D}^{1.5} \Delta p}{\mu_\mathrm{f}^2 \phi L} \tag{7.7}$$

Figure 7.11 plots $\mathrm{Nu}_{\sqrt{K_\mathrm{D}}}$ calculated from experimental data against these correlations. In general, the trends for both experimental results and correlations are similar, showing an increase in $\mathrm{Nu}_{\sqrt{K_\mathrm{D}}}$ for an increase in $\mathrm{Re}_{\sqrt{K_\mathrm{D}}}$. All three correlations match quite closely to the data obtained from the IR camera and PDRS, but not with that of the thermocouple. A closer match between

experimental data and correlations was obtained here, as compared to a previous experiment by Hermann et al. [117], but more thorough and meticulous measurements were required before the use of these correlations in transpiration cooling could be validated.

7.3.2 Bottom surface temperature improvement

Based on the results obtained in Section 7.3.1 for porous ZrB_2, it was apparent that the experimental framework was able to extract consistent h_v values using both optical diagnostic techniques. However, h_v values extracted from thermocouple measurements on the bottom surface of the sample, $T_s(x = L, t)$ were found to be an order of magnitude larger than the rest. Thermocouples exhibit a number of limitations when used to measure surface temperatures:

- Adhesive bonding to the surface of interest is required to achieve adequate thermal contact. Permanent bonding would be ideal in respect of heat transfer, but would make it cumbersome to assemble and disassemble the porous sample onto the plenum
- Use of an adhesive affects the permeability of the porous sample, as it can seep through the pores, blocking gas from transpiring locally. This would have been detrimental to the wider project, as these samples were limited in number and in high demand for various different characterisation experiments
- Bonding via adhesive perturbs the flow of coolant, as the gas is prevented from flowing through the localised adhesive-filled area. This leads to measured temperatures not being representative of actual flow conditions.
- The thermocouple sheath is exposed to hot gas in the plenum. This leads to additional forced convection, causing the measured temperatures to be larger than that of the surface

For these reasons, a more accurate approach to measure the sample bottom surface temperature was needed. Subsequent experiments were conducted using an IR pyrometer (Optris CT LT22), replacing the thermocouple. Its sensing head was equipped with an external M12 $\times$ 1.0 thread,

allowing incorporation into the existing setup via a tapped hole at the bottom of the plenum. This hole was positioned centrally, allowing the sensing head to aim at the centre of the sample's bottom surface. For such a configuration, the pyrometer measurement spot size was calculated to be approximately 8 mm in diameter, covering about 3 % of the sample's total surface area (40 mm × 40 mm).

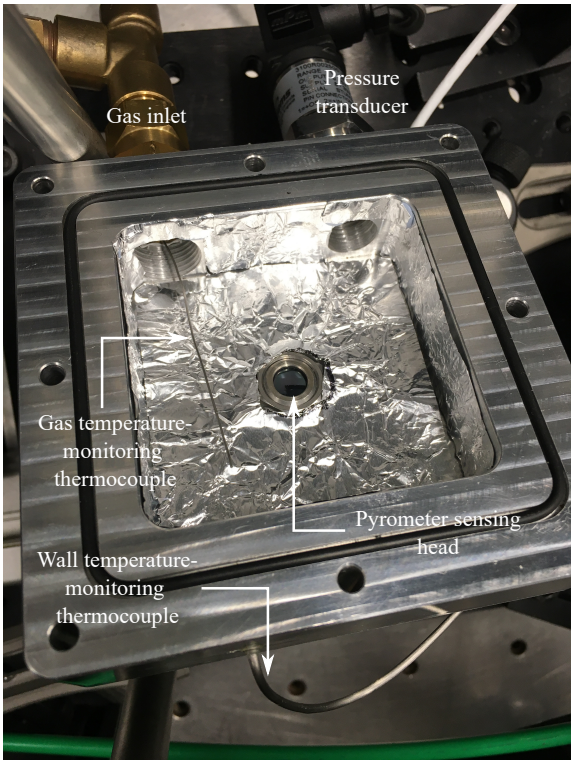


Figure 7.12: Pyrometer assembly onto bottom of plenum

7.4 Measurement calibrations

This section describes several characterisation experiments that were performed in order to ensure data quality, and feed into data post-processing.

7.4.1 Sample emissivity and initial ambient radiation

Prior to IR measurements, the surface emissivity, ϵ, of the tested sample needed to be measured. This is typically entered into the IR device before measurements are made, so that radiation

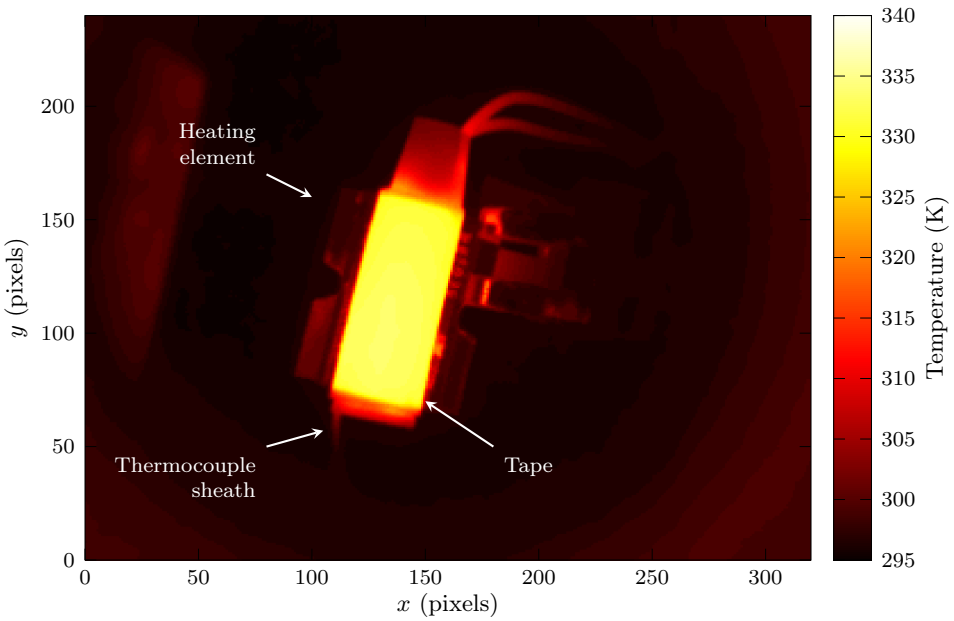


Figure 7.13: IR thermographic image of heating element

signals can be converted into temperature. ϵ values for the most common materials are documented by IR device manufacturers, but many of these are specific to the wavelength band in which the measurements were made (short, mid or long wave IR), as well as unique to material surface conditions (rough, polished, surface treated etc.) which can be quite vague and hard to compare. The standard procedure for measuring ϵ is as described in Section 2.4.3. It involves comparing the 'supposed' temperature of the sample to that of a highly emissive material in thermal equilibrium with the sample, and adjusting the device ϵ setting until both temperatures match. A simple but highly effective method for achieving this is by attaching a piece of black vinyl electrical tape onto the sample of interest. Electrical tape is documented as having a high ϵ of 0.96 [80], thus IR temperatures recorded for this material are reliable. A simple demonstration of this is shown in Figures 7.13 and 7.14. The former figure shows an IR thermograph image of a piece of electrical tape attached to a 12 V aluminium heating element that had been turned on. The latter figure shows a comparison of IR temperatures extracted from the tape, with temperatures measured from a thermocouple embedded in the same spatial location. The heating element was turned on and off twice to create an arbitrary transient temperature evolution.

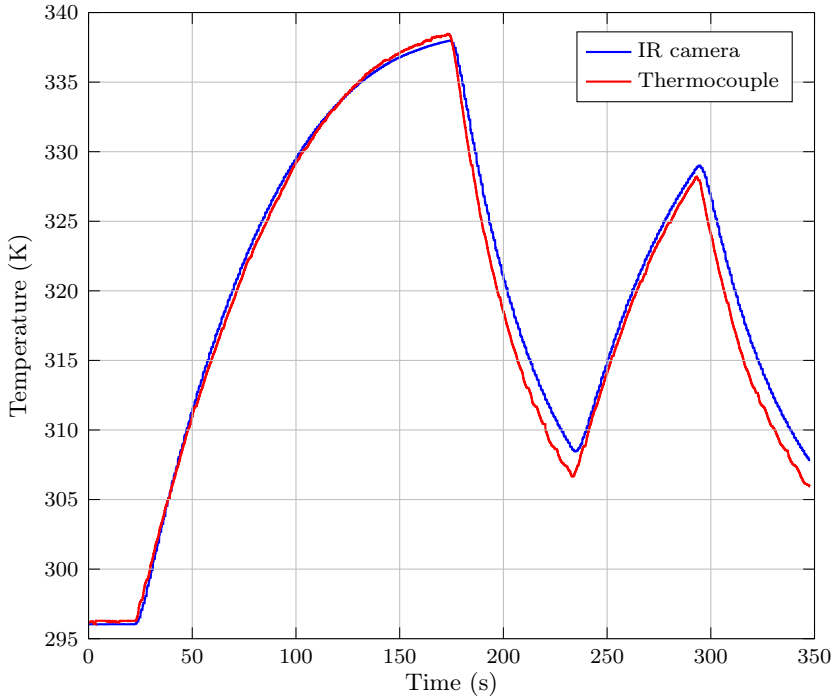


Figure 7.14: Transient temperature profile of heating element measured with a thermocouple and IR camera

From Figure 7.14, it is evident that IR temperatures matched those of the thermocouple very well, especially during heating transients. They deviated slightly during cooling, possibly as a result of the embedded thermocouple bead retaining heat, while the taped surface cooled faster due to direct exposure to colder ambient air.

Figure 7.15 shows IR images of the emissivity measurement process for each sample. Tape, typically having the larger emissivity, displayed much larger temperatures as the device received more IR radiation from it compared to the sample. Table 7.2 lists the emissivity values obtained for each sample for both top and bottom surfaces.

Table 7.2: Emissivity values for each sample on top and bottom surfaces

Position	Siperm B	UHTC	C/C
Top surface ($x = 0$)	0.46	0.59	0.68
Bottom surface ($x = L$)	0.55	0.59	0.70

In addition to ϵ, IR devices also require information about the ambient radiation being reflected off the surface of interest. This is characterised by the reflected temperature, T_{refl}. Thus, before

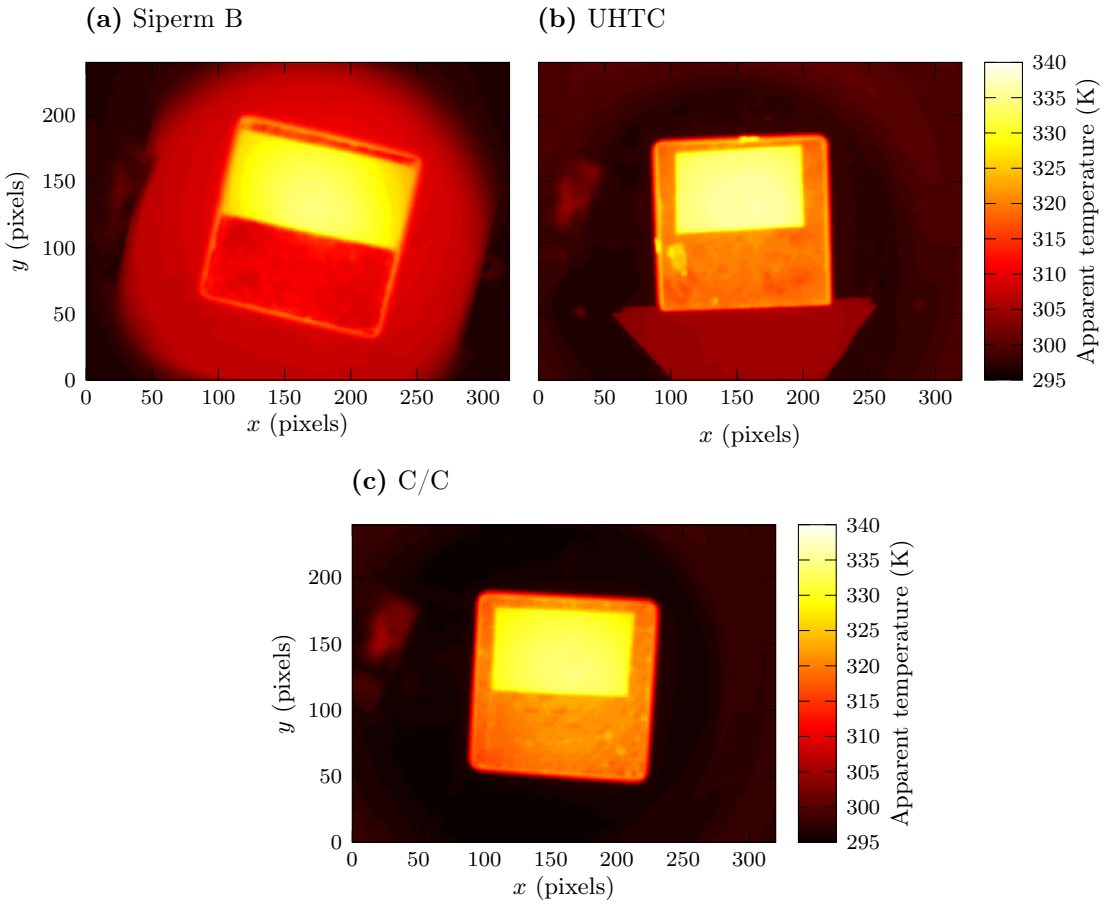


Figure 7.15: IR thermographs of each sample during ϵ measurement. Note that the colours indicated by the colour bar represent the apparent temperature, as the IR camera assumes a fixed ϵ across the image.

starting each experimental run, the initial T_{refl} for both the IR camera and the pyrometer was measured. As indicated in Section 2.4.3, this was achieved by placing a piece of crumpled and flattened aluminium foil on the measurement area, assembled in its experimental configuration, and recording the apparent temperature of the foil with the device set to an ϵ of 1. This was performed on the top surface for the IR camera, and also on the bottom surface for the pyrometer, meaning for each experimental run the plenum was initially disassembled. Initial T_{refl} were recorded, and set on the measurement device before starting an experimental run. For the IR camera, ambient radiation came from the laboratory environment, which was a large open space, thus, it was justified to assume that T_{refl} stayed constant throughout the duration of the test. However, this was not the case for the pyrometer, as will be discussed in the next section.

7.4.2 Dynamic reflected temperature compensation

The main difficulty with using the pyrometer is ambient radiation compensation. As previously described, IR measurements require accurate knowledge of ϵ of the material probed, as well as T_{refl}. In a steady environment, background radiation remains constant - thus a single calibration at the start of the experiment accounting for this would be sufficient. However, the environment inside the plenum was not steady - the walls of the plenum transiently heated up during the test as a result of convective heat transfer with the incoming hot pressurised gas. This meant that the level of background radiation changed throughout the test, so a dynamic compensation for T_{refl} was required.

To enable this, a dynamic calibration procedure was developed, where a relationship between $T_{\text{refl}}(x = L\,,\,t)$ and $T_{\text{w}}(x = L\,,\,t)$ was established. This allowed inferring $T_{\text{refl}}(x = L\,,\,t)$ from $T_{\text{w}}(x = L\,,\,t)$ during an experimental run, in order to transiently correct the pyrometer measurement. The first step in this calibration was to measure $T_{\text{w}}(x = L\,,\,t)$. To this end, a K-type thermocouple (1 mm diameter sheath) was embedded into a 1 mm diameter hole, drilled into the side wall of the plenum, as shown in Figure 7.12. This hole was drilled to a depth of 1 mm away from the inner wall of the plenum. Next, a square piece of crumpled and re-flattened aluminium foil was attached centrally onto the bottom surface of the porous sample, such that it covered the measurement spot of the pyrometer. The plenum was then sealed and ϵ set to 1 on the pyrometer. Subsequently, gas passed through the plenum and out of the porous sample, while being transiently heated by the inline heater. Temperatures from the pyrometer and the two thermocouples (inside, and in the wall of the plenum) were logged simultaneously until the plenum gas temperature reached the maximum gas temperature attained during the experiment (mimicking experimental conditions). This procedure was repeated for all test flow rates.

The reflected temperature, $T_{\text{refl}}(x = L\,,\,t)$, was expected to be a function of $T_{\text{w}}(x = L\,,\,t)$, leading to a one-to-one relationship between $T_{\text{w}}(x = L\,,\,t)$ and $T_{\text{refl}}(x = L\,,\,t)$. Figure 7.16 plots the

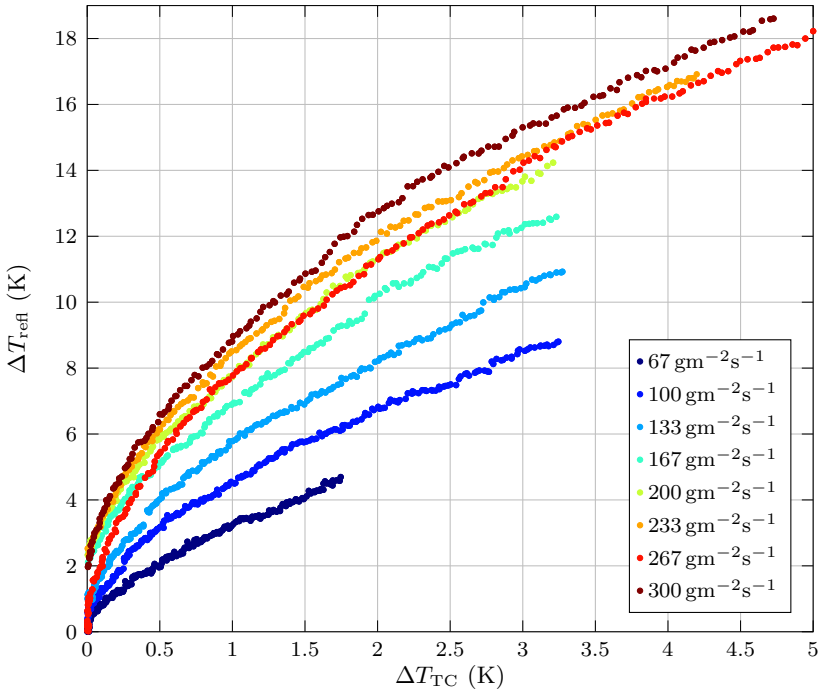


Figure 7.16: Change in T_{refl} plotted against change in wall thermocouple temperature, T_{TC}, for the UHTC sample

change in $T_{\mathrm{refl}}\,(x = L\,,\,t)$ against the change in plenum-embedded thermocouple temperature, $T_{\mathrm{TC}}\,(t)$, for the UHTC sample. From this figure, two main observations are apparent. Firstly, the change in $T_{\mathrm{refl}}\,(x = L\,,\,t)$ is dependent on the gas flow rate - higher flow rates lead to a faster rise in $T_{\mathrm{refl}}\,(x = L\,,\,t)$. Secondly, there is a large initial gradient present for all flow rates. Both these observations are indicative of the thermocouple recording temperatures that lag behind the true inner plenum wall temperature, $T_{\mathrm{w}}\,(x = L\,,\,t)$. While the embedded thermocouple provided some indication of $T_{\mathrm{w}}\,(x = L\,,\,t)$, it was placed 1 mm away from the inner surface, and was embedded using an epoxy adhesive. Conduction and contact heat resistances were probably present, leading to this lag in response. The thermocouple could not be placed inside the plenum for the same reasons described in Section 7.3.2. Thus, $T_{\mathrm{w}}\,(x = L\,,\,t)$ needed to be evaluated from measured temperatures, before the relationship between $T_{\mathrm{refl}}\,(x = L\,,\,t)$ and $T_{\mathrm{w}}\,(x = L\,,\,t)$ could be established. Equation (7.9) describes a simple heat balance within the plenum, relating the gas and wall temperatures.

$$h\big(T_{\mathrm{f}}\left(t\right)-T_{\mathrm{w}}\left(t\right)\big)\big|_{x=L}=k\frac{\mathrm{d}T_{\mathrm{w}}\left(t\right)}{\mathrm{d}x}\bigg|_{x=L} \tag{7.8}$$

$$\approx k\frac{T_{\mathrm{w}}\left(x=L\,,\,t\right)-T_{\mathrm{TC}}\left(t\right)}{l_{\mathrm{TC}}} \tag{7.9}$$

Here, h is the convective heat transfer coefficient between the gas and plenum wall, l_{TC} is the distance between the thermocouple tip and plenum inner wall, and k is a composite thermal conductivity that incorporates contact as well as conduction resistances in the wall of the plenum. Since h is a function of the gas flow rate, V, via the Reynolds number, this equation can be modified and rearranged to obtain an expression for $T_{\mathrm{w}}\left(x=L\,,\,t\right)$.

$$T_{\mathrm{w}}\left(x=L\,,\,t\right)=\frac{V^{A}\,T_{\mathrm{f}}\left(x=L\,,\,t\right)+B\,T_{\mathrm{TC}}\left(t\right)}{V^{A}+B} \tag{7.10}$$

where A and B are both constants incorporating h, k and l_{TC}. In order to establish a relationship between $T_{\mathrm{w}}\left(x=L\,,\,t\right)$ and $T_{\mathrm{refl}}\left(x=L\,,\,t\right)$, $T_{\mathrm{w}}\left(x=L\,,\,t\right)$ was first evaluated using an initial guess for A and B. These values were then modified in a least-squares optimisation routine using all calibration data until a unique relationship independent of gas flow rate was obtained. Figure 7.17 presents a flow chart of how this procedure was implemented.

Figure 7.18 plots the change in $T_{\mathrm{refl}}\left(x=L\,,\,t\right)$ against the change in $T_{\mathrm{w}}\left(x=L\,,\,t\right)$ obtained post least-squares optimisation for the UHTC sample. A linear relationship was obtained between $T_{\mathrm{refl}}\left(x=L\,,\,t\right)$ and $T_{\mathrm{w}}\left(x=L\,,\,t\right)$ in dynamic calibrations for all samples. In addition, a similar value for A of approximately 0.5 was obtained across calibrations for all samples. This constant is the exponent the Reynolds number is raised to in Nusselt number correlations - the value obtained is identical and of a similar order of magnitude to many other common correlations present in the literature [51].

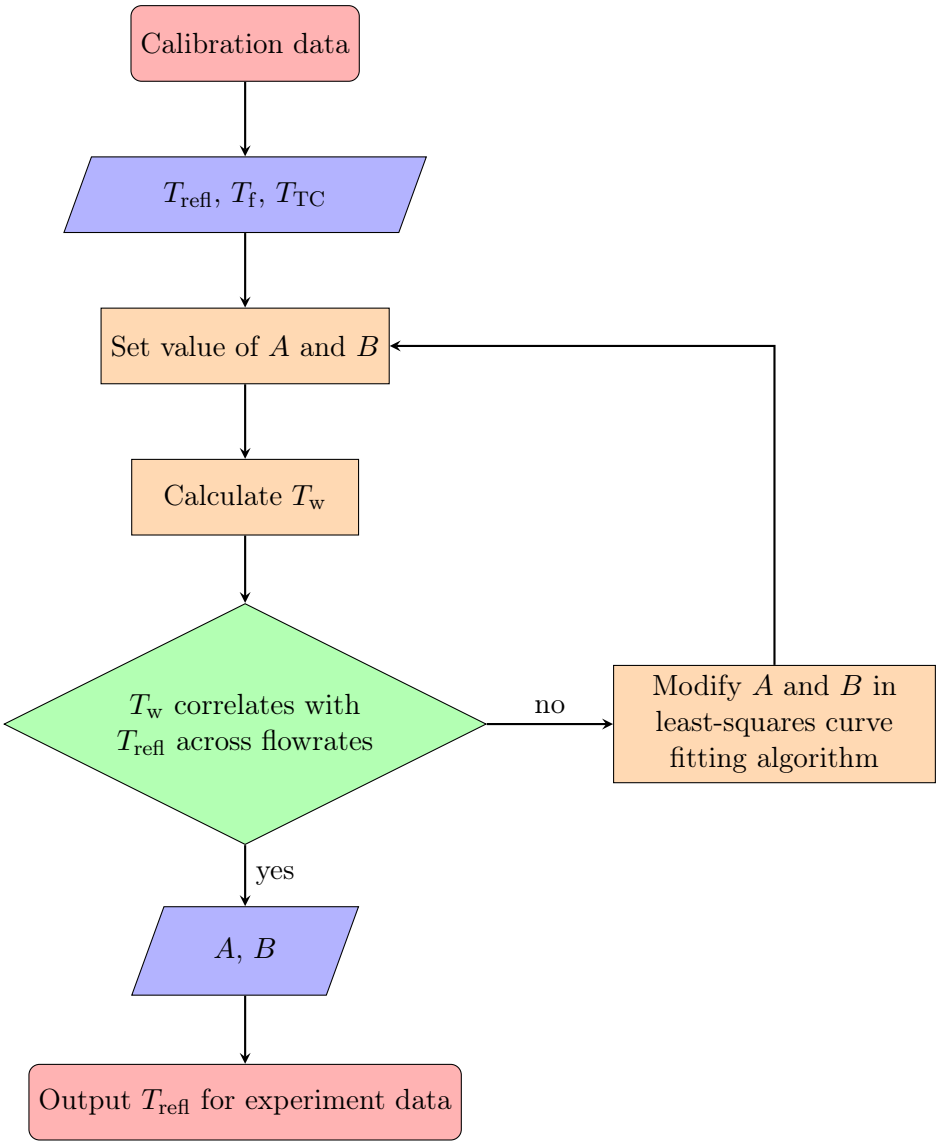


Figure 7.17: Flow chart describing calibration procedure for dynamic reflected temperature compensation

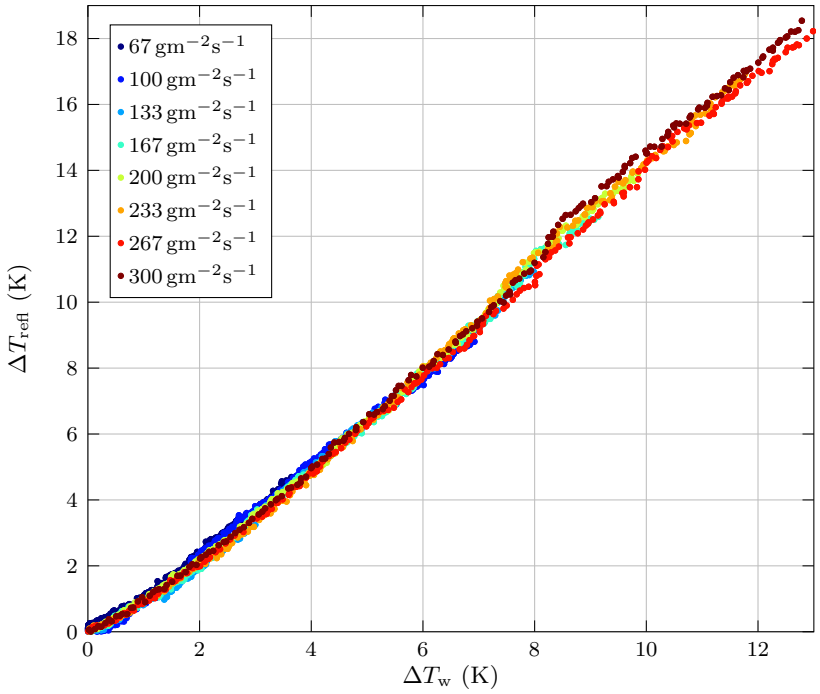


Figure 7.18: Change in T_{refl} plotted against change in T_{w} for the UHTC sample

7.4.3 Through flow area

The mass flux to be used in the numerical scheme was evaluated using the mass flow rate set on the MFC, and through flow area of the porous sample. Nominally, each sample was manufactured to have a through flow area of 40 mm × 40 mm. In some cases, the through flow area was reduced due to blockage from silicone adhesive seeping into the sample's pores, during its assembly onto the plenum cover plate. This was found to be the case mainly for the C/C sample. To account for this, hot-wire anemometry tests were performed in order to characterise the effective through flow area of the sample. The system used was a pre-built rig created as part of the wider research programme [131]. This system consisted of a miniature hot wire probe (Dantec Dynamics P14) held stationary over the plenum, which was in turn mounted on a set of motorised traverses (Thorlabs MTS50/M-Z8) enabling movement in a horizontal $x - y$ plane. During operation, flow velocity measurements were made with the hot-wire in pre-defined step sizes of 1 mm, automatically controlled using the motorised traverses. The probe was positioned 1 mm above the sample surface. A moderate flow rate was used to prevent effused gas from

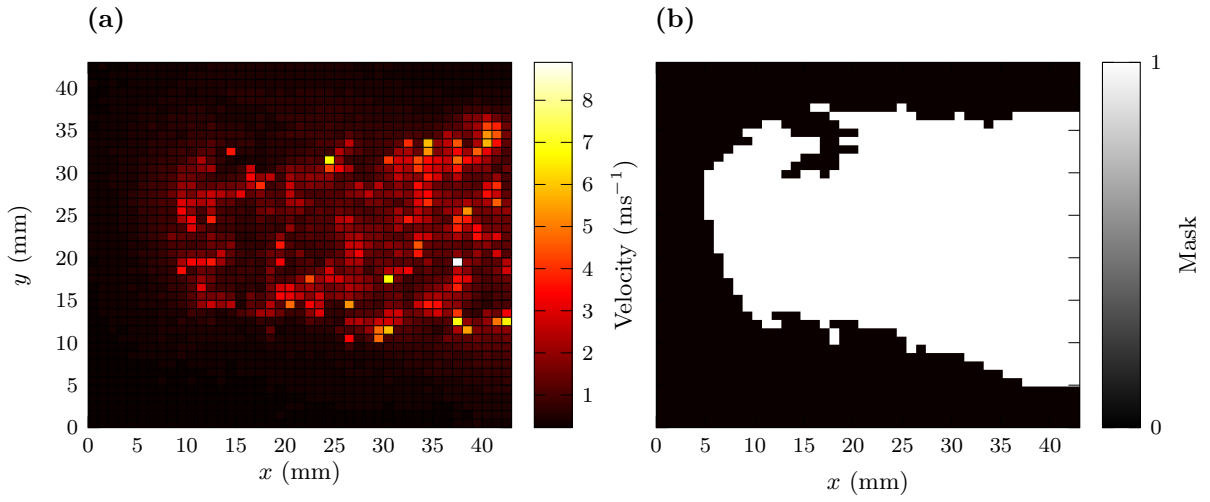


Figure 7.19: C/C hotwire velocity map and binarised flow mask

diffusing laterally before reaching the probe, leading to an inaccurate measurement of area. In the case of C/C, this was the median tested flow rate of 15 slpm. Figure 7.19 (a) shows the hot-wire velocity map for the C/C sample. Bright regions represent areas of high velocity, while dark regions represent areas of low velocity. Figure 7.19 (a) was binarised, yielding a flow mask that isolated blocked regions from the remaining through flow area. The resulting flow mask obtained is shown in Figure 7.19 (b) - this was used to calculate the true flow area for use in the numerical scheme. This investigation found an area blockage of 37 %, and negligible blockage for all other samples.

7.5 Data post-processing

This section describes the process applied to raw measured data to convert it into temperature transients. Figure 7.20 presents a flow chart summarising the relevant steps.

Thermocouple, pyrometer and pressure transducer data were streamed via the Pico Technology USB TC-08 Thermocouple Logger. Data from these transducers were recorded on the PicoLog 6 data logging software at a frequency of 10 Hz. This was then down-sampled to a frequency of 1 Hz using trigger pulse cues from a digital pulse delay generator (Berkeley Nucleonics Model 575), synchronising all measurements. Trigger signals were streamed via a separate data logger (Pico

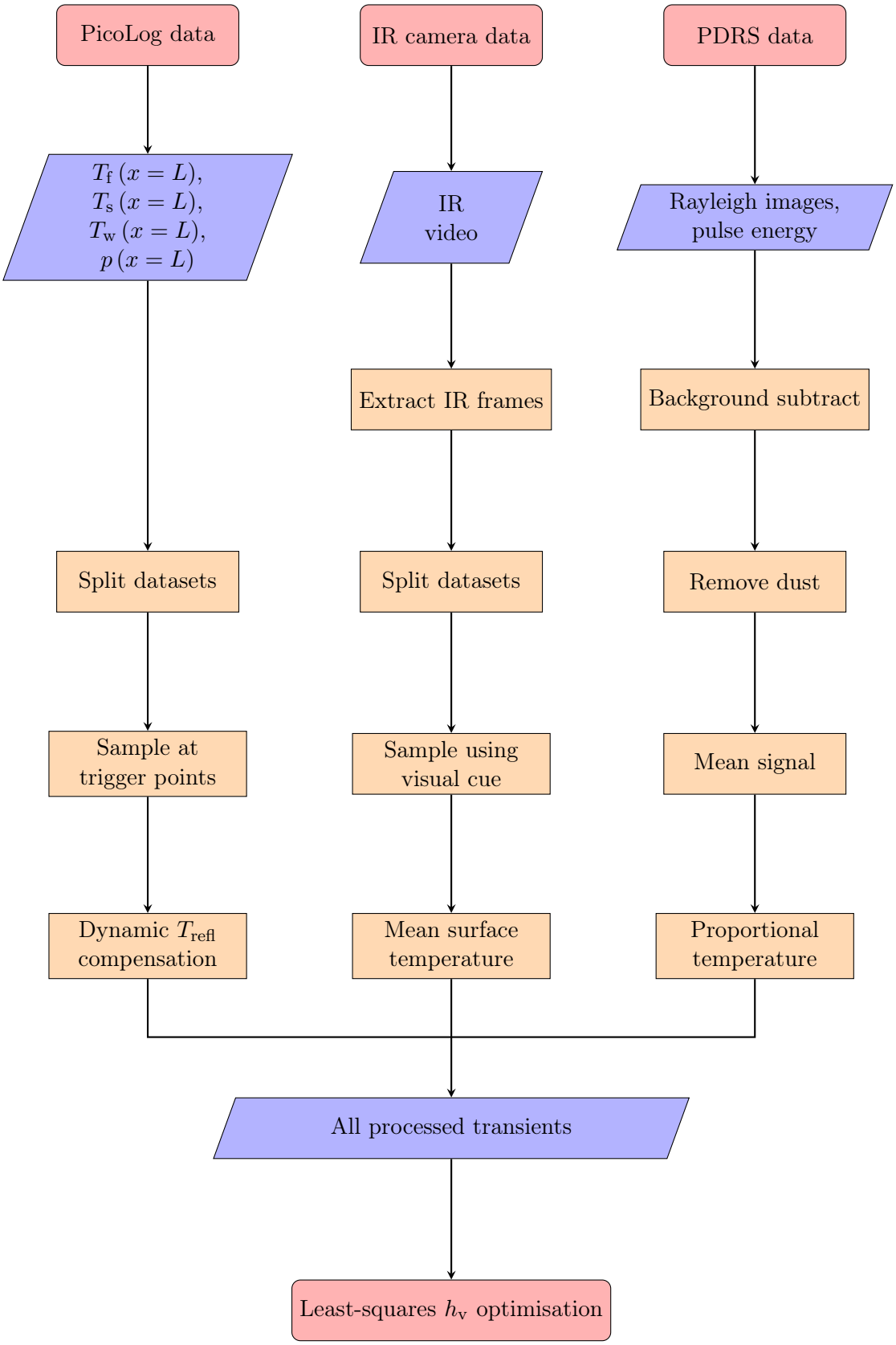


Figure 7.20: Flow chart describing post-processing procedure for measured data in preparation for use in least-squares optimisation algorithm

Technology DrDAQ) but recorded on the same software, as this device had a finer temporal resolution (1 kHz sampling) and was more suited for scope input signals. Thermocouple and pressure transducer data was then saved without further modification.

Pyrometer temperature data was split into two separate datasets, one for the experiment and one for the cool-down phase. The experiment data was then corrected using the dynamic T_{refl} calibration data obtained using the procedure described in Section 7.4.2. Calibration constants A and B were used along with experimental T_{f} and T_{TC} transients to evaluate T_{w}. Subsequently, the established correlation between T_{w} and T_{refl} was used to obtain transient ambient radiation in the plenum during the experiment. Pyrometer measured data was then corrected using Equation (2.31) (refer to Section 2.4) with true values of T_{refl}.

IR camera images were recorded by first streaming live video using VLC Media Player, and subsequently using a frame grabbing software (Virtual Dub) to extract image frames from the saved video. As with the pyrometer, IR camera frames were split into experimental and cool-down datasets. Images were streamed at a 10 Hz frame rate, from which experiment data was down-sampled as before using a *visual* cue triggered by the digital pulse delay generator. This was necessary as the camera used did not have an external trigger input. The visual cue used was a linear solenoid actuator, placed in the field of the view of the IR camera, actuating at a frequency of 1 Hz. Synchronisation of data was attained by sampling frames in which the solenoid had actuated. Figure 7.21 shows two consecutive IR images, demonstrating the linear motion of the actuator. Average surface temperatures were then evaluated from sampled experiment images and cool-down images.

PDRS data was processed in a similar manner to that described in Chapter 5, with minor modifications. Since a 1-D approach was used in these experiments, the output composition of the gas was forced to be uniform. As a result, composition effects on the Rayleigh signal were omitted - thus only one camera was necessary. This removed the need for obtaining a grid image,

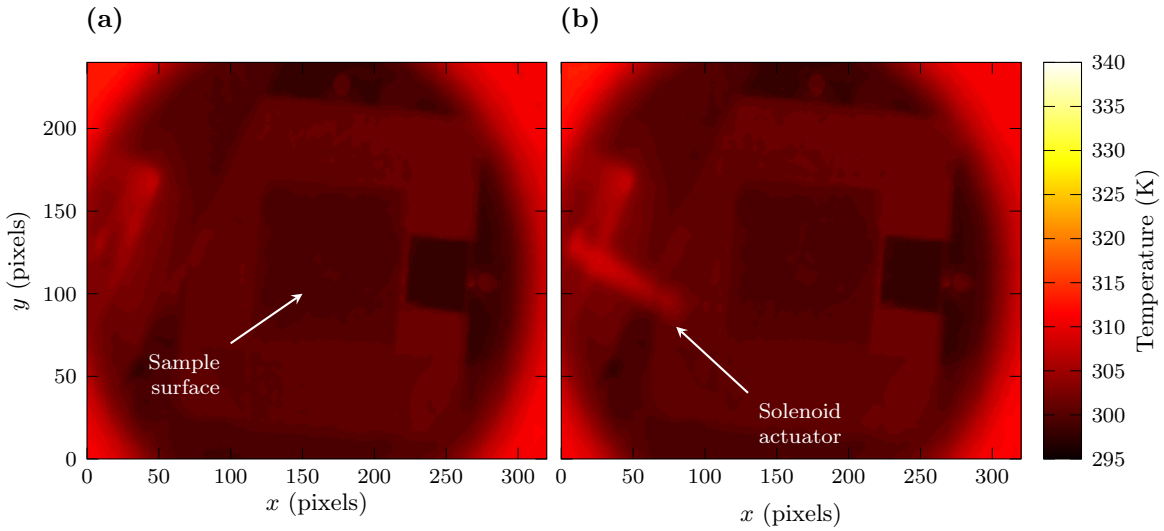


Figure 7.21: Consecutive images from IR camera demonstrating linear actuator motion

as pixel-to-pixel mapping was not required. Sheet uniformity corrections were also omitted as average signals across the illuminated region were obtained. The laser sheet profile was assumed to remain constant from shot-to-shot. The camera was triggered by the digital pulse delay generator, so no temporal resampling was required. Images were first background subtracted by subtracting the mean signal in the region outside laser illumination. Next, stray dust particles were masked and interpolated inwards. The mean signal across the laser-illuminated region was then evaluated as a time series. This was then corrected for shot-to-shot total pulse energy fluctuations as follows. The transient pulse energy profile measured by the energy meter was divided by the mean signal - this produced a time series that was proportional to temperature. Outliers were removed, before the initial steady state constant temperature (pre-heating) was used to scale proportional temperatures into absolute temperatures.

7.6 Results and discussion

In this section, results from the combined 1-D experimental and numerical investigation are presented for all tested samples. In particular, fitted h_v values are provided as a function of mass flux. All results were obtained using N_2 as the effused gas.

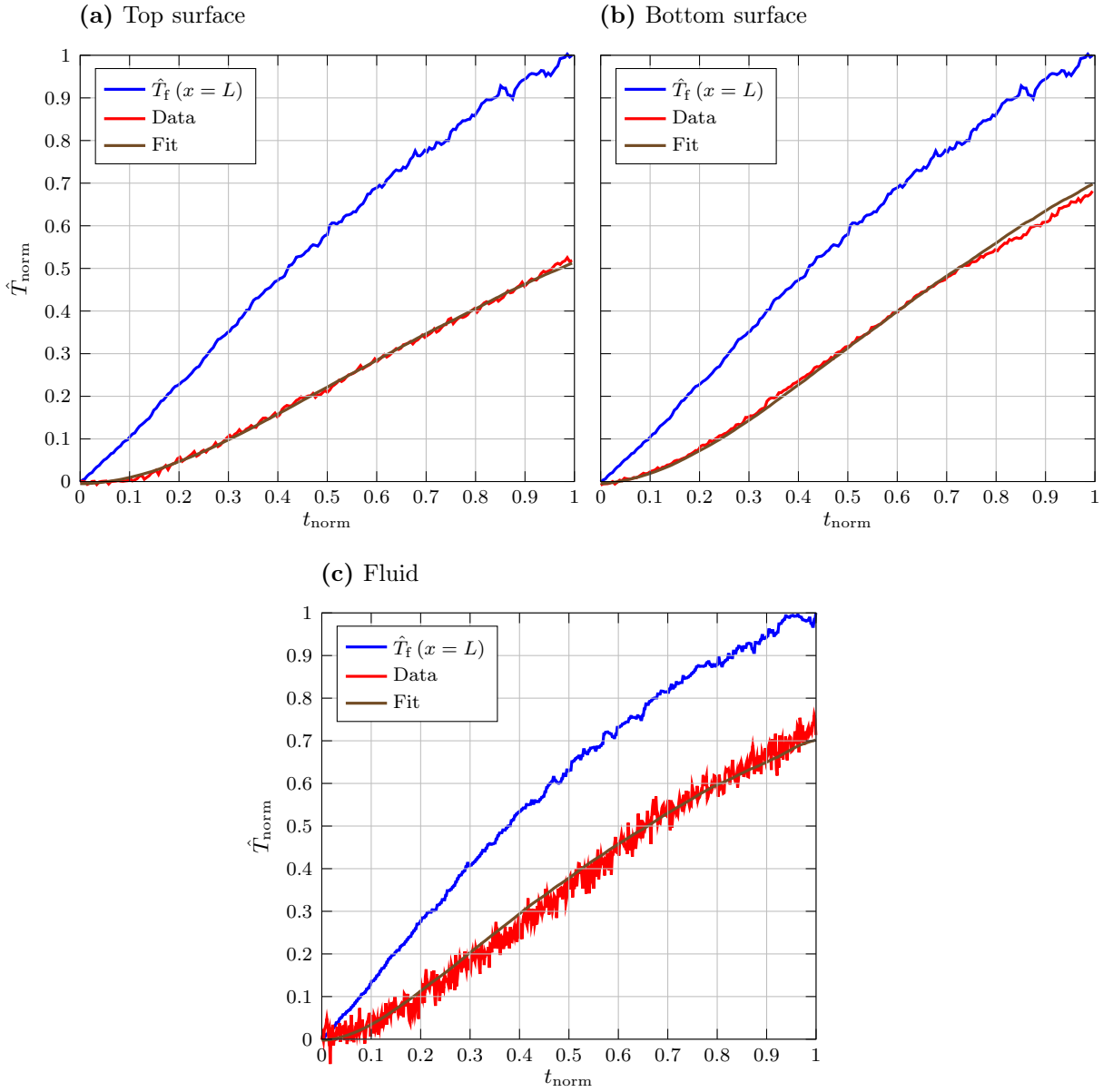


Figure 7.22: Comparison between experimentally measured and numerically modelled data for calculation of h_{v}. Transients have been truncated to omit the initial constant temperature period, and normalised by the final change in input gas temperature $\hat{T}_{\mathrm{f}}\,(x=L)$, as well as time

Figures 7.22 and 7.23 present example comparisons between measured data and modelled transients - Figure 7.22 for the experiment dataset (h_{v} estimation) and Figure 7.23 for the cool-down dataset (a estimation). Transients have been plotted in terms of the normalised temperature, T_{norm}, and time, t_{norm}, where normalisation is defined in Equation (7.11).

$$x_{\mathrm{norm}} = \frac{x - x_{\mathrm{start}}}{x_{\mathrm{end}} - x_{\mathrm{start}}} \tag{7.11}$$

where x is the parameter being normalised, and subscripts 'start' and 'end' refer to the first and last values of the transient respectively. Note that the starting value has been defined according to the start of gas heating, i.e. the initial constant temperature period is ignored.

Figures 7.22 and 7.23 arbitrarily present results from the UHTC sample for $\dot{m}_A = 200\,\mathrm{gm^{-2}s^{-1}}$, but the closeness of fit seen here is identical across all samples and $\dot{m}_A$. As mentioned previously, a termination tolerance of 1×10^{-8} was used in the optimisation routine. In general, there is a very close agreement in transient profile between numerical and experimental results. The scatter of data points evident in Figure 7.22 (c) arises from photon shot noise in Rayleigh scattering signals. The standard deviation of this scatter is approximately 0.2 % of the temperature being measured. Raw Rayleigh signals exhibited data scatter larger than this, amounting to about 5 % of the mean signal value. However, this scatter was found to be highly correlated with the measured laser pulse energy, thus accounting for this led to the present higher precision.

As mentioned in Chapter 6, estimation of the heat loss parameter a could theoretically be achieved using two separate surface temperatures i.e. the top or bottom surfaces. In practice, only the top surface was used. The closeness of fit obtained from top surface transients (Figure 7.23 (a)) was much better than that of bottom surface transients (Figure 7.23 (b)). Measured bottom surface temperatures exhibited a larger gradient at the start of the cool-down, and shallower gradients towards the end. The reason for this behaviour is cooling of the inner

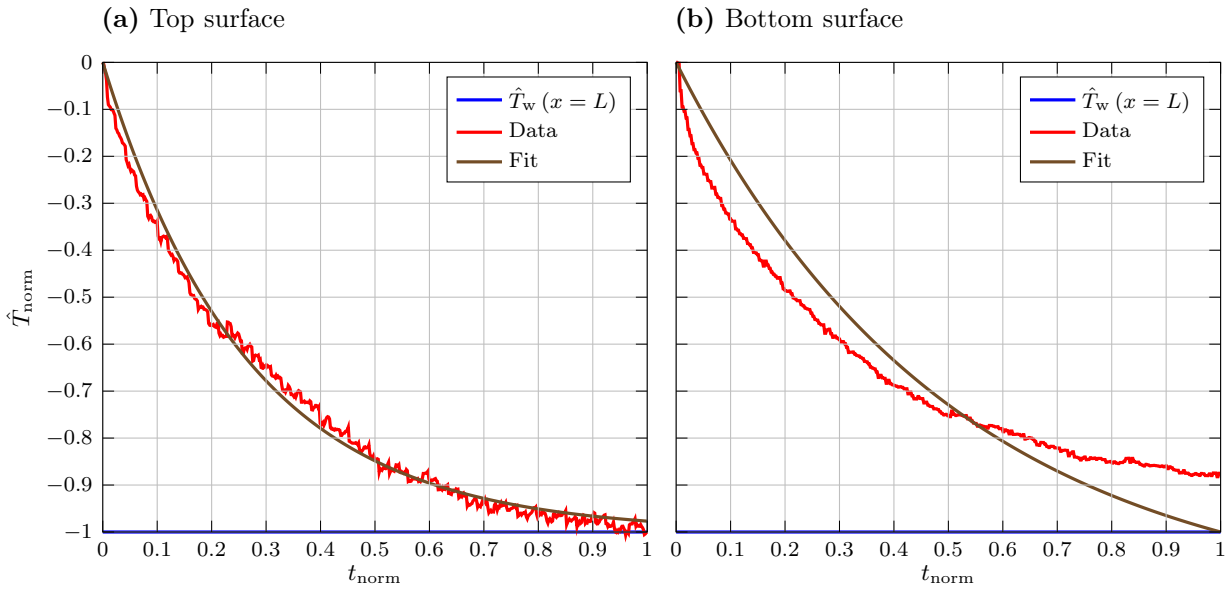


Figure 7.23: Comparison between experimentally measured and numerically modelled data for calculation of a. Transients have been normalised by the final change in modelled temperature and time

plenum wall during the cool-down phase. This leads to a decreasing T_{refl} inside the plenum, causing the apparent bottom surface temperature to drop quickly. Accounting for this change in inner plenum wall temperature during cool-down would require a separate model and calibration procedure, thus it was not attempted.

In the following sections, note that the material properties quoted (apart from ϕ) represent those of a fully-dense material i.e. non-porous. The effect of porosity on ρ_{s} and k_{s} is accounted for in the governing transport equations presented in Section 6.2. As mentioned previously, uncertainty in fitted h_{v} was obtained using the method of Moffat [123]. Measurement uncertainties for all devices used are presented in Table 7.3, while individual uncertainties of sample material properties are provided in the subsequent sections. Table 7.4 presents physical properties and Sutherland's law constants (for calculation of μ_{f}) of N_2 used in the numerical scheme. Values used for $c_{p,\mathrm{f}}$ and k_{f} were fixed, and evaluated at a mean gas temperature of 318 K. Variation of these values in the range of tested temperatures were neglected, as they were small (± 0.1 % for $c_{p,\mathrm{f}}$, and ± 5 % for k_{f}).

Table 7.3: General measurement uncertainties of the experimental framework

p	u_m	$T_\mathrm{s}\,(x=0)$	$T_\mathrm{s}\,(x=L)$	$T_\mathrm{f}\,(x=0)$	$T_\mathrm{f}\,(x=L)$
0.06 bar	1 %	2 %	1 %	1 %	0.5 K + 0.2 %

Table 7.4: Physical properties of N_2 gas. R is the individual gas constant, used in the determination of ρ_f with the ideal gas law

R ($\mathrm{Jkg^{-1}K^{-1}}$)	$c_{p,\mathrm{f}}$ ($\mathrm{Jkg^{-1}K^{-1}}$)	k_f ($\mathrm{mWm^{-1}K^{-1}}$)	T_ref (K)	C_ref (K)	μ_ref (Pa s)
297	1040	27.3	301	111	1.78×10^{-5}

7.6.1 Siperm B: Packed bed of sintered bronze spheres

The Siperm B sample was tested first as a means to validate the combined numerical and experimental framework. Table 7.5 lists the material properties of the Siperm B sample used, along with their uncertainties.

Table 7.5: Material properties of Siperm B sample

L (mm)	k_s ($\mathrm{Wm^{-1}K^{-1}}$)	$c_{p,\mathrm{s}}$ ($\mathrm{Jkg^{-1}K^{-1}}$)	ρ_s ($\mathrm{kgm^{-3}}$)	ϕ
3	59.0 ± 4.5	376	8700 ± 100	0.385 ± 0.025

Figure 7.24 presents the distribution of measured h_v against $\dot{m}_A$. An increase in $\dot{m}_A$ leads to an increase in h_v as expected. Here, a close agreement between h_v obtained from all three transients, including bottom surface measurements, is present. Bottom surface h_v estimates start to deviate slightly for larger $\dot{m}_A$, possibly as a result of the adiabatic bottom surface boundary condition becoming invalid at larger flow speeds. Forced convection between the bottom surface and impinging hot gas is the likely cause for enhanced heat transfer, leading to larger h_v estimates. In this figure, data points denoted 'combined' represent the uncertainty-weighted averages of all other measurements, where the weight assigned to each h_v measurement when calculating the 'combined' h_v is inversely proportional to its squared error.

A number of correlations and experimental results exist in the literature for internal heat transfer in packed bed of spheres. The vast majority of these are compiled for large Reynolds numbers, as a result of using large diameter spheres [53, 133, 134, 54]. The current tested sample had a high permeability of $K_\mathrm{D} = 65 \times 10^{-12}\,\mathrm{m^2}$, allowing large flow rates to be tested. Nonetheless,

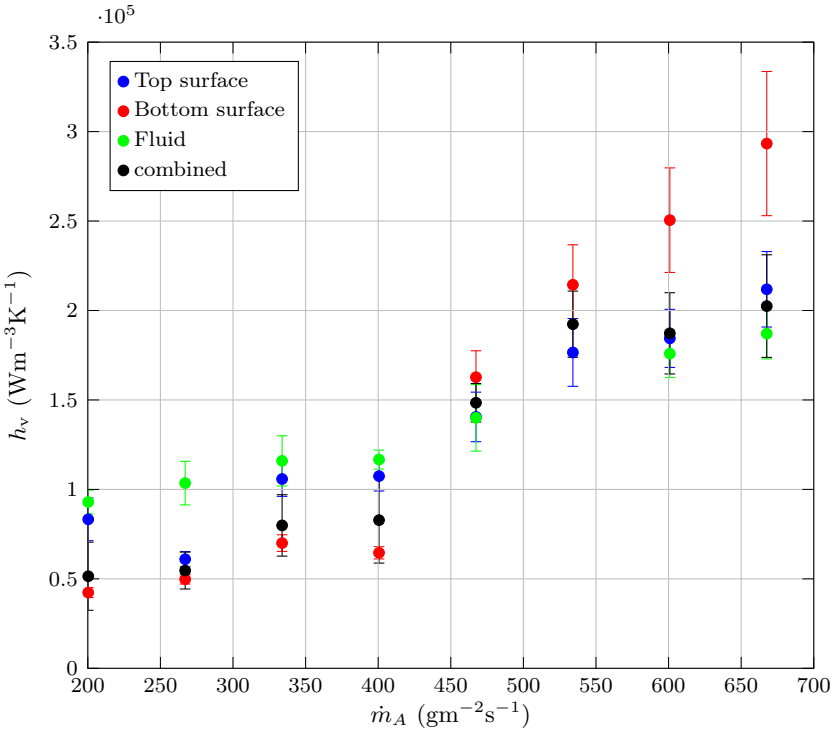


Figure 7.24: Extracted h_v for Siperm B sample against $\dot{m}_A$

the spheres in the tested sample were small by comparison, with an average diameter of 286 µm, thus achievable Reynolds numbers were below those tested in most correlations. A review by Kunii and Suzuki [135] compiles results from a number of experimental investigations testing low Reynolds number heat and mass transfer in packed beds, thus measured h_v were compared to these. Reynolds numbers for packed beds, $\mathrm{Re_p}$, were defined using the sphere diameter, d_p, as the characteristic length, as shown in Equation (7.12).

$$\mathrm{Re_p} = \frac{\rho_f d_p u_m}{\mu_f} \tag{7.12}$$

Results were compiled in terms of the Peclet, $\mathrm{Pe_p}$, and Nusselt, $\mathrm{Nu_p}$, numbers, where the former is defined as $\mathrm{Pe_p} = \mathrm{Re_p} \cdot \mathrm{Pr}$, and the latter is defined according to Equation (7.13)

$$\mathrm{Nu_p} = \frac{h_p d_p}{k_f} \tag{7.13}$$

where h_p represents the internal convective heat transfer coefficient. h_v is related to h_p via the surface area per unit volume, α_v, according to $h_v = h_p \cdot \alpha_v$, and α_v is defined in Equation (7.14) [53]. For this sample, $\alpha_v = 1.3 \times 10^4\,\mathrm{m}^{-1}$.

$$\alpha_v = \frac{6\,(1-\phi)}{d_p} \tag{7.14}$$

Figure 7.25 plots the weighted average results obtained experimentally along with a number of literature results in the relevant Pe_p range. Legend entries provided have been listed exactly as they were presented in the original compilation from Kunii and Suzuki, for ease of reference. 'G' refers to works from Grootenhuis [136], 'E' refers to works by Eichhorn and White [137], and 'D' refers to data from Donnadieu [138]. Two main observations can be made from this figure. Firstly, there is a wide spread of Nu_p measured by different authors - for example, there is an order of magnitude difference in Nu_p between 'G3' and 'D' at $Pe_p = 10$. The difference in results between authors has been attributed mainly to the use of different sized spheres, amongst other reasons. Secondly, a very close agreement is seen between the region 'G3' and the results measured in this work. Experiments by Grootenhuis were conducted on sintered metal spheres, while others were not, and this provides further validation that the 1-D modelling framework was capable of recreating experimental results. The specific 'G3' dataset was for $d_p = 64\,\mu\mathrm{m}$, while that of 'G2' was for $d_p = 210\,\mu\mathrm{m}$, both of which are comparable to the sphere size tested in this work. An almost direct comparison of sphere size can be made with the dataset 'E3' which used $d_p = 280\,\mu\mathrm{m}$, but Kunii and Suzuki claim that results from this work are likely to be over-estimates due to a lack of axial conduction effects being considered. This tallies with current observations as well.

Overall results from this section have demonstrated the ability of the established experimental framework to reproduce results in the literature to a high accuracy. This provides validation that the technique works, and can be used to measure h_v for candidate transpiration cooling

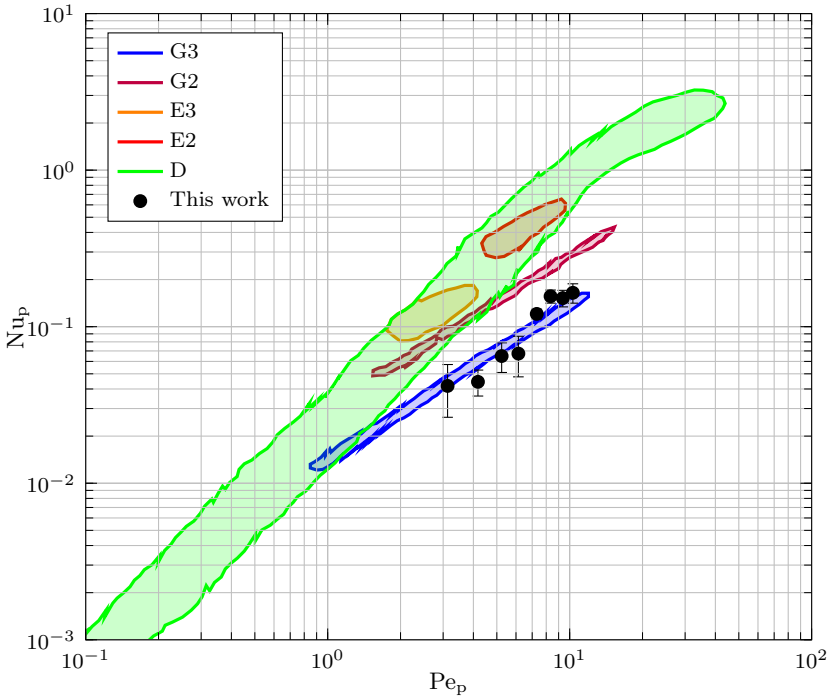


Figure 7.25: $\mathrm{Nu_p}$ plotted against $\mathrm{Pe_p}$ for Siperm B sample. Included are experimental results obtained from other investigations in the literature in the relevant $\mathrm{Pe_p}$ range; data obtained from compilation by Kunii and Suzuki [135]

materials.

7.6.2 UHTC: Zirconium diboride Ultra High Temperature Ceramic

The first transpiration cooling candidate material tested was the UHTC. The specific sample investigated in this second set of tests was different to the one tested in Section 7.3 (sample UHTC-8 from [131]). Nonetheless, its material properties were the same - these can be found in Table 7.1.

Figure 7.26 presents the distribution of measured h_v against $\dot{m}_A$ for this sample. As before, an increase in h_v is evident as $\dot{m}_A$ increases. A very strong agreement in fitted h_v for all three measured transients and $\dot{m}_A$ is seen, yet again. In general, h_v values were in the 10^4 range, which is similar to results obtained by Hermann [117], albeit with different mass fluxes being tested. An estimate for the porous particle size, d_p, can be obtained using the Ergun approximation [139], given in Equation (7.15)

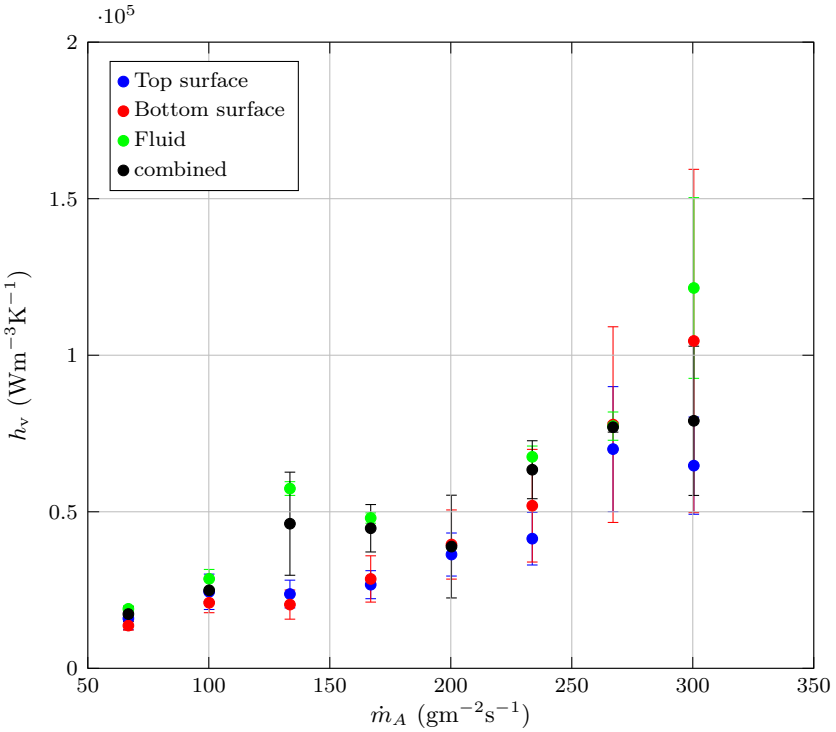


Figure 7.26: Extracted h_v for UHTC sample against $\dot{m}_A$

$$K_D = \Psi^2 \frac{\phi^3 d_p^2}{150\,(1-\phi)^2} \tag{7.15}$$

where Ψ is the particle sphericity, which is equal to 1 for a perfect sphere and less than 1 for anything else. Here, extracted d_p for the UHTC sample may be slightly inaccurate, as Ψ is estimated to be 1. Nonetheless, an estimate for α_v can be obtained from a known d_p, which enables isolation of internal cooling capabilities caused by porous material packing characteristics. Using $K_D = 3.775 \times 10^{-14}\,\mathrm{m}^2$ [131], a value of $d_p = 5.4\,\mu\mathrm{m}$ was obtained. This corresponds to $\alpha_v = 6.6 \times 10^5\,\mathrm{m}^{-1}$ which is high, relative to the Siperm B sample. Thus, the bulk of the internal cooling effect in this particular UHTC material seems to originate from the large internal surface area for heat transfer.

Figure 7.27 compares the results obtained for the UHTC sample in this work against the Florio correlations (elaborated in Section 7.3), as well as results from Hermann [117]. In general, experimental results, including those of Hermann, seem to be larger than those predicted by

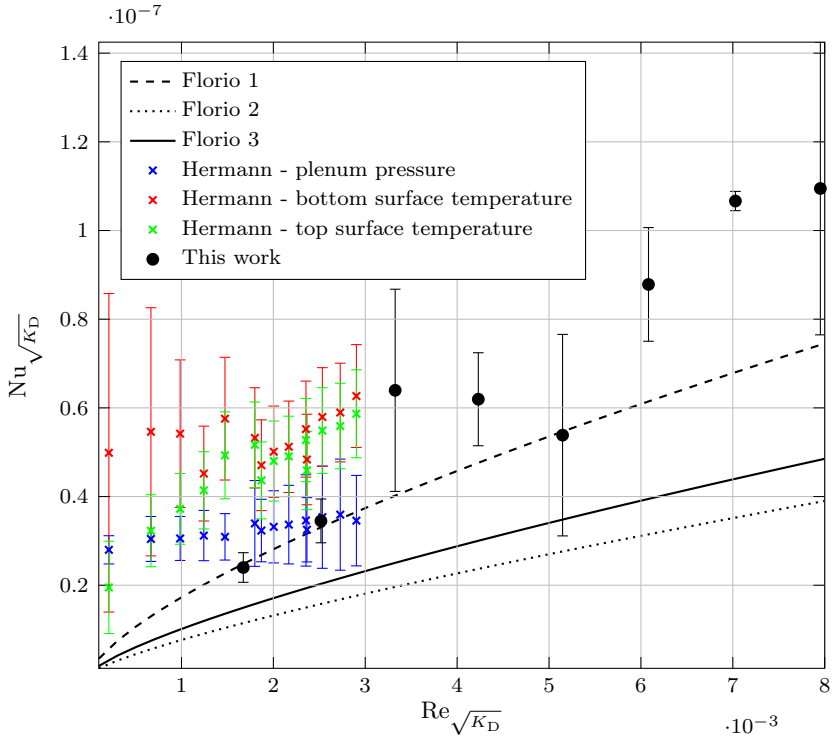


Figure 7.27: $\mathrm{Nu}_{\sqrt{K_\mathrm{D}}}$ plotted against $\mathrm{Re}_{\sqrt{K_\mathrm{D}}}$ for UHTC sample. Included are experimental results obtained from Hermann [117] and correlations from Florio [113]

Florio's correlations. This does not come as a surprise, since the configurations being tested were fairly different. In the existing correlations, the use of K_D as the characteristic length was justified by the author considering no single consistent length scale could be identified in a decomposing material. This however, is not the case when considering an intact porous medium. When comparing current results with those of Hermann, not much overlap of tested $\mathrm{Re}_{\sqrt{K_\mathrm{D}}}$ is present, however continuity of $\mathrm{Nu}_{\sqrt{K_\mathrm{D}}}$ is evident across both sets of data. In summary, this work has provided an extension of $\mathrm{Nu}_{\sqrt{K_\mathrm{D}}}$ data to larger $\mathrm{Re}_{\sqrt{K_\mathrm{D}}}$ for this particular UHTC material, which will prove useful in complete systems-level design of hypersonic vehicles using transpiration cooling.

7.6.3 C/C: Carbon-fiber-reinforced carbon composite

The second transpiration cooling candidate material tested was C/C. Table 7.6 lists the material properties of the C/C sample used, along with their uncertainties.

Figure 7.28 presents the distribution of measured h_v against $\dot{m}_A$ for this sample. Similar trends

Table 7.6: Material properties of C/C sample

L (mm)	k_s ($\mathrm{Wm^{-1}K^{-1}}$)	$c_{p,s}$ ($\mathrm{Jkg^{-1}K^{-1}}$)	ρ_s ($\mathrm{kgm^{-3}}$)	ϕ
5	2.01 ± 0.20	1650 ± 66	1581 ± 16	0.13

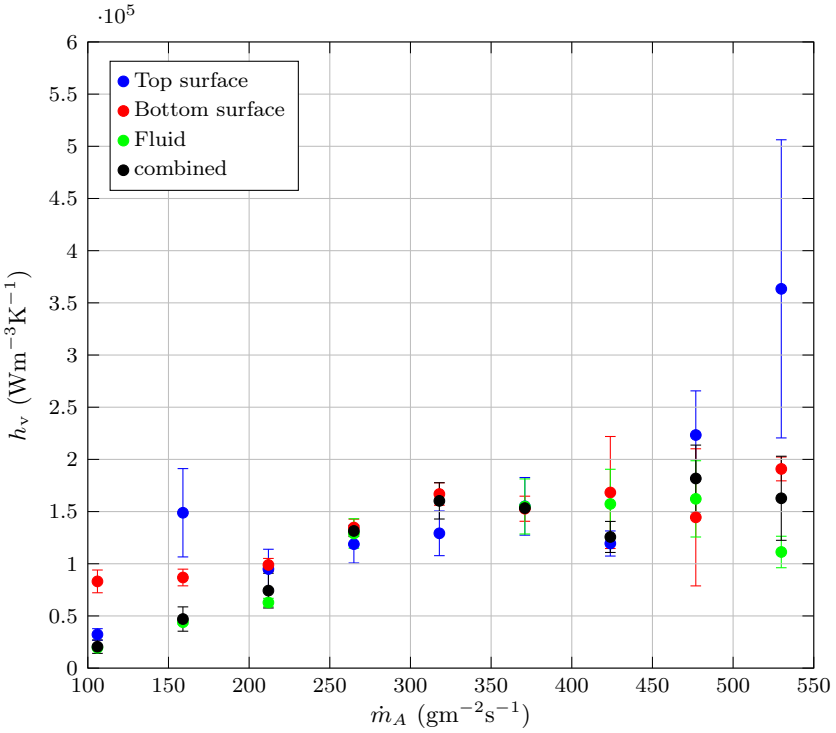


Figure 7.28: Extracted h_v for C/C sample against $\dot{m}_A$

and observations to the previous samples are evident in this figure, albeit with slightly larger disagreement between the three fitted values at higher $\dot{m}_A$. This may be attributed to a change in depth-wise blockage at higher plenum pressures, as more gas starts to be forced through partially impacted regions of the sample. This effectively changes the through flow area, thus changing $\dot{m}_A$ to varying extents across the thickness of the sample.

Figure 7.29 compares the h_v values measured for the UHTC and C/C sample, to highlight which performs better. When compared to the UHTC sample, h_v for C/C lies mainly in the 10^5 range for similar mass fluxes, implying enhanced internal cooling. Previous works have hypothesised this observation due to the large number of micro-dimensional internal cavities in C/C, but the h_v values estimated by other authors have been an order of magnitude larger than those measured here [125, 129]. A similar use of the Ergun approximation (again, inaccurate, but provides an order of magnitude estimate) with sample K_D =1.65 × 10^{-13} $\mathrm{m^2}$ yields d_p = 92 µm

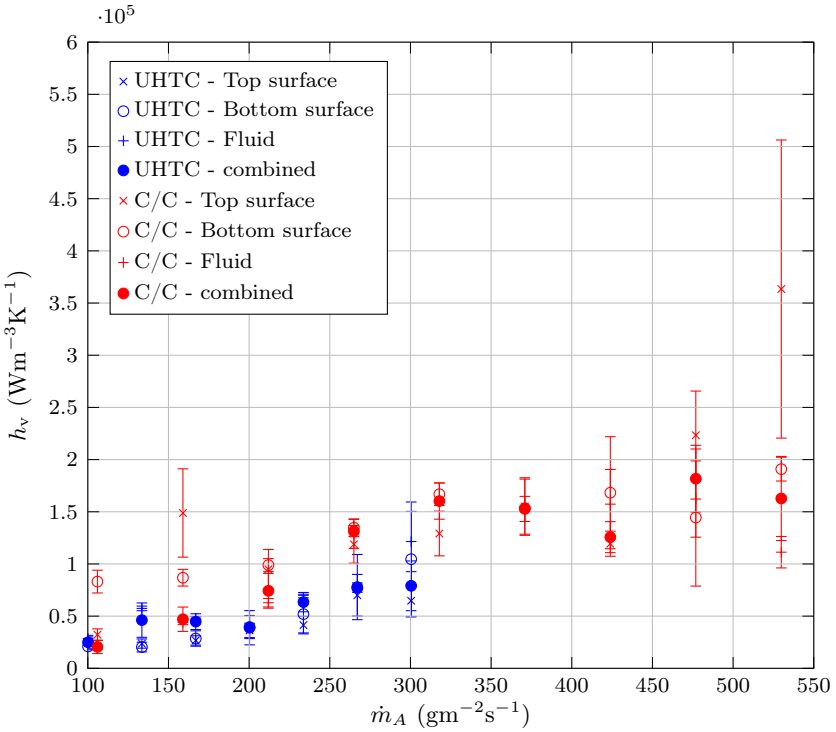


Figure 7.29: Comparison of h_v variation with $\dot{m}_A$ for UHTC and C/C sample

and $\alpha_v = 5.7 \times 10^4\,\mathrm{m}^{-1}$. Accounting for the highly non-spherical shape of 'particles' in C/C via a sphericity, i.e. $\Phi \ll 1$ reduces α_v even further. Thus, the internal cooling capability of C/C is much better than the UHTC, especially considering a smaller internal packing surface area.

Figure 7.30 compares the results obtained for the C/C sample in this work against the Florio correlations. A similar observation to the UHTC sample is seen here, in that measured results give larger predictions compared to Florio's correlations. To the author's knowledge, this represents the first measured set of data for internal cooling of C/C.

7.7 Summary

This chapter detailed the development of an experimental framework employing two simultaneous planar optical diagnostic techniques, namely Rayleigh Scattering and IR thermography, to infer the internal cooling mechanisms of transpiring porous media. The framework was utilised in a 1-D manner to measure the volumetric heat transfer coefficient, h_v, of candidate porous materials of this cooling technology. Measured temperature transients of samples subjected to

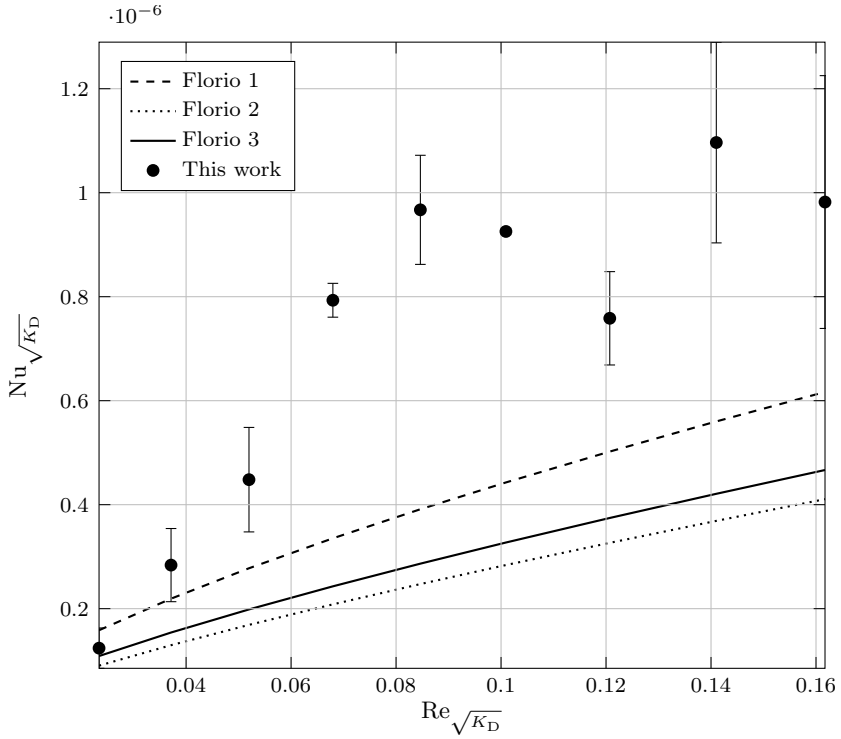


Figure 7.30: $\mathrm{Nu}_{\sqrt{K_\mathrm{D}}}$ plotted against $\mathrm{Re}_{\sqrt{K_\mathrm{D}}}$ for C/C sample. Included are correlations from Florio [113]

a gas heat input were compared to modelled transients (obtained using the numerical scheme described in Chapter 6) in order to extract this parameter. The framework was first validated by measuring h_v for a packed bed of spheres, as correlations exist in the literature for such materials. Comparable results were obtained, demonstrating that the framework is reliable. Volumetric heat transfer coefficients were then measured for two materials of interest, namely a ZrB_2 Ultra High Temperature Ceramic (UHTC), and a carbon-fibre-reinforced carbon (C/C) ceramic matrix composite (CMC). Results demonstrated that existing correlations that had been used to estimate h_v for these materials led to under-predictions. In addition, C/C outperforms UHTC in internal cooling, a result that has been stated by other authors, but this work demonstrates that it does so to a lesser extent than previously assumed. These findings will contribute to more accurate modelling of a complete transpiration cooling system's design, and will aid in choosing the appropriate material and injection conditions necessary for optimal cooling performance of hypersonic vehicles.

Chapter 8

Conclusions

This chapter summarises the achievements of this work and explores future investigations, improvements and applications of the techniques developed.

8.1 Research summary

The aim of this work was to develop multiparameter optical diagnostic techniques for use in high-speed flow research. The specific application of interest was transpiration cooling, a proposed TPS for hypersonic vehicles and jet engine turbines. Two techniques were proposed for their significant potential to add value in high-speed flow research; these were Fluorescent Particle Image Velocimetry (FPIV) and Polarised-depolarised Rayleigh Scattering (PDRS). The former is a simultaneous velocimetry and thermometry tool, capable of tackling one of PIV's main limitations, which is strong laser flare from surfaces and sprays. The latter is a simultaneous gas composition and temperature diagnostic, identified as an ideal candidate for characterising mixing flows, having previously been used in flame investigations. Both of these techniques were progressed independently.

8.1.1 Particle Image Velocimetry

Research on PIV began by first identifying key criteria for successful application of the technique for high-speed flow applications. These were established as the need for a uniform seeding density, high tracer-flow fidelity, adequate scattering signal from particles and a short inter-frame time camera. The former two requirements were ensured by sourcing a droplet aerosol generator from

LaVision, capable of producing a large quantity of small-sized droplets, with a modal diameter of 380 nm. Strong scatter signals from particles were ensured by using a suitable high-powered dual-cavity laser (New Wave Gemini PIV 200-15), while an inexpensive CCD camera (ImperX Bobcat B1621) capable of a 200 ns inter-frame time was sourced.

A PIV system was subsequently built *ab initio*, by assembling and synchronising key components previously listed. This system was tested on the wake of a cylinder in a confined channel to verify its reliability. Both qualitative and quantitative results satisfied expectations. The system was next applied to a novel active fluidic switching device to validate its flow switching mechanism at high Reynolds numbers. Comparison with CFD results was strikingly similar, with predicted prominent flow features being clearly highlighted. These investigations established that the PIV system was operational and capable of high-speed velocity measurements, whilst also clarifying the fluid mechanics of an active fluidic switching device.

8.1.2 Fluorescent Particle Image Velocimetry

FPIV was proposed as a variant of PIV, intended to allow simultaneous velocity and temperature measurements from particles, while tackling strong laser flare from elastic scattering off surfaces and sprays. The ability of FPIV to spectrally isolate elastic scatter from both surfaces and other gas streams was demonstrated using Rhodamine 6G dye-doped water droplets. Properties of an ideal fluorescent tracer for droplet PLIF measurements were then listed, the main considerations being its handling safety, fluorescence signal strength and relevant physical properties, such as its boiling point and volatility.

Diethyl-hexyl sebacate (DEHS), a common seeding substance in PIV experiments, was subsequently identified as being excitable by 266 nm radiation, leading to fluorescence at longer UV wavelengths, with a peak emission at 333.9 nm. This led to the novel discovery of temperature-dependent fluorescence emission from liquid DEHS. This seeding substance is widely used for thermo-fluid PIV experiments, as it has a number of desirable qualities. It is also commonly

sold in commercial boxed PIV systems. With the discovery of its fluorescence emission characteristics, DEHS shows great potential for use as a combined velocity and temperature tracer in FPIV experiments. This has substantial potential impact since the 'installed base' of DEHS PIV experiments is so large.

Fluorescence photo-bleaching of liquid DEHS was subsequently characterised, as a result of repeated high energy laser excitation. Next, a proof-of-concept experiment involving a simple heated jet was investigated to demonstrate the ability to extract temperature information from DEHS droplets. Initial attempts revealed differences in fluorescence emission between liquid and droplet forms of DEHS. Droplet emission was spectrally broader compared to liquid emission, both to shorter and longer wavelengths. Spectral broadening to shorter wavelengths led to a shift in peak emission wavelength to 285 nm. This effect was caused by reduced fluorescence self-absorption in droplet form, at emission wavelengths that overlap with the absorption spectrum. Broadening to longer wavelengths led to a distinct and separate fluorescence peak at 405 nm that was absent in liquid form. The cause of formation of this peak remains uncertain. Finally, this work demonstrated the ability to extract temperature information from DEHS droplets using the TC-PLIF method from a heated jet experiment.

8.1.3 Polarised-depolarised Rayleigh scattering

Development of PDRS began by identifying key criteria for its successful application. These were established as the need for gases with different depolarisation ratio r_{p}, high incident laser energy and a particle free environment. The former requirement was first investigated via a numerical sensitivity analysis. This quantified expected uncertainties from using gases better suited for a high speed facility, such as air and CO_2 (with closer r_{p} values). The latter two requirements were explored through a bench-top demonstration involving mixing of two different gases at varying temperatures. This demonstration was the first use of the technique in a non-flame related application. Insights gained from this preliminary experiment guided a feasibility

study on the applicability of PDRS to a high-speed flow facility, namely the Oxford High Density Tunnel (HDT). Lack of achievable signal was deemed the most crucial factor in confirming that applying PDRS to the HDT was unfeasible, using current resources.

8.1.4 Internal cooling of porous media

Good signal-to-noise ratio (SNR) achieved from the preliminary experiment motivated the use of PDRS in a bench-top investigation of transpiration cooling. The internal cooling efficiency of candidate porous media was investigated using a combined numerical and experimental framework. Rayleigh scattering was utilised for gas temperature measurements, while IR thermography provided simultaneous surface temperature measurements.

A 1-D numerical model was first developed, based on the impulse response convolution method, to predict the internal cooling mechanisms of transpiring porous media. The model was built upon a version used in a previous investigation [117]. Several key enhancements of the previous version were accomplished. Firstly, this work expanded the model's use to apply coolant gas heating as the heat input to the system, as opposed to a heat flux on the solid surface. Secondly, ambient heating contributions from an increase in plenum wall temperature were incorporated. Next, a new method for case-by-case heat loss estimation was implemented. Finally, a key modelling strategy was identified, that would yield sufficient temporal resolution of the input impulse, while ensuring acceptable code execution times. With the established model, the fluid-solid system behaviour was characterised as a result of changing various input parameters.

The complementary experimental framework was designed using PDRS and IR thermography, with the aim of providing spatially-resolved temperature and composition measurements in non-uniform transpiring porous media. In this work, uniformly porous samples were first tested, as a means to validate the framework. Average temperature results were evaluated, and compared to predictions from the numerical model, to extract the volumetric heat transfer coefficient, h_{v}, for candidate porous media. A novel technique for dynamic compensation of background infrared

radiation was also formulated, allowing infrared measurements in internal transiently heated environments.

The combined numerical-experimental framework was first validated by comparing h_v results for a packed bed of bronze spheres with existing correlations in the literature. Subsequently, the framework was applied to two candidate porous media for transpiration cooling, namely, a ZrB_2 Ultra High Temperature Ceramic (UHTC), and a carbon-fibre-reinforced carbon (C/C) ceramic matrix composite (CMC). This work obtained an extended dataset of h_v values for the UHTC material, and demonstrated that a correlation previously used to estimate h_v led to under-predictions of the material's internal cooling efficiency. In addition, the first ever dataset of h_v values for C/C samples were obtained, enabling comparison with a number of previous investigations where this parameter had been approximated. A similar observation to the UHTC material was found for C/C, when compared to the existing correlation. It was also verified that C/C samples perform better than UHTCs at internal cooling, but not to the extent suggested in previous published work. These findings would aid in producing more accurate models of complete transpiration cooling systems, leading to better predictions of their efficiency.

8.2 Future prospects

This work has led to a substantial development of the two chosen diagnostic techniques. From the experiments and analyses conducted, a number of improvements were identified - these are listed briefly here, and elaborated in Appendix 9.2. In addition, further uses of these techniques were determined.

8.2.1 Fluorescent Particle Image Velocimetry

Chapter 4 highlighted the benefits of FPIV, both as a scatter reduction tool, as well as a multi-property diagnostic. Considerable effort was devoted towards demonstrating the ability to extract temperature information from DEHS droplets using PLIF methods. Results presented showed

promise of expanding the use of existing commercial PIV systems for simultaneous gas velocimetry and thermometry. This section lists the requirements, improvements and further work needed for this to become a reality.

The use of DEHS for simultaneous velocity and temperature measurements would require:

- High-energy double-pulsed UV laser
- Two UV-sensitive intensified or electron multiplying cameras, with at least one capable of PIV-mode imaging
- Aerosol generator producing mono-disperse, repeatable aerosols of small sized droplets
- Filters for fluorescence spectral isolation

The main difficulty encountered in using DEHS for FPIV is weak signal strength. This work used the laser nearing its maximum output energy, intensifier gain almost set to maximum, and a dense droplet distribution that cannot be used for normal PIV. A number of steps can be taken in order to improve signal strength from DEHS:

- Use larger uniform-sized droplets
- Use larger filters
- Use a more sensitive camera
- Dope DEHS with another tracer

Finally, further work is needed to investigate the differences in liquid and droplet DEHS emission. The physics of the formation of a second emission peak at 405 nm remains uncertain. It is not clear whether specific experimental conditions cause its formation, or if this is simply a natural photo-physical behaviour of DEHS. Future experiments should seek to validate DEHS' temperature-dependent emission for varying experimental conditions, so as to ensure that it can be applied reliably in a range of applications.

Future application of DEHS (or droplets in general) in FPIV is constrained to subsonic and supersonic flows, as droplets are relatively large compared to solid seeding particles, but have been used in supersonic investigations in the past. High flow velocities and strong compression and expansion artefacts introduce velocity and temperature lags that lead to erroneous measurements. In addition, particle images can be distorted by the refraction of scattered light through these features. High speeds also make it more difficult to 'freeze' the flow in each image. For PIV, nanosecond pulsed lasers are typically used, as they provide sufficient temporal resolution and pulse energy to scatter light off particles. As flow speeds increase to supersonic and faster, it becomes important that motion blur is not induced as a result of significant particle motion during laser illumination and fluorescence emission.

8.2.2 Polarised-depolarised Rayleigh scattering

Chapter 5 demonstrated the first successful use of PDRS in a non-combustion application. The maximum SNR achieved in this bench-top demonstration was 13.15 corresponding to the polarised signal, while the minimum SNR was 1.85 corresponding to the depolarised signal. In comparison with other demonstrations of PDRS in the literature [71, 72], these values are small. As alluded to by the feasibility study presented in Appendix 9.1, such SNRs would be insufficient in more challenging environments like the Oxford HDT. A number of steps are proposed to improve the SNR of this technique:

- Increase laser pulse energy
- Use a more sensitive camera
- Use gases with larger scattering cross-section

In applying PDRS to a high-speed flow facility, there are further constraints apart from the requirements listed to improve SNR. As previously mentioned, this diagnostic relies on the assumption of constant pressure. If this condition cannot be met, a separate diagnostic is required

in order to resolve temperature information. This could cause problems when applying the technique to flow regions containing multiple compression and expansion artefacts where significant spatial pressure variations can be expected. In addition, thermochemistry further limits the application of PDRS. Any molecular dissociation (that can be expected in high enthalpy flows) introduces a change in r_{p} as dissociated species have different r_{p} values to their constituent molecules. Unless this occurs in a controlled manner in fixed regions and can be pre-modelled or calibrated, flow enthalpy conditions should be limited to ensure no molecular dissociation takes place. Lastly, strong density gradients can introduce the problem of beam steering. This can affect laser sheet intensity profiles and also cause refraction of imaged signals, particularly if 3-D density gradients are present (for example around bow shocks).

Chapter 7 demonstrated the combined use of PDRS and IR thermography to infer the internal cooling characteristics of uniform transpiring porous media. The assembled framework was used in a 1-D manner to obtain average transient temperatures of both solid and gas. However, the experimental framework is capable of producing spatially-resolved temperatures and gas composition, as demonstrated in Chapter 5. Thus, the next steps would be to apply the framework to investigate non-uniform coolant injection from a porous medium. As described in Chapter 6, custom porosity materials can be used in transpiration cooling to preferentially direct coolant towards areas that experience higher heat fluxes (for example, at the leading edge of the hypersonic vehicle). Such materials would induce 3-D internal cooling interactions, as a result of spatially and temporally varying temperature and pressure fields. Computational models that may predict the behaviour of such systems can be validated using measurements from the established experimental framework. This would enable further refinement of transpiration cooling technology for next-generation optimisation of cooling performance.

Bibliography

[1] P. Friedlingstein, M. W. Jones, M. O'sullivan, R. M. Andrew, J. Hauck, G. P. Peters, W. Peters, J. Pongratz, S. Sitch, C. Le Quéré, et al. Global carbon budget 2019. *Earth System Science Data*, 11(4):1783–1838, 2019.

[2] D. S. Lee, D. W. Fahey, A. Skowron, M. R. Allen, U. Burkhardt, Q. Chen, S. J. Doherty, S. Freeman, P. M. Forster, J. Fuglestvedt, et al. The contribution of global aviation to anthropogenic climate forcing for 2000 to 2018. *Atmospheric Environment*, 244:117834, 2021.

[3] F. K. Lu. *Advanced hypersonic test facilities*, volume 198. AIAA, 2002.

[4] Z. Deng, M. C. Richmond, G. R. Guensch, and R. P. Mueller. Study of fish response using particle image velocimetry and high-speed, high-resolution imaging. Technical report, Pacific Northwest National Lab.(PNNL), Richland, WA (United States), 2004.

[5] R. D. Keane and R. J. Adrian. Theory and simulation of particle image velocimetry. In *Fifth International Conference on Laser Anemometry: Advances and Applications*, volume 2052, pages 477–493. International Society for Optics and Photonics, 1993.

[6] R. D. Keane and R. J. Adrian. Optimization of particle image velocimeters. I. Double pulsed systems. *Measurement science and technology*, 1(11):1202, 1990.

[7] A. Melling. Tracer particles and seeding for particle image velocimetry. *Measurement Science and Technology*, 8(12):1406, 1997.

[8] A. B. Basset. *A treatise on hydrodynamics: with numerous examples*, volume 2. Deighton, Bell and Company, 1888.

[9] J. Boussinesq. Sur la résistance qu'oppose un fluide indéfini au repos. *CR Acad. Sci*, 1885.

[10] C. W. Oseen. *Neuere methoden und ergebnisse in der hydrodynamik*. Leipzig: Akademische Verlagsgesellschaft mb H., 1927.

[11] G. G. Stokes et al. On the effect of the internal friction of fluids on the motion of pendulums. 1851.

[12] M. Samimy and S. K. Lele. Motion of particles with inertia in a compressible free shear layer. *Physics of Fluids A: Fluid Dynamics*, 3(8):1915–1923, 1991.

[13] F. Scarano and B. W. Van Oudheusden. Planar velocity measurements of a two-dimensional compressible wake. *Experiments in Fluids*, 34(3):430–441, 2003.

[14] F. F. J. Schrijer, F. Scarano, and B. W. Van Oudheusden. Application of PIV in a Mach 7 double-ramp flow. *Experiments in fluids*, 41(2):353–363, 2006.

[15] W. D. Urban and M. G. Mungal. Planar velocity measurements in compressible mixing layers. *Journal of Fluid Mechanics*, 431:189–222, 2001.

[16] N. Lawson, G. Page, N. Halliwell, and J. Coupland. Application of particle image velocimetry to a small-scale de Laval nozzle. *AIAA Journal*, 37(7):798–804, 1999.

[17] M. Mair, M. Bacic, K. Chakravarthy, and B. Williams. Fluid dynamics of a bistable diverter under ultrasonic excitation—Part II: Flow visualization and fundamental mechanisms. *Journal of Fluids Engineering*, 143(7):071202, 2021.

[18] M. P. Wernet. Development of digital particle imaging velocimetry for use in turbomachinery. *Experiments in Fluids*, 28(2):97–115, 2000.

[19] N. Rostamy, D. Sumner, D. J. Bergstrom, and J. D. Bugg. Local flow field of a surface-mounted finite circular cylinder. *Journal of Fluids and Structures*, 34:105–122, 2012.

[20] E. Paterna, P. Moonen, V. Dorer, and J. Carmeliet. Mitigation of surface reflection in PIV measurements. *Measurement science and technology*, 24(5):057003, 2013.

[21] S. Watanabe, H. Kato, D. Y. Kwak, M. Shirotake, and K. Rinoie. Stereoscopic PIV measurements of leading edge separation vortices on a cranked arrow wing. *Measurement Science and Technology*, 15(6):1079, 2004.

[22] B. J. Petrosky, K. T. Lowe, P. M. Danehy, C. J. Wohl, and P. I. Tiemsin. Improvements in laser flare removal for particle image velocimetry using fluorescent dye-doped particles. *Measurement Science and Technology*, 26(11):115303, 2015.

[23] N. Dronniou and J. Dec. Investigating the development of thermal stratification from the near-wall regions to the bulk-gas in an HCCI engine with planar imaging thermometry. *SAE International Journal of Engines*, 5(3):1046–1074, 2012.

[24] S. A. Kaiser, M. Schild, and C. Schulz. Thermal stratification in an internal combustion engine due to wall heat transfer measured by laser-induced fluorescence. *Proceedings of the combustion institute*, 34(2):2911–2919, 2013.

[25] J. E. Dec and W. Hwang. Characterizing the development of thermal stratification in an HCCI engine using planar-imaging thermometry. *SAE International Journal of Engines*, 2(1):421–438, 2009.

[26] M. C. Thurber, F. Grisch, and R. K. Hanson. Temperature imaging with single-and dual-wavelength acetone planar laser-induced fluorescence. *Optics letters*, 22(4):251–253, 1997.

[27] E. Fanning, T. Donnelly, J. G. Lunney, D. B. Murray, and T. Persoons. Application of gaseous laser-induced fluorescence in low-temperature convective heat transfer research. *Experiments in Fluids*, 61(5):1–20, 2020.

[28] C. F. Kaminski, J. Engström, and M. Aldén. Quasi-instantaneous two-dimensional temperature measurements in a spark ignition engine using 2-line atomic fluorescence. In *Symposium (International) on Combustion*, volume 27, pages 85–93. Elsevier, 1998.

[29] J. Borggren, I. S. Burns, A. L. Sahlberg, M. Aldén, and Z. Li. Temperature imaging in low-pressure flames using diode laser two-line atomic fluorescence employing a novel indium seeding technique. *Applied Physics B*, 122(3):58, 2016.

[30] S. Einecke, C. Schulz, and V. Sick. Measurement of temperature, fuel concentration and equivalence ratio fields using tracer LIF in IC engine combustion. *Applied Physics B*, 71(5):717–723, 2000.

[31] P. C. Palma, P. M. Danehy, and A. F. P. Houwing. Fluorescence imaging of rotational and vibrational temperature in shock-tunnel nozzle flow. *AIAA journal*, 41(9):1722–1732, 2003.

[32] M. M. Prenting, M. I. Dzulfida, T. Dreier, and C. Schulz. Characterization of tracers for two-color laser-induced fluorescence liquid-phase temperature imaging in sprays. *Experiments in Fluids*, 61(3):1–15, 2020.

[33] B. Peterson, E. Baum, B. Böhm, V. Sick, and A. Dreizler. Evaluation of toluene LIF thermometry detection strategies applied in an internal combustion engine. *Applied Physics B*, 117(1):151–175, 2014.

[34] M. Luong, R. Zhang, C. Schulz, and V. Sick. Toluene laser-induced fluorescence for in-cylinder temperature imaging in internal combustion engines. *Applied Physics B*, 91(3):669–675, 2008.

[35] V. K. Natrajan and K. T. Christensen. Two-color laser-induced fluorescent thermometry for microfluidic systems. *Measurement Science and Technology*, 20(1):015401, 2008.

[36] M. Cundy, P. Trunk, A. Dreizler, and V. Sick. Gas-phase toluene LIF temperature imaging near surfaces at 10 khz. *Experiments in fluids*, 51(5):1169–1176, 2011.

[37] P. Lavieille, F. Lemoine, G. Lavergne, and M. Lebouché. Evaporating and combusting droplet temperature measurements using two-color laser-induced fluorescence. *Experiments in fluids*, 31(1):45–55, 2001.

[38] G. Castanet, P. Lavieille, M. Lebouché, and F. Lemoine. Measurement of the temperature distribution within monodisperse combusting droplets in linear streams using two-color laser-induced fluorescence. *Experiments in fluids*, 35(6):563–571, 2003.

[39] A. Labergue, V. Deprédurand, A. Delconte, G. Castanet, and F. Lemoine. New insight into two-color LIF thermometry applied to temperature measurements of droplets. *Experiments in fluids*, 49(2):547–556, 2010.

[40] W. Chaze, O. Caballina, G. Castanet, and F. Lemoine. The saturation of the fluorescence and its consequences for laser-induced fluorescence thermometry in liquid flows. *Experiments in Fluids*, 57(4):58, 2016.

[41] J. Vogt and P. Stephan. Using microencapsulated fluorescent dyes for simultaneous measurement of temperature and velocity fields. *Measurement Science and Technology*, 23(10):105306, 2012.

[42] F. Cellini, S. D. Peterson, and M. Porfiri. Flow velocity and temperature sensing using thermosensitive fluorescent polymer seed particles in water. *International Journal of Smart and Nano Materials*, 8(4):232–252, 2017.

[43] J. Massing, R. Irwansyah, C. Kähler, and C. Cierpka. Optische temperaturmessung in der mikrofluidik mittels temperatursensitiver fluoreszenter partikel. In *Fachtagung Lasermethoden in der Strömungsmesstechnik*, 2014.

[44] A. Omrane, P. Petersson, M. Aldén, and M. A. Linne. Simultaneous 2d flow velocity and gas temperature measurements using thermographic phosphors. *Applied Physics B*, 92(1):99–102, 2008.

[45] N. Jain, J. Seitzman, T. Jenkins, and B. Heeg. Characterization of thermophosphor particles for simultaneous imaging of velocity and temperature. In *49th AIAA Aerospace Sciences Meeting Including the New Horizons Forum and Aerospace Exposition*, page 1230, 2011.

[46] B. Fond, C. Abram, A. L. Heyes, A. M. Kempf, and F. Beyrau. Simultaneous temperature, mixture fraction and velocity imaging in turbulent flows using thermographic phosphor tracer particles. *Optics express*, 20(20):22118–22133, 2012.

[47] C. Abram, B. Fond, A. L. Heyes, and F. Beyrau. High-speed planar thermometry and velocimetry using thermographic phosphor particles. *Applied Physics B*, 111(2):155–160, 2013.

[48] D. Witkowski, D. A. Rothamer, A. Lynch, and V. Belovich. Measurements of the temperature and velocity fields in a free shear flow between a vitiated stream and clean air stream using a Pr:YAG thermographic phosphor. *Measurements*, pages 070DI–00321, 2013.

[49] N. J. Neal, J. Jordan, and D. Rothamer. Simultaneous measurements of in-cylinder temperature and velocity distribution in a small-bore diesel engine using thermographic phosphors. *SAE International Journal of Engines*, 6(1):300–318, 2013.

[50] L. Fan, Y. Gao, A. Hayakawa, and S. Hochgreb. Simultaneous, two-camera, 2d gas-phase temperature and velocity measurements by thermographic particle image velocimetry with zno tracers. *Experiments in Fluids*, 58(4):1–12, 2017.

[51] T. L. Bergman, A. S. Lavine, F. P. Incropera, and D. P. DeWitt. *Introduction to heat transfer*. John Wiley & Sons, 2011.

[52] O. B. Cecil and R. H. Munch. Thermal conductivity of some organic liquids. *Industrial & Engineering Chemistry*, 48(3):437–440, 1956.

[53] S. Whitaker. Forced convection heat transfer correlations for flow in pipes, past flat plates, single cylinders, single spheres, and for flow in packed beds and tube bundles. *AIChE Journal*, 18(2):361–371, 1972.

[54] W. E. Ranz and W. R. Marshall. Evaporation from droplets. *Chem. Eng. Prog*, 48(3):141–146, 1952.

[55] F. M. White. *Heat and Mass Transfer*. (Series in Mechanical Engineering). Addison-Wesley, 1988.

[56] J. Panda and R. G. Seasholtz. Measurement of shock structure and shock–vortex interaction in underexpanded jets using Rayleigh scattering. *Physics of Fluids*, 11(12):3761–3777, 1999.

[57] W. M. Pitts and T. Kashiwagi. The application of laser-induced Rayleigh light scattering to the study of turbulent mixing. *Journal of Fluid Mechanics*, 141:391–429, 1984.

[58] S. C. Graham, A. J. Grant, and J. M. Jones. Transient molecular concentration measurements in turbulent flows using Rayleigh light scattering. *AIAA Journal*, 12(8):1140–1142, 1974.

[59] K. Fiedler, O. Sieber, and C. Jakiel. Quantitative density measurements by rayleigh scattering behind a plane turbine cascade. *AIAA journal*, 35(8):1303–1308, 1997.

[60] J. R. Smith. Rayleigh temperature profiles in a hydrogen diffusion flame. In *Laser Spectroscopy: Applications and Techniques*, volume 158, pages 84–91. International Society for Optics and Photonics, 1978.

[61] V. Bergmann, W. Meier, D. Wolff, and W. Stricker. Application of spontaneous Raman and Rayleigh scattering and 2D LIF for the characterization of a turbulent CH4/H2/N2 jet diffusion flame. *Applied Physics B*, 66(4):489–502, 1998.

[62] R. W. Dibble and R. E. Hollenbach. Laser rayleigh thermometry in turbulent flames. In *Symposium (International) on Combustion*, volume 18, pages 1489–1499. Elsevier, 1981.

[63] S. H. Stårner, R. W. Bilger, R. W. Dibble, and R. S. Barlow. Piloted diffusion flames of diluted methane near extinction: detailed structure from laser measurements. *Combustion science and technology*, 72(4-6):255–269, 1990.

[64] S. H. Stårner, R. W. Bilger, K. M. Lyons, J. H. Frank, and M. B. Long. Conserved scalar measurements in turbulent diffusion flames by a Raman and Rayleigh ribbon imaging method. *Combustion and flame*, 99(2):347–354, 1994.

[65] S. H. Stårner, R. W. Bilger, J. H. Frank, D. F. Marran, and M. B. Long. Mixture fraction imaging in a lifted methane jet flame. *Combustion and flame*, 107(3):307–313, 1996.

[66] S. H. Stårner, R. W. Bilger, M. B. Long, J. H. Frank, and D. F. Marran. Scalar dissipation measurements in turbulent jet diffusion flames of air diluted methane and hydrogen. *Combustion science and technology*, 129(1-6):141–163, 1997.

[67] A. Sevault, M. Dunn, R. S. Barlow, and M. Ditaranto. On the structure of the near field of oxy-fuel jet flames using Raman/Rayleigh laser diagnostics. *Combustion and Flame*, 159(11):3342–3352, 2012.

[68] J. H. Frank, K. M. Lyons, D. F. Marran, M. B. Long, S. H. Stårner, and R. W. Bilger. Mixture fraction imaging in turbulent nonpremixed hydrocarbon flames. In *Symposium (International) on Combustion*, volume 25, pages 1159–1166. Elsevier, 1994.

[69] F. Fuest, R. S. Barlow, J. Y. Chen, and A. Dreizler. Raman/rayleigh scattering and CO-LIF measurements in laminar and turbulent jet flames of dimethyl ether. *Combustion and Flame*, 159(8):2533–2562, 2012.

[70] J. Fielding, J. H. Frank, S. A. Kaiser, M. D. Smooke, and M. B. Long. Polarized/depolarized Rayleigh scattering for determining fuel concentrations in flames. *Proceedings of the Combustion Institute*, 29(2):2703–2709, 2002.

[71] J. H. Frank, S. A. Kaiser, and M. B. Long. Reaction-rate, mixture-fraction, and temperature imaging in turbulent methane/air jet flames. *Proceedings of the Combustion Institute*, 29(2):2687–2694, 2002.

[72] J. H. Frank, S. A. Kaiser, and M. B. Long. Multiscalar imaging in partially premixed jet flames with argon dilution. *Combustion and Flame*, 143(4):507–523, 2005.

[73] R. S. Barlow and J. H. Frank. Effects of turbulence on species mass fractions in methane/air jet flames. In *Symposium (International) on Combustion*, volume 27, pages 1087–1095. Elsevier, 1998.

[74] M. F. Zulkifli, F. Beyrau, and B. Williams. Temperature, OH and CH2O structure in the near field of oxy-fuel flames. 2017.

[75] M. F. Zulkifli. *Characterisation of oxy-fuel flames using laser based diagnostics techniques*. PhD thesis, 2016.

[76] J. A. Sutton and J. F. Driscoll. Rayleigh scattering cross sections of combustion species at 266, 355, and 532 nm for thermometry applications. *Optics letters*, 29(22):2620–2622, 2004.

[77] W. C. Gardiner Jr, Y. Hidaka, and T. Tanzawa. Refractivity of combustion gases. *Combustion and Flame*, 40:213–219, 1981.

[78] R. Miles and W. Lempert. Two-dimensional measurement of density, velocity, and temperature in turbulent high-speed air flows by UV Rayleigh scattering. *Applied Physics B*, 51(1):1–7, 1990.

[79] W. L. Wolfe and G. J. Zissis. *The infrared handbook*. The Office of Naval Research, Department of the Navy, Washington, DC, 1978.

[80] FLIR. User's manual FLIR Exx series, 2013.

[81] D. Ragni, F. Schrijer, B. W. Van Oudheusden, and F. Scarano. Particle tracer response across shocks measured by PIV. *Experiments in Fluids*, 50(1):53–64, 2011.

[82] J. Bouguet and P. Perona. Camera calibration from points and lines in dual-space geometry. In *Proc. 5th European Conf. on Computer Vision*, pages 2–6. Citeseer, 1998.

[83] W. Thielicke and E. Stamhuis. Pivlab–towards user-friendly, affordable and accurate digital particle image velocimetry in MATLAB. *Journal of Open Research Software*, 2(1), 2014.

[84] M. Sahin and R. G. Owens. A numerical investigation of wall effects up to high blockage ratios on two-dimensional flow past a confined circular cylinder. *Physics of Fluids*, 16(5):1305–1320, 2004.

[85] S. Okamoto and Y. Sunabashiri. Vortex shedding from a circular cylinder of finite length placed on a ground plane. *Journal of Fluids Engineering*, 114(4):512–521, 1992.

[86] E. Konstantinidis and S. Balabani. Symmetric vortex shedding in the near wake of a circular cylinder due to streamwise perturbations. *Journal of Fluids and Structures*, 23(7):1047–1063, 2007.

[87] M. D. Griffith, J. Leontini, M. C. Thompson, and K. Hourigan. Vortex shedding and three-dimensional behaviour of flow past a cylinder confined in a channel. *Journal of Fluids and Structures*, 27(5-6):855–860, 2011.

[88] M. S. Bloor. The transition to turbulence in the wake of a circular cylinder. *Journal of Fluid Mechanics*, 19(2):290–304, 1964.

[89] A. Prasad and C. H. Williamson. The instability of the shear layer separating from a bluff body. *Journal of Fluid Mechanics*, 333:375–402, 1997.

[90] A. Michalke. On spatially growing disturbances in an inviscid shear layer. *Journal of Fluid Mechanics*, 23(3):521–544, 1965.

[91] S. Rajagopalan and R. A. Antonia. Flow around a circular cylinder—structure of the near wake shear layer. *Experiments in Fluids*, 38(4):393–402, 2005.

[92] M. Mair, M. Bacic, and P. Ireland. On dynamics of acoustically driven bistable fluidic valves. *Journal of Fluids Engineering*, 141(6), 2019.

[93] B. Peterson and V. Sick. Simultaneous flow field and fuel concentration imaging at 4.8 khz in an operating engine. *Applied Physics B*, 97(4):887–895, 2009.

[94] B. Peterson, E. Baum, B. Böhm, V. Sick, and A. Dreizler. High-speed PIV and LIF imaging of temperature stratification in an internal combustion engine. *Proceedings of the combustion institute*, 34(2):3653–3660, 2013.

[95] G Charalampous, Y Hardalupas, and AMKP Taylor. Optimisation of the droplet sizing accuracy of the combined scattering (mie)/laser induced fluorescence (lif) technique. In *Proceedings of the 12th International Symposium of Applications of Laser Techniques to Fluid Mechanics, Lisbon, Portugal*, pages 8–11, 2004.

[96] Y. N. Mishra, A. Yoganantham, M. Koegl, and L. Zigan. Investigation of five organic dyes in ethanol and butanol for two-color laser-induced fluorescence ratio thermometry. *Optics*, 1(1):1–17, 2020.

[97] M. C. Thurber and R. K. Hanson. Pressure and composition dependences of acetone laser-induced fluorescence with excitation at 248, 266, and 308 nm. *Applied Physics B*, 69(3):229–240, 1999.

[98] F. Grossmann, P. B. Monkhouse, M. Ridder, V. Sick, and J. Wolfrum. Temperature and pressure dependences of the laser-induced fluorescence of gas-phase acetone and 3-pentanone. *Applied Physics B*, 62(3):249–253, 1996.

[99] J. D. Koch and R. K. Hanson. Temperature and excitation wavelength dependencies of 3-pentanone absorption and fluorescence for PLIF applications. *Applied Physics B*, 76(3):319–324, 2003.

[100] H. Du, R. C. A. Fuh, J. Li, L. A. Corkan, and J. S. Lindsey. PhotochemCAD‡: a computer-aided design and research tool in photochemistry. *Photochemistry and photobiology*, 68(2):141–142, 1998.

[101] M. Taniguchi and J. S. Lindsey. Database of absorption and fluorescence spectra of> 300 common compounds for use in photochemCAD. *Photochemistry and photobiology*, 94(2):290–327, 2018.

[102] C. Willman. *Laser diagnostics for spatially resolved thermometry in combustion and flows*. PhD thesis, 2016.

[103] B. H. Cheung. *Tracer-based planar laser-induced fluorescence diagnostics: quantitative photophysics and time-resolved imaging*. PhD thesis, Stanford University, 2011.

[104] F. Lizal, J. Jedelsky, J. Lippay, T. Halasova, F. Mravec, and M. Jicha. Aerosol transport in a model of human lungs. In *EPJ Web of Conferences*, volume 25, page 01050. EDP Sciences, 2012.

[105] W. Koban, J. D. Koch, R. K. Hanson, and C. Schulz. Absorption and fluorescence of toluene vapor at elevated temperatures. *Physical chemistry chemical physics*, 6(11):2940–2945, 2004.

[106] W. Pauli. Über den zusammenhang des abschlusses der elektronengruppen im atom mit der komplexstruktur der spektren. *Zeitschrift für Physik*, 31(1):765–783, 1925.

[107] Gustaf Särner, Mattias Richter, and Marcus Aldén. Two-dimensional thermometry using temperature-induced line shifts of zno: Zn and zno: Ga fluorescence. *Optics letters*, 33(12):1327–1329, 2008.

[108] J. W. Strutt. *The theory of sound*, volume 1. 1877.

[109] M. Boni, I. R. Andrei, M. L. Pascu, and A. Staicu. Fluorescence and time-delayed lasing during single laser pulse excitation of a pendant mm-sized dye droplet. *Molecules*, 24(24):4464, 2019.

[110] J. Palmer, V. Reddemann, M. A.and Kirsch, and R. Kneer. Applying 2D-2cLIF-EET thermometry for micro-droplet internal temperature imaging. *Experiments in Fluids*, 59(3):1–18, 2018.

[111] H. Azzouz, L. Alkhafadiji, S. Balslev, J. Johansson, N. A. Mortensen, S. Nilsson, and A. Kristensen. Levitated droplet dye laser. *Optics express*, 14(10):4374–4379, 2006.

[112] W. Schottky. On spontaneous current fluctuations in various electrical conductors. *Journal of Micro/Nanolithography, MEMS, and MOEMS*, 17(4):041001, 2018.

[113] J. Florio Jr, J. B. Henderson, F. L. Test, and R. Hariharan. Characterization of forced convection heat transfer in decomposing, glass-filled polymer composites. *Journal of Composite Materials*, 25(11):1515–1539, 1991.

[114] T. Hermann, M. McGilvray, and I. Naved. Performance of transpiration-cooled heat shields for reentry vehicles. *AIAA Journal*, 58(2):830–841, 2020.

[115] D. E. Glass, A. D. Dilley, and H. N. Kelly. Numerical analysis of convection/transpiration cooling. *Journal of Spacecraft and Rockets*, 38(1):15–20, 2001.

[116] H. Boehrk, O. Piol, and M. Kuhn. Heat balance of a transpiration-cooled heat shield. *Journal of Thermophysics and Heat Transfer*, 24(3):581–588, 2010.

[117] T. A. Hermann, M. McGilvray, H. S. Ifti, F. Hufgard, and S. Loehle. Fluid-solid heat exchange in porous media for transpiration cooling systems. In *AIAA Scitech 2019 Forum*, page 0537, 2019.

[118] T. Langener, J. V. Wolfersdorf, and J. Steelant. Experimental investigations on transpiration cooling for scramjet applications using different coolants. *AIAA Journal*, 49(7):1409–1419, 2011.

[119] D. P. Gaver Jr. Observing stochastic processes, and approximate transform inversion. *Operations research*, 14(3):444–459, 1966.

[120] H. Stehfest. Algorithm 368: Numerical inversion of Laplace transforms [D5]. *Communications of the ACM*, 13(1):47–49, 1970.

[121] M. L. Oldfield. Impulse response processing of transient heat transfer gauge signals. *Journal of Turbomachinery*, 130(2):021023, 2008.

[122] R. Courant, K. Friedrichs, and H. Lewy. On the partial difference equations of mathematical physics. *IBM journal of Research and Development*, 11(2):215–234, 1967.

[123] R. J. Moffat. Describing the uncertainties in experimental results. *Experimental thermal and fluid science*, 1(1):3–17, 1988.

[124] M. Ewenz Rocher, M. McGilvray, T. A. Hermann, H. S. Ifti, F. Hufgard, M. F. Eberhart, A. Meindl, S. Loehle, T. Giovannini, and L. J. Vandeperre. Testing a transpiration cooled zirconium-di-boride sample in the Plasma Tunnel at IRS. In *AIAA Scitech 2019 Forum*, page 1552, 2019.

[125] S. Schweikert, J. von Wolfersdorf, M. Selzer, and H. Hald. Characterization of actively cooled porous C/C wall segments according to pressure loss and internal temperature distribution. In *7th European Workshop on Thermal Protection Systems & Hot Structures*. ESA Conference Bureau Noordwijk, The Netherlands, 2013.

[126] C. Dittert, M. Selzer, and H. Böhrk. Flowfield and pressure decay analysis of porous cones. *AIAA Journal*, 55(3):874–882, 2017.

[127] S. Löhle, S. Schweikert, and J. von Wolfersdorf. Method for heat flux determination of a transpiration-cooled wall from pressure data. *Journal of Thermophysics and Heat Transfer*, 30(3):567–572, 2016.

[128] T. Langener, J. von Wolfersdorf, T. Laux, and J. Steelant. Experimental investigation of transpiration cooling with subsonic and supersonic flows at moderate temperature levels. In *44th AIAA/ASME/SAE/ASEE Joint Propulsion Conference & Exhibit*, page 5174, 2008.

[129] F. Hufgard, S. Löhle, M. McGilvray, T. Hermann, S. Schweikert, J. von Wolfersdorf, J. Steelant, and S. Fasoulas. Plenum pressure behavior in transiently heat loaded transpiration cooling system. *Journal of Thermophysics and Heat Transfer*, 35(2):256–267, 2021.

[130] K. Chakravarthy, L. Le Page, T. Hermann, M. McGilvray, and B. Williams. Characterisation of internal heat transfer mechanisms in transpiring porous media using optical diagnostics. In *International Conference on Flight Vehicles, Aerothermodynamics and Reentry Missions and Engineering*. European Space Agency, 2019.

[131] H. S. Ifti, T. Hermann, and M. McGilvray. Flow characterisation of transpiring porous media for hypersonic vehicles. In *22nd AIAA International Space Planes and Hypersonics Systems and Technologies Conference*, page 5167, 2018.

[132] W. Sutherland. The viscosity of gases and molecular force. *Lond. Edinb. Dublin Philos. Mag. J. Sci*, 36:507–531, 1893.

[133] E. Achenbach. Heat and flow characteristics of packed beds. *Experimental Thermal and Fluid Science*, 10(1):17–27, 1995.

[134] N. Wakao and S. Kagei. *Heat and mass transfer in packed beds*. Taylor & Francis, 1982.

[135] D. Kunii and M. Suzuki. Particle-to-fluid heat and mass transfer in packed beds of fine particles. *International Journal of Heat and Mass Transfer*, 10(7):845–852, 1967.

[136] P. Grootenhuis, R. C. A. Mackworth, and O. A. Saunders. Heat transfer to air passing through heated porous metals. *Proceedings of General Discussion on Heat Transfer*, page 363, 1951.

[137] J. Eichhorn and R. R. White. Particle to fluid heat transfer in fixed and fluidized beds. In *Chemical Engineering Progress Symposium Series*, volume 48, 1952.

[138] G. Donnadieu. Transmission de la chaleur dans les milieux granulaires: étude du lit fixe et du lit fluidisé. Revue de l'Institut français du pétrole et annales des combustibles liquides, 1961.

[139] S. Ergun. Fluid flow through packed columns. *Chem. Eng. Prog.*, 48:89–94, 1952.

[140] M. McGilvray, L. J. Doherty, A. J. Neely, R. Pearce, and P. Ireland. The Oxford High Density Tunnel. In *20th AIAA International Space Planes and Hypersonic Systems and Technologies Conference*, page 3548, 2015.

[141] T. Hermann, H. S. Ifti, M. McGilvray, L. Doherty, and R. Penty Geraets. Mixing characteristics in a hypersonic flow around a transpiration cooled flat plate model. 2018.

[142] H. Ifti, T. Hermann, and M. McGilvray. Transpiration cooling at Mach 5 employing porous UHTC. In *Conference on Flight vehicles, Aerothermodynamics and Re-entry Missions and Engineering (FAR)*. European Space Agency.

[143] A. Hyslop, L. J. Doherty, M. McGilvray, A. Neely, L. P. McQuellin, J. Barth, and G. Mullen. Free-flight aerodynamic testing of the Skylon space plane. *Journal of Spacecraft and Rockets*, 58(5):1487–1497, 2021.

[144] A. Gülhan and S. Braun. An experimental study on the efficiency of transpiration cooling in laminar and turbulent hypersonic flows. *Experiments in fluids*, 50(3):509–525, 2011.

[145] H. Tanno, T. Komuro, K. Itoh, M. Kuhn, I. Petkov, and B. Esser. Transpiration cooling experiments in free-piston shock tunnel HIEST. 2016.

[146] A. Cerminara, R. Deiterding, and N. Sandham. Direct numerical simulations of coolant injection through a porous layer for transpiration cooling in hypersonic flow. 2019.

[147] A. Cerminara, T. Hermann, H. S. Ifti, R. Deiterding, N. Sandham, and M. McGilvray. Influence of instability modes on cooling performance in hypersonic boundary layer with slot injection. *Aerospace Science and Technology*, 109:106409, 2021.

[148] L. Wolf Jr, H. J. Obremski, and W. J. Christian. Transpiration cooling in an arc-jet environment. *AIAA Journal*, 4(4):747–749, 1966.

[149] V. Gopal and L. Maddalena. Review of Filtered Rayleigh Scattering technique for mixing studies in supersonic air flow. *Progress in Aerospace Sciences*, 120:100679, 2021.

[150] J. George, T. P. Jenkins, and R. B. Miles. Diagnosis of high speed flows using filtered Rayleigh scattering. In *30th AIAA Aerodynamic Measurement Technology and Ground Testing Conference*, page 2231, 2014.

[151] R. B. Miles, W. R. Lempert, and J. N. Forkey. Laser rayleigh scattering. *Measurement Science and Technology*, 12(5):R33, 2001.

[152] M. P. Bogaard, A. D. Buckingham, R. K. Pierens, and A. H. White. Rayleigh scattering depolarization ratio and molecular polarizability anisotropy for gases. *Journal of the Chemical Society, Faraday Transactions 1: Physical Chemistry in Condensed Phases*, 74:3008–3015, 1978.

Appendix

9.1 Application of PDRS to the Oxford HDT

An initial aim of this work was to apply PDRS in a hypersonic flow to quantify the cooling effectiveness of transpiration cooling as a thermal protection system (TPS) for hypersonic vehicles. As elaborated in Section 1.1.3, there are a number of ways in which this technology achieves cooling. One mechanism of interest is the formation of a protective film by the effused coolant on the surface of the vehicle. This film reduces heat flux incident on the vehicle surface. The effectiveness of heat flux mitigation is dictated by the complex interactions between the effused coolant and the hypersonic freestream. For example, enhanced 3-D mixing of these gases can cause rapid spread of the coolant, leading to low vehicle surface coverage downstream of coolant effusion. PDRS was proposed as an ideal technique to characterise and quantify these complex flow mixing interactions through simultaneous measurements of composition and temperature. Gas composition measurements would enable spatially-resolving the spread of coolant to determine vehicle surface coverage. Gas temperature measurements would allow evaluation of the heat flux reduction as a result of coolant presence. Thus, the goal was to apply PDRS in an experimental investigation of a transpiration-cooled model in a hypersonic flow. The effect of varying parameters such as type of coolant used, coolant mass flux and freestream flow conditions would be characterised - these results would provide experimental validation for a computational model.

The facility that would be used for this investigation is the Oxford High Density Tunnel (HDT), located at the Oxford Thermofluids Institute [140]. Figure 9.1 shows a schematic of this facility. Its operation involves expanding a highly pressurised test gas through a contoured nozzle, creating supersonic or hypersonic conditions in the test section downstream of the nozzle. The test time

of this facility is in the order of tens of milliseconds [141, 142, 143], and freestream Mach numbers ranging from 3 to 7 can be produced by changing contoured nozzles. The test section has two large windows, separated by a distance of approximately 1 m, that can provide optical access for lasers and cameras.

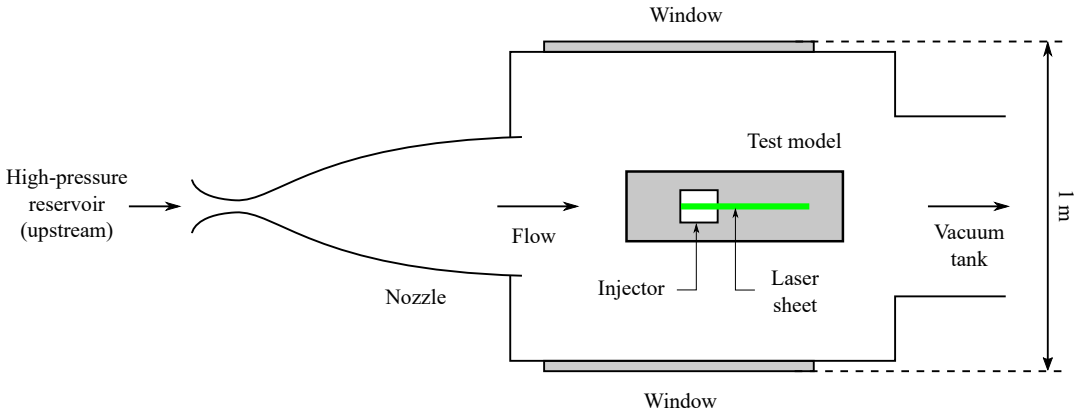


Figure 9.1: Plan view schematic of the HDT - adapted from [141]. The laser sheet probes a vertical plane above the test model surface

To investigate transpiration cooling in the HDT, a flat horizontal plate would be used as the test model, as shown in Figure 9.1. This is one of the preferred models for transpiration cooling investigations, as it has been extensively used in the literature [144, 145, 146, 147], and it removes complex geometric flow interactions. A porous injector is assembled onto this model, and is supplied with coolant gas from a pressurised plenum mounted underneath it. Coolant is injected from this porous material into the boundary layer, creating a film above and downstream from the injector. The intention was to apply PDRS above the surface of the flat plate model using a vertical laser sheet propagating parallel to the flow direction. Coolant composition and temperature measurements would be made probing the boundary layer above and downstream of the injector. Air would be used in the freestream, mimicking atmospheric re-entry conditions, while CO_2 would be used as the injected gas. It should be noted that the use of CO_2 as the coolant is *not* the most ideal solution in transpiration cooling. Wolf et al. [148] stated that the mass flux of coolant required to achieve a certain level of transpiration cooling is approximately inversely proportional to the specific heat capacity of the gas used. Thus, gases with large spe-

cific heat capacities such as He, H_2 and N_2 are better candidates. The choice to use CO_2 is motivated by its large r_p which will enable PDRS - results from these experiments would then serve as validation cases for computational models, allowing the use of more suitable gases to be simulated.

To apply PDRS in the HDT, four requirements were investigated:

- High sensitivity of technique using air and CO_2
- Optical access for lasers and cameras
- Minimal elastic scattering from other sources
- High signal-to-noise ratio

The first requirement was investigated in Section 5.1, where the use of air as the HDT test gas with CO_2 as the effused coolant was found to produce an acceptable 4 % uncertainty. The following sections elaborate on the remaining requirements. Section 5.2 discovered achievable SNRs in a bench-top experiment, while establishing the necessary procedure for composition and temperature reconstruction. This test will serve as a baseline for predicting achievable SNR in the HDT.

9.1.1 Optical access

As described previously, the HDT has two large optical access windows located opposite one another along the horizontal centreline of the HDT. They would have to provide access for a laser beam, as well as an unobstructed view for two cameras. Ideally, the flow should be probed along the central vertical plane of the HDT, above and downstream of the porous injector (as shown in Figure 9.1) in order to characterise the effused flow mixing with the freestream. This can be achieved in two ways.

The first method would require forming and directing the laser sheet along the longitudinal axis of the facility. In this instance, the sheet height would be set according to the boundary layer

thickness. The main drawback is that some sheet forming, directing and terminating optics would have to be placed in the path of the high-speed test gas. Not only would this partially obstruct the flow and generate undesired flow features such as shock waves and expansions, altering test conditions, but the risk of damaging optics is also present. One may consider forming the laser sheet downstream and directing it upstream with no means of beam termination - while this would prevent flow disturbance, the high pulse energy of the beam could damage parts of the facility where it is forced to terminate. In addition, this is a safety hazard, and could also lead to background stray light affecting any measurement. The second method would require directing the laser sheet down towards the porous injector via a mirror mounted on the ceiling of the facility - in this instance, the sheet width would have to be set according to the longitudinal distance of interest. While this configuration avoids disturbing the flow, the beam would have to terminate on the test model itself. This would generate an unmanageable quantity of scattered light, overwhelming the Rayleigh signal and rendering the diagnostic useless.

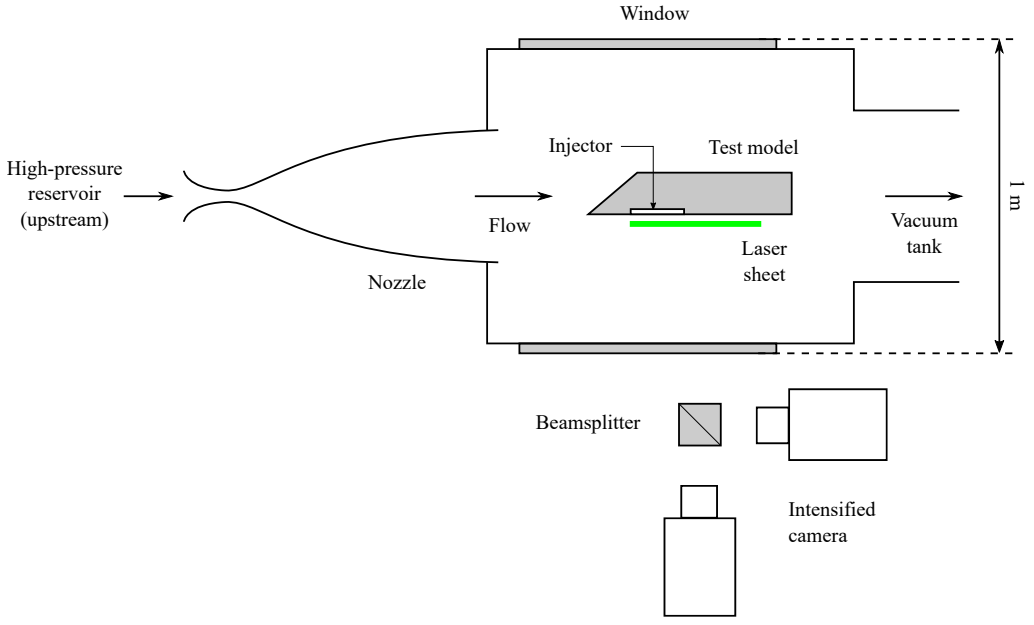


Figure 9.2: Plan view HDT schematic of rotated test model with cameras imaging from the same window using a beamsplitter. The laser sheet travels into the plane of the diagram, parallel to the surface of the model

Another option involves rotating the test model 90° around the central longitudinal axis, such

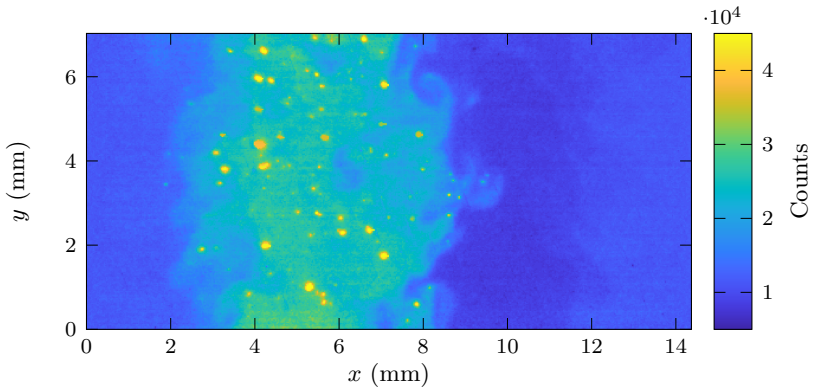


Figure 9.3: Polarised signal of dual-jet experiment showing dry ice particles in the CO_2 jet

that the model surface faces a window, as shown in Figure 9.2. This would allow a laser sheet to be sent downwards as described in the second method above, but this time with the ability to safely terminate the beam in an appropriate beam trap mounted on the floor of the facility. This would also mean characterising a plane parallel to the model surface, which is likely to be less scientifically interesting as the mixing is more wall-normal. The appropriate layout for such a configuration would involve sending the laser sheet into the facility via the window to the rear of the test model, and using the other window for imaging purposes. In order to ensure both cameras have the same view of the model, a beamsplitter imaging layout may be required, which would lead to a loss in signal strength - this is considered in Section 9.1.3.

To summarise the optical access requirement, there exists a safe method of sending the laser sheet into the facility and imaging Rayleigh signals. However, this method could lead to less scientific insight and a reduction in potential signal strength.

9.1.2 Other sources of elastic scattering

The presence of scattering bodies such as surfaces and particles (e.g. dust, condensed water droplets) hinders the ability to make Rayleigh measurements as their scattering overwhelms molecular signal. Figure 9.3 shows an example polarised signal obtained from the investigation in Section 5.2 in which many small particles were present in the field of view. This illustrates the sensitivity of the technique even to small particles in the flow.

Laser energies for Rayleigh scattering measurements are typically very high ($> 100\,\mathrm{mJ}$), but even a small amount of energy ($\sim 1\,\mathrm{mJ}$) can cause surface scatter to saturate a non-intensified camera. If intensified cameras are used with high gain settings in order to detect Rayleigh signals, pixel saturation and camera damage becomes a concern. It became apparent during the proof of principle tests that controlling the presence of particles in the flow is hard enough on the bench-top, even when shielded with a clean co-flow. This is likely to be much worse in the $\sim 30\,\mathrm{m}$ long HDT facility; there is no existing mechanism to thoroughly clean the inside of the tunnel, or to filter the freestream from particles (without disrupting flow conditions). In addition, the introduction of the laser beam through a facility window is likely to produce strong laser reflections that add stray light to the measured Rayleigh signals, as was demonstrated by Gopal et al. [149].

Filtered Rayleigh Scattering (FRS) was developed to eliminate undesirable elastic scattering from particles, however it relies on blocking the fundamental scattering wavelength and only transmitting Doppler-broadened scatter from faster-moving molecules[1] [78]. While this removes unwanted surface and particle scatter, much of the molecular Rayleigh signal is lost, as this broadened light is a fraction of the total Rayleigh scattered signal (through careful tuning of the filter, 50 % transmission may be possible [150, 151]). This loss of signal is considered in the analysis presented in Section 9.1.3.

To summarise the requirement of minimal elastic scattering from other sources, there is no obvious way to filter particles from the HDT freestream, which can overwhelm molecular Rayleigh signal. FRS may be used to overcome this limitation, but it would lead to a further reduction in potential signal strength.

[1] Successful application of FRS typically requires the use of an injection-seeded laser to ensure a narrow linewidth. Such a laser was not available in this work, and would have to be sourced if this technique were attempted.

9.1.3 Achievable SNR

The main limitation in the use of PDRS is low SNR. The depolarised Rayleigh component is weak - at best, 4 % of the polarised signal is achievable if CO_2 is used. Thus, maximising signal strength becomes a priority for successful use in the HDT. Unfortunately, there are a number of hindrances to this.

- Available pulse energy

  A large pulse energy density is needed for PDRS. Prior characterisations have shown that the boundary layer height above the flat plate model during coolant injection in the HDT is of a similar order of magnitude to the laser sheet height used in Section 5.2, meaning that these tests already captured this characteristic [141]. However, the laser used in Section 5.2 was the most powerful available - bench-top experiments were shown to produce a minimum SNR of 1.85 at maximum laser output. The use of the same laser in the HDT would lead to a reduction in incident pulse energy at the imaging region, leading to drop in SNR from 1.85, for the following reasons.

  Firstly, pulse energy will decrease due to optical losses. This is because the beam needs to travel $> 1\,\mathrm{m}$ before reaching the region of interest, traverse through optical windows and be directed by turning mirrors. Secondly, Section 5.2 elucidated the need for shot-to-shot laser sheet intensity correction as part of the PDRS post-processing procedure. This requirement is more important and less trivial in the HDT - here, co-flows are not present, so shot-to-shot correction can only be achieved by sampling the beam prior to test section entry (to then illuminate a uniform gas and image this using a separate camera[2]). Clearly, this leads to a further loss of available energy at the region of interest. The assumption that the laser sheet intensity distribution remains uniform from shot-to-shot is typically reasonable, however, the presence of large unsteady gas density variations (shock waves and

[2]Even if this were attempted, a suitable third camera that would serve the purpose of imaging the laser sheet intensity profile was not available.

expansion fans) in the HDT test gas introduces the problem of beam steering. This rules out the option of obtaining average sheet intensity maps that can be measured separately, before or after an experimental run, and in the absence of a hypersonic flow.

In short, use of the same laser in the HDT will lead to lower pulse energies at the imaging region, and thus lower SNR, due to the experimental configuration. A 10 % loss of signal due to beam sampling is estimated in the most optimistic case, based on providing a weak, but sufficient ∼60 mJ for obtaining the laser sheet intensity profile.

- Camera position and layout

  Incoherent Rayleigh scatter is emitted spherically in all directions. As such, signal intensities attenuate with squared distance between scattering molecules and collection optics. Considering the HDT (Figure 9.1), a minimum distance of 500 mm between laser sheet and camera lens is required. For context, the equivalent distance in Section 5.2 was ∼100 mm. Thus, it is expected that ∼25 times fewer photons would reach the camera, which by itself, would render the diagnostic unusable if all other conditions were replicated.

  Section 9.1.1 elucidated the potential need for both cameras to be placed on the same side of the tunnel, using the layout shown in Figure 9.2. This could necessitate the use of a beamsplitter which would further reduce the signal for each camera, and potentially introduce signal ghosting or cross-talk between polarised and depolarised components. Using a standard polarising beamsplitter, 10 % less signal can be expected.

  In summary, the size of the HDT test section reduces the attainable signal strength by a factor of ∼25 (from that of the bench-top), while optical access considerations could reduce this by a further 10 %.

- Gas density

  Rayleigh signals inherently depend on the number of molecules present in the imaging region (i.e. the gas density). Thus far, analysis has been simplified by relating the number

of molecules to the temperature of the gas using the ideal gas law, assuming constant pressure. While this assumption is still applicable for temperature analysis in the HDT injected gas region, the pressure, and thus gas density, is lower than atmospheric conditions by about two orders of magnitude [141]. This means a further 100-fold reduction in signal compared to the bench-top.

In summary, the low density conditions created in the HDT reduce the attainable signals by a factor of 100 from that of the bench-top, which in isolation, would make PDRS unusable.

The combined effect of all items listed above result in very low predicted SNRs for applying PDRS to the HDT. Some steps are considered to try and mitigate these signal losses, and they are explored below.

- Shorter laser wavelength

  Rayleigh scattering cross-sectional areas scale with wavelength raised to the power of -4, so shorter wavelengths should, in theory, improve signal. Halving the laser wavelength will give 16 times the number of scattered photons previously achieved. However, this requires fourth harmonic generation with the available laser, which is cumbersome to operate (as described in Chapter 4), and also has an intrinsic conversion efficiency of roughly 30 %, so an actual increase in Rayleigh scattered photons of about 5 times can be expected. Signal detection then requires that cameras used have similar quantum efficiencies at 532 nm and 266 nm. This is rarely the case - UV wavelengths typically have quantum efficiencies at least 2-3 times smaller than that of visible wavelengths. As such, an optimistic factor of 2.5 times improvement in signal strength can be expected when using shorter laser wavelengths. Practically, working in the UV also imposes the requirement that all lenses and windows are made of fused silica, and it makes the experiment more dangerous and difficult to align as UV wavelengths are not visible to the human eye.

- Larger objective lens

Larger objective lenses would alleviate some loss of signal, but only marginally, as signal strength is proportional to squared lens diameter. The objective lens used in this work (85 mm f/1.2 Mitakon Speedmaster) has a maximum aperture size of ∼70 mm. Lenses with larger aperture than this are very rare, so signal improvements using this method would be hard to achieve.

- Gas combination

  Significant improvements in signal strength could be achieved by choosing the right gases. Signal strength scales with scattering cross-section, so choosing larger cross-section gases is beneficial. Hydrocarbons are the best candidates for this, but they are usually flammable, posing a safety hazard for their use. Similarly, gases with large r_p will produce stronger depolarised signals. CO_2 is already one of the best candidates for this diagnostic since it has a large scattering cross-section and also one of the largest known r_p values. Several other gases have similar, if not larger r_p - for example, CS_2 has an r_p of 7 %, N_2O has 6 %, while allenes and COS have 4 % [152]. However, most of these options have associated health risks to their use, making CO_2 the best contender in this application.

- Available cameras

  Intensified or electron-multiplying cameras are best-suited to PDRS, as Rayleigh signals are weak. The cameras used in Section 5.2 were operated at moderate gain settings - a further five-fold enhancement of signal would have been possible. Thus, signal amplification using camera gain could alleviate the loss of signal, but would also amplify camera noise. Since the effect of noise was already evident for the bench-top experiment, this can only get worse when applied to the HDT. Newer cameras with higher quantum efficiencies at 532 nm might resolve this problem, but were not available.

Table 9.1 compiles the various signal loss factors and (realistic) mitigation strategies listed above, to provide an estimate of the total anticipated signal reduction (relative to the bench-top experiment) when PDRS is applied in the HDT.

Table 9.1: Signal reduction and improvement factors, relative to bench-top experiment, for applying PDRS in the HDT. Note that − denotes a reduction, while + denotes an improvement. Factors presented are the most optimistic values

Description	Gain (+) / Loss (−)	Factor
Available pulse energy	−	1.1
Camera position	−	25.0
Camera layout	−	1.1
Gas density	−	100.0
Filtered Rayleigh Scattering	−	2.0
Laser wavelength	+	2.5
Camera gain	+	5.0

From Table 9.1, applying PDRS in the HDT is likely to produce 484 times less signal, compared to the bench-top experiment. This will unfortunately drop the SNR to values less than 1, rendering the diagnostic impractical.

To summarise the requirement of high SNR, various factors that arise from the experimental configuration in the HDT lead to significantly lower SNR compared to that of the bench-top experiment, meaning that this condition cannot be achieved. More powerful lasers and highly sensitive cameras might improve chances of success but were not available.

9.1.4 Summary of HDT feasibility

This section considered a number of criteria for successful application of PDRS to the HDT. The findings from this feasibility study can be summarised as follows:

1. The combination of air and CO_2 for use in PDRS exhibited sufficient sensitivity, with an estimated 4 % uncertainty in mixture fraction and temperature. This would enable the use of air as the HDT test gas, mimicking atmospheric re-entry conditions, and reducing cost.

2. The two windows on the HDT provide a limited amount of optical access for implementation of the technique. A suitable method of illuminating the region of interest exists, but would lead to either low quality results, or reduced signal.

3. Elastic scatter from particles in the flow, and from windows on the test section is highly

likely. This can be mitigated using FRS, but would lead to a reduction in signal.

4. A significant reduction in SNR of PDRS can be expected in the HDT, when compared to a bench-top configuration. No sufficient means to mitigate this were available.

Table 9.2: Summary of feasibility study for the application of PDRS to the Oxford HDT. Note that '✓' denotes 'feasible', − denotes ambiguity, and '×' denotes 'unfeasible'

Requirement	Feasible?
Sensitivity of technique	✓
Optical access	−
Particle/surface scatter suppression	−
High SNR	×

Table 9.2 summarises these findings concisely. It is evident from these discoveries that the application of PDRS in the HDT was not feasible, using available resources.

9.2 Improvements to diagnostics

This section elaborates on the steps listed to improve the developed diagnostics.

9.2.1 Fluorescent Particle Image Velocimetry

The use of DEHS for simultaneous velocity and temperature measurements would require:

- High-energy double-pulsed UV laser

  One candidate for this is the Quantel Q-smart Twins, capable of pulsing two laser heads independently, with each head producing a maximum of 90 mJ 266 nm pulses. It has a modular design allowing harmonic generation modules to be bolted on as needed, significantly reducing alignment time and effort. This would allow PIV to be performed while meeting the pulse energy requirement for adequate signals in fluorescence measurements of DEHS.

- Two UV-sensitive intensified or electron multiplying cameras, with at least one capable of PIV-mode imaging

As demonstrated in Chapter 4, using a single camera would work in a split-imaging layout, but two would be easier for accurate image registration and optimised usage of the camera's dynamic range (i.e. independent gain control of R and B signals). Photo-bleaching effects should be considered if utilising the second PIV pulse - this could be avoided by performing thermometry measurements using only the first PIV pulse.

- Aerosol generator producing known and repeatable aerosols of small sized droplets

  The LaVision aerosol generator used in this work is a suitable candidate, but other mono-disperse droplet generators could work well too.

- Filters for fluorescence spectral isolation

  The combination of filters used in this work has been shown to work, but other isolation strategies should be tested for increased temperature sensitivity without compromising on signal strength.

A number of steps can be taken in order to improve signal strength from DEHS:

- Use larger uniform-sized droplets

  A fixed and mono-disperse droplet size distribution is required, as this reduces the signal discrepancy between the smallest and largest droplets. Since fluorescence signal scales with the number of molecules, i.e with d_{p}^3, doubling droplet diameters could lead to 8 times more signal. A consequence of this is a change in the droplet velocity and thermal response, so care should be taken to ensure that these are still adequate for the flow of interest.

- Use larger filters

  This work utilised 1" optics to image signals. Incoherent spontaneous emission is radiated equally in all directions spherically from the point of origin. Higher signals may be obtained by capturing light from a larger collection surface area of this sphere, as more photons will be captured. This means brighter optics with lower f-number and larger diameter filters. Signal scales with area, thus doubling the diameter of the optics will quadruple the signal.

- Use a more sensitive camera

  The intensified camera used in this work has an average quantum efficiency of 20 % across the range of DEHS emission wavelengths. Back-illuminated electron-multiplying CCD cameras can double this.

- Dope DEHS with another tracer

  With the goal of maintaining non-intrusiveness, DEHS' fluorescence signal strength may be improved by doping it with a small quantity of a separate fluorescent tracer. Ideally, tracers with a large absorption cross-section at 266 nm and high fluorescence quantum yield should be chosen, as this would significantly increase attainable signals. A suitable candidate for this is toluene (refer to Table 4.1 for its relevant characteristics). It absorbs strongly at 266 nm and fluoresces at similar wavelengths to DEHS. Toluene also has a very low chance of self-absorption, as there is little overlap between its absorption and emission spectra. Naturally, only small amounts of toluene should be used, as it is toxic and presents a number of other safety hazards. Further work needs to be performed to investigate the fluorescence emission spectra (both in liquid and droplet form), signal enhancement and temperature sensitivity as a result of doping DEHS with varying small amounts of toluene. Note that doping DEHS with another tracer may make the use of DEHS in FPIV unattractive for general audience, due to safety hazard considerations and the need for manual tracer preparation.

9.2.2 Polarised-depolarised Rayleigh scattering

A number of steps are proposed to improve the SNR of this technique:

- Increase laser pulse energy

  Rayleigh signals scale linearly with pulse energy, so the use of a stronger laser can lead to enhanced SNR. For context, the output of the laser used in this work was 650 mJ, while the laser used in the works of Frank et al. [72] output 1.8 J. This is inevitably limited

by available costs, as high energy lasers may be prohibitively expensive. An alternative solution would be to retro-reflect the incident laser sheet onto itself, as shown in Figure 9.4. While this doubles the incident laser energy, the laser sheet energy distribution becomes unsteady, due to beam steering effects. Shot-to-shot laser profile corrections become a necessity as a result.

- Use a more sensitive camera

  The cameras used in Chapter 5 have quantum efficiencies of about 8 % at 532 nm. Newer cameras have significantly larger quantum efficiencies, which can increase Rayleigh SNR. For example, the Teledyne Photometrics Kinetix has a quantum efficiency of 92 % at 532 nm, which is an order of magnitude improvement from the cameras used in this work. As before, higher signal amplification would also be beneficial, but the expected improvement from this is limited by simultaneous noise amplification.

- Use gases with larger scattering cross-section

  Rayleigh signals also scale linearly with effective scattering cross-sectional area. Hydrocarbons are thus the best candidates for strong Rayleigh signals. For example C_2H_6 and C_3H_8 have 6.3 and 12.8 times the scattering cross-section of N_2 at 532 nm, respectively [69]. Naturally, the use of such gases may not be suitable in an application such as transpiration cooling, since these gases have vastly different physical properties to candidate coolant gases. In addition, they can also combust under the right conditions of temperature and pressure.

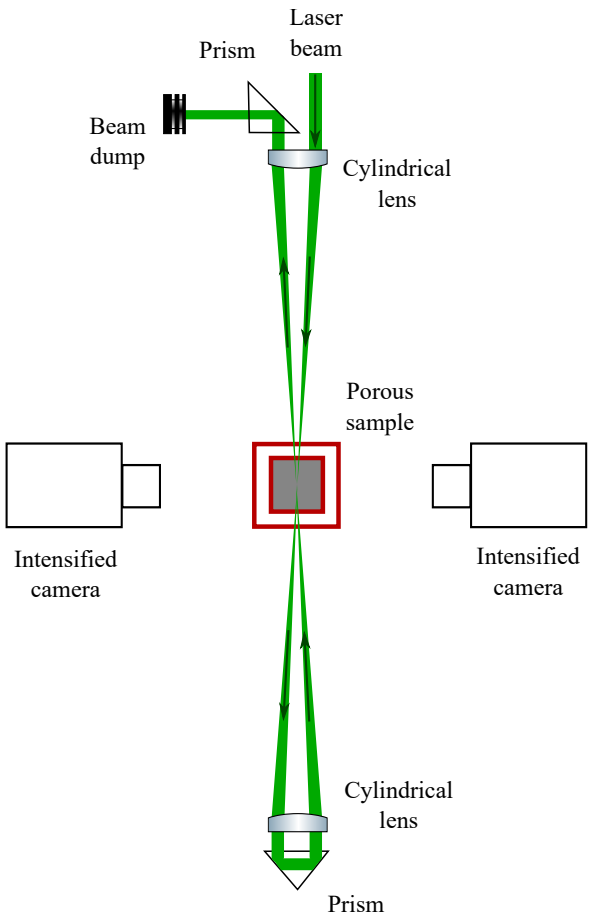


Figure 9.4: Schematic of optical components to retro-reflect a laser sheet. Pulse energy doubles at the intersection of the incident and return beams